

**Modelling Subglacial Erosion and Englacial Sediment Transport  
of the North American Ice Sheets**

by

Dave Henry Degast Hildes

B.Sc. (Honours), Queen's University, 1991

A THESIS SUBMITTED IN PARTIAL FULFILLMENT OF  
THE REQUIREMENTS FOR THE DEGREE OF  
**Doctor of Philosophy**

in

THE FACULTY OF GRADUATE STUDIES  
(Department of Earth and Ocean Sciences)

We accept this thesis as conforming  
to the required standard

**The University of British Columbia**

December 2001

© Dave Henry Degast Hildes, 2001

In presenting this thesis in partial fulfilment of the requirements for an advanced degree at the University of British Columbia, I agree that the Library shall make it freely available for reference and study. I further agree that permission for extensive copying of this thesis for scholarly purposes may be granted by the head of my department or by his or her representatives. It is understood that copying or publication of this thesis for financial gain shall not be allowed without my written permission.

Department of EOS

The University of British Columbia  
Vancouver, Canada

Date DEL. 06, 2001

# Abstract

The glacial geology of North America is a rich resource upon which reconstructions of ice sheets are made. Numerical modelling of ice sheets based on ice physics is an alternate avenue for cryospheric reconstruction. However, such algorithms are unable to draw from the full wealth of geomorphic data because a large-scale forward model of basal processes, necessary to link the ice and the bed, is not available. I develop a process-based model of sediment production, entrainment, deposition and transport to fill this conspicuous gap. Subglacial abrasion is modelled following *Hallet* [1979, 1981] and a quarrying model, dependent on subcritical crack growth, is constructed. Entrainment proceeds predominantly by intrusion into the sediment [*Iverson and Semmens*, 1995] and when basal melt exceeds the rate of entrainment, englacial sediment is deposited. Both vertical redistribution of englacial sediment within an ice column and lateral transport of debris is considered.

Ice entrains loose debris from the bed, transports it downstream and deposits an allochthonous debris train, observable on the modern landscape. This can be modelled when an accurate geologic representation of the bed is used, allowing the exploitation of distinct lithologies as natural tracers of ice motion. Also, incorporation of the differences in physical properties between various lithologies is possible with such a lithologically realistic description of the bed. Several processes are functions of bed topography and a description of small-scale topography within a large-scale grid is required; a downscaling method is therefore developed.

Basal-ice processes must be coupled to both ice sheet conditions and subglacial hydrology. The Marshall-Clarke thermo-mechanical ice sheet model [*Marshall*, 1996; *Marshall and Clarke*, 1997a,b; *Marshall et al.*, 2000] gives the necessary ice sheet fields and provides the forcing for the hydrology model of *Flowers* [2000] which in turn delivers subglacial water pressure, used for both the quarrying and entrainment simulations. Comparisons of model results with the documented large-scale debris trains of Hudson Bay Paleozoic sedimentary rocks and Dubawnt Group detritus are used to test the veracity of the transport model while estimates of paleo-erosion are used to assess the erosion model.

# Contents

<b>Abstract</b>	<b>ii</b>
<b>Contents</b>	<b>iii</b>
<b>List of Tables</b>	<b>vi</b>
<b>List of Figures</b>	<b>vii</b>
<b>List of Symbols</b>	<b>ix</b>
<b>Acknowledgements</b>	<b>xvi</b>
<b>Dedication</b>	<b>xviii</b>
<b>1 Introduction</b>	<b>1</b>
1.1 Evidence of an ice age . . . . .	1
1.2 Modelling an ice age . . . . .	3
1.3 Elements of the basal processes model . . . . .	5
1.4 Thesis objectives and structure . . . . .	7
1.4.1 Scales, weights and measures . . . . .	8
1.4.2 Outline of chapters . . . . .	8
<b>2 Downscaling Bed Slopes</b>	<b>10</b>
2.1 Direct bed slope calculation from DEM data . . . . .	11
2.2 Fractal parameters of bed slope . . . . .	15
2.3 Downscaling methodology . . . . .	16
2.4 Application to North America . . . . .	22
<b>3 Erosion</b>	<b>24</b>
3.1 Abrasion . . . . .	24
3.1.1 Adhesive and abrasive wear . . . . .	24
3.1.2 Glaciological abrasion . . . . .	25
3.1.3 Parameter determination — geological . . . . .	29
3.1.4 Parameter determination — non-geological . . . . .	32
3.2 Quarrying . . . . .	35

3.2.1	Subcritical crack propagation . . . . .	35
3.2.2	Subcritical crack parameter determination . . . . .	37
3.2.3	Effect of topography . . . . .	41
3.2.4	Cavity size . . . . .	47
3.2.5	A quarrying model . . . . .	48
3.2.6	Quarrying sensitivity . . . . .	51
<b>4</b>	<b>Englacial Processes</b>	<b>53</b>
4.1	Entrainment . . . . .	53
4.1.1	Overriding of pre-existing ice . . . . .	55
4.1.2	Freeze-on . . . . .	55
4.1.3	Intrusion by regelation . . . . .	57
4.1.4	Englacial tectonics . . . . .	59
4.1.5	An entrainment model . . . . .	61
4.2	Englacial mixing . . . . .	67
4.2.1	Englacial tectonics — mixing . . . . .	68
4.2.2	Particles in a shear flow . . . . .	69
4.2.3	A mixing model . . . . .	69
4.3	Advection . . . . .	71
<b>5</b>	<b>Model Inputs</b>	<b>74</b>
5.1	Ice model . . . . .	74
5.1.1	Theory . . . . .	74
5.1.2	Examples of the ice sheet model . . . . .	76
5.2	Hydrological model . . . . .	78
5.2.1	Sheet flow . . . . .	78
5.2.2	Groundwater flow . . . . .	80
5.2.3	The aquitard . . . . .	81
5.2.4	Examples of hydrological results . . . . .	83
5.3	Geological inputs . . . . .	84
5.3.1	Bedrock geology . . . . .	84
5.3.2	Surficial geology . . . . .	88
<b>6</b>	<b>Modelled Simulations of North American Ice Sheets</b>	<b>91</b>
6.1	Transport results . . . . .	91
6.1.1	Southward carbonate transport . . . . .	91
6.1.2	Eastward Dubawnt Group transport . . . . .	98
6.2	Erosion results . . . . .	103
6.2.1	Cordilleran erosion . . . . .	103
6.2.2	Laurentide erosion . . . . .	107
<b>7</b>	<b>Conclusions</b>	<b>110</b>
7.1	Summary of work . . . . .	110

7.2 Outlook . . . . .	112
<b>References</b>	<b>114</b>
<b>Appendices</b>	<b>133</b>
<b>Appendix A 2D Stress</b>	<b>133</b>
A.1 Evaluation of state of stress . . . . .	133
A.1.1 Normal loading . . . . .	133
A.1.2 Shear loading . . . . .	137
A.2 Evaluation of failure criterion . . . . .	139
<b>Appendix B Single Clast Rotational Mixing</b>	<b>143</b>
B.1 Perturbation due to a cylinder . . . . .	143
B.2 Steady state rotation . . . . .	147
B.3 Resultant mixing . . . . .	148

# List of Tables

2.1	Details of sub-grid analysis areas . . . . .	12
2.2	Coefficients for downscaling . . . . .	17
3.1	Hardness of geological materials . . . . .	29
3.2	Thermal resistivity of geological materials . . . . .	30
3.3	Parameters for erosion sensitivity test for $Z_r$ . . . . .	31
3.4	Parameters for erosion sensitivity tests for $R$ and $\theta$ . . . . .	34
3.5	$K_I^*$ for various geological material . . . . .	37
3.6	$n_I$ for various geological materials . . . . .	40
3.7	Case details for FRANC2D stress analysis . . . . .	41
3.8	Parameters for stress cross section . . . . .	51
3.9	Parameters for quarrying sensitivity tests . . . . .	52
4.1	Parameters for vertical grid. . . . .	63
5.1	Parameters for ice sheet model . . . . .	77
5.2	Parameters for hydrology model . . . . .	83
5.3	Bedrock types of North America . . . . .	86
5.4	Surficial materials of North America . . . . .	89
6.1	Parameters for model runs . . . . .	94
6.2	Correlation coefficients . . . . .	108

# List of Figures

1.1	Stable oxygen isotope record for the past 2.5 Ma . . . . .	2
1.2	Conceptual diagram of inversion and forward modelling . . . . .	4
1.3	Medial moraines . . . . .	6
2.1	Abrasion sensitivity to $\theta$ . . . . .	10
2.2	Sub-grid analysis areas . . . . .	11
2.3	A sketch showing sub-grid discretization . . . . .	13
2.4	Slope histograms . . . . .	14
2.5	Mean slope scaling . . . . .	15
2.6	Fractal dimension . . . . .	16
2.7	Variance downscaling . . . . .	18
2.8	Fourth moment downscaling . . . . .	19
2.9	Histograms for sampled and downscaled data . . . . .	21
2.10	Corrected and uncorrected dip angles of North America . . . . .	23
3.1	Sketch of local bed dip and velocity components . . . . .	26
3.2	Abrasion sensitivity test for $Z_r$ . . . . .	31
3.3	Grain-size distribution . . . . .	32
3.4	Erosion sensitivity tests . . . . .	34
3.5	Mesh for FRANC2D stress analysis . . . . .	42
3.6	$\sigma_{xx}$ results for the FRANC2D stress analysis . . . . .	44
3.7	$\sigma_{yy}$ results for the FRANC2D stress analysis . . . . .	45
3.8	Sketch of topography simplification . . . . .	46
3.9	Maximum shear stress results for the FRANC2D stress analysis . . . . .	46
3.10	2-D stress cross sections . . . . .	50
3.11	Quarrying sensitivity tests . . . . .	51
4.1	Debris-laden basal ice . . . . .	54
4.2	A sketch of intrusion . . . . .	58
4.3	Entrainment processes . . . . .	62
4.4	Grid for basal ice and sediment . . . . .	64
4.5	Sketch of energy density used in freeze-on calculation . . . . .	66
4.6	Dependence of $\bar{l}_a$ on $C$ . . . . .	67
4.7	A conceptual picture of dispersion by collision. . . . .	70

4.8	A sketch the of <i>Prather</i> [1986] advection scheme . . . . .	72
4.9	An example of the <i>Prather</i> [1986] advection scheme . . . . .	73
5.1	LGM ice sheet reconstruction . . . . .	77
5.2	LGM hydrology reconstruction . . . . .	82
5.3	Bedrock geology . . . . .	85
5.4	Initial sediment depth . . . . .	90
6.1	Bedrock lithology and observed carbonate dispersal in the Hudson Bay area . . . . .	93
6.2	Simulation results of the Hudson Bay carbonate dispersal train . . . . .	95
6.3	Simulation results of the Hudson Bay carbonate dispersal train . . . . .	96
6.4	Simulation results of the Hudson Bay carbonate dispersal train . . . . .	97
6.5	Bedrock lithology and observed Dubawnt Group dispersal in western Nunavut . . . . .	99
6.6	Simulation results of the Dubawnt Group dispersal train . . . . .	100
6.7	Simulation results of the Dubawnt Group dispersal train . . . . .	101
6.8	Simulation results of the Dubawnt Group dispersal train . . . . .	102
6.9	Volume of Cordilleran ice . . . . .	104
6.10	Model results of Cordilleran erosion . . . . .	106
6.11	Model results of continental erosion . . . . .	109
A.1	Sketch of an infinite line of force normal to the plane . . . . .	134
A.2	Sketch of discretization for normal loading convolution integral . . . . .	135
A.3	Sketch of an infinite line of force tangential to the plane . . . . .	137
A.4	Sketch of discretization for tangential loading convolution integral . . . . .	138
A.5	A sketch of $\bar{\sigma}'_N$ versus $\bar{\sigma}_S$ showing a Mohr circle and failure envelope . . . . .	141
B.1	Geometry of rotating cylinder problem . . . . .	144
B.2	Vertical component of total velocity field . . . . .	149

# List of Symbols

Symbol	Description	Units	Page reference
$a, b$	indices of stress tensor	—	
$A$	unit area	$\text{m}^2$	25
$\dot{A}$	areal abrasion rate	$\text{m s}^{-1}$	10, 25, 106, 108
$a, b, c_q^{\text{scale}}$	downscaling coef.	—	17–19
$A_{i,s}^t$	grid transformation parameter	—	63–64
$a_C$	advection polynomial coefficient	$\text{m}^{-3,-4,-5}$	71–72
$A_G$	Glen flow law parameter	$\text{a}^{-1} \text{Pa}^{-3}$	47
$A_L$	subcritical crack growth parameter	$\text{m s}^{-1}$	36, 48–49
$a_m, b_m$	ratios of cell size in mesh segment	—	42
$\dot{A}_v^{\text{abr}}$	volumetric abrasive abrasion rate	$\text{m}^3 \text{s}^{-1}$	25
$\dot{A}_v^{\text{ad}}$	volumetric adhesive abrasion rate	$\text{m}^3 \text{s}^{-1}$	25
$\dot{b}$	mass balance rate	$\text{m s}^{-1}$	74–75
$b^f$	fraction of uncovered bed	—	88–89
$j^{\text{melt}}$	basal melting rate	$\text{m s}^{-1}$	27, 65, 75, 76, 78
$B_0$	Glen flow law parameter	$\text{Pa}^{-3} \text{s}^{-1}$	47, 75, 77
$B_s$	sliding law parameter	$\text{m s}^{-1} \text{Pa}^{-1}$	76, 77, 102
$C$	debris fraction	—	25, 28, 54, 66, 67, 69–73
$C^{\text{reg}}$	max. $C$ for Weertman regelation	—	67
$c_0$	cohesion	Pa	141
$c_i$	specific heat capacity of ice	$\text{J kg}^{-1} \text{K}^{-1}$	56, 65, 75, 77
$d$	depth of sediment	m	28, 48, 67, 81–82, 88–90
$\mathcal{D}$	general data space	—	3–4
$\check{d}$	characteristic depth of sediment	m	28, 49
$\check{d}_0$	coefficient of sediment depth	m	28
$\check{d}_1$	coefficient of sediment depth	m	28
$\mathbf{d}^\circ$	observed data	—	3–4
$\mathbf{d}^P$	predicted data	—	3–4
$d^{\text{reg}}$	max. Weertman regelation layer	m	67

$d^t$	aquitard thickness	m	81–83
$d_{\min}^w$	minimum aquifer thickness	m	81, 83
$D_{\text{col}}$	collisional diffusion parameter	$\text{m}^2 \text{s}^{-1}$	69, 92
$D_{\text{ed}}$	debris eddy-diffusion parameter	$\text{m}^2 \text{s}^{-1}$	68
$\check{D}_{\text{ed}}$	characteristic diffusion parameter	$\text{m}^2 \text{s}^{-1}$	68, 92, 98
$d_{\max}$	maximum initial sediment depth	m	88
$d_{\min}$	minimum initial sediment depth	m	88
$D_{\text{rot}}$	rotational-diffusion parameter	$\text{m}^2 \text{s}^{-1}$	69, 92, 148
$D'_{\text{rot}}$	single rotational-diffusion parameter	$\text{m}^2 \text{s}^{-1}$	69
$D_{\text{thrust}}$	thrust diffusion parameter	$\text{m}^2 \text{s}^{-1}$	68, 92, 98
$D_{\text{tot}}$	total diffusion parameter	$\text{m}^2 \text{s}^{-1}$	69
$\mathcal{E}_{ab}$	excess stress constant	—	48
$E_{\Delta\delta}[-]$	expected value	—	15
$\mathcal{F}$	energy available for freeze-on	$\text{J m}^{-2}$	65–66
$\mathcal{F}^{-1}$	inverse model	—	3–4
$\mathcal{F}^{\parallel}$	activated forward model	—	3–4
$\mathcal{F}^{\perp}$	unactivated forward model	—	3–4
$F^N$	normal load on erosional surface	N	25–27
$\bar{F}^N$	2-D normal boundary forcing	$\text{Pa m}^{-1}$	49–50, 132
$f_{\text{bed}}^N$	viscous drag modifier	—	26
$\bar{F}^S$	2-D tangential boundary forcing	$\text{Pa m}^{-1}$	49–50, 136
$f_{\text{bed}}^T$	viscous drag modifier	—	27
$\mathcal{F}_d$	depth of freeze-on	m	65
$\mathcal{F}_g$	crushing strength modifier	—	49
$\mathbf{g}$	acceleration of gravity	$\text{m s}^{-2}$	
$\mathcal{G}_{ab}^{\parallel}$	Green's function tangential force	$\text{m}^{-1}$	137
$\mathcal{G}_{ab}^{\perp}$	Green's function normal force	$\text{m}^{-1}$	132
$h$	slope and dip class index	—	12
$H^{gw}$	groundwater thickness	m	80–83
$H^{\text{ice}}$	thickness of ice	m	65, 74–76, 132
$H^w$	subglacial sheet thickness	m	78–80
$H_{\text{crit}}^w$	critical sheet thickness	m	79–80, 83, 108
$h_p$	abrading particle hardness	Pa	25, 28, 29, 84–87
$h_s$	abraded surface hardness	Pa	25, 28, 29, 84–87
$i, j$	model-grid indices	—	
$\mathcal{K}$	apparent conductivity of sediment	$\text{m}^2 \text{Pa}^{-1} \text{s}^{-1}$	58–59, 65
$K^{gw}$	aquifer conductivity	$\text{m s}^{-1}$	81, 83
$K^t$	aquitard conductivity	$\text{m s}^{-1}$	81–83

$K^w$	conductivity of sheet	$\text{m s}^{-1}$	78–80
$K_{\text{max}}^w$	max. sheet conductivity	$\text{m s}^{-1}$	79–80, 83
$K_{\text{min}}^w$	min. sheet conductivity	$\text{m s}^{-1}$	79–80, 83
$k_a$	hydraulic conductivity parameter	—	79, 83
$k_{\text{abr}}$	abrasive wear coefficient	—	25, 28–30
$k_{\text{ad}}$	adhesive wear coefficient	—	25
$k_b$	hydraulic conductivity parameter	—	79, 83
$K_{\text{frozen}}$	frozen ground conductivity	$\text{m s}^{-1}$	80, 81, 83
$k_i$	thermal conductivity of ice	$\text{W m}^{-1} \text{K}^{-1}$	56, 58–59, 65, 75, 77
$K_L$	stress intensity factor	$\text{Pa m}^{1/2}$	35–37, 48–49
$K_L^0$	minimum stress intensity factor	$\text{Pa m}^{1/2}$	36
$K_L^*$	critical stress intensity factor	$\text{Pa m}^{1/2}$	35–38, 48–49, 84–87
$K_L^{\sigma N}$	confined critical stress intensity	$\text{Pa m}^{1/2}$	38
$k_r$	thermal conductivity of clast	$\text{W m}^{-1} \text{K}^{-1}$	58–59
$L$	crack mode index	—	36
$l$	lithology index	—	
$l_a$	effective depth of basal ice	$\text{m}$	58, 65–67
$\tilde{l}_a$	array depth modifier	—	66, 67
$l_a^{\text{eq}}$	equilibrium $l_a$	$\text{m}$	65–67
$l_a^{\text{max}}$	max. intrusion per $\Delta t$	$\text{m}$	67
$L_c$	cavity size	$\text{m}$	47–48
$l_c$	half crack length	$\text{m}$	36, 38, 48
$L_c^{\text{max}}$	maximum normalized cavity size	—	47
$L_c'$	normalized cavity size	—	47–48
$L_{\text{fus}}$	latent heat of fusion	$\text{J kg}^{-1}$	26, 58, 65
$l_{i,s}$	model layer thickness	$\text{m}$	63–64
$L_t$	topographical wavelength	$\text{m}$	41, 47–48
$\mathcal{M}$	general model space	—	3–4
$\mathcal{M}_1$	Model 1	—	98–102, 108
$\mathcal{M}_2$	Model 2	—	94, 105–108
$m^N$	slope of normal line forcing	$\text{Pa m}^{-2}$	133
$m^F$	recovered model	—	3–4
$m^S$	slope of tangential line forcing	$\text{Pa m}^{-2}$	137
$m_g$	geometric modifier of $K_L$	—	36
$m, n$	sub-grid indices	—	
$n^{gw}$	aquifer porosity	—	81, 83
$n^s$	porosity of sediment	—	58–59
$n_G$	Glen flow law exponent	—	47, 75, 77

$N_{i,s}$	number of ice or sediment layer	m	63-64
$n_L$	subcritical crack growth exponent	—	36-39, 48-49, 84-87
$N_m$	# of longitudinal sub-grid cells	—	88
$N_{\text{mesh}}$	number of cells in mesh segment	—	42
$N_n$	# of latitudinal sub-grid cells	—	88
$\mathbf{p}$	perturbation velocity field	$\text{m s}^{-1}$	143-146
$\mathcal{P}$	general property	—	15
$P_c$	pressure melting coefficient	$\text{K Pa}^{-1}$	26, 58
$P_{gw}$	groundwater pressure	Pa	80-83
$P_i$	ice overburden pressure	Pa	41, 47-51, 58, 65, 79, 83
$P_w$	subglacial water pressure	Pa	41, 47-51, 58, 65, 78-83, 106
$q$	distribution moment index	—	15-19
$\dot{Q}$	areal quarrying rate	$\text{m s}^{-1}$	48, 106, 108
$\mathbf{Q}^{\text{gw}}$	groundwater flux	$\text{m}^2 \text{s}^{-1}$	80
$\mathbf{Q}^{\text{w}}$	subglacial sheet flux	$\text{m}^2 \text{s}^{-1}$	78
$Q_i$	creep activation energy of ice	$\text{J mol}^{-1}$	47, 75, 77
$\mathbf{q}_i$	heat flux through ice	$\text{W m}^{-2}$	56
$R$	radius of englacial particle	m	10, 26-27, 32-33, 69, 143-148
$r$	grain size index	—	
$r, \theta, z$	polar coordinates	—	
$R^{\text{gas}}$	ideal gas constant	$\text{J mol}^{-1} \text{K}^{-1}$	47, 75
$R_*$	transition radius	m	26-27, 30
$R_e$	radius of the Earth		
$S_c$	crushing strength of ice	Pa	49
$S_s$	shear strength of ice	Pa	49
$t$	time		
$T$	characteristic adfreezing time	s	65
$T_i$	temperature of ice	K	47, 56, 65-76
$T_i^{\text{bed}}$	basal ice temperature	K	75, 76
$T_{\text{pmp}}$	pressure melting point	K	75
$\mathbf{u}$	fluid velocity field	$\text{m s}^{-1}$	143-148
$v_{\text{ext}}$	longitudinal extension velocity	$\text{m s}^{-1}$	27
$\mathbf{v}_i$	ice velocity	$\text{m s}^{-1}$	69, 71-73, 75, 76, 142-144
$\bar{\mathbf{v}}_i$	vertically averaged ice velocity	$\text{m s}^{-1}$	74
$v_L$	mode $L$ crack speed	$\text{m s}^{-1}$	36, 48-49
$v_n$	ice velocity normal to bed	$\text{m s}^{-1}$	26-27
$\mathbf{v}_p$	particle sliding velocity	$\text{m s}^{-1}$	25, 27-28
$v_r$	speed of intrusion	$\text{m s}^{-1}$	58-59

$\mathbf{v}_s$	sliding velocity of ice	$\text{m s}^{-1}$	27, 33, 47, 68, 71–76, 106
$\check{v}_s$	characteristic sliding speed	$\text{m s}^{-1}$	68
$\mathbf{w}$	vorticity field	$\text{s}^{-1}$	144
$\tilde{x}$	coordinate in direction of sliding	—	48
$x'$	convolution integration variable	m	133
$x_a$	general coordinate	—	
$x, y, z$	Cartesian coordinates	—	
$\check{z}$	characteristic depth	m	68
$z^{\text{bed}}$	bed elevation	m	12, 79
$z^{\text{sd}}$	normalized standard deviation	—	17
$Z_r$	thermal resistivity of particle	$\text{m K W}^{-1}$	26, 30–31
$\alpha^{gw}$	aquifer compressibility	$\text{Pa}^{-1}$	81, 83
$\alpha^{\text{ice}}$	ice-surface dip	—	137
$\beta$	velocity gradient	$\text{s}^{-1}$	69, 142–148
$\beta_w$	compressibility of water	$\text{Pa}^{-1}$	80, 83
$\chi$	convolution integration variable	m	135
$\Delta z^{\text{bed}}$	elevation difference	m	15
$\delta_{ab}$	Kronecker delta	—	139
$\Delta \tilde{\phi}$	longitude interval	—	
$\Delta \tilde{\theta}$	latitude interval	—	
$\Delta x$	Cartesian coordinate interval	m	132
$\Delta y$	Cartesian coordinate interval	m	132
$\Delta z$	Cartesian coordinate interval	m	132
$\Delta z^{\text{mix}}$	mixed layer depth	m	69
$\dot{\epsilon}_i$	shear strain rate in ice	$\text{s}^{-1}$	27
$\dot{\epsilon}_i^{\text{bed}}$	shear strain rate of basal ice	$\text{s}^{-1}$	76
$\dot{\epsilon}_{iab}$	shear strain rate in ice	$\text{s}^{-1}$	75
$\epsilon_T$	slide enabling modifier	K	65, 75, 77
$\epsilon_x$	cut-off length for 2-D stress	m	138
$\eta$	effective viscosity	$\text{Pa s}$	26, 33, 143
$\gamma$	arbitrary angle	—	139
$\gamma_q$	fractal dimension of $q^{\text{th}}$ moment	—	15–16
$\lambda^{(a)}$	principal stress	Pa	48–51, 139
$\mu$	rock friction coefficient	—	25, 27, 30
$\check{\mu}_2^{1 \times 10^{-5}}$	parameter for downscaling	—	20
$\mu^{\text{int}}$	internal friction	—	141
$\mu_{\text{ice}}$	internal angle of friction of ice	—	50
$\mu_{\text{int}}$	$K_L^*$ internal coefficient of friction	—	38

$\mu_q^{\Delta\bar{\theta}}$	$q^{\text{th}}$ moment of distribution	—	15–22
$\hat{\nu}_a$	principal axis direction	—	139
$\Omega$	angular velocity	$\text{s}^{-1}$	143–148
$\bar{\phi}$	longitude		
$\phi^{\text{fric}}$	internal angle of friction	—	141
$\phi^{r:a}$	runoff and groundwater exchange	$\text{m s}^{-1}$	80, 82
$\phi^{s:a}$	sheet and groundwater exchange	$\text{m s}^{-1}$	78, 80–81
$\Phi_d$	strain heating	$\text{J m}^{-3} \text{s}^{-1}$	75
$\phi_{\text{grain}}^{\text{mean}}$	mean logarithmic particle size	—	33
$\phi_{\text{grain}}^{\text{sd}}$	standard dev. of log particle size	—	33
$\phi_l^{\text{sed}}$	vertical exchange of sediment	$\text{m s}^{-1}$	71
$\psi$	stream function	$\text{m}^2 \text{s}^{-1}$	144–146
$\psi^w$	hydraulic head	m	78–79
$\rho_i$	density of ice	$\text{kg m}^{-3}$	74, 77
$\rho_r$	density of englacial particle	$\text{kg m}^{-3}$	26–27
$\rho_w$	density of water	$\text{kg m}^{-3}$	78, 80
$\bar{\sigma}_{ab}$	alternate stress tensor	Pa	139
$\bar{\sigma}'_N$	modified normal stress	Pa	141
$\Sigma'_2$	2 <sup>nd</sup> of deviatoric stress	$\text{Pa}^2$	75
$\sigma_{ab}$	stress tensor	Pa	36, 43–46, 74, 132–139
$\sigma'_{ab}$	deviatoric stress tensor	Pa	75
$\sigma_{ab}^{\text{ex}}$	excess boundary stress	Pa	48
$\sigma_N$	normal stress	Pa	38, 139
$\sigma_S$	shear stress	Pa	139
$\sigma_S^{\text{max}}$	maximum shear stress	Pa	45
$\bar{\sigma}_S^{\text{max}}$	modified maximum shear stress	Pa	45, 48–51
$\tau$	basal shear forcing	N	76
$\tau$	basal shear stress	Pa	41, 47–51
$\tau^{\text{ice}}$	shear stress in the basal ice	Pa	27
$\Theta$	$\vartheta$ freq. count	—	17–21
$\theta$	bed dip	—	10–23, 26–28, 33, 45–47, 68
$\acute{\Theta}$	modified $\vartheta$ freq. count	—	20–21
$\acute{\theta}$	modified freq. count of bed slope	—	33
$\check{\theta}$	characteristic bed dip	—	68
$\bar{\theta}$	latitude		
$\theta_{\text{mean}}$	mean bed dip	—	22–23, 28
$\vartheta$	bed slope	—	11–23
$\check{\vartheta}$	parameter for downscaling	—	20

$\vartheta^{ew}$	east-west bed slope	—	12
$\vartheta^{ns}$	north-south bed slope	—	12
$\vartheta^{DS}$	downscaled bed slope	—	17
$\xi_{i,s}$	transformed grid	—	63–64

# Acknowledgements

I have been fortunate in the course of my graduate career. I came to UBC to study glaciology on somewhat of a whim and have often wondered at my luck of landing where I did. Glaciology attracts all types from wild to wonderful and it has been a pleasure to work alongside Urs Fischer, Shawn Marshall, Doug LaPrairie, Alun Hubbard, Jeff Kavanaugh, Gwenn Flowers, Dori Kovanen, Tim Creyts, Fern Webb and Nicholas Lhomme. Garry Clarke, my research supervisor, of course has had an important hand to play and deserves many thanks. He has always given me plenty of line to run with resulting in an eclectic and varied (if not short) graduate experience.

While it was evident that Trapridge would not haunt the pages of this thesis, Garry nevertheless gave me the opportunity to participate in four Yukon field seasons. Trapridge is a magical place that has indelibly marked me. Garry, Alun, Jeff, Gwenn, Kuan-Neng, Thomas and the fine folk at Kluane Base Camp all played a part in brightening the experience.

It was the nature of the people involved in earth sciences that wooed me away from my undergraduate beginnings in chemical physics. I cannot imagine a more stimulating and enjoyable work atmosphere than that which exists in our department. In particular I would like to thank John Amor and Gerry Grieve for their extensive computer support; Chris Wijns and Dave MacMillan for late night jams; Stephane Rondenay, Camille Li and Lara Fletcher for being excellent housemates; Eldad Haber, Phil Hammer, Mathieu Dumberry, Len Pasion and Yuval for being amiable coffee room occupants and ski partners. For the company of Shawn and Gwenn in conferences (inclusive of late night preparations), road- and ski-trips I am grateful. It is not clear whether Alun helped or hindered my doctorate, but there is no doubt he contributed a dose of adventure to my time at UBC which, along with his continued friendship, I value greatly.

I am appreciative that my family have always been accepting of my choices with surprisingly few sniggers along the way. Tracey Wallace has been patient and supportive during my times of thesis angst for which I am thankful. My daughter Micah has helped immensely by being oblivious and always ready to play.

I would like to thank my committee for their input to this thesis. Garry in particular has helped enormously with the polishing of rough drafts. Thanks also to Tim Creyts, Gwenn Flowers and

Kim Goodliffe whose generous editing has improved the final product. Any errors are no doubt last minute inclusions, bypassing all my careful readers. The National Science and Engineering Research Council (NSERC) provided funding for my studies and the Northern Scientific Training Program (NSTP) provided partial support for field research at Trapridge Glacier.

DAVE HENRY DEGAST HILDES

*The University of British Columbia*  
*October 2001*

To the memory of my father who piqued my interest in the North, who instilled a wonderment of wild places and who cultured an interest in the nature of things. My path to glaciology is a direct result of all three.

# Chapter 1

## Introduction

### 1.1 Evidence of an ice age

*In my opinion, the only way to account for all these facts and relate them to known geological phenomena is to assume that ... the earth was covered by a huge ice sheet which buried the Siberian mammoths, and reached just as far south as did the phenomenon of erratic boulders. ... Springs dried up, streams ceased to flow, and sunrays riding over that frozen shore (if they ever reached it) were met only by the whistling of northern winds and rumbling of the crevasses as they opened across the surface of that huge ocean of ice. [Agassiz, 1840, translated by Carozzi [1967]]*

With his assertion that great ice sheets stretched from the Pole to the Mediterranean, Agassiz, a great intellect of his day, established the idea that glacial periods and large climate oscillations occurred in Earth's history (not to mention the eponymous Mt. Agassiz, Manitoba, the ski area of my childhood). He was not alone in recognizing that glaciers alter the landscape, as his peers applied this principle to infer a greater past extent of Alpine glaciers.<sup>1</sup> However it was Agassiz who pushed these ideas forward to invoke large-scale, continental glaciation<sup>2</sup>; the new theory was not well received. Nevertheless, in addition to data provided by his predecessors, Agassiz amassed a large body of corroborating evidence from the Jura mountains and the Alps, the British Isles and North America. This substantial collection of observations comprising erratics and striated

---

<sup>1</sup>The "glacial theory" explained the existence of allochthonous boulders and striated rocks distant from the observed glacier terminus by assuming greater ice extent in the geologic past. It was developed by I. Venetz and J. G. de Charpentier starting in 1818 with a large amount of field evidence. Agassiz was a summer guest of de Charpentier in 1836, where he obtained an introduction to glaciology and de Charpentier's theories.

<sup>2</sup>K. Schimper, Agassiz's collaborator on the theory of continental glaciation, was the first to coin the term "ice-age".

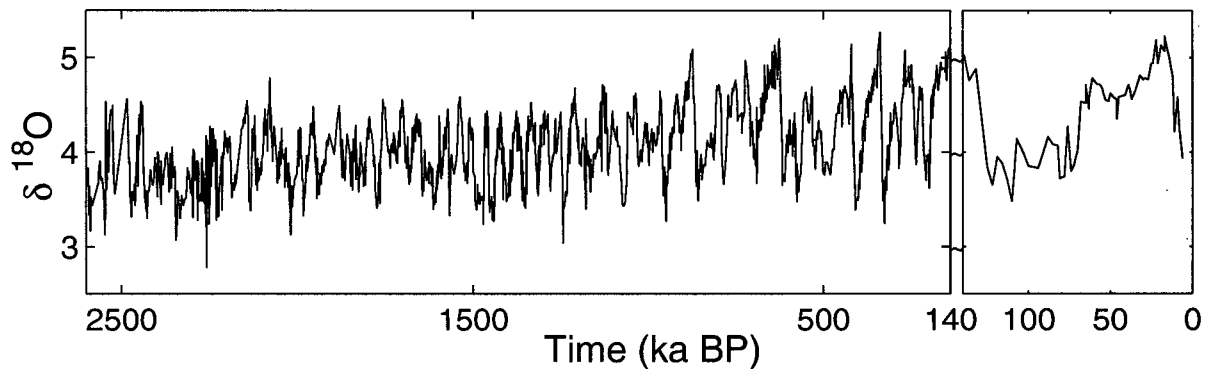


Figure 1.1. The stable oxygen isotope record of benthic foraminifera from Ocean Drilling Program site ODP-677 (1.2°N, 83.73°W) [Shackleton *et al.*, 1990]. As a proxy for global ice volume, the  $\delta^{18}\text{O}$  record suggests an oscillating climate over the past  $\approx 2.5$  Ma coinciding with the period of northern, mid-latitude Pleistocene glaciation. The most recent data, which includes the period modelled in this study, is expanded in scale from 140 ka BP to present.

rocks gave enough credence to the theory that it was eventually accepted as mainstream geology.

Evidence that Earth has undergone many glacial oscillations is plentiful. Deep ocean cores are a rich resource because they contain records of global ice volume, through proxies such as the  $\delta^{18}\text{O}$  stratigraphy<sup>3</sup> (Figure 1.1) obtained by analysing benthic foraminifera. The character of the time series in Figure 1.1 has a marked shift at  $\approx 1$  Ma before present (BP) where the oscillation amplitude increases and a 100 ka cyclicity becomes apparent. In Chapter 6, simulation results are presented from 120 ka BP to present day, encompassing a full 100 ka glacial cycle.

In addition to the wealth of paleoclimatic information recoverable from ocean basins, cores from modern ice sheets provide high resolution coverage of the most recent glacial cycle, the Wisconsin Glaciation. While these data represent the time evolution of quantities at one point in space, the terrestrial evidence for past glaciations has good spatial coverage but poor temporal extent. The terrestrial database, which inspired Agassiz's early ideas, continues to be refined and expanded today.

${}^3\delta^{18}\text{O} = \left[ \frac{(\text{H}_2^{18}\text{O}/\text{H}_2^{16}\text{O}) - (\text{H}_2^{18}\text{O}/\text{H}_2^{16}\text{O})_{\text{SMOW}}}{(\text{H}_2^{18}\text{O}/\text{H}_2^{16}\text{O})_{\text{SMOW}}} \right] \times 1000$  where SMOW is standard mean ocean water.

## 1.2 Modelling an ice age

To examine landforms on the ground and infer the glaciological conditions that created them is a fundamental task of glacial geology. The data — observable landforms — are inverted to give a reconstruction of paleo-ice conditions. This style of qualitative continental-scale reconstruction, pioneered by *Agassiz* [1840], has yielded considerable insight regarding the ultimate Pleistocene glaciation; a sample of Laurentide Ice Sheet reconstructions derived from geomorphic data include those of *Dyke et al.* [1982], *Dyke and Prest* [1987] and *Boulton and Clark* [1990]. Continued debate over the form and evolution of the Laurentide Ice Sheet highlights the nonuniqueness of these reconstructions arising from an ill-posed problem.

Inversion of ill-posed problems is well studied in geophysics, and some of the formalisms developed in this field may be used to identify shortcomings of ice sheet reconstruction. Figure 1.2 is a schematic illustration of the concepts discussed below. Consider a model space  $\mathcal{M}$  with each element<sup>4</sup> represented by a vector  $\mathbf{m}^r$  and a data space consisting of geomorphological observations  $\mathcal{D}$  with each element represented by a vector  $\mathbf{d}^o$  of glacial geology observations. The inverse operator  $\mathcal{F}^{-1}$  maps data space onto model space while the forward operator  $\mathcal{F}$  maps model space onto data space. If the observed data  $\mathbf{d}^o$  are inverted by the operator  $\mathcal{F}^{-1}$  (not generally formalized in glacial geology) to result in two recovered models<sup>5</sup>,  $\mathbf{m}_1^r$  and  $\mathbf{m}_2^r$ , the question must be asked: which model is better?

The most basic test of goodness is whether the predicted data  $\mathbf{d}^p$ , calculated from a recovered model, satisfactorily match the observations  $\mathbf{d}^o$ . To apply this test, a forward operator  $\mathcal{F}$  must be defined such that  $\mathcal{F}[\mathbf{m}^r] = \mathbf{d}^p$ . Herein lies the problem for glacial geology: a rigorous and satisfactory forward model has not been developed.

That an inverse formulation exists with no established forward counterpart may appear surprising; however, note that the processes are hidden from view (by time in the geological sense and by ice in the glaciological sense) and only end results are visible. The absence of a forward algorithm does not diminish the accomplishments of glacial geologists whose work has provided the best picture of ancient ice sheets to date. *Agassiz* knew little of glaciology when developing the ice-age theory and presented it with a far-fetched forward model. Nevertheless, his reconstruction was based on copious observations, which eventually convinced mainstream geologists of the theory's merits. From experience then, we know an insightful reconstruction can be made without a detailed knowledge of the processes involved.

Sophisticated forward models do exist in glaciology and cryospheric numerical modelling is an integral tool for exploring the complex relationship between ocean, ice and atmosphere. The ice

<sup>4</sup>Each element of  $\mathcal{M}$  represents one realization of time-evolving paleoclimatic conditions.

<sup>5</sup>The inversion operator  $\mathcal{F}^{-1}$  is not a 1 : 1 mapping if the dimension of  $\mathcal{M}$  is greater than the dimension of  $\mathcal{D}$ .

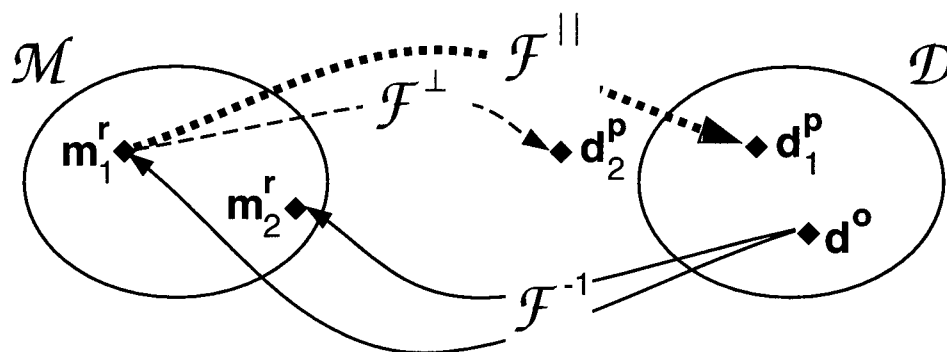


Figure 1.2. A conceptual diagram of inversion and forward modelling.  $\mathcal{M}$  represents model space which is of greater dimension than the data space  $\mathcal{D}$ .  $\mathcal{F}^{\parallel}$  is a forward operator that operates on an element of  $\mathcal{M}$  to predict a data vector  $\mathbf{d}_1^p$  such that  $\mathbf{d}_1^p \in \mathcal{D}$ .  $\mathcal{F}^{\perp}$  operates on an element of  $\mathcal{M}$  to predict a data vector  $\mathbf{d}_2^p$  such that  $\mathbf{d}_2^p \notin \mathcal{D}$ . The inverse operator  $\mathcal{F}^{-1}$  maps an element of data space onto a non-unique element of model space.

and hydrology models described in Chapter 5 are examples of algorithms based on first principles driven by paleoclimatic records and from an element of model space  $\mathbf{m}_1^r$ , associated predicted data  $\mathbf{d}_2^p$  are generated. However, these algorithms predict subglacial water pressure, ice thickness and ice temperature rather than Quaternary geology. The mapping  $\mathcal{F}^{\perp}$  that represents these forward models produce data largely outside the defined data space<sup>6</sup>, therefore glacial geologic observations cannot be directly predicted or used as constraints (Figure 1.2). This view of  $\mathcal{D}$ , comprising only glacial geology data, is selective and other types of observables can be used to partially ascertain the veracity of the models. For example, growing and disintegrating ice sheets produce a measurable visco-elastic response that can be used to impose bounds on paleo-ice thickness [e.g. *Peltier*, 1994, 1996]. Nevertheless, most of our knowledge of Quaternary ice sheets comes from the present-day landscape.

Thus there is a conspicuous gap in the current method of ice sheet reconstruction. A great effort has been made to map glacial features and infer the ice history that produced them. However, this approach is hampered by a shortage of verification tools and a limited temporal extent. Although numerical ice sheet models exist, prediction of glacial landforms is not within their scope; I address this problem by presenting a forward model of basal processes, enabling geological predictions from ice sheet modelling.

<sup>6</sup>Counterexamples exist. The geographical limits of the Wisconsin Glaciation are geomorphic data that can be predicted by ice physics algorithms.

### 1.3 Elements of the basal processes model

The erosive prowess of glaciers is well-documented, though widely debated, in the literature [e.g. *Laine*, 1980; *Bell and Laine*, 1985; *Nesje and Whillans*, 1994; *Hallet et al.*, 1996; *Elverhøi et al.*, 1998]. Although without the detail or quantitative weight of the aforementioned glacial erosion studies, none match the imagery of *Ball* [1906]:

*An ice-sheet, ponderous in mass and irresistible in power, forms a destructive engine of almost illimitable capacity; by its influence fragments of the living rock are ripped from their bed, crushed to pieces, reduced to mud.*

While avoiding the question of animate rocks, I seek to defuse the *illimitable capacity* of glacial erosion through a model that predicts (most often) finite results.

Glacial erosion is known to be selective rather than irresistible because it depends on the thermal basal regime. Cold-bedded glaciers are poor excavators compared to warm-bedded<sup>7</sup> ones [*Sugden*, 1978]. Preglacial landscapes that survive ice coverage relatively unchanged have primarily supported cold-bedded ice [*Dyke*, 1993; *Kleman*, 1994]. In addition to the thermal regime, erosive potential is also controlled by englacial debris content; glaciers need tools to abrade. This was apparent to the eminent glaciologist James Forbes who wrote,

*It is not the wheel of a lapidary which slits a pebble, but the emery with which it is primed. The gravel, sand and impalpable mud are the emery of the glacier.* [*Forbes*, 1845]

I develop a process-based forward model, consistent with these controls (among others), to calculate erosion. Model results are compared to geological estimates of erosion.

After the modelled sediment is produced, there are several possibilities for its evolution. It may remain at the glacier bed, protecting the underlying bedrock from further erosive assault, or it may be entrained into the ice. Englacial debris is subject to redistribution processes that reorganize the sediment in the ice column and deposit it as till. Lateral advection with the ice flow yields modelled dispersal trains that are compared to observed debris trains.

In general I use Occam's razor sparingly, and consider a great number of processes and associated parameters. This approach is appropriate in a study where there is little prior work to act as guidance on process significance. In addition, the subglacial conditions varied wildly over the

<sup>7</sup>A glacier that is warm-bedded is at the pressure melting point at its bed.

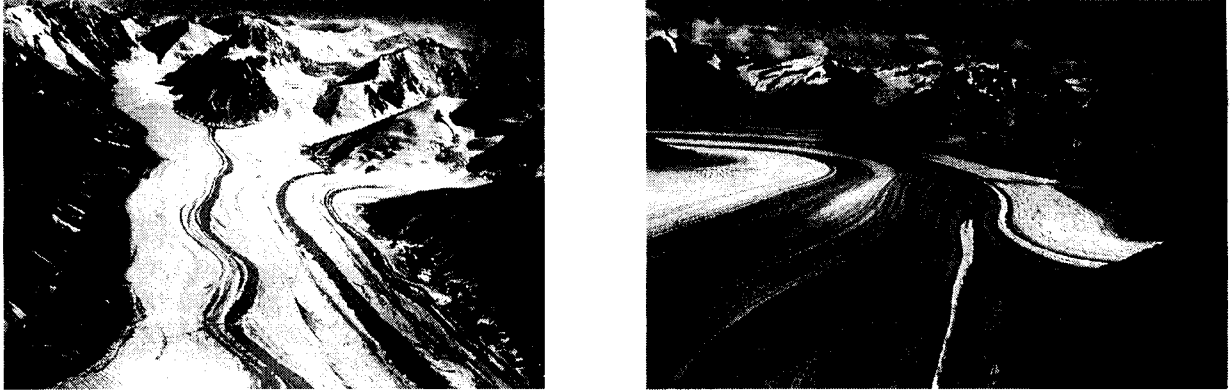


Figure 1.3. Medial moraines on the Kaskawalsh Glacier, St. Elias Range, Yukon Territory. Under present ice conditions, supraglacial moraines are a significant debris transport mechanism. In a climate that produces a large enough ice volume to drown the exposed rock, this mechanism would become unimportant.

modelled domain and period; to determine a priori that a process will remain insignificant over the entire domain for a complete glacial cycle is not a trivial task. I therefore favour a complete, if slightly bloated, model over a sparse one.

### Excluded processes

This thesis is by no means exhaustive in the analysis of geomorphic features. I present a forward model for sediment transport arising from basal-ice processes, though there are other means of sediment dispersion. On modern glaciers, medial moraines carrying debris of subaerial provenance<sup>8</sup> are ubiquitous; a model of debris transport by medial moraines is presented by *Anderson* [2000]. Figure 1.3 illustrates that this process can be effective only when valley walls and nunataks are exposed. As ice volume grows and engulfs mountaintops, debris generated by mass wasting will be increasingly insignificant, especially in areas of low relief. Therefore it is not a serious limitation to assume that supraglacial debris transport is unimportant in this study. A notable exception is the Cordillera, characterized by high relief and variable climate throughout the Wisconsinan, where this assumption is suspect<sup>9</sup>.

A more serious omission in this thesis is the debris transport by sediment deformation. Subglacial sediment deformation accounts for an estimated 90% of the total motion of Breidamerkurjökull, Iceland [*Boulton and Jones*, 1979] and is thought to be the cause of fast flow at Ice Stream B, Antarctica [*Blankenship et al.*, 1986; *Alley et al.*, 1986, 1987]. *Clarke* [1987], *Jenson et al.* [1995,

<sup>8</sup>distinct from the supraglacial debris originating from thrust faults, discussed in Section 4.1.4

<sup>9</sup>A well-documented example of a debris train of subaerial provenance is the belt of angular erratics extending in excess of 1000 km from their source area, the Athabasca Valley [*Prest and Nielsen*, 1987].

1996] and *Boulton* [1996] present models of deforming-sediment transport and several recent continental-scale simulations include fast flow caused by basal sediment deformation [*Clark et al.*, 1996; *Marshall and Clarke*, 1997a,b].

Despite the acknowledged occurrence of sediment deformation in some cases, neglecting it does not necessarily compromise the sediment transport model or the results. Sliding and sediment deformation compete with each other and depend on the ice-bed coupling strength at the ice-bed interface. A well-coupled ice-bed interface promotes sediment deformation while a decoupled interface serves to enhance sliding. These two modes of glacier motion are generally observed to be out of phase at Trapridge Glacier, Yukon Territory [*Kavanaugh*, 2000]. Since both mechanisms are dependent on basal shear stress but only one is active at a time, it is not disastrous in most instances to assume all basal transport occurs by sliding. Following *Marshall et al.* [2000] I do include a sediment enhancement factor for sliding, designed to represent ice motion from basal deformation (Section 5.1.1).

The most serious errors arising from this omission will occur when sliding and sediment deformation do not act in concert. For example, high subglacial water pressure inhibits sediment entrainment and by consequence basal-ice transport, but enables sediment failure and subglacial transport. An accurate partitioning of sliding versus sediment deformation would require knowledge of the basal boundary condition which is not generally available on a large scale. In areas where there is strong geological evidence for prolonged fast flow enabled by sediment deformation, an advective model such as that presented by *Jenson et al.* [1995, 1996] would be a more suitable choice than the sediment transport model presented here.

## 1.4 Thesis objectives and structure

The subglacial landscape is hidden from view and direct observation is both costly and logistically challenging; this has limited our understanding of subglacial operation. The primary aim of this thesis is to advance the theoretical description of subglacial processes at the continental scale. As part of this work I refine relevant parameter values through numerical experiments.

Through accurate lithological representation of the bed and careful tracking of each lithological component, the basal transport model is predictive of glacial erratics data — long recognized as one of glacial geology's most tractable archives. Mapped subglacially derived debris trains can now be more rigorously exploited to constrain numerical reconstructions of ice sheets.

### 1.4.1 Scales, weights and measures

The Late Pleistocene ice examined in this study was extensive, covering almost all of Canada; Figure 5.1 on page 77 shows the modelled ice extent at LGM (Last Glacial Maximum). In order to simulate a continental-scale problem, current computing power demands a relatively coarse spatial grid. The grid size chosen for this project is  $120 \times 1^\circ$  meridional cells and  $100 \times 0.5^\circ$  zonal cells, corresponding to  $\approx 55$  km zonal resolution.

This coarse grid creates a problem of disparate scales. To include physical processes that operate on much smaller scales than the grid, I develop methods to incorporate sub-grid scale information. Throughout this thesis, the indices  $i, j$  are reserved for model cell longitude and latitude while  $m, n$  are used for sub-grid indexing.

System Internationale (SI) units are mostly used in the text and these are the internal units of the algorithms developed to produce the results presented throughout this thesis. However these are not always the most intuitive units for the reader and often non-SI units (particularly annum) appear in the text where their use is justified by familiarity and tradition.

### 1.4.2 Outline of chapters

Between the introductory and concluding chapters, this thesis consists of three model development chapters, one chapter describing model inputs and one chapter summarizing simulation results. Details of a 2D stress analysis and the fluid velocity solution of a rotating cylinder in a viscous shear flow are appended to the body of this thesis. The main chapters are outlined below.

Scaling is a theme that threads through the thesis, as small-scale processes must be accounted for within the framework of the continental-scale study area. Chapter 2 explores the scaling of topography; a downscaling method is developed to transform calculated bed slopes from coarse-scale sampling to an estimate of the result that fine-scale sampling would yield. It is calibrated with six areas where both coarse and fine data are available and then applied to the complete study domain.

Erosion of the glacier bed is the topic of Chapter 3. There are two distinct mechanisms that cause subglacial erosion: abrasion and quarrying, addressed in Sections 3.1 and 3.2 respectively. Current glacial abrasion theory is reviewed and extended in Section 3.1.2, followed by a discussion of parameter determination. Subcritical crack growth, the controlling process of quarrying, is examined as are its associated physical parameters. For both abrasion and quarrying, sub-grid information is extracted from geological data sets. The effect of topography on quarrying is explored and the role of cavities is quantified. A quarrying model is presented at the end of the

chapter.

In Chapter 4, the discussion moves upward from the bed to address processes that occur in basal ice. Modes of entrainment are reviewed and quantified in Section 4.1, followed by an examination of englacial debris redistribution mechanisms. Section 4.2 explores vertical redistribution through mixing while lateral transport by advection is considered in Section 4.3.

A large amount of debris may be an island but the debris model is not and cannot exist in isolation but must be connected with auxiliary models. These are the ice and hydrology input models, which are both physics-based, predictive, forward models developed by *Marshall* [1996] and *Flowers* [2000] respectively; a brief overview of these is given in Sections 5.1 and 5.2. Geological Survey of Canada (GSC) maps [*Fulton*, 1996; *Wheeler et al.*, 1997] are used to cast the geology of Canada into a form compatible with the terrestrial model. This facilitates the sub-grid parameterizations of Chapter 3 as well as enabling lithological tracking in the englacial transport model developed in Chapter 4.

Chapter 6 contains simulation results for the Wisconsin Glaciation (120 ka BP to present). The eastward transport of the Dubawnt red beds in western Nunavut and the southern transport of Paleozoic carbonates of the Hudson Bay area are contrasted with simulated debris transport in Section 6.1. Finally, geological estimates of paleo-erosion come from a number of sources and are compared to modelled results in Section 6.2.

Modelling a system as complex as the cryosphere, comprising ice, climate, water and terrain components, requires an integrated approach. The final result of this thesis is a union of the individual state-of-the-art models into a single, self-consistent forward model of the North American cryosphere through the last glacial cycle.

## Chapter 2

# Downscaling Bed Slopes

Scaling issues are endemic in ice sheet modelling; variables that control important physical processes change at scales much smaller than those that are computationally tractable for large-scale models. One problematic variable is the bed dip  $\theta$  appearing in the basic erosion laws detailed in Chapter 3. Note that  $\theta$  is the surface dip of the bed, not the dip of sub-bed internal strata; this is illustrated in Figure 3.1 on page 26. As seen from Figure 2.1, the variation of  $\theta$  gives rise to over an order of magnitude change of the abrasion rate.

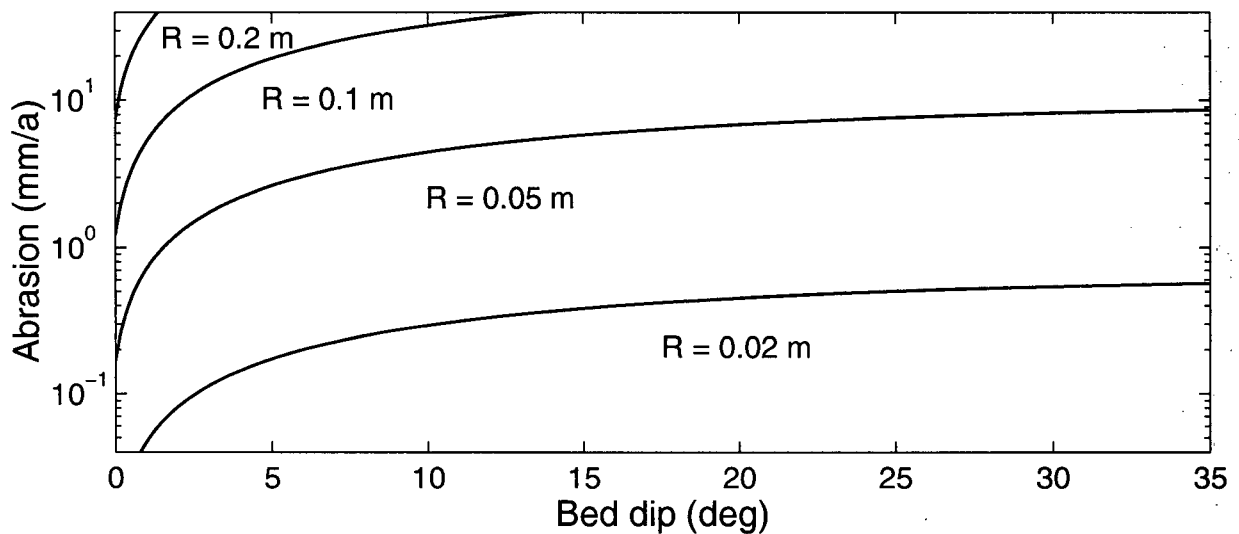


Figure 2.1. Abrasion rate versus bed dip for various grain sizes  $R$ . The abrasion is calculated by Equation (3.12) using the method developed in Section 3.1. The effective viscosity  $\eta$  is taken as  $1 \times 10^6$  Pa s and the thermal resistivity  $Z_r$  as  $0.3$  m K W $^{-1}$  with other parameters identical to those in Tables 3.3 and 3.4 on pages 31 and 34.

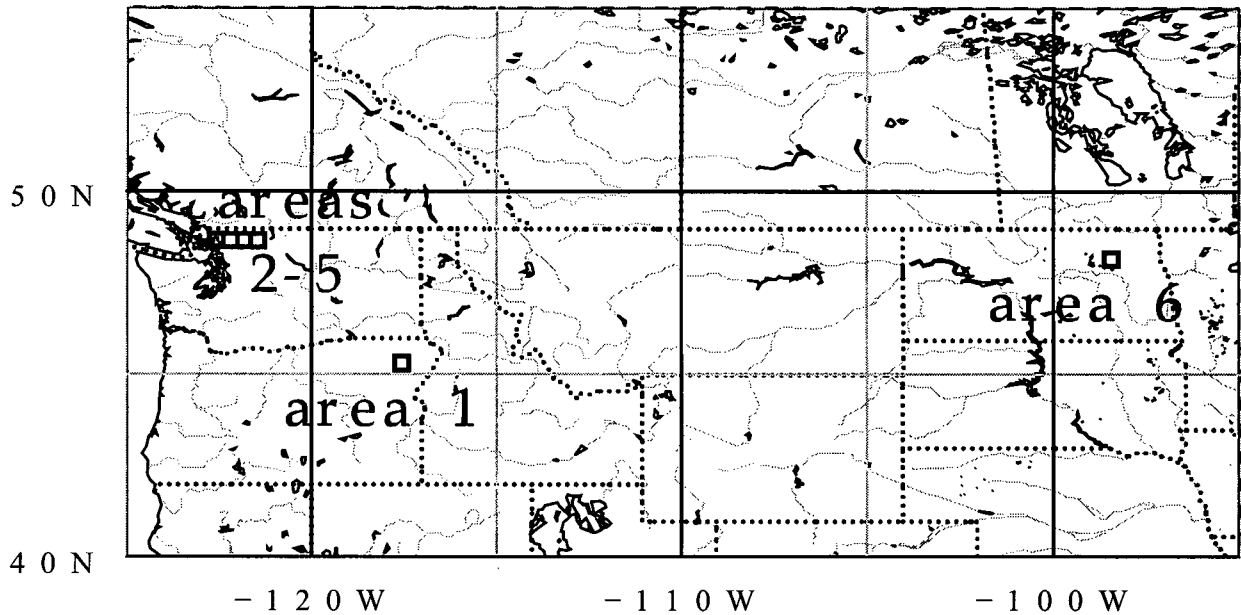


Figure 2.2. Areas (denoted by small boxes) on which sub-grid bed slopes are analysed to determine a slope downscaling relationship. Table 2.1 gives further details.

Existing meso- and large-scale erosion models rely on two static values of  $\theta$  (one for abrasion, the other for quarrying) regardless of cell topography [Tulley, 1995] or use simplified erosion laws with no  $\theta$  dependence [e.g. Oerlemans, 1985; MacGregor et al., 2000]. An accurate description of the bed dip without having to resort to untenably fine grids is desirable. This is achieved through direct calculation of bed slope  $\vartheta$  (related to the bed dip through  $\theta = \tan^{-1} \vartheta$ ) from a digital elevation model (DEM) followed by a downscaling procedure.

## 2.1 Direct bed slope calculation from DEM data

To calculate bed slope, a digital elevation model is needed. The finest comprehensive data set available for North America is a 1000 m DEM [Geophysical Data Center, 1998]. However, erosion processes act at scales much less than 1000 m; the equations for erosion are appropriate on scales of 1 → 10 m. A method to downscale the calculated bed slopes from the 1000 m sampling to an appropriate scale is paramount. To elucidate such a downscaling relationship, elevation sampling and direct bed slope calculation is done at a variety of sub-grid cell sizes in select areas where 30 and 10 m DEMs [EROS Data Center, 2000] are available to extend the analysis. Six areas are used, shown in Figure 2.2, each  $0.375^\circ \times 0.375^\circ$ ; Table 2.1 details the selected areas.

The 1000 m data uses a Lambert conformal conic projection, while the 30 and 10 m data use universal transverse Mercator (UTM) coordinates (Zones 10, 11 and 14). These are projected

Area	State	Longitude	Latitude	Data
1	OR	117.750° W	45.125° N	1000, 30
2	WA	122.375° W	48.500° N	1000, 30 & 10
3	WA	121.625° W	48.500° N	1000, 30 & 10
4	WA	122.750° W	48.500° N	1000, 30 & 10
5	WA	122.000° W	48.500° N	1000, 30 & 10
6	ND	98.625° W	48.000° N	1000, 30

Table 2.1. Details of the selected areas used to determine a slope downscaling relationship. Longitude and latitude are given for the south-west corner of each  $0.375^\circ \times 0.375^\circ$  area. The data sets used are a 1000 m DEM [Geophysical Data Center, 1998], 30 m DEM [EROS Data Center, 2000] and 10 m DEM [EROS Data Center, 2000]; the 10 m data are not universally available. Figure 2.2 shows a location map.

to geographical coordinates and resampled to a specified cell size using standard ARC-INFO packages with cubic interpolation. The elevation  $z^{\text{bed}}$  is sampled at the cell centre of each  $(m, n)$  sub-grid cell and north-south and east-west slopes are calculated on the nodes using the following 4-point stencil with second order accuracy,

$$\vartheta_{m,n}^{\text{ns}} = \frac{1}{2R_e} \left[ \frac{z_{m-\frac{1}{2},n+\frac{1}{2}}^{\text{bed}} - z_{m-\frac{1}{2},n-\frac{1}{2}}^{\text{bed}}}{\Delta\tilde{\theta}_{m-\frac{1}{2},n}} + \frac{z_{m+\frac{1}{2},n+\frac{1}{2}}^{\text{bed}} - z_{m+\frac{1}{2},n-\frac{1}{2}}^{\text{bed}}}{\Delta\tilde{\theta}_{m+\frac{1}{2},n}} \right], \quad (2.1a)$$

$$\vartheta_{m,n}^{\text{ew}} = \frac{1}{2R_e \sin(\pi/2 - \tilde{\theta}_{m,n})} \left[ \frac{z_{m+\frac{1}{2},n-\frac{1}{2}}^{\text{bed}} - z_{m-\frac{1}{2},n-\frac{1}{2}}^{\text{bed}}}{\Delta\tilde{\phi}_{m,n-\frac{1}{2}}} + \frac{z_{m+\frac{1}{2},n+\frac{1}{2}}^{\text{bed}} - z_{m-\frac{1}{2},n+\frac{1}{2}}^{\text{bed}}}{\Delta\tilde{\phi}_{m,n+\frac{1}{2}}} \right], \quad (2.1b)$$

where  $R_e$  is the radius of the Earth. Discrete slopes categories are defined and frequency histograms are made of all  $\vartheta_{m,n}^{\text{ns}}$  and  $\vartheta_{m,n}^{\text{ew}}$  that fall within the  $0.375^\circ$  square. Figure 2.3 is a sketch illustrating the above.

The histograms are made with slope divisions of 0.012. There are 200 slope categories indexed by  $h$  from  $-1.2$  to  $+1.2$  (corresponding to  $\pm 50^\circ$  for the discrete dip classes); this even distribution in  $\vartheta$  space achieves the desired concentration of dip divisions close to zero in  $\theta$  space. Histograms for areas 3, 4 and 5 using a sample spacing of  $0.01875^\circ$  from the 1000 m data and  $0.003^\circ$  from the 30 m data are shown in Figure 2.4. A cell size of  $0.01875^\circ$  gives  $20 \times 20$  sub-grid blocks within the  $0.375^\circ$  test area which is enough for a reasonable statistical analysis, while  $0.003^\circ$  sampling gives  $125 \times 125$  sub-grid blocks. The most obvious difference between the two sets of histograms is that finer sampling yields more extreme slope representation: the coarse sampling of data results in underestimating the variability of the slope distribution. This effect must be quantified in order to downscale.

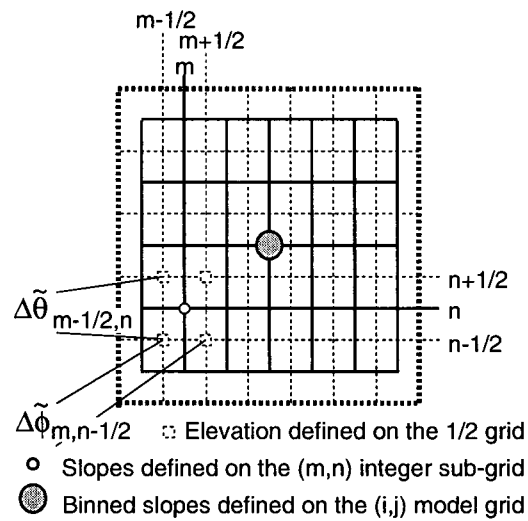
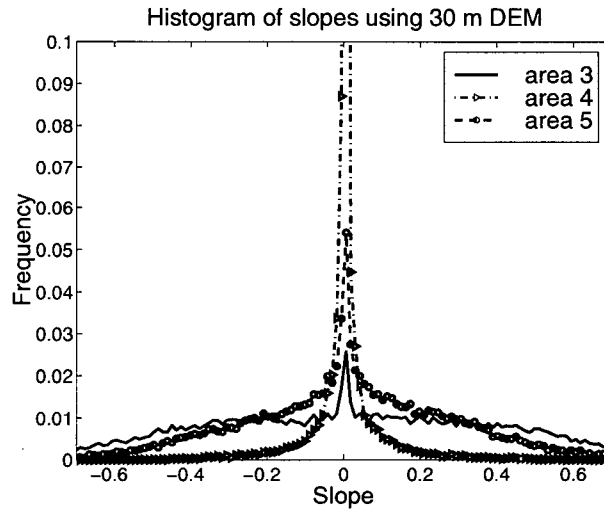
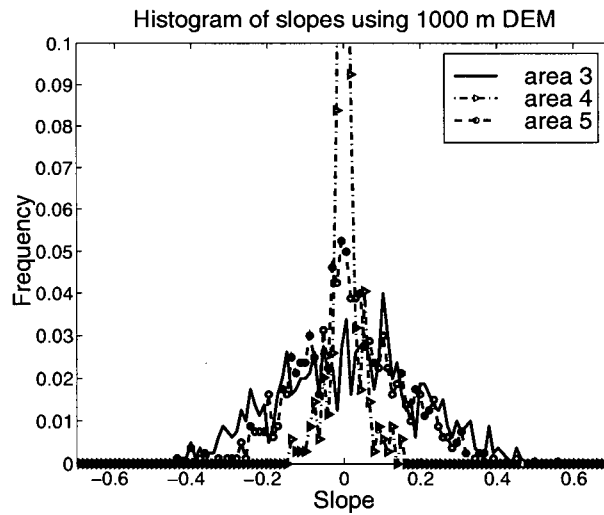


Figure 2.3. A sketch (in latitude  $\tilde{\theta}$  and longitude  $\tilde{\phi}$ ) showing the sub-grid scale in light dashed lines on which the elevations are sampled and solid lines where the slopes are calculated. The heavy dashed line denotes a  $0.375^\circ \times 0.375^\circ$  area which is comparable to the model grid cell — frequency histograms are summed within this block.



(a) Cell size =  $0.003^\circ$ , giving 15625 ( $125 \times 125$ ) cells in the  $0.375^\circ$  test block.



(b) Cell size =  $0.01875^\circ$ , giving 400 ( $20 \times 20$ ) cells in the  $0.375^\circ$  test block.

Figure 2.4. Slope (average north-south and east-west) histograms from a 30 m DEM in (a) and a 1000 m DEM in (b). The histograms are formed with discrete slope bins of 0.012. Positive slopes have southern and western aspects.

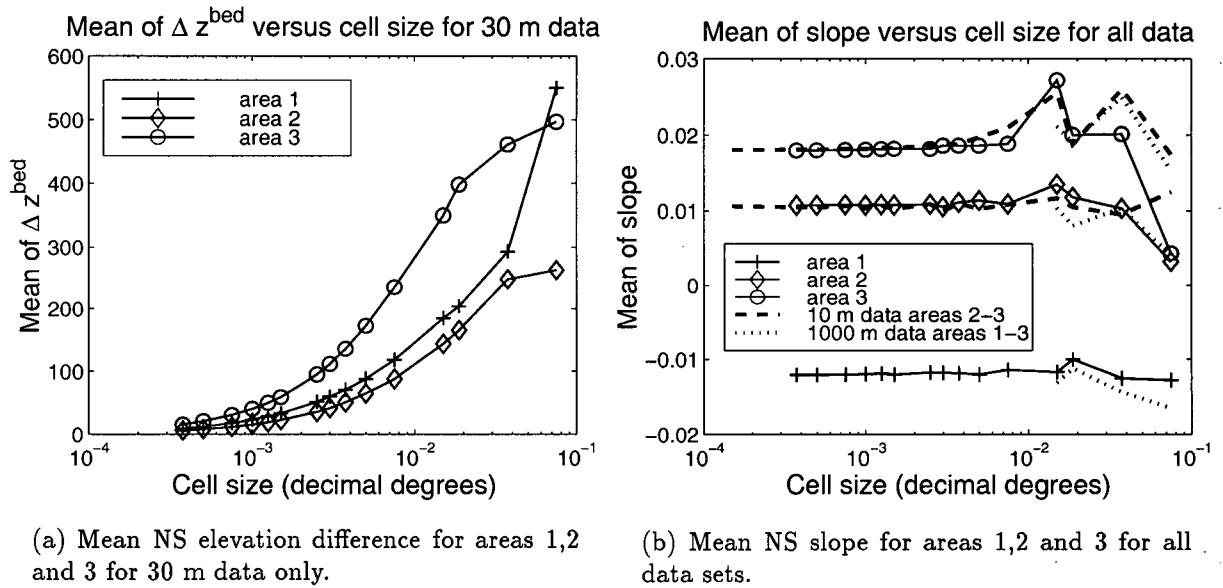


Figure 2.5. The mean slope is approximately stationary with scale while the mean elevation difference is not; therefore bed slope is the preferred variable over elevation difference.

## 2.2 Fractal parameters of bed slope

Downscaling is often quantized through the assumption of exponential, or fractal behaviour [e.g. *Dubayah et al.*, 1997]). For example if the distribution of a property  $\mathcal{P}$  measured with a cell size  $\Delta\tilde{\theta}$  has an expected variance  $E_{\Delta\tilde{\theta}}[\text{var}(\mathcal{P})]$  then a fractal scaling relationship would be

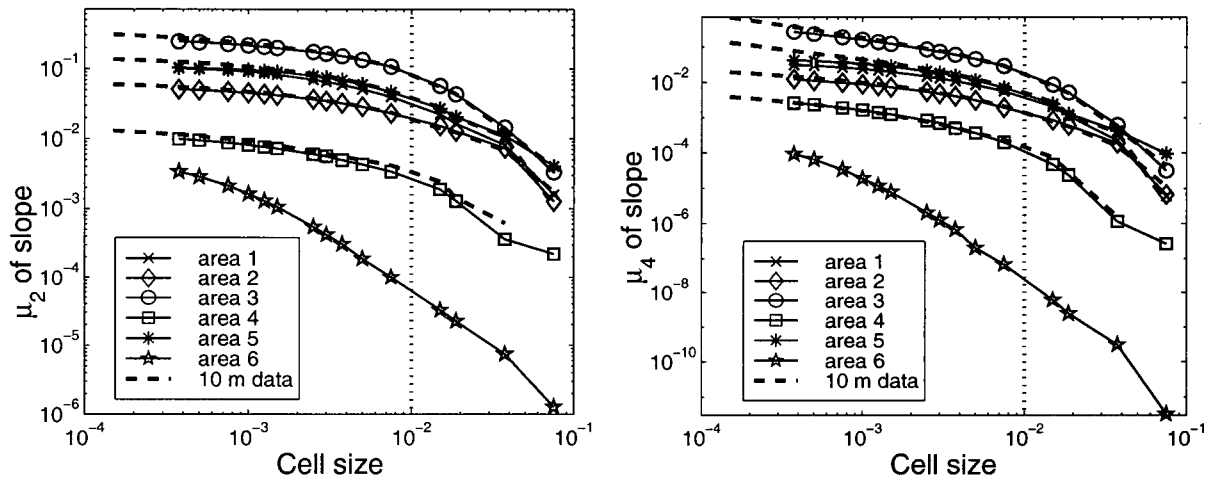
$$\frac{E_{(\Delta\tilde{\theta})_1}[\text{var}(\mathcal{P})]}{E_{(\Delta\tilde{\theta})_2}[\text{var}(\mathcal{P})]} \propto \left( \frac{(\Delta\tilde{\theta})_1}{(\Delta\tilde{\theta})_2} \right)^{\gamma_{\text{var}}} \quad (2.2)$$

where  $\gamma_{\text{var}}$  is the fractal dimension for the variance. This can be extended to any  $q^{\text{th}}$  moment of the distribution (for  $q \geq 2$ ) by

$$\mu_q^{\Delta\tilde{\theta}} = E_{(\Delta\tilde{\theta})}[(\mathcal{P} - \text{mean})^q] \quad (2.3)$$

which would have a fractal dimension  $\gamma_q$ . Note that when  $q = 2$ , (2.3) is equivalent to the definition of the variance, thus  $\gamma_2 \equiv \gamma_{\text{var}}$ . A simple scaling relationship is sought and it is desirable to work with a distribution where the mean of  $\mathcal{P}$  is constant with scale (i.e.  $\gamma_1 = 0$ ) such that  $\mathcal{P}$  is the only non-stationary variable in (2.3). The gradient of the elevation, or bed slope, rather than direct elevation difference satisfies this criterion as shown by Figure 2.5.

To test the appropriateness of (2.2), each area is sampled with a variety of sub-grid cell sizes: the 1000 m data are sampled at  $0.075 \rightarrow 0.015$  deg, the 30 m data at  $0.075 \rightarrow 3.75 \times 10^{-4}$  deg and



(a) A log-log plot of variance against cell size to show fractal dimension.

(b) A log-log plot of the fourth moment against cell size to show fractal dimension.

Figure 2.6. The break in slope at cell size  $\approx 10^{-2}$  deg shows that (2.2) does not hold over the range of scales considered.

the 10 m data at  $0.075 \rightarrow 1 \times 10^{-4}$  deg. A log-log plot of the  $q^{\text{th}}$  moment of bed slope versus the cell size should result in a straight line of slope  $\gamma_q$  if (2.2) holds.

Figure 2.6 indicates that the scaling of  $\mu_2$  (the variance) and  $\mu_4$  do not have a constant  $\gamma_q$  over the range of sample scales; there is a break in slope at a cell size of approximately  $0.01^\circ$  (corresponding to 1.1 km of latitude). This is suggestive of the break between “short” and “long” scales at  $\approx 0.6$  km seen by a number of authors in topographic data [e.g. *Mark and Aronson, 1984; Chase, 1992; Lavallée et al., 1993*]. The fractal dimension plot for area 6 has a markedly different form from the other curves in Figure 2.6: the others are translations of a master curve while area 6 marches to its own tune. This is not surprising as it is the only area in the group in the plains and completely covered by sediments.

### 2.3 Downscaling methodology

Because of the difficulties introduced by the scale-break in the data, (2.2) is not assumed to hold and I take an empirical approach. Plots of  $\mu_q$  against cell size, extracted from the finest resolution DEM (either 10 or 30 m), are extrapolated to  $1 \times 10^{-5}$  deg; this is  $\approx 1$  m in latitude, an estimate of the scale on which erosion acts. For each test area  $\mu_q^{0.01875}$  from the 1000 m data set is plotted against  $\mu_q^{1 \times 10^{-5}}$  from the extrapolation; a second order polynomial is fit and results

	$a_q^{\text{scale}}$	$b_q^{\text{scale}}$	$c_q^{\text{scale}}$
$q = 2$	$1.797 \times 10^2$	4.102	$6.025 \times 10^{-3}$
$q = 4$	$1.171 \times 10^5$	-27.966	$4.243 \times 10^{-3}$

Table 2.2. Coefficients for equation (2.4). They are the coefficients for best fit 2<sup>nd</sup> order polynomials from Figures 2.7(c) and 2.8(c) for  $\mu_2$  and  $\mu_4$  respectively.

in a downscaling relationship

$$\mu_q^{1 \times 10^{-5}} = a_q^{\text{scale}} (\mu_q^{0.01875})^2 + b_q^{\text{scale}} \mu_q^{0.01875} + c_q^{\text{scale}}. \quad (2.4)$$

The 2<sup>nd</sup> and 4<sup>th</sup> moments of the 10 and 30 m data are plotted in Figures 2.7(a) and 2.8(a) along with the extrapolation to  $1 \times 10^{-5}$  deg; the 1000 m data are shown in Figures 2.7(b) and 2.8(b). The shaded points ( $1 \times 10^{-5}$  and 0.01875 deg) are plotted against each other in Figures 2.7(c) and 2.8(c) with the best fit second order polynomial; the coefficients are listed in Table 2.2. A similar analysis is not shown for  $\mu_3$  because there is wider disagreement between the different data sets and a second order polynomial does not satisfactorily describe the downscaling relationship. A possible explanation is that  $\mu_3$  describes a directional property. This would be strongly influenced by factors that are specific to each area (e.g. predominant geological strike) and therefore no global rule would be applicable.

Once it is known how the moments change with scale, the distribution can be downscaled. In every model grid cell  $(i, j)$ , each slope class  $h$  has a normalized standard deviation  $z_h^{\text{sd}}$  associated with  $\vartheta_h$  through

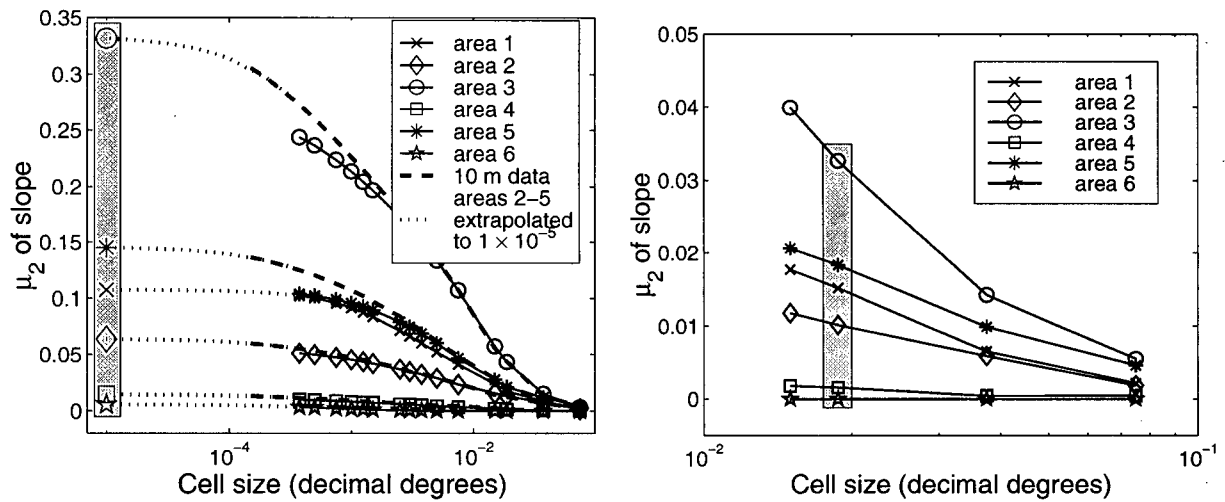
$$z_h^{\text{sd}} = \frac{\vartheta_h - \mu_1}{\sqrt{\mu_2^{0.01875}}}. \quad (2.5)$$

Recall from Figure 2.5 that the mean  $\mu_1$  is independent of cell size. The frequency count for each component of  $z_h^{\text{sd}}$  remains constant through the downscaling procedure; however the slope classes are modified through  $\mu_2^{1 \times 10^{-5}}$ , the downscaled variance from (2.4). The downscaled slope classes are given by

$$\vartheta_h^{\text{DS}} = z_h^{\text{sd}} \sqrt{\mu_2^{1 \times 10^{-5}}} + \mu_1 \quad (2.6)$$

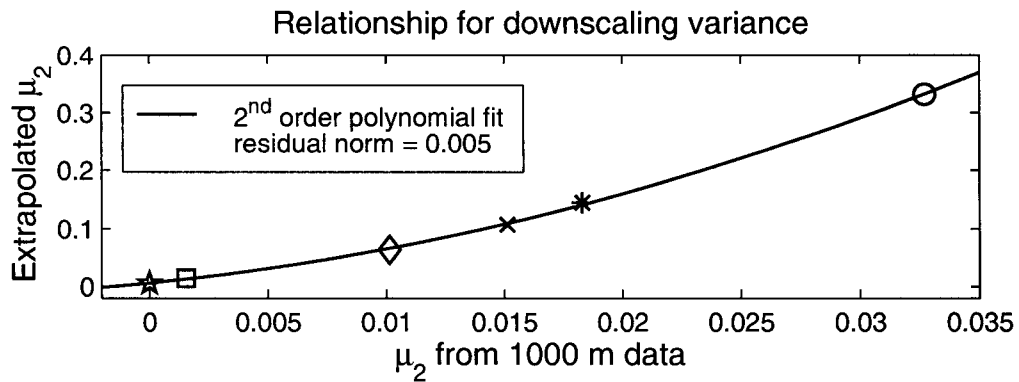
where  $\vartheta_h^{\text{DS}}$  are unique to every  $(i, j)^{\text{th}}$  model cell; therefore the frequency counts  $\Theta_{i,j,h}$  are interpolated back to the original slope classes  $\vartheta_h$  for consistency between model cells.

Comparison of sampled and downscaled data to the same cell size show that this methodology tends to overestimate both  $\mu_2$  and  $\mu_4$ . The sharp central peak in the finely sampled data has no counterpart in data from the 1000 m DEM (see Figure 2.4) and this is the root of the downscaled overestimation. A further empirical relationship is used to modify the downscaled frequency



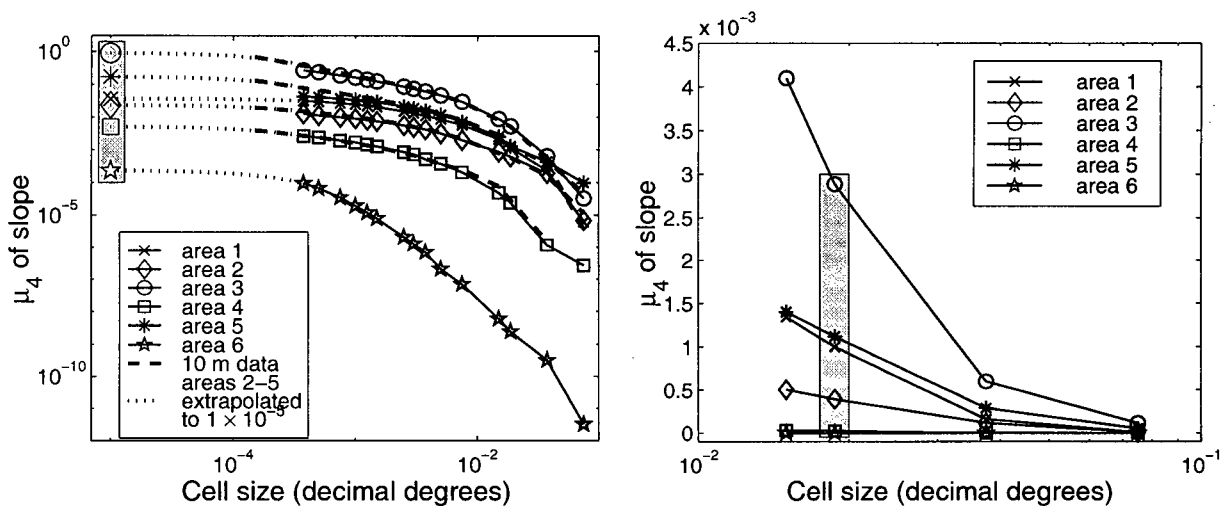
(a) Variance using the 30 and 10 m DEMs with sub-grid cell sizes from  $1 \times 10^{-4} \rightarrow 7.5 \times 10^{-2}$  deg. The curves are extrapolated to  $1 \times 10^{-5}$  deg using 10 m data when available, or 30 m data.

(b) Variance using the 1000 m DEM with sub-grid cell sizes from  $1.5 \times 10^{-2} \rightarrow 7.5 \times 10^{-2}$  deg.



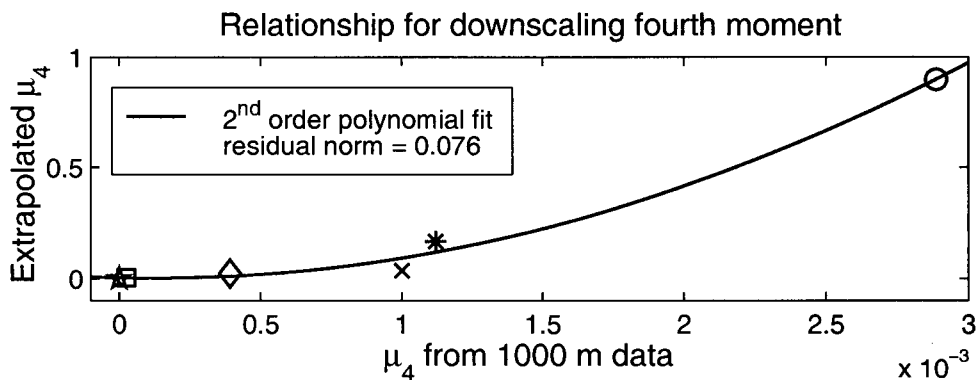
(c) The variance of the shaded data from (a) and (b). The 1000 m DEM data sampled at 0.01875 deg are plotted against the 10 m DEM data extrapolated to  $1 \times 10^{-5}$  deg to result in a downscaling relationship which transforms the 1000 m DEM data to  $1 \times 10^{-5}$  deg corrected data.

Figure 2.7. Variance of bed slope (averaged north-south and east-west) for a large range of sub-grid cell sizes. The shaded data are plotted against each other in (c) and are fit with a second order polynomial  $\mu_2^{1 \times 10^{-5}} = a_2^{\text{scale}} (\mu_2^{0.01875})^2 + b_2^{\text{scale}} \mu_2^{0.01875} + c_2^{\text{scale}}$  where  $a_2^{\text{scale}} = 1.797 \times 10^2$ ,  $b_2^{\text{scale}} = 4.1017$  and  $c_2^{\text{scale}} = 6.0245 \times 10^{-3}$ . This defines the downscaling relationship for the variance.



(a) The fourth moment using the 30 and 10 m DEMs with sub-grid cell sizes from  $1 \times 10^{-4} \rightarrow 7.5 \times 10^{-2}$  deg. Extrapolation is made to  $1 \times 10^{-5}$  deg using 10 m data when available, or the 30 m data.

(b) The fourth moment using the 1000 m DEM with sub-grid cell sizes from  $1.5 \times 10^{-2} \rightarrow 7.5 \times 10^{-2}$  deg.



(c) The fourth moment of the shaded data from (a) and (b). The 1000 m DEM data sampled at 0.01875 deg are plotted against the 10 m DEM data extrapolated to  $1 \times 10^{-5}$  deg to result in a downscaling relationship which transforms the 1000 m DEM data to  $1 \times 10^{-5}$  deg corrected data.

Figure 2.8. Fourth moment of bed slope (averaged north-south and east-west) for a large range of sub-grid cell sizes. The shaded data are plotted against each other in (c) and are fit with a second order polynomial so that  $\mu_4^{1 \times 10^{-5}} = a_4^{\text{scale}} (\mu_4^{0.01875})^2 + b_4^{\text{scale}} \mu_4^{0.01875} + c_4^{\text{scale}}$  where  $a_4^{\text{scale}} = 1.1709 \times 10^5$ ,  $b_4^{\text{scale}} = -2.7966 \times 10^1$  and  $c_4^{\text{scale}} = 4.2430 \times 10^{-3}$ . This defines the downscaling relationship for the fourth moment.

distribution to ameliorate the disagreement; it is

$$\hat{\Theta}_{ijh} = \Theta_{ijh} \left[ 1 + \exp\left(-\frac{\vartheta}{\check{\vartheta}}\right) \exp\left(\frac{\mu_2^{1 \times 10^{-5}}}{\check{\mu}_2^{1 \times 10^{-5}}}\right) \right] \quad (2.7)$$

where  $\check{\vartheta}$  and  $\check{\mu}_2^{1 \times 10^{-5}}$  are parameters taken as 0.012 (which is  $\Delta\vartheta$ ) and 0.2 (an approximate median value for the set of downscaled variances) respectively. Examples of applying the methodology are shown in Figure 2.9. These examples are downscaled to  $3 \times 10^{-4}$  deg to allow for comparison to a directly calculated histogram from the 30 m DEM.

The fourth moment is not explicitly used to downscale the bed dip. Nevertheless, similarities in the analysis of  $\mu_2$  and  $\mu_4$  and agreement of  $\mu_4$  between downscaled and sampled distributions bolster the method.

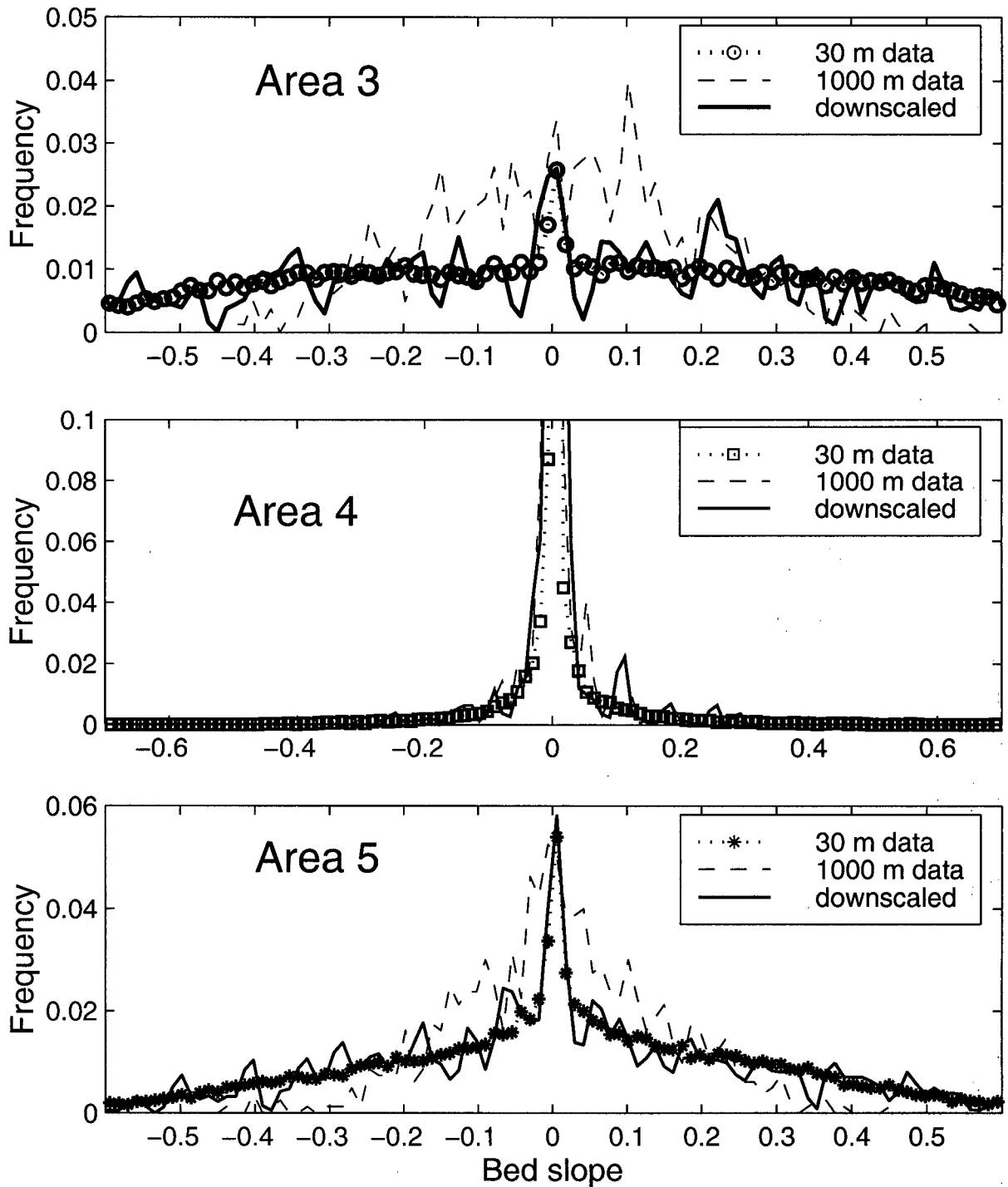


Figure 2.9. Slope (average north-south and east-west) histograms for areas 3,4 and 5 using the modified frequency  $\Theta'_{ijh}$  from (2.7). The 1000 m data are downsampled to  $3 \times 10^{-4}$  deg and plotted with a sampled histogram of the same cell size.

## 2.4 Application to North America

The topography of the study area, which covers a wide extent of North America, can now be downscaled. The input data are from a 1000 m DEM from *Geophysical Data Center* [1998] for land data and 5 min DEM from *NOAA* [1988] for marine areas. Figure 2.10 (upper panel) is a map showing contours of the mean absolute slope (north, south, east and west) for blocks of  $0.5^\circ \times 0.5^\circ$ . They are calculated from the raw (unscaled) discretized slopes with  $0.02^\circ$  sampling.

The lower panel of Figure 2.10 shows the corrected version of the upper panel; the methodology of Section 2.3 is applied to downscale the slopes to  $1 \times 10^{-5}$  deg sampling in each  $0.5^\circ \times 0.5^\circ$  cell. The maximum corrected mean slope, which is off the scale in Figure 2.10(b), is  $\approx 25^\circ$ .

The end result of this analysis is a normalized, downscaled histogram for each  $0.5^\circ \times 1.0^\circ (i, j)$  model cell. Each process that is dependent on bed slope (e.g. Equation (3.7)) is calculated by a linear superposition of weighted results of each slope class.

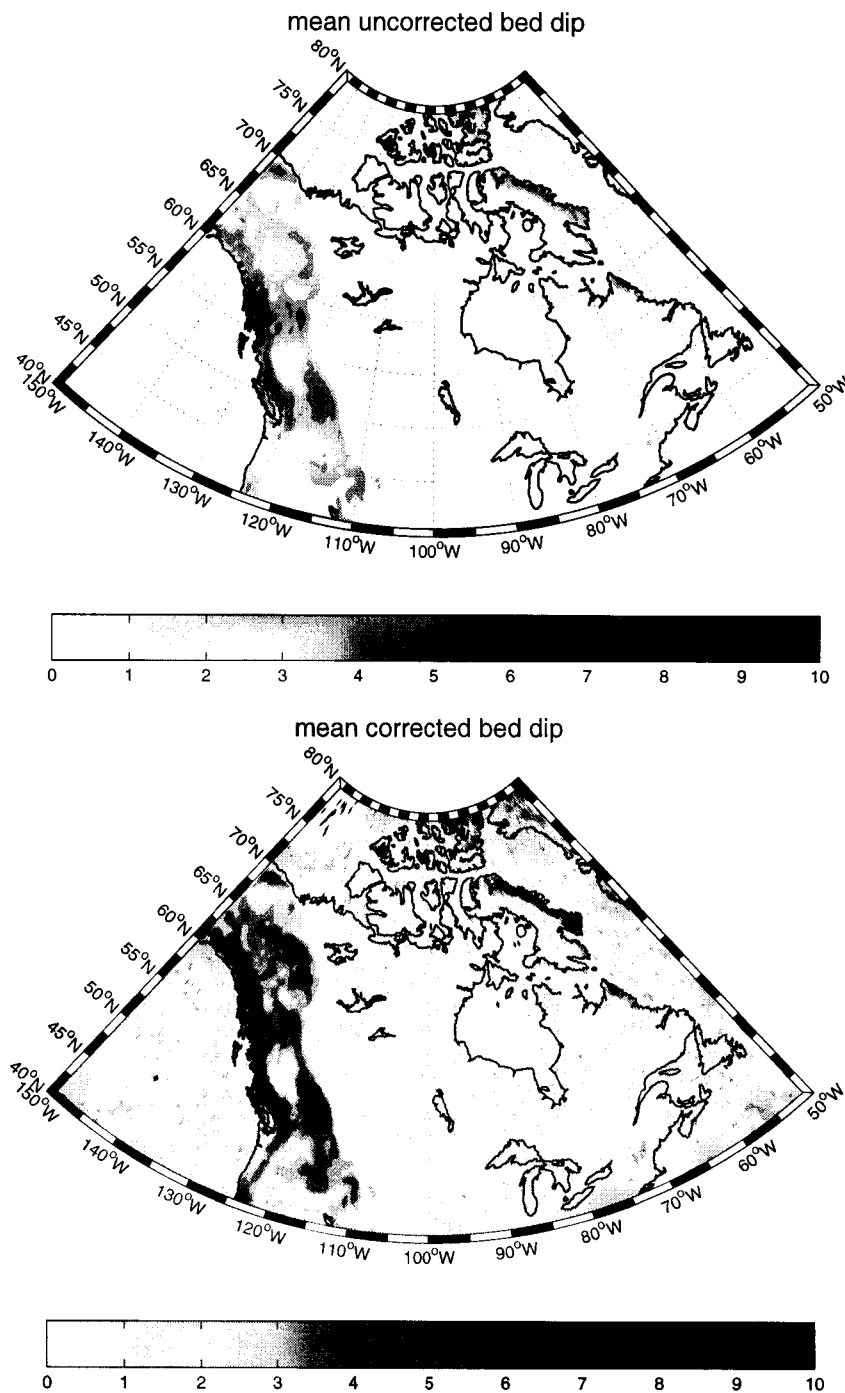


Figure 2.10. Discretized mean of uncorrected and corrected absolute value of bed dip for North America ( $0.5^\circ$  cell size). Sub-grid data are sampled at  $0.02^\circ$  from the 1000 m land DEM [Geophysical Data Center, 1998] and 5 minute marine DEM [NOAA, 1988] then binned into 200 slope classes from  $-50^\circ \rightarrow +50^\circ$  for the uncorrected figure. The correction is made using the methodology outlined in Section 2.3 to a  $1 \times 10^{-5}$  deg sample size. Filled contours of 2.5, 5, 7.5 and  $10^\circ$  are plotted.

## Chapter 3

# Erosion

### 3.1 Abrasion

The study of friction and wear, tribology, hails from before the early days of scientific investigation; Assyrian villages were skilled in the use of bearings before 6000 BP. It was not until the 15<sup>th</sup> century that the effect of sliding objects over each other was treated in a truly scientific manner by Leonardo da Vinci. One of the earliest applications of tribology to glaciology is the description by *Gilbert* [1910] of the reduction of bedrock to fine fragments via sliding of debris-laden basal ice.

To date, subglacial erosion has mostly been treated crudely in large-scale models; simplified erosion laws dependent only on sliding velocity or globally prescribed erosion rates have been used [e.g. *Oerlemans*, 1985; *Puranen*, 1988]. A similar approach has been taken in valley-scale modelling of erosion: only a linear dependence on sliding velocity is assumed [e.g. *Harbor*, 1992; *MacGregor et al.*, 2000], albeit with results that successfully reproduce observed landforms. *Tulley* [1995] presents a process-driven approach to abrasion modelling; I extend this by recognizing and honouring both inter-cell and intra-cell parameter variability.

#### 3.1.1 Adhesive and abrasive wear

There are two types of wear: adhesive wear and abrasive wear [see *Rabinowicz*, 1995]. Adhesive wear occurs when two solids are pressed together with microscopic attraction between the surfaces. If the force required to break the surface-to-surface junction is greater than the force required to create an internal fracture, the internal fissure forms: this is wear. The process is largely independent of the roughness and occurs on both surfaces even if the junction is made of dissimilar

solids. The process was quantified by both *Holm* [1946] and *Archard* [1953] as

$$\dot{A}_v^{\text{ad}} = \frac{k_{\text{ad}} F^N v_p}{3h_s} \quad (3.1)$$

where  $\dot{A}_v^{\text{ad}}$  ( $\text{m}^3 \text{s}^{-1}$ ) is the volumetric abrasion rate,  $k_{\text{ad}}$  is the probability that an adhesive junction will form for any given contact,  $F^N$  (N) is the normal load,  $v_p$  ( $\text{m s}^{-1}$ ) is the particle sliding speed and  $h_s$  (Pa) is the hardness of the surface.

Abrasive wear occurs when a particle of hardness  $h_p$  slides against a softer surface of hardness  $h_s$  and creates a groove. Although the physical process is not analogous to adhesion wear at all, the quantitative form is almost identical

$$\dot{A}_v^{\text{abr}} = \frac{k_{\text{abr}} F^N v_p}{h_s}. \quad (3.2)$$

In general  $k_{\text{abr}}$  is a few orders of magnitude greater than  $k_{\text{ad}}$ . *Rabinowicz* [1995, Figure 6.21] shows a relationship between the friction coefficient  $\mu$  and  $k_{\text{ad}}$  that results in  $k_{\text{ad}} \approx 2 \times 10^{-5}$  if  $\mu$  is taken as 0.85 (see Section 3.1.3) while typical geological values for  $k_{\text{abr}}$  are much higher than this (see Section 3.1.3). It is clear that abrasion wear will dominate and adhesion wear will not be discussed further.

The resultant wear of abrasion is a function of the hardness ratio between the abrading particle  $h_p$  and the wear surface  $h_s$  [*Rabinowicz*, 1995, Figure 7.10], which is approximated to a step function; if the abrading particle is softer than the wear surface, the wear is zero. Applying the step function to (3.2) over a unit area gives

$$\dot{A} = \begin{cases} \frac{k_{\text{abr}}}{h_s} \sum_r \left[ F^N \frac{v_p C_r}{A} \right] & \text{if } h_p \geq h_s, \\ 0 & \text{if } h_p < h_s, \end{cases} \quad (3.3)$$

where  $C_r$  is the areal fraction of debris (assumed equivalent to the volume fraction) with radius  $R_r$  and  $\dot{A}$  is the abrasion rate in m/s. Note that  $v_p C/A$  gives the particle flux. The grain-size distribution, indexed by  $r$ , is discussed in Section 3.1.4.

### 3.1.2 Glaciological abrasion

Modern treatments of glaciological abrasion follow the form of (3.3) but differ in the analysis of  $F^N$ . *Boulton* [1979] asserts an  $F^N$  dependence on effective pressure while *Hallet* [1979, 1981] champions no such dependence. Laboratory experiments generally support the theory of *Hallet* [1979, 1981] although there appears to be a weak dependence on effective pressure due to a presumed thinning of a microscopic water film [*Iverson*, 1990]. Nevertheless, the dependence is weak and the analysis of *Hallet* [1979, 1981] is used for the calculation of  $F^N$  in this study.

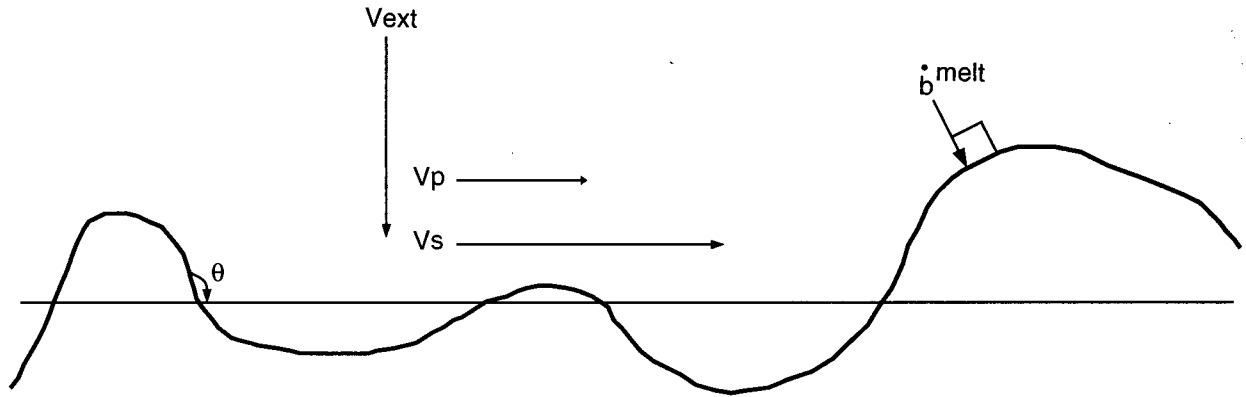


Figure 3.1. A sketch showing the local bed dip  $\theta$ , the sliding and particle velocities  $v_s, v_p$  and the melting and extensional velocities  $\dot{b}^{\text{melt}}, v_{\text{ext}}$ .

The rate of abrasion is identical to (3.3) when the constant of proportionality of *Hallet* [1979, 1981] is identified with the more fundamental parameters  $k_{\text{abr}}/h_s$ .  $F^N$  has two components, a buoyancy term and a viscous drag term,

$$F^N = \underbrace{\frac{4}{3}\pi R^3(\rho_r - \rho_i)g \cos \theta}_{\text{buoyancy}} + \underbrace{f_{\text{bed}}^N \frac{4\pi\eta R^3}{R_*^2 + R^2} v_n}_{\text{viscous drag}}, \quad (3.4)$$

where  $R$  (m) is the radius of the particle,  $\rho_r$  and  $\rho_i$  ( $\text{kg m}^{-3}$ ) are the densities of the particle and ice,  $g$  ( $\text{m s}^{-2}$ ) is the vertical acceleration of gravity and  $\theta$  is local bed dip angle (see Figure 3.1). The variables in the drag term  $f_{\text{bed}}^N$ ,  $\eta$ ,  $v_n$  and  $R_*$  are described below. Typically the buoyancy term is overshadowed by the drag term.

The second term is the viscous drag, derived by *Watts* [1974] and modified by *Hallet* [1981] with the inclusion of the bed modification factor  $f_{\text{bed}}^N$ . Without  $f_{\text{bed}}^N$  the expression gives the viscous drag of a sphere in ice, moving at a relative speed  $v_n$ . The modifier is necessary due to the proximity of the inclusion to the bed; an appropriate empirically-determined value for  $f_{\text{bed}}^N$  is 2.4 [*Goran*, 1970].

$R_*$  (m) is a parameter analogous to the transition radius of regelation versus enhanced creep [*Weertman*, 1964] and is calculated by [*Watts*, 1974]

$$R_* = \left( \frac{3\eta\mathcal{P}_c}{L_{\text{fus}}\rho_i Z_r} \right)^{\frac{1}{2}} \quad (3.5)$$

where the pressure melting coefficient  $\mathcal{P}_c$  and the latent heat of fusion  $L_{\text{fus}}$  for pure ice are taken as  $7.42 \times 10^{-8} \text{ K Pa}^{-1}$  and  $3.34 \times 10^5 \text{ J kg}^{-1}$  respectively [*Paterson*, 1994];  $Z_r$  ( $\text{m K W}^{-1}$ ) is the thermal resistivity of the inclusion. The effective viscosity of the ice  $\eta$  (Pa s) is calculated by

$$\eta = \frac{\tau^{\text{ice}}}{\dot{\epsilon}_i} \quad (3.6)$$

where the shear stress  $\tau^{\text{ice}}$  and the shear strain rate  $\dot{\epsilon}_i$  are given by the ice sheet model (see Section 5.1).

The viscous drag term is also proportional to  $v_n$ , the component normal to the bed of the relative velocity of ice over the particle, in (3.4). A particle in contact with the bed must be zero normal velocity and the relative velocity is due solely to the ice.  $v_n$  has three components: a melting component, a sliding component and a component from longitudinal extension of the ice  $v_{\text{ext}}$  such that

$$v_n = \dot{b}^{\text{melt}} + v_s \sin \theta + v_{\text{ext}} \cos \theta. \quad (3.7)$$

Figure 3.1 illustrates the relative directions of the velocities.  $v_{\text{ext}}$  is derived from applying the continuity equation to the sliding velocity ( $\nabla \cdot \mathbf{v}_s = 0$ ). Taking the appropriate length scale as the diameter of the particle,

$$v_{\text{ext}} = 2R \left[ \frac{1}{R_e \sin \bar{\phi}} \frac{\partial v_{s\bar{\phi}}}{\partial \bar{\theta}} + \frac{1}{R_e \sin \bar{\phi}} \frac{\partial}{\partial \bar{\phi}} (v_{s\bar{\phi}} \sin \bar{\phi}) \right] \quad (3.8)$$

where  $R_e$  is the radius of the Earth. As  $R \ll R_e$ ,  $v_{\text{ext}}$  is negligible.

The particles embedded in the ice generally move at a different rate than the ice; for a particle speed  $v_p$  and a sliding speed  $v_s$ , the relative speed of the ice over the particle is  $v_s - v_p$ . If the particle is in steady state, the tangential forces of viscous drag of the ice, gravitational buoyancy and friction against the bed are in balance as

$$\underbrace{\mu F^N}_{\text{frictional}} = \underbrace{\frac{4\pi R^3}{3} (\rho_r - \rho_i) g \sin \theta}_{\text{buoyancy}} + \underbrace{f_{\text{bed}}^T \frac{4\pi\eta R^3}{R_*^2 + R^2} (v_s - v_p)}_{\text{viscous drag}} \quad (3.9)$$

or in terms of the particle speed (which is needed to calculate  $\dot{A}$  in equation 3.3)

$$v_p = v_s - \frac{1}{f_{\text{bed}}^T} \frac{R_*^2 + R^2}{4\pi\eta R^3} \left[ \mu F^N - \frac{4\pi R^3}{3} (\rho_r - \rho_i) g \sin \theta \right], \quad (3.10)$$

where the friction coefficient  $\mu$  is discussed in Section 3.1.3 and an appropriate tangential bed modifier for viscous drag  $f_{\text{bed}}^T$  is 1.7 [O'Neill, 1968].

Force balance in (3.9) is only valid if there is frictional contact between bed and particle. If  $v_n < 0$ , the particle is moving away from the interface and erosion is zero.

When  $v_p$  from (3.10) is less than zero, the particle lodges itself into the bed and becomes part of the subglacial sediment. Typically the frictional force overcomes any buoyancy contribution and  $v_p$  can be estimated as

$$v_p = v_s (1 - \mu f_{\text{bed}}^N \sin \theta / f_{\text{bed}}^T) - \dot{b}^{\text{melt}} (\mu f_{\text{bed}}^N / f_{\text{bed}}^T) \quad (3.11)$$

by using (3.4) and (3.7). With this simplified expression it is clear that, for beds of moderate slope,  $v_p$  can only become less than zero in conditions where  $\dot{b}_{\text{melt}}$  is the same order of magnitude of  $v_s$ .

The laboratory experiments of *Iverson* [1990] show there are a number of factors complicating the scenario, such as clast rotation, angular clasts and dense packing of particles. Nevertheless, the experiments found good agreement with Hallet's theory and confirmed the most important variable as the normal velocity of the particle, which translates into contact force by (3.4).

The final step towards a complete abrasion law is to describe the shielding power that existing sediment has on further abrasion. *Cuffey and Alley* [1996] argue that there is no significant erosion resulting from the abrasion of a deforming till on the bed except in instances of exceptional bed softness or strong till divergence. However a model depth of sediment  $d$  is unlikely to represent a case of uniform thickness throughout the cell. Sediment depth has spatial variability within a model cell, so typically there will be some area of the cell with negligible cover and thus subject to erosion. To account for this (3.3) is modified to

$$\dot{A} = \begin{cases} \frac{k_{\text{abr}}}{h_s} \sum_r \left[ F^N \frac{v_p C_r}{\mathcal{A}} \right] e^{-d/\check{d}} & \text{if } h_p \geq h_s, \\ 0 & \text{if } h_p < h_s, \end{cases} \quad (3.12)$$

where  $\check{d}$  is a characteristic sediment depth linked to the mean surface slope to represent increased spatial variability of sediment in regions of rough topography. The characteristic depth is calculated by

$$\check{d} = \check{d}_1 \theta_{\text{mean}} + \check{d}_0. \quad (3.13)$$

The parameters  $\check{d}_1$  and  $\check{d}_0$  are chosen as 10.0 m and 2.0 m respectively. Using values of  $\theta_{\text{mean}}$  shown in Figure 2.10<sup>1</sup>,  $\check{d}$  has a range of 2.0 – 6.5 m with this parameter choice, which is reasonable.

In summary, the abrasion is calculated as follows: particles of radius  $R_r$  with concentration  $C_r$ , present a force  $F^N$  on the bed calculated by (3.4) due to a normal velocity  $v_n$  from (3.7) for each  $\theta_h$  (see Chapter 2). The particle moves across the bed at speed  $v_p$  given by (3.10). These processes depend on the viscosity of the ice  $\eta$  and the transition radius  $R_*$ , which is a function of the thermal resistivity of the clast  $Z_r$  and  $\eta$ . Finally, the erosion rate is given by (3.12) which is dependent on the hardness of the bed and the clast and summed for all particle radii. The dependence of  $R_*$  on  $\eta$  and  $Z_r$  through (3.5), the inclusion of the sediment shielding term  $e^{-d/\check{d}}$  and the explicit dependence on hardness  $h_{s,p}$  are expansions on the model of *Hallet* [1979, 1981].

<sup>1</sup>Equation (3.13) requires the mean bed dip  $\theta_{\text{mean}}$  in radians, as do all formulae in this thesis. Figure 2.10 shows  $\theta_{\text{mean}}$  in degrees, a more standard unit for bed dip.

### 3.1.3 Parameter determination — geological

#### Hardness

The hardness  $h_s$  or  $h_p$  is not a fundamental material property [Chandler, 1999]; it is determined by arbitrary engineering tests. An appropriate test for hardness (in this study) is one that mimics the geometry of an englacial particle being dragged over a bed. In Vicker's hardness test a loaded diamond tip is pressed into the substrate and a length scale of the resulting indentation is measured; this is an acceptable measure of hardness for the purpose of calculating abrasion. Table 3.1 is a compilation from Mott [1956] of Vicker hardness numbers that have been modified to be dimensionally consistent with (3.3). The common scale for hardness used by mineralogists (Mohs' hardness number) is also listed in Table 3.1 as this can be used as a guide to the hardness of other geologic materials for which no Vicker hardness data are available.

As the quantification of hardness is somewhat arbitrary, relative values are more instructive than their absolute value. Typically the geological materials that are considered can be split up into two main groups: the silicates which are of hardness  $\approx 7 \times 10^{-9}$  Pa and the calcareous rocks which are of hardness  $\approx 1.5 \times 10^{-9}$  Pa. Low-grade metamorphic minerals such as chlorite (Mohs' hardness = 2.5) also fall within the softer group. Evaporites are softer still, but do not play a significant role in the geological makeup of North America. Rocks do not favour sweeping generalizations and there is a wide range of published values for hardness; for example Boulton [1979] lists metamorphic rocks such as marble and slate approximately 2.5 and 3 times harder than limestone. Nevertheless, a bimodal hardness grouping of  $7 \times 10^{-9}$  and  $1.5 \times 10^{-9}$  Pa is expedient and used in this study.

Mineral	Hardness (Pa) $\times 10^{-9}$	Mohs' Hardness
Quartz ( $\text{SiO}_2$ )	11 - 12	7
Orthoclase ( $\text{KAlSi}_3\text{O}_8$ )	7.0 - 7.8	6
Magnetite ( $\text{Fe}_3\text{O}_4$ )	4.7 - 7.3	5.5 - 6.5
Limestone ( $\text{CaCO}_3$ )	1.9 - 2.6	3
Marble ( $\text{CaCO}_3$ )	1.2 - 1.6	3
Halite ( $\text{NaCl}$ )	0.26 - 0.46	2.5

Table 3.1. Vicker and Mohs' hardness as reported by Mott [1956]

#### Abrasive wear coefficient

Finding appropriate values for  $k_{abr}$  in the literature is difficult as the vast majority of research in tribology concerns itself with metal upon metal friction rather than geological materials. Never-

Rock Type	$Z_r$ range <sup>a</sup> m K W <sup>-1</sup>	$Z_r$ median m K W <sup>-1</sup>	$R_*$ range for $\eta = 1 \times 10^5$ Pa a <sup>b</sup>
clays shales	0.27 – 4.0	2.1	0.09 – 0.02
basalt	0.23 – 2.0	1.1	0.10 – 0.03
limestones	0.23 – 1.1	0.67	0.10 – 0.05
marble	0.25 – 0.77	0.51	0.010 – 0.06
granite	0.20 – 0.77	0.49	1.08 – 0.06
dolomite	0.15 – 0.63	0.39	1.12 – 0.06
ultrabasic intrusive	0.20 – 0.28	0.24	1.08 – 0.09

<sup>a</sup>from *Kobranova* [1989]

<sup>b</sup>This value is the same as used by *Hallet* [1979] and *Iverson* [1990] and is in the range produced by the ice sheet model (see Section 5.1).

Table 3.2. Values of thermal resistivity and corresponding  $R_*$  for a variety of geologic materials. *Hallet* [1979, 1981] uses  $R_* = 0.11$  m which corresponds to  $Z_r = 0.56$  m K W<sup>-1</sup> for limestone and *Iverson* [1990] uses  $R_* = 0.13$  m corresponding to  $Z_r = 0.475$  m K W<sup>-1</sup> for granite.

theless there are experiments for a sandstone [*Scholz*, 1987] and a granite [*Yoshioka*, 1986] that both give an estimate of  $k_{abr}$  as 0.3; this is consistent with *Hallet* [1979] where a value of  $k_{abr} = 0.2$  is implied from the attritvity coefficient for limestone ( $\equiv k_{abr}/h_s$ ) of  $1 \times 10^{-10}$  using  $h_s = 2 \times 10^9$  Pa. However, a value of  $k_{abr} \approx 15$  is calculated by *Metcalf* [1979]<sup>2</sup>. In an experiment specific to debris-laden ice abrading its bed, fragment rotation is frequent [*Iverson*, 1990]: this changes the problem from 2-body to 3-body wear which typically decreases  $k_{abr}$  by a factor of 10–100 [*Rabinowicz*, 1995]. Thus there is a range of possibilities for  $k_{abr}$  spanning 2 orders of magnitude; an appropriate choice is discussed in Section 6.2.

### Thermal resistivity, coefficient of friction

Values of the thermal resistivity  $Z_r$  and the corresponding  $R_*$  (for a particular value of  $\eta$ ) are shown in Table 3.2 for a variety of geologic materials. A sensitivity test using the parameters in Table 3.3 is shown in Figure 3.2; the erosion rates differ by up to two orders of magnitude between cases of maximum and minimum  $Z_r$ . However the intra-rock type variability of  $Z_r$  is large compared to the inter-rock type variability and no obvious patterns emerge from the data to guide assignment of thermal resistivities (apart from clays which tend to be good heat conductors). Therefore a global value of  $Z_r = 0.35$  m K W<sup>-1</sup> will be used for all lithologies. This value is in the range of almost all rock types reported in *Kobranova* [1989].

Although several authors report different values for  $\mu$  the coefficient of friction for different rock types [see *Ohnaka*, 1975; *Jaeger and Cook*, 1979], in a compilation of friction results *Byerlee* [1978]

<sup>2</sup>*Metcalf* [1979] uses attritvity (kg J<sup>-1</sup>) and does not explore  $k_{abr}$  whatsoever. Attritvity is defined in terms of indentation hardness not Vicker's hardness, which may account for the difference in abrasive wear coefficients.

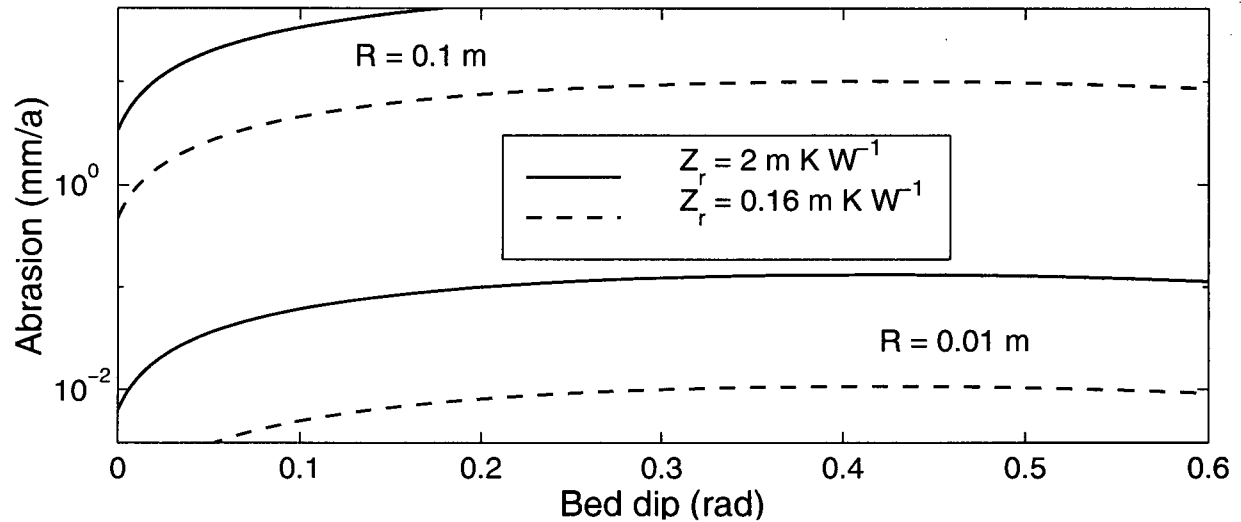


Figure 3.2. Sensitivity tests for various values of grain size  $R$ , bed dip  $\theta$  and thermal resistivity  $Z_r$ . See Table 3.3 for parameter details.

Parameter	Value	Units	Parameter	Value	Units
$k_{abr}/h_s$	$1 \times 10^{-10}$	$\text{Pa}^{-1}$	$C$	1.0	—
$\rho_i$	900	$\text{kg m}^{-3}$	$\rho_r$	2100	$\text{kg m}^{-3}$
$g$	9.81	$\text{m s}^{-2}$	$\eta^a$	$1 \times 10^6$	$\text{Pa a}$
$\mathcal{P}_c$	$7.42 \times 10^{-8}$	$\text{K Pa}^{-1}$	$L_{fus}$	$3.34 \times 10^5$	$\text{J kg}^{-1}$
$j_{melt}$	0.5	$\text{m a}^{-1}$	$v_s$	100	$\text{m a}^{-1}$
$v_{ext}$	0	$\text{m a}^{-1}$	$f_{bed}$	1.7	—
$\mu$	0.85	—	$Z_r$	0.16 / 2.0	$\text{m K W}^{-1}$

<sup>a</sup>This value of  $\eta$  leads to  $R_* = 0.38 \text{ m}$  for  $Z_r = 0.16 \text{ m K W}^{-1}$  and  $R_* = 0.11 \text{ m}$  for  $Z_r = 2.0 \text{ m K W}^{-1}$

Table 3.3. Parameters used for sensitivity tests of Figure 3.2. Non-SI units are used for some variables as this is standard in the literature and facilitates comparisons. However, internally the model code uses strictly SI.

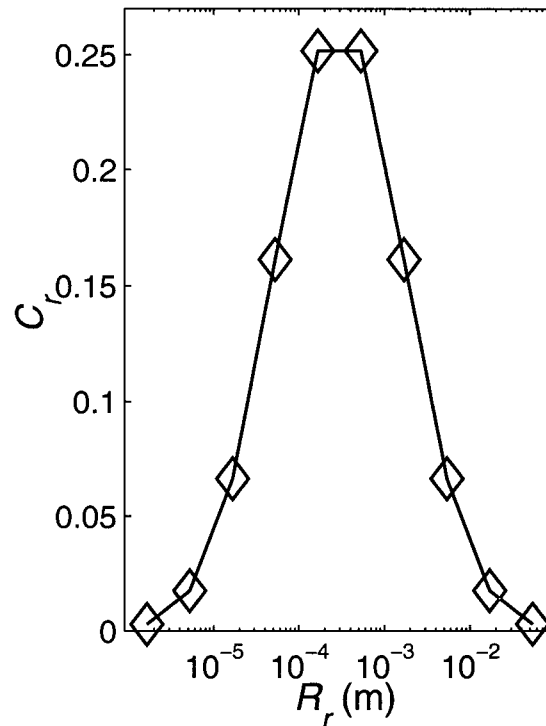


Figure 3.3. The basal ice grain-size distribution.

finds no significant and reproducible dependence on rock type for low to intermediate pressure and concludes that a universal designation of  $\mu = 0.85$  is appropriate. I adhere to this and, as for the thermal resistivity, globally set  $\mu = 0.85$  for all lithologies.

### 3.1.4 Parameter determination — non-geological

#### Englacial particle radius

The radius of the englacial clast  $R$ , assumed to be non-lithologically controlled, must be determined. The most expedient method is to choose a representative clast size; in the recent process-driven large-scale erosion model of *Tulley* [1995], a single clast size of 0.1 m is used with the argument that all other clast sizes are washed away by subglacial waterflow. An appropriate distribution of  $R$  is preferable to this approach.

Many subglacial tills appear to show fractal distributions of particle sizes [*Hooke and Iverson*, 1995; *Fischer*, 1995], though this result is not universally accepted [*Hubbard et al.*, 1996]. There are also arguments against this distribution holding within the ice; *Alley et al.* [1997] suggest that

the high surface energy associated with fine particles could impede their inclusion into the ice by intrusion (Section 4.1.3).

Sedimentological analyses of basal ice from Matanuska Glacier, a large ( $\approx 400 \text{ km}^2$ ) Alaskan coastal glacier [Lawson, 1979], several outlet glaciers of West Greenland [Knight, 1994] and eleven Alpine glaciers [Hubbard *et al.*, 1996] may be used as examples for grain-size distribution within basal ice. Many facies of sediment-laden ice are identifiable and different facies may have distinct grain distributions. For example, the *clotted-dispersed* facies of Knight [1994] and the *suspended* facies of Lawson [1979] both comprise predominantly silt-size particles. However, these facies do not make up a large fraction of the total debris. A mean grain size<sup>†</sup>  $\phi_{\text{grain}}^{\text{mean}} = 0.75$  and a standard deviation of  $\phi_{\text{grain}}^{\text{sd}} = 2.5$  is consistent with all three analyses, excluding the englacial and dispersed facies. This distribution, shown in Figure 3.3 is what is used in the erosion model.  $N_r$  size classes are evenly distributed in  $\phi_{\text{grain}}$ -space from  $R \approx 0.05 \text{ m}$  to  $R \approx 2 \times 10^{-6} \text{ m}$ . Processes dependent on  $R$  are calculated for each discrete  $R_r$ , weighted by the concentration  $C_r$  and then summed over all  $r$  radii classes.

### Bed dip, viscosity and sensitivity tests

The determination of the frequency distribution for north-south and east-west bed dip  $\hat{\Theta}^{\text{ns}}$  and  $\hat{\Theta}^{\text{ew}}$  is described in Chapter 2. A directional frequency distribution of bed dip  $\hat{\Theta}$  is derived by taking the projection of the bed dip distribution<sup>4</sup> in the direction of sliding. Therefore  $\hat{\Theta}$  is given by

$$\hat{\Theta} = \frac{v_{s_{\hat{\Theta}}} \hat{\Theta}^{\text{ns}} + v_{s_{\hat{\phi}}} \hat{\Theta}^{\text{ew}}}{v_{s_{\hat{\Theta}}} + v_{s_{\hat{\phi}}}}. \quad (3.14)$$

The effective viscosity of the ice  $\eta$  is determined by the ice model (see Section 5.1) and exhibits a range of several orders of magnitude (from  $2 \times 10^4 - 3 \times 10^7 \text{ Pa a}$ ); as  $\eta$  has such a large range, it becomes an important parameter for determining erosion rates.

Sensitivity tests to show the effects of  $\theta$ ,  $R$  and  $\eta$  on the erosion rate are shown in Figure 3.4. The parameters and constants used in the sensitivity calculations are given in Table 3.4.

<sup>†</sup>The logarithmic  $\phi_{\text{grain}}$  scale is common in sedimentology. It is defined as  $\phi_{\text{grain}} = -\log_2(2 \times 10^3 R)$  where  $R$  is in metres.

<sup>4</sup>Each pair  $(\hat{\Theta}_h^{\text{ew}}, \hat{\Theta}_h^{\text{ns}})$  is considered a vector.

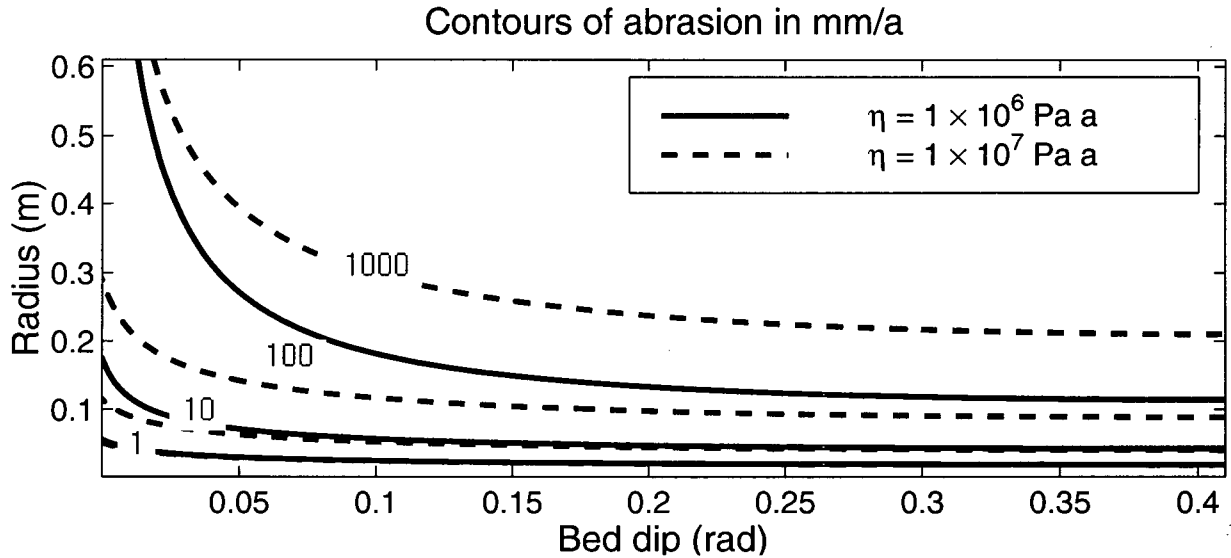


Figure 3.4. Sensitivity tests for various values of grain size  $R$ , bed dip  $\theta$  and ice effective viscosity  $\eta$ . See Table 3.4 for parameter details. Contours of 1, 10, 100 and 1000 mm/a are plotted.

Parameter	Value	Units	Parameter	Value	Units
$k_{abr}/h_s$	$1 \times 10^{-10}$	$\text{Pa}^{-1}$	$C$	1.0	—
$\rho_i$	900	$\text{kg m}^{-3}$	$\rho_r$	2100	$\text{kg m}^{-3}$
$g$	9.81	$\text{m s}^{-2}$	$\eta$	$1 \times 10^6 / 1 \times 10^7$	$\text{Pa a}$
$\mathcal{P}_c$	$7.42 \times 10^{-8}$	$\text{K Pa}^{-1}$	$L_{fus}$	$3.34 \times 10^5$	$\text{J kg}^{-1}$
$j^{melt}$	0.5	$\text{m a}^{-1}$	$v_s$	100	$\text{m a}^{-1}$
$v_{ext}$	0	$\text{m a}^{-1}$	$f_{bed}$	1.7	—
$\mu$	0.85	—	$Z_r^a$	0.3	$\text{m K W}^{-1}$

<sup>a</sup>This value of  $Z_r$  leads to  $R_* = 0.28$  m for  $\eta = 1 \times 10^6$  Pa a and  $R_* = 0.88$  m for  $\eta = 1 \times 10^7$  Pa a

Table 3.4. Parameters used for sensitivity tests of Figure 3.4

## 3.2 Quarrying

Quarrying, or plucking, is when part of the bed is pulled off through the action of sliding ice. It is less readily accepted (and studied) than abrasion; some contend that quarrying is merely the removal of previously loose parts of the bed and cannot lead to sustained erosion [see *Lindstöm*, 1988]. Calculations in support of this minimalist view of quarrying indicate that the stress induced by a sliding glacier over a bedrock hump is unable to meet the Coulomb failure (shear) criterion [*Morland and Boulton*, 1975; *Morland and Morris*, 1977].

Nevertheless asymmetric subglacial landforms such as roches moutonnées (bedrock mounds with a smooth and gentle upstream surface and a steep, broken downstream flank) challenge the notion that abrasion is the only significant agent of erosion. The above-noted problem of glacier-induced stress being insufficient to instigate bedrock failure can be circumvented by process-based theories of quarrying that assume the existence of water-filled cavities [*Iverson*, 1991; *Hallet*, 1996]. Fast-varying water pressure within fissures can facilitate and enable rock fracture through fatigue [*Iverson*, 1991]. However, these conditions of rapid change are unlikely to exist under large ice sheets and do not play a lead role in ice sheet erosion. *Hallet* [1996] develops a model for quarrying based on subcritical mode I (tensile) crack growth due to differential normal loading of the ice and a water-filled cavity; this forms a basis for the treatment of quarrying in the present study.

I begin with a discussion of subcritical fracture and associated parameters. The state of stress in the bed is required to solve for the rate of subcritical fracture and the effect of topography is examined using a 2-D stress solver. The existence of a cavity is crucial to quarrying; without cavities, subglacial cracks cannot grow. I therefore briefly examine a solution for the extent of cavitation and its effect on the state of stress. Lastly the salient points are compiled into a comprehensive quarrying model.

### 3.2.1 Subcritical crack propagation

#### Stress intensity factor

There are three modes of crack propagation: a mode I crack is formed under tension while modes II and III are shear propagated. Crack growth in any mode can proceed very quickly (approaching the acoustic velocity) when the stress intensity factor  $K_L$  exceeds the critical stress intensity (synonymous with fracture toughness)  $K_L^*$  for a mode  $L$  crack. The stress intensity near the tip of a crack is given by [*Lawn and Wilshaw*, 1975]

$$K_L = m_g \sigma_L \sqrt{\pi l_c} \quad (3.15)$$

where  $\sigma_L$  is the far-field stress (for a crack with its major axis oriented in the  $x$  direction,  $\sigma_I = \sigma_{yy}$ ,  $\sigma_{II} = \sigma_{xy}$  and  $\sigma_{III} = \sigma_{zy}$ ),  $l_c$  is the half-crack length and  $m_g$  is a modification factor to account for crack geometry and loading conditions. For example  $m_g = 2/\pi$  for a favorably oriented penny-shaped crack and  $m_g = 1.12$  when the crack is single ended in a semi-infinite space.

*Kachanov and Laures* [1989] examine the effect of interacting cracks within a network, which is a plausible scenario for quarrying because a crack is unlikely to exist in isolation. Their results show that both stress amplification and shielding is possible depending on the orientation of the interacting cracks. Some conclusions that can be drawn from their work: Mode III stress intensity factors are small compared to mode II except in certain exceptional geometric situations and both amplification and shielding of mode I and mode II cracks is negligible if the inter-crack distance is more than 15% of the crack length.

In this study a single-ended penny-shaped crack in a favorable orientation is assumed to exist with no significant interactions with other cracks. Mode III cracks are not considered in this thesis.

### Crack growth

When the stress intensity factor reaches the critical value, the crack propagates catastrophically; however subcritical crack growth can occur for  $K_L < K_L^*$  through a number of micro-processes and the most important at low temperatures is stress corrosion. A non-negative entropy condition implies a minimum stress intensity  $K_L^0$  below which no subcritical crack growth can occur in brittle materials [*Rice*, 1978] although this does not necessarily apply to heterogeneous, multiphase solids such as rocks [*Segall*, 1984]. Theoretical and heuristic arguments suggest that  $K_L^0 \approx 0.2K_L^* - 0.3K_L^*$  [*Atkinson*, 1984; *Atkinson and Meredith*, 1987b] despite the experimental failure to observe a subcritical crack growth limit in rocks.

The simplest equation for subcritical crack growth is based on the power law of *Charles* [1958]

$$v_L = \mathcal{A}_L \left( \frac{K_L}{K_L^*} \right)^{n_L} \quad (3.16)$$

where  $v_L$  is the speed of propagation and  $n_L$  is the subcritical crack growth exponent for a mode  $L$  crack. The parameter  $\mathcal{A}_L$  has large uncertainty associated with it and has rarely been published for geological materials [*Atkinson and Meredith*, 1987b, page 136] therefore it is used as a tuning parameter and a single value will be used for all geological materials. There are other empirical formulae that honour the thermodynamic limit of  $K_L^0$ , however the difference between results is miniscule as  $n_L$  is large ( $> 10$ ) for geological materials. Aside from being a simple relationship, (3.16) has the advantage of being widely used, therefore there are some compilations of the parameters  $K_L^*$  and  $n_L$ . There is a satisfactory fit of (3.16) to empirical data as long as stress corrosion is the rate limiting step — this occurs at  $K_L < 0.75K_L^*$  [*Atkinson*, 1984]. At

values of  $K_L$  beyond this point there is very little increase in  $v_L$  (until critical  $K_L$  is reached);  $v_L$  will be taken as constant for  $K_L \geq 0.75K_L^*$  in this study.

### 3.2.2 Subcritical crack parameter determination

The following sections discuss the subcritical crack growth parameters and list compilations gathered from the literature of these parameters. Assignment of  $K_I^*$ ,  $K_{II}^*$ ,  $n_I$  and  $n_{II}$  to the lithologies identified and used in the transport model is left until Section 5.3.1.

#### Critical stress intensity

A selection of published values for  $K_I^*$  is presented in Table 3.5. Experiments that did not meet the criteria set out in *Atkinson and Meredith* [1987a] for true critical stress intensities are not listed. These values form the basis for assignment of  $K_I^*$  values to the lithologies of North America in Section 5.3.

Table 3.5: Compiled values for mode I critical stress intensity of various geological material

Rock Type	$K_I^*$ MPa m <sup>1/2</sup>	Reference
sandstone	0.34, 0.79, 0.92, 2.66	[ <i>Meredith et al.</i> , 1984]
	0.45	[ <i>Atkinson</i> , 1979]
	<b>mean</b>	1.18
	<b>minimum</b>	0.34
marble	0.64	[ <i>Atkinson</i> , 1979]
	0.87	[ <i>Meredith et al.</i> , 1984]
	1.40	[ <i>Costin and Mecholsky</i> , 1983]
	1.49	[ <i>Atkinson et al.</i> , 1985]
	<b>mean</b>	1.10
	<b>minimum</b>	0.64
limestone	0.87, 1.01	[ <i>Atkinson</i> , 1984]
	1.14, 1.65	[ <i>Meredith et al.</i> , 1984]
	<b>mean</b>	1.17
	<b>minimum</b>	0.87
novaculite	1.34	[ <i>Atkinson</i> , 1980]
	1.60	[ <i>Meredith et al.</i> , 1984]
	<b>mean</b>	1.47
	<b>minimum</b>	1.34
quartzite	2.10	[ <i>Atkinson</i> , 1984]

*continued on next page*

Table 3.5: *continued*

Rock Type	$K_I^*$ MPa m <sup>1/2</sup>	Reference
granite	1.66, 2.48	[Atkinson, 1984]
	2.43, 2.45, 3.52, 3.50	[Atkinson et al., 1984]
	2.28	[Meredith et al., 1984]
	1.74	[Atkinson and Rawlings, 1981]
	2.17	[Der et al., 1978]
	1.80	[Swanson, 1980]
	2.00	[Ingraffea, 1981]
	1.85	[Costin and Mecholsky, 1983]
<b>mean</b>	2.32	
<b>minimum</b>	1.66	
basalt	2.54	[Meredith et al., 1984]
	2.58	[Meredith and Atkinson, 1983]
	<b>mean</b>	2.56
	<b>minimum</b>	2.54
gabbro	2.88	[Atkinson and Rawlings, 1981]
	2.72, 3.03	[Meredith and Atkinson, 1985]
	3.75	[Atkinson et al., 1985]
	<b>mean</b>	3.10
<b>minimum</b>	2.72	
diabase	3.28	[Meredith et al., 1984]
	3.32	[Meredith and Atkinson, 1983]
	<b>mean</b>	3.30
	<b>minimum</b>	3.28

Table 3.5: Compiled values for mode I critical stress intensity of various geological material. This table provides the basis for values assigned to North American lithologies in Section 5.3. From *Atkinson and Meredith [1987a]*.

The lion's share of data are for mode I cracks, yet subcritical growth can occur in all three modes [*Atkinson and Meredith, 1987a*]. Mode III fracture toughness is shown to be 3–4 times the mode I fracture toughness for granite and limestone at atmospheric pressure [*Cox and Scholz, 1985*]; it is assumed that values of  $K_{II}^*$  are comparable to  $K_{III}^*$ . To obtain the fracture toughness under compression, a Coulomb-like (linear) relationship is assumed with a coefficient of internal friction  $\mu_{int}$  taken as 0.6 (from examination of results reported in *Cox and Scholz [1985]* and consistent with the general trend indicated by *Jaeger and Cook [1979]*). Therefore  $K_{III}^{*\sigma_N}$ , the fracture toughness with a normal stress acting on the plane of the crack  $\sigma_N$ , is given by

$$K_{III}^{*\sigma_N} = \begin{cases} K_{III}^* + \mu_{int} \sigma_N \sqrt{l_c} & \sigma_N \geq 0, \\ K_{III}^* & \sigma_N < 0. \end{cases} \quad (3.17)$$

The linear form (3.17) is motivated by the direct dependence of the stress intensity factor on the far-field stress and the success of the Coulomb fracture criterion for undamaged rock.

**Subcritical crack growth exponent**

A physical interpretation of  $n_L$  relates it to multiple fractures and branching:  $n_L$  tends to increase with increasing tortuosity of the forming crack [Swanson, 1984]. When a crack encounters a heterogeneity it is more likely to branch, thereby explaining the general trend that more complex material exhibit higher values of  $n_I$  (corresponding to lower susceptibility to subcritical cracking). Linking of pre-existing cracks can decrease tortuosity; this can explain the large variability in published values of  $n_I$  for similar materials.

Values for mode I subcritical crack growth indices are given in Table 3.6. Due to a lack of experimental data for either mode II or mode III, it will be assumed that  $n_I = n_{II} = n_{III}$ . All values reported in Table 3.6 were determined under similar experimental conditions; measurement of  $n_I$  is a challenging experimental task and as discussed above there is large natural variability present in geologic materials. However the general trend of higher  $n_I$  associated with higher heterogeneity is reflected in Table 3.6. The lowest values of  $n_I$  are the homogeneous samples of marble and sandstone; the highest values of  $n_I$  correspond to the more complex igneous rock types.

Rock Type	Mode I Crack Growth Index $n_I$	Reference
sandstone	14	[Atkinson, 1984]
marble	9 26-29 <sup>a</sup> 15	[Costin and Mecholsky, 1983] [Henry and Paquet, 1976] [Atkinson, 1984]
<b>mean</b>	17.2	
<b>minimum</b>	9	
novaculite	25	[Atkinson, 1980]
andesite	26	[Waza et al., 1980]
micrite	26	[Henry and Paquet, 1976]
limestone	27 <sup>b</sup>	[Atkinson, 1984]
<b>minimum</b>	26	
basalt	24 33	[Meredith and Atkinson, 1983] [Waza et al., 1980]
<b>mean</b>	28.5	
<b>minimum</b>	24	
diabase	29	[Meredith and Atkinson, 1983]
gabbro	32.5 <sup>c</sup>	[Atkinson and Rawlings, 1981]
<b>minimum</b>	29	
quartzite	34 <sup>d</sup>	[Atkinson, 1984]
<b>minimum</b>	30	
granite	50 34 35 35-46 <sup>e</sup> 24 53	[Atkinson et al., 1984] [Atkinson, 1980] [Atkinson and Rawlings, 1981] [Atkinson, 1984] [Costin and Mecholsky, 1983] [Swanson, 1980]
<b>mean</b>	39.4	
<b>minimum</b>	24	

Table 3.6. Compiled values for  $n_I$  the subcritical crack growth exponent for mode I cracks. This table provides the basis for values assigned to North American lithologies in Section 5.3. From Atkinson and Meredith [1987a].

<sup>a</sup>27.5 taken as representative value

<sup>b</sup>A range of 26-28 was reported by the author

<sup>c</sup>A range of 29-36 was reported by the authors

<sup>d</sup>A range of 30-38 was reported by the author

<sup>e</sup>40.5 taken as a representative value

Topography Case	Radius of Curvature	Amplitude (crest $\rightarrow$ trough)
Case 1	18.03 m	16.06 m
Case 2	29.15 m	8.31 m
Case 3	42.72 m	5.44 m
Case 4	57.01 m	4.02 m

Table 3.7. Four different cases for topographical amplitude are imposed on the mesh template shown in Figure 3.5.

### 3.2.3 Effect of topography

By (3.15)  $K_L$  is directly proportional to the state of stress. Local topography affects the state of stress in the subsurface [see *Morland and Boulton, 1975; Morland and Morris, 1977*] and is of primary importance in cavity formation. How significant is topography in terms of a stress enhancing role given the existence of a cavity? To resolve this question FRANC2D, a two-dimensional, finite-difference package to analyse stress [*Ingraffea et al., 1997; Ingraffea and Wawrzynek, 1995*], is used to simulate a subglacial bed with topography. The package uses a linear elastic stress solver for an isotropic material to solve two dimensional stress problems.

#### FRANC2D setup

A mesh, shown schematically in Figure 3.5, is created to define the domain of the problem. It is designed to maximize cell density in the upper centre of the domain, specifically at the trough of the topography as this is the presumed area of maximal crack growth. The mesh is large enough that boundary conditions of the sides and bottom do not affect the solution; the domain is effectively infinite.

Four different topographies (consisting of circular arcs) with topographical wavelength  $L_t$  are used. Specifics of each case are detailed in Table 3.7.

Boundary conditions (BC) drive the problem. The boundary is fixed on the sides and the bottom of the domain; this is an identical condition to the familiar requirement that all stresses and strains of a point source vanish as  $r \rightarrow \infty$ . The BC on the upper boundary defines the nature of the imposed load. The goal is to elucidate patterns of stress in the bed and because the bed response is linear with the surface loading, absolute BC values are irrelevant and dimensionless loads are used. A body of ice approximately 200 m in length is represented by a vertical load  $P_i$  of 10 and a tangential load  $\tau$  of 1. Where a cavity is inserted, there is a normal load  $P_w$  of 5 with zero shear. The ratios of ice-overburden to shear (10:1) and ice-overburden to water pressure (2:1) are representative of observed values.

### Mesh for FRANC2D Analysis

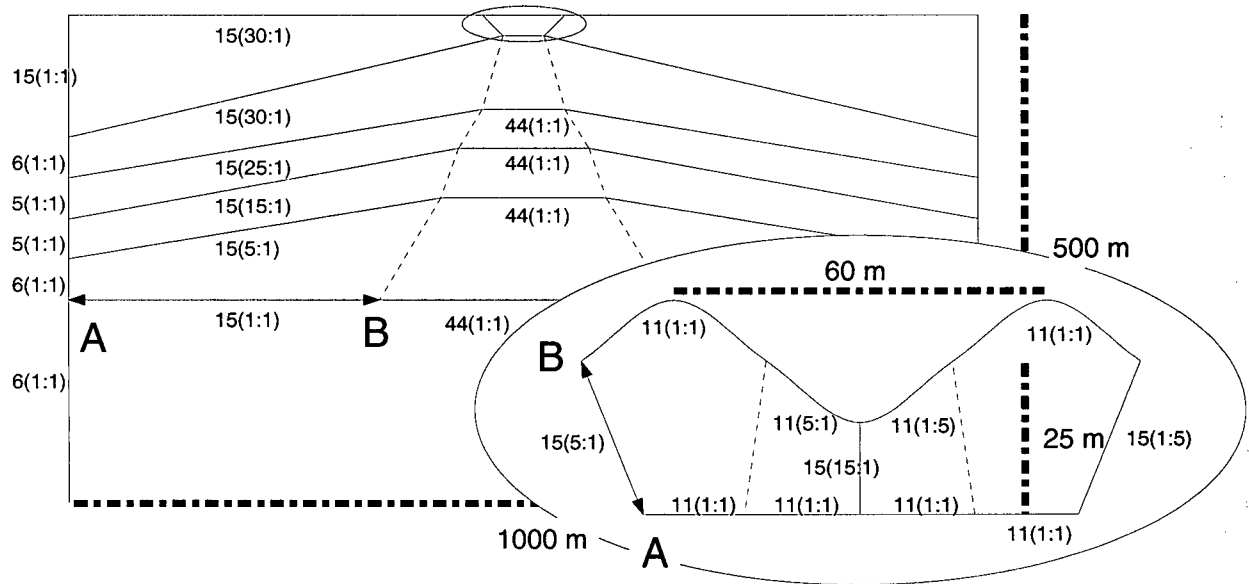


Figure 3.5. Mesh used for the FRANC2D stress analysis. Each segment  $A \longleftrightarrow B$  is labelled with  $N_{\text{mesh}}(a_m : b_m)$  where  $N_{\text{mesh}}$  is the number of cells assigned for  $\bar{AB}$  and the ratio  $(a_m : b_m)$  indicates the relative cell size at the point  $A$  and point  $B$ . Only two segments have the points  $A$  and  $B$  explicitly labelled. The cell size varies linearly through the segment. The mesh is designed to concentrate nodes at the downstream edge of the cavity where fracture is most likely to occur.

A cavity of length  $L_t/3$  is assumed to exist on the downstream slope of the bump; this cavity size is large for the normalized effective pressure chosen (0.5) and equation 3.19 requires the ice to be thin (on the order of 100 m) when  $v_s = 200 \text{ m a}^{-1}$ .

### FRANC2D results

Figure 3.6 shows contours of the horizontal stress  $\sigma_{xx}$  for each of the four cases outlined in Table 3.7. The points in Figure 3.6 represent mesh points where stress is calculated, concentrated at the downstream cavity-ice junction. The thick contour lines represent integral contour values, while the thin lines are half-integral values. The grey shaded regions have cracks with a net tensile  $\sigma_{xx}$ ; they are under the cavity and thus have water pressure acting against the compressive load of the ice. This is where vertical mode I cracks can grow subcritically.

This analysis shows that, contrary to the notion that topography enhances local stress regimes, increased topography inhibits vertical mode I crack growth for this geometry. This is due to the increased compressive stress  $\sigma_{xx}$  added through vertical loading of the following downstream bump (extending from  $x = 0 \text{ m}$  to  $x = 30 \text{ m}$  in Figure 3.6). Caution should be exercised in the interpretation of Figure 3.6 as such simple-minded tests do not capture important points: for example there is no feedback from topography to cavity size. Nevertheless as a test of the effect of topography on the stress regime it is instructive.

Figure 3.6 indicates that the most likely location for vertical mode I crack growth is in the vicinity of the downstream cavity-ice junction, in agreement with the model of *Hallet* [1996]. However *Iverson* [1991] calculates stress on only the upstream cavity-ice junction, justified by field observations of the asymmetry of roches moutonnées and “bullet boulders” [*Iverson*, personal communication]. Whether or not downstream cavity-ice quarrying can reproduce the steep leeward sides of these landforms is dependent on complex feedbacks between the position of the cavity, topography and quarrying. This simple model cannot capture such complexity.

Vertical stress  $\sigma_{yy}$  results are shown in Figure 3.7; they show similar behaviour to the  $\sigma_{xx}$ . Interestingly, there is a more balanced likelihood of upstream/downstream crack growth. In general, assuming the absence of regional stresses that may exert significant influence in mountainous regions,  $\sigma_{yy}$  is more compressive than  $\sigma_{xx}$ : horizontal mode I cracks are more difficult to propagate than vertical mode I cracks.

These results are dependent on the specific geometry chosen and a wide variety of subglacial geometries are possible ranging from the smooth topography examined in this section to jagged steps. Nevertheless a general result can be extracted: tensile crack growth is not significantly affected by topography (aside from the role that topography plays in cavity formation). This allows the transformation of a complicated topographic stress regime to a simple one as shown

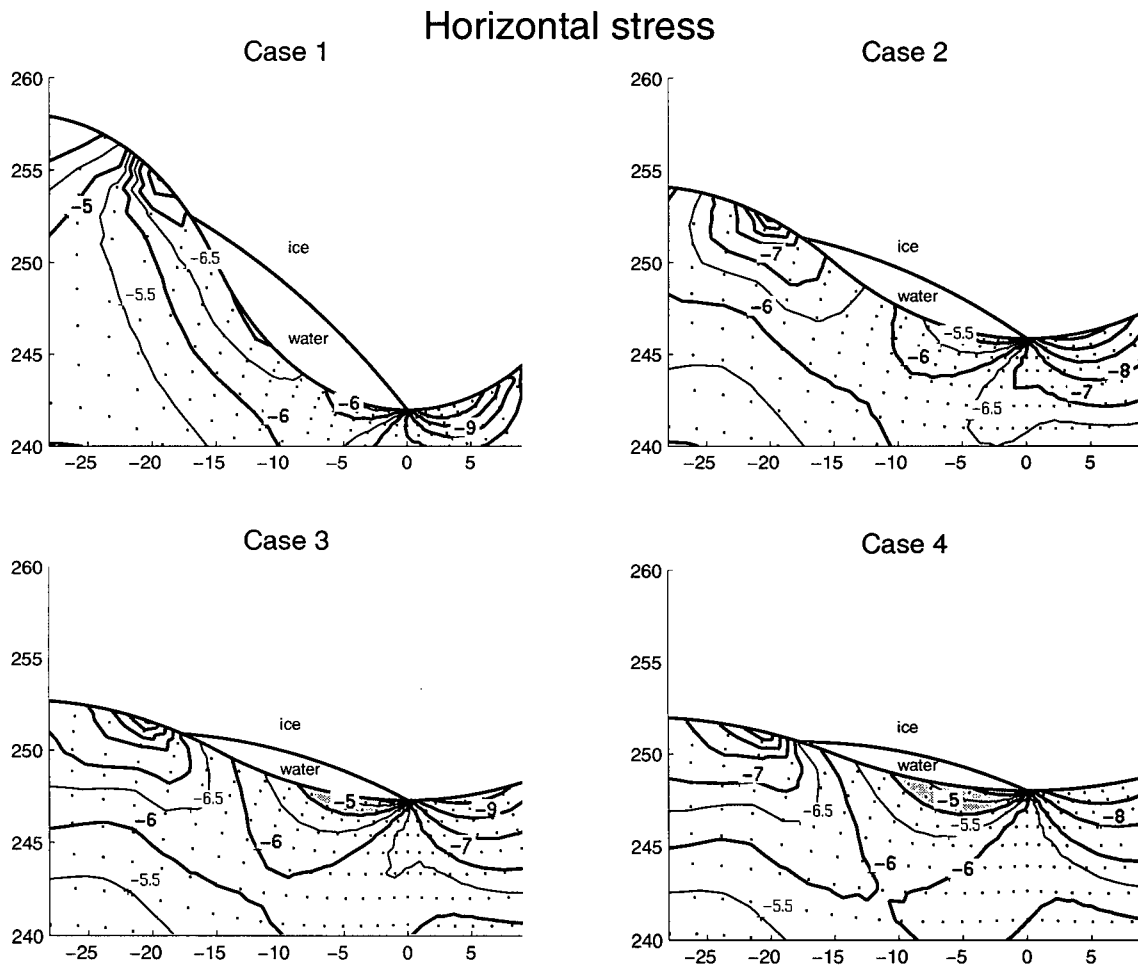


Figure 3.6.  $\sigma_{xx}$  (horizontal) results for the FRANC2D test of topography. All axes are in metres, and contours are in normalized units of stress where the surface loading is  $P_i = 10$ ,  $P_w = 5$  and  $\tau = 1$ . See text for further details.

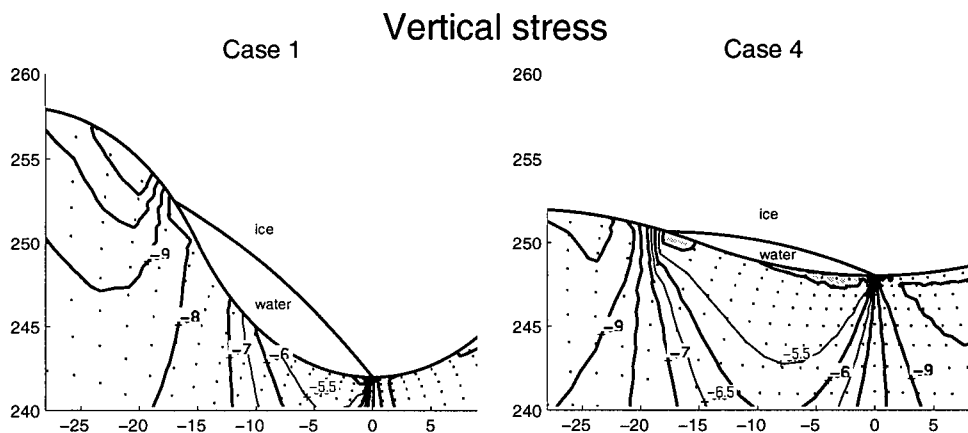


Figure 3.7.  $\sigma_{yy}$  (vertical) results for the FRANC2D test of topography. All axes are in metres, and contours are in normalized units of stress where the surface loading is  $P_i = 10$ ,  $P_w = 5$  and  $\tau = 1$ . See text for further details.

by Figure 3.8.

The maximum shear stress results shown in Figure 3.9 have a different response to topography. The most likely location for shear fracture occurs at the upstream cavity-ice junction and tends to increase with increasing topography; this is more akin to the results of *Morland and Boulton* [1975]; *Morland and Morris* [1977]. This observed topographic enhancement is heuristically modelled as a function of local bed dip  $\theta$  through

$$\sigma_S^{\max} = (2\theta + 1)\sigma_S^{\max}. \quad (3.18)$$

This linear enhancement satisfies two requirements: there is no modification for  $\theta = 0$  and, based on the examination of Figure 3.9, an enhancement of  $\approx 2.5$  results from  $\theta = \pi/4$ .

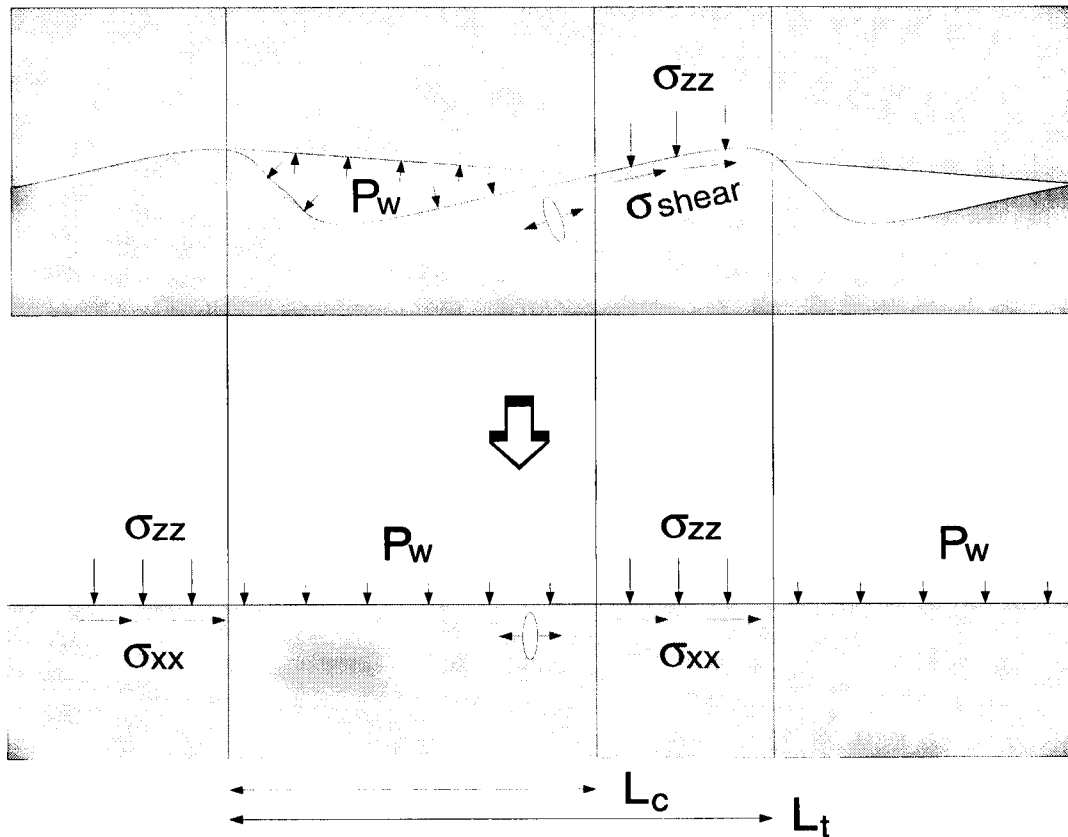


Figure 3.8. The assumption that the topography does not significantly affect the cavity dominated stress field allows for considerable simplification of the top panel to the bottom panel.

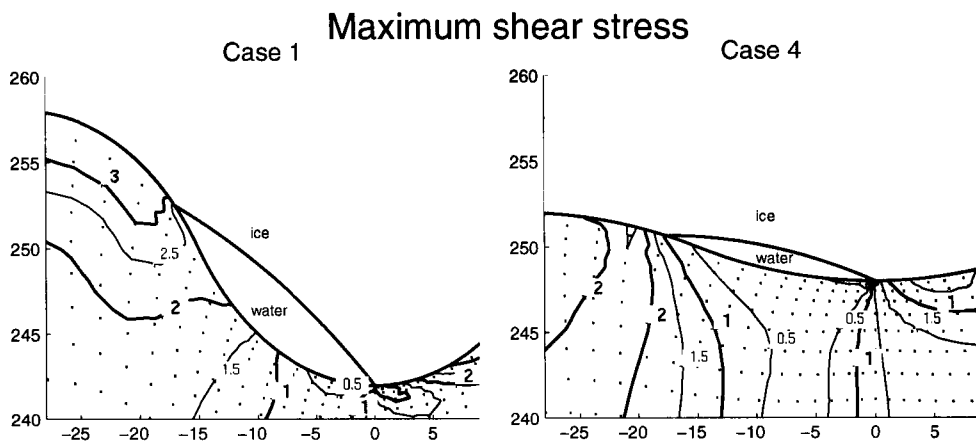


Figure 3.9. Maximum shear stress results for the FRANC2D test of topography. All axes are in metres, and contours are in normalized units of stress where the surface loading is either 10 (vertical), 5 (normal) or 1 (tangential). See text for further details.

### 3.2.4 Cavity size

The existence of a subglacial cavity is a prerequisite for quarrying; the stress regime without cavitation is generally insufficient to achieve the minimum stress intensity  $K_L^0$  needed to propagate cracks. Cavities arise when ice separates from the bed on the downstream side of bedrock knobs [Agassiz, 1876; Lliboutry, 1958, 1968]. Sliding, which generates the cavity, competes with closure by ice creep; balancing sliding and creep closure allows the prediction of steady state cavitation [Walder, 1986].

The size of the cavity  $L_c$  can range from zero to the topographical length scale  $L_t$ . Defining the normalized cavity extent  $L'_c \equiv L_c/L_t$ , I assume linear interpolation between two endpoints can be used to determine  $L'_c$ . The upper endpoint  $L'_c = 1$  represents complete decoupling of ice and bed; this can be expected when subglacial water pressure equals ice overburden pressure and there is no creep closure. The lower endpoint  $L'_c$ , modified from Walder [1986], is when the creep closure balances sliding. This is written as

$$P_w = P_i \qquad L'_c = 1, \qquad (3.19a)$$

$$P_w \leq P_i - n_G B_G \sqrt[n_G]{\frac{v_s \sin \theta}{L_t}} \qquad L'_c = 0, \qquad (3.19b)$$

where  $B_G$  is the Glen flow law parameter and  $n_G$  is the flow exponent, taken as  $4.19 \times 10^7 \text{ Pa s}^{1/3}$  and 3 respectively from Table 5.1 and Equation (5.3)<sup>5</sup>.

The endpoint (3.19a) is the flotation condition where complete decoupling is expected, while (3.19b) is where sliding equals creep closure velocity [Nye, 1953] with the radius of curvature of the ice surface taken as the topographic wavelength  $L_t$ . (3.19b) is a modification of the analysis of Walder [1986] where a single cavity size is calculated for a bedrock step. With the geometric inclusion of  $\sin \theta$ , I generalize to a variety of bed topography and the present formulation is appropriate to find the areal extent of cavitation over the entire bed. Equation (3.19) reproduces the fundamental features that  $L'_c \rightarrow 1$  as  $P_w \rightarrow P_i$  and that cavitation is suppressed in regions of low bed dip  $\theta$ . In the limiting case of a flat bed, no cavitation can occur until  $P_w$  reaches flotation. To avoid the non-physical solution of  $L'_c > 1$  when the water pressure exceeds flotation,  $L'_c$  is capped at  $L'_c^{\text{max}}$ , which is taken as 0.9.

#### Excess stress due to cavity

The integrated stress on the bed is determined by the ice height (for the  $\sigma_{zz}$  boundary condition) and surface slope (for the  $\sigma_{xz}$  boundary condition). The existence of a cavity will not change the integrated stress, but will redistribute it, concentrating stress on the portion of the bed in

<sup>5</sup>  $B_G = [B_0 \exp(-Q_i/R^{\text{gas}}T_i)]^{-1/3}$

direct contact with ice. The excess stress  $\sigma_{ab}^{ex}$  on bed with ice contact must satisfy the following conservation equations of the integrated stress

$$\int_{L_c}^{L_t} \sigma_{zz}^{ex}(\tilde{x}) d\tilde{x} = L_c(P_i - P_w), \quad (3.20a)$$

$$\int_{L_c}^{L_t} \sigma_{\tilde{x}z}^{ex}(\tilde{x}) d\tilde{x} = L_c\tau, \quad (3.20b)$$

where  $\tilde{x}$  is the coordinate coinciding with the direction of  $\mathbf{v}_s$ . The right-hand side of (3.20) represents the “missing” stress because of the presence of a cavity with length  $L_c$ . The left-hand side is the integrated redistribution of the excess stress over the portion of the bed in direct contact with the ice.

The form of the stress excess is taken as

$$\sigma_{ab}^{ex} = \mathcal{E}_{ab} \left( \tilde{x} - \frac{L_c + L_t}{2} \right)^2 \quad (3.21)$$

which reproduces the required property of greater stress concentration towards cavity-ice junctions [Iverson, 1991]. The constants  $\mathcal{E}_{ab}$ , determined by satisfying (3.20), are

$$\mathcal{E}_{zz} = \frac{24L'_c(P_i - P_w)}{L_t^2 \left[ (1 - L'_c)^3 - (L'_c - 1)^3 \right]}, \quad (3.22a)$$

$$\mathcal{E}_{xz} = \frac{24L'_c\tau}{L_t^2 \left[ (1 - L'_c)^3 - (L'_c - 1)^3 \right]}. \quad (3.22b)$$

### 3.2.5 A quarrying model

Any process-based quarrying law must be proportional to the rate of crack propagation; (3.16) is used for mode I and mode II crack growth. Unlike the model of *Hallet* [1996] there is no direct geometrical dependence on cavity extent. I do not attempt to explain the full process of quarrying and ignore the quandaries of how cracks connect and how blocks are evacuated; these details are geometry-specific and defy modelling efforts at this level. The important variable is crack growth velocity and therefore this is the only process variable used. The quarrying rate  $\dot{Q}$  is given by

$$\dot{Q} = [v_I + v_{II}] e^{-d/\check{d}} \quad (3.23)$$

where the rationale for the exponential term is identical to that given in Section 3.1.2 and  $\check{d}$  is calculated by (3.13).  $v_I$  and  $v_{II}$  are given by

$$v_I = \begin{cases} 0 & K_I < 0.25K_I^*, \\ \mathcal{A}_I \left[ \frac{m_g \sqrt{\pi l_c} (-\lambda^{(1)} + P_w)}{K_I^*} \right]^{n_I} & 0.25K_I^* \leq K_I \leq 0.75K_I^*, \\ \mathcal{A}_I 0.75^{n_I} & K_I > 0.75K_I^*, \end{cases} \quad (3.24)$$

and

$$v_{II} = \begin{cases} 0 & K_{II} < 0.25K_{II}^{*(-\lambda^{(1)} + P_w)}, \\ \mathcal{A}_{II} \left[ \frac{m_g \sqrt{\pi l_c} \check{\sigma}_S^{\max}}{K_{II}^{*(-\lambda^{(1)} + P_w)}} \right]^{n_{II}} & 0.25K_{II}^{*(-\lambda^{(1)} + P_w)} \leq K_{II} \leq 0.75K_{II}^{*(-\lambda^{(1)} + P_w)}, \\ \mathcal{A}_{II} 0.75^{n_{II}} & K_{II} > 0.75K_{II}^{*(-\lambda^{(1)} + P_w)}, \end{cases} \quad (3.25)$$

where  $\lambda^{(1)}$  is the minimum principal stress. The calculation of  $\lambda^{(1)}$  and  $\sigma_S^{\max}$ , which is modified to  $\check{\sigma}_S^{\max}$  by (3.18), is outlined in Appendix A.<sup>6</sup> The normal loading  $\bar{F}^N$  and tangential loading  $\bar{F}^S$  ( $\text{N m}^{-1}$ ) used in Appendix A as boundary conditions are driven by the cavity water pressure  $P_w$  (both as a direct BC and for determination of cavity extent through (3.19)), the ice overburden pressure  $P_i$  and the basal shear stress  $\tau$ , modified by the effect of the cavity as described in Section 23.<sup>7</sup>  $P_w$  is determined by the hydrological model (see Section 5.2) and  $P_i$  and  $\tau$  by the ice model (see Section 5.1). The parameters  $n_I, n_{II}, K_I^*$  and  $K_{II}^*$  have a lithological dependence and are assigned in Section 5.3.  $\mathcal{A}_{I,II}$  are tunable parameters and are explored in Section 6.2.

There are limitations on  $\bar{F}^N$  and  $\bar{F}^S$  because ice has finite strength; ice fracture puts a maximal limit on the interface stress. *Hallet* [1996] argues that  $P_i - P_w$  cannot exert more than 10 MPa on the bed based on the tensile strength of ice; however the ice never exists in a state of tension. A more appropriate measure is the crushing strength<sup>8</sup>  $S_c$ , which is 2 MPa for ice at  $0^\circ$  [*Butkovich*, 1954]. The crushing strength is a function of many parameters and can vary by a factor of  $\approx 3$  with different loading rates [*Butkovich*, 1955]. For slow (order of minutes) loading conditions that exist under ice sheets and glaciers, a crushing strength of 6.5 MPa is expected for samples with loading area  $\geq 0.25 \text{ m}^2$ . This is multiplied by a factor  $\mathcal{F}_g$  to account for the confinement of the ice. Therefore the condition on the normal loading will be

$$P_i + \sigma_N^{\text{ex}} - P_w < \mathcal{F}_g S_c. \quad (3.26)$$

The limit for the boundary condition for shear stress will necessarily involve  $S_s$ , the shear strength of ice, taken as 1.2 MPa [*Butkovich*, 1954]. This value is corrected to a confining pressure of  $P_i$

<sup>6</sup>Note that  $\sigma_S^{\max}$  is not the maximum shear stress but rather the shear stress on the plane of failure.

<sup>7</sup>The linear boundary conditions  $\bar{F}^N$  and  $\bar{F}^S$  are divided by a unit length to get the pressures  $P_i + \sigma_{zz}^{\text{ex}}$ ,  $P_w$  and shear stress  $\tau + \sigma_{xz}^{\text{ex}}$ .

<sup>8</sup>The crushing strength is the maximum compressive pressure on an unconfined sample of ice before fracture.

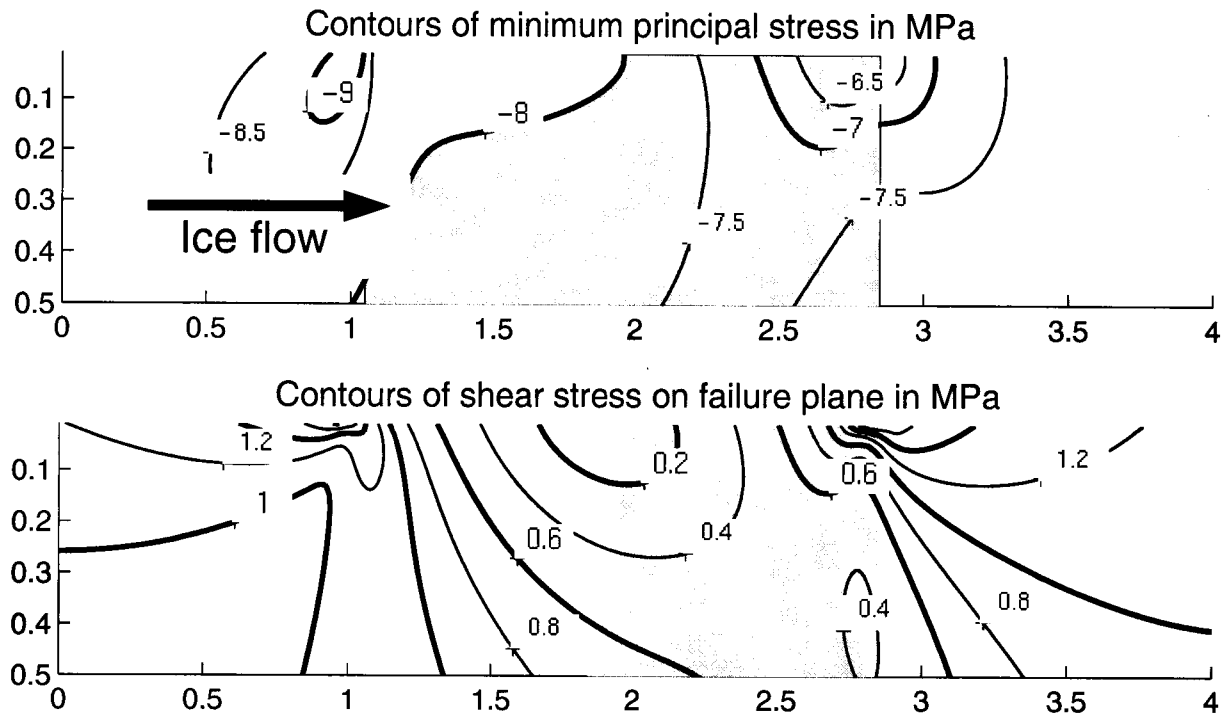


Figure 3.10. Cross sections of the minimum principal stress  $\lambda^{(1)}$  and the shear stress on the failure plane  $\sigma_S^{\max}$ . The cavity length is 1.7 m (while the topographical length scale is 10.0 m)

through  $\mu_{ice}$  the coefficient of internal friction for ice

$$\tau + \sigma_S^x < \mu_{ice} P_i + S_s \quad (3.27)$$

where  $\mu_{ice}$  is assumed to be 0.3.

A realization of the calculated stress due to a  $P_i = 9.00$  MPa,  $P_w = 8.10$  MPa,  $\tau = 1.00$  MPa and  $v_s = 150 \text{ m a}^{-1}$  is shown in Figure 3.10 (other parameters listed in Table 3.8). The shaded region is the area under the cavity (which has  $L_c = 1.7$  m) where the water pressure exceeds compressive forces acting on the crack: the crack is in tension. The area is not as extensive in the bottom panel because the orientation for maximum probability of shearing is not coincident with the minimum principal stress, i.e. on the failure surface,  $\sigma_N > \lambda^{(1)}$ . The most likely location of fracture (both mode I and II) are again predicted to be on the downstream cavity-ice junction (ice flows from left to right in Figure 3.10).

Parameter	Value	Units	Parameter	Value	Units
$n_G$	3	—	$B_G$	$4.19 \times 10^7$	$\text{Pa s}^{1/3}$ <sup>a</sup>
$S_c$	$6.5 \times 10^6$	$\text{Pa}$ <sup>b</sup>	$\mathcal{F}_g$	3	—
$S_s$	$1.2 \times 10^6$	$\text{Pa}$ <sup>c</sup>	$\mu_{\text{ice}}$	0.3	—
$\theta$	$45^\circ$	deg	$L_t$	10	m

Table 3.8. Parameters used to generate the stress cross-section in Figure 3.10 and the sensitivity tests of Figure 3.11

<sup>a</sup>From Paterson [1994]

<sup>b</sup>From Butkovich [1954, 1955]

<sup>c</sup>From Butkovich [1954]

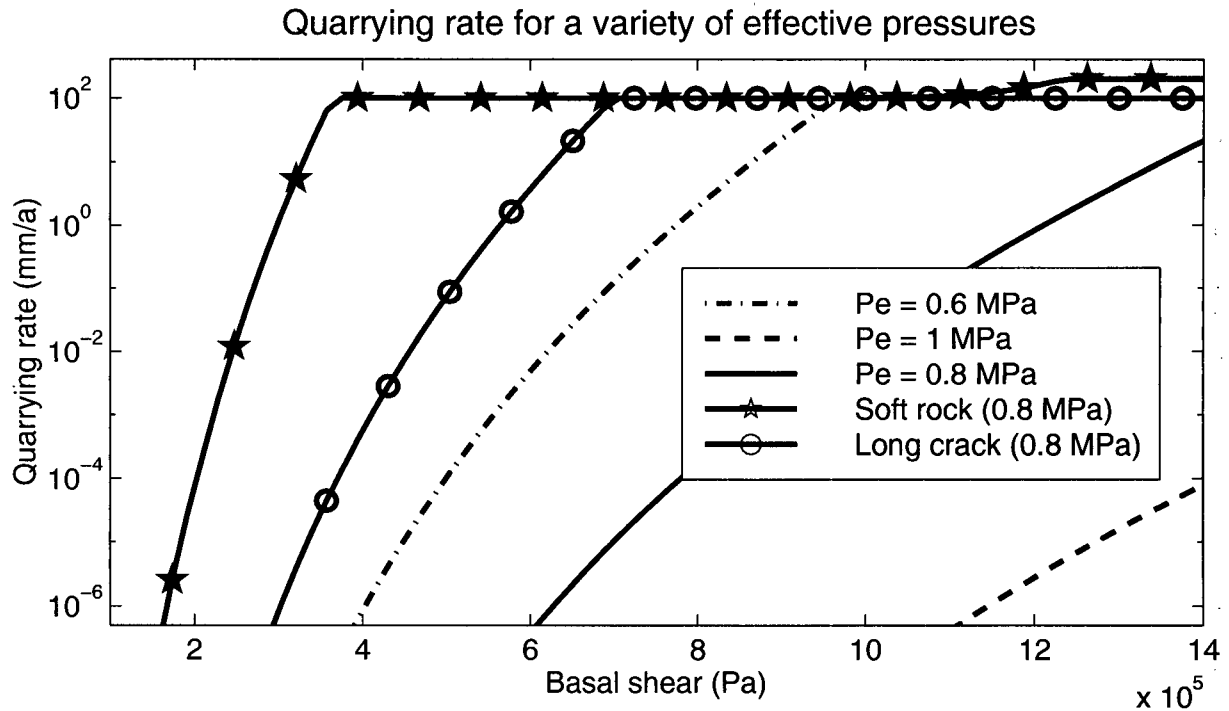


Figure 3.11. Quarrying sensitivity tests using  $\lambda^{(1)}$  and  $\sigma_S^{\text{max}}$  extracted from many two dimensional cross sections as shown in Figure 3.10. Effective pressure  $P_e$  is defined as  $P_i - P_w$ .

### 3.2.6 Quarrying sensitivity

Many analyses such as the example shown in Figure 3.10 are calculated for a range of basal shear stress and water pressure.  $\sigma_S^{\text{max}}$  and  $\lambda^{(1)}$  are extracted from each realization; the quarrying rate is then determined by (3.23), (3.24) and (3.25) using parameters from Table 3.9. This assemblage of results is plotted in Figure 3.11 .

Fairly low effective pressure (defined by  $P_e \equiv P_i - P_w$ ) is required for quarrying in this model.

Parameter	Value	Units	Parameter	Value	Units
$K_I^*$	1.76/0.34 $\times 10^6$	Pa m <sup>1/2</sup>	$K_{II}^*$	7.0/1.2 $\times 10^6$	Pa m <sup>1/2</sup>
$n_I, n_{II}$	20.0	—	$\mathcal{A}_I, \mathcal{A}_{II}$	$1 \times 10^{-6}$	m s <sup>-1</sup>
$v_s$	150	m s <sup>-1</sup>	$H^{\text{ice}}$	1000	m <sup>a</sup>
$m_g$	0.7	—	$l_c$	0.02 / 0.1	m
$\mu_{\text{int}}$	0.6	—			

Table 3.9. Parameters used for sensitivity tests of Figure 3.11. Dual values are given for standard and soft rock for  $K_I^*$  and  $K_{II}^*$ , standard and long crack length for  $l_c$ .

<sup>a</sup>with  $\rho_i = 900 \text{ kg m}^{-3}$  and  $g = 9.812 \text{ m s}^{-2}$

By (3.19b) a 2000 m thick ice sheet sliding at  $100 \text{ m a}^{-1}$  with 10 m bed topography of  $45^\circ$  bed dip, water pressure that is 95% of flotation is needed to form a cavity. Cavities occur at a lower fraction of flotation water pressure for thinner ice; it is the absolute effective pressure that controls the cavity size and the quarrying rate. For a given effective pressure the quarrying rate is very insensitive to the height of the ice column.

In general the results are also insensitive to the strength of the ice as the quarrying is limited by the  $0.75K_I^*$  cap rather than the crushing strength of the ice (similarly for mode II cracking).

Mode II subcritical cracking is only possible in very soft rocks. Even in these cases, it mostly remains insignificant compared to the mode I cracking. The only exception to this is at high values of  $\tau$  when the mode II crack growth catches up to the mode I crack growth, already curtailed at the  $0.75K_I^*$  limit. This is seen in the upper right hand corner of Figure 3.11.

This model produces much lower quarrying rates than the model of *Hallet* [1996]. The main reason for this discrepancy lies in the calculation of stress in the bed. *Hallet* [1996] contends that tensile stresses,  $2/3$  the magnitude of the loading stress, are induced in the bed. From the stress analysis of *Hetényi* [1960] (upon which the claim of *Hallet* [1996] is made) this can only happen under very specific conditions: when the corner of an infinite quarter plane is loaded. Possibly this situation could manifest itself subglacially when a very large proportion of the stepped bed is covered by cavities; I assume that the realization of this possibility does not play a significant role and take the more conventional view that the bed is in a state of compression due to ice loading.

## Chapter 4

# Englacial Processes

*The basal layer of glaciers and ice sheets is of immense significance not only to glaciology, but to the whole of Quaternary science. [Knight, 1997]*

This chapter deals with the mechanics and modelling of englacial activity. Entrainment (and complementary deposition) are those processes that directly exchange sediment with the bed through the bottom of the ice; they are discussed in Section 4.1. Englacial mixing (Section 4.2) controls the vertical motion of the sediment after entrainment (and prior to deposition). Lastly the lateral motion of sediment is considered in Section 4.3.

### 4.1 Entrainment

The margins of glaciers can have debris within the basal portion of the ice (see Figure 4.1); this is typical especially of cold or polythermal glaciers and surge-type glaciers [Boulton, 1970; Hambrey *et al.*, 1999]. Bore holes from modern ice sheets show that this phenomenon is not exclusive to the margins, and the central portions of ice sheets also have “dirty” basal ice [e.g. Gemmell *et al.*, 1986; Gow and Meese, 1996]. This debris is unquestionably of subglacial rather than supraglacial origin [Lawson and Kulla, 1978; Gemmell *et al.*, 1986; Strasser *et al.*, 1996] and the mechanism of its entrainment has captured the attention of glaciologists for over a century. Chamberlain [1895] asks:

*How does a glacier take up its material? How does it carry it forward? How does it put it down? What functions do water and topography play in the process? A glacier's methods in respect to lateral and medial moraines, which are superficial, are simple*

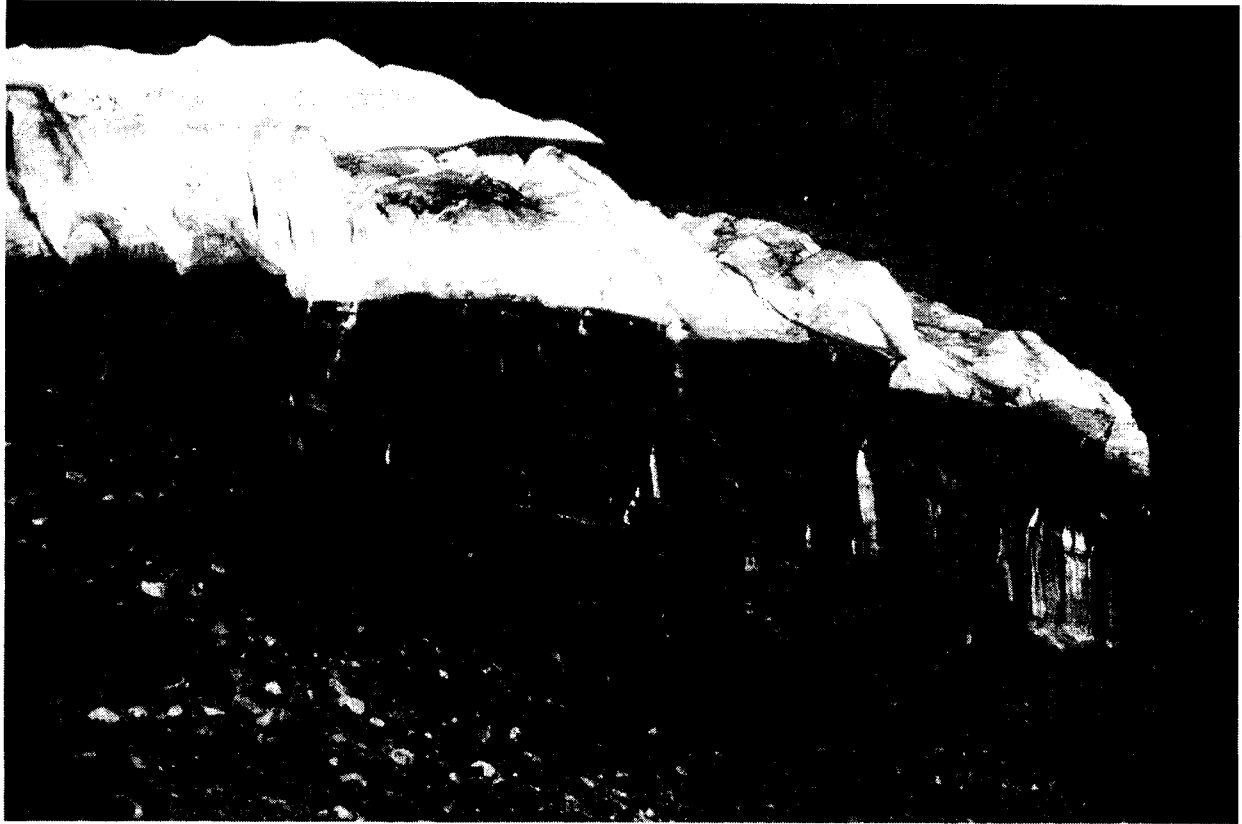


Figure 4.1. An example of debris-laden basal ice. This unnamed surge-type glacier flanks Mt. Wood in the St. Elias Range, Yukon Territory.

*and well known. Its methods respecting basal material, which is largely concealed, constitute the problem.*

A century of glaciological research has yet to fully answer these questions. The concealed nature of entrainment that beset the study of basal ice in the era of *Chamberlain* [1895] continues to limit workers today. Nevertheless advances from theory and experiment (both laboratory and ice tunnel) have contributed greatly to the modern discussion on entrainment of debris and our understanding of the subglacial processes responsible for basal ice is substantial, though not complete.

The subject of basal ice has direct consequence on the present study. I use englacial sediments as lithological tracers of the bed and the need for a process-driven model of entrainment is self-evident. There are also feedbacks to other modelled components; the debris volume fraction  $C$  affects the erosive power of ice (Equation (3.12) on page 28). To determine the time evolution of the volume fraction of lithology  $l$  in the  $(i, j, k)^{\text{th}}$  cell of ice  $C_{ijkl}$  is the objective of the englacial model.

Basal ice differs rheologically from pure ice although the relationship is complex [Hubbard and Sharp, 1989]. Despite basal ice typically representing a small volumetric fraction of the ice mass, deformation is concentrated towards the lower ice and differences in basal rheology may assume a substantial importance in ice sheet models. This represents an avenue of potential feedback to the ice sheet model.

A number of mechanisms can entrain debris into ice (see Alley *et al.* [1997]; Knight [1997] for comprehensive reviews); these include incorporation of pre-existing ice, freeze-on, regelation and englacial tectonics. Each is discussed below followed by a description of the modelling strategy used in the present study.

#### 4.1.1 Overriding of pre-existing ice

The simplest method by which ice sheets entrain debris is the cannibalisation of pro-glacial aprons<sup>1</sup> or peri-glacial frozen soils<sup>2</sup>. During an advance the ice can incorporate this debris-rich material instead of overrunning it as exhibited by the advance of Trapridge Glacier over its stagnant apron [Clarke and Blake, 1991]. Isotopic, gas, solute and sedimentological analysis suggest that this method accounts for dirty basal ice at Law Dome, Antarctica [Goodwin, 1993], GISP2 [Gow and Meese, 1996] and GRIP [Souchez *et al.*, 1994] stations in Greenland.

#### 4.1.2 Freeze-on

The entrapment of debris through the freezing-on of water at the sole of the glacier has several guises. In appropriate thermal conditions net basal freezing indiscriminantly adfreezes both ice and sediment. In the absence of a downward migrating freezing front, melting and refreezing cycles of Weertman regelation and glaciohydraulic supercooling (both discussed below on pages 56 and 57) can result in accretion of basal debris by freeze-on.

Stable isotope analysis has been instrumental in the identification of basal ice accreted by freeze-on; Gow *et al.* [1979] provides the first concrete evidence using  $\delta^{18}\text{O}$  analysis. During freezing, fractionation between heavy and light isotopes takes place giving frozen-on basal ice an isotopic signature. The co-analysis of  $\delta^{18}\text{O}$  and  $\delta\text{D}^\dagger$  can extend the stable isotope conclusions by offering information concerning the origin of the initial liquid [Jouzel and Souchez, 1982; Souchez and Jouzel, 1984].

<sup>1</sup>Glaciers can terminate by a steep margin with an apron of fallen-ice blocks, snow and sediment at the toe.

<sup>2</sup>Frozen ground on the perimeter of an ice sheet.

$\dagger\delta\text{D} = \left[ \frac{(\text{HD}^{16}\text{O}/\text{H}_2^{16}\text{O}) - (\text{HD}^{16}\text{O}/\text{H}_2^{16}\text{O})_{\text{SMOW}}}{(\text{HD}^{16}\text{O}/\text{H}_2^{16}\text{O})_{\text{SMOW}}} \right] \times 1000$  where SMOW is a standard of water.

### Net basal freezing

The thermodynamic evolution of the ice is calculated by the Marshall–Clarke ice sheet model, described in Section 5.1.1 on page 74. By momentarily ignoring the advective and strain heating terms, the energy balance equation (5.4) can be rewritten as

$$\rho_i c_i \frac{\partial T_i}{\partial t} = \nabla \cdot \mathbf{q}_i \quad (4.1)$$

where  $\mathbf{q}_i$  is the heat flux through the ice. Using Fourier's Law, with the assumption that vertical gradients dominate their lateral counterparts, the vertical heat flux is given by

$$q_i^z = -k_i \frac{dT_i}{dz}. \quad (4.2)$$

Under a warm-bedded glacier with available water, the temperature is fixed at  $T_{pmp}$  the pressure melting point therefore (4.1) demands that  $\mathbf{q}_i$  be solenoidal and the vertical heat flux must balance the basal boundary conditions. If the ice thins and the thermal gradient  $dT_i/dz$  steepens, the increased heat flux from (4.2) must be accompanied by an extra boundary condition: the freezing front migrates downward, releasing latent heat of freezing. This mechanism was first proposed by *Weertman* [1961] and has been invoked as the entrainment mechanism for many glaciers and ice sheets [e.g. *Gow et al.*, 1979; *Herron and Langway*, 1979; *Sugden et al.*, 1987; *Tison et al.*, 1989; *Knight*, 1994; *Zdanowicz et al.*, 1996].

### Weertman regelation

The sliding of glaciers partly relies on regelation around small topography of the bed [*Weertman*, 1957]; this involves local melting of ice on the upstream side of an asperity and freezing on the downstream side (see Section 4.1.3). The downstream refreezing has the propensity to freeze-on fine particles suspended in the subglacial water. Generally this mechanism does not produce an appreciable net gain of ice because the newly formed basal ice on the lee side of an asperity is mostly melted on the upstream side of the following bump. Net accretion can form in bed troughs although the thickness, which is a function of bed roughness, is limited to  $\approx 10$  cm [*Hubbard and Sharp*, 1993]. This thickness is based on a model of multiple melting-refreezing cycles and is in accordance with observational data.

*Lliboutry* [1993] offers an alternate theory for Weertman regelation in which the temperature of the ice is completely determined by its stress regime and the water source for the accretionary ice is englacial. Although the theory differs from the classical theory used by *Hubbard and Sharp* [1993] where the water originates and travels along the bedrock surface, the results are similar: a layer of accreted ice  $\approx 3.5$  cm thick. Laboratory work supports the theory of englacial water

transport and this vein flow is observed to entrain fine grained debris [Knight and Knight, 1994, 1999].

Thin bands of debris are expected from the regelation mechanism of either Weertman [1957] or Lliboutry [1993] and laminated facies of basal ice are commonly attributed to this process [Hubbard and Sharp, 1993; Sharp et al., 1994; Hubbard and Sharp, 1995]. Regelation is also the foremost entrainment hypothesis for a dispersed clotted facies observed in Arctic outlet glaciers [Sugden et al., 1987; Souchez et al., 1988; Knight, 1994].

### Glaciohydraulic supercooling

Water flowing into a region of lower ice-overburden pressure may become supercooled if it cannot warm quickly enough to accommodate the changing melting point; this supercooled water can freeze-on debris [Lawson et al., 1998; Alley et al., 1998]. However the opposite effect occurs when the water descends a bedrock slope and no net accretion would normally be expected via this mechanism. Also, large volumes of subglacial water flow are required for glaciohydraulic supercooling to be effective as an agent of entrainment [Alley et al., 1997]; this may exist in alpine glaciers where surface melt can reach the bed via crevasses and moulins but is unlikely in ice sheets where such surface-bed communication does not exist (Section 5.2).

### 4.1.3 Intrusion by regelation

#### Background

The first modern definition of regelation is given by Thomson [1859/60] as “melting by pressure and freezing again on relief of pressure” ten years after Faraday first described the phenomenon as a curiosity in a lecture for the Royal Society. It is the process by which ice melts from higher pressure on one side of a grain (or asperity) and refreezes on the opposite side with heat flow through the grain driving the process. An early quantitative experiment describing a wire mesh passing through a block of ice [Bottomley, 1871/72] anchored the qualitative regelation theory of Thomson [1859/60]; the possible importance to subglacial processes was noted by Bottomley [1871/72].

A comprehensive regelation theory was outlined by Ornstein [1906] and Deeley and Parr [1914] developed an early glacial sliding mechanism reliant on regelation. Experiments of regelation around geologic materials [Deeley and Parr, 1914] buoyed the early theory (which is remarkably similar to the modern theory of Weertman [1957]) by allowing predictions of glacial sliding speed, which were in good accordance with observation. Refinements to regelation theory and

quantitative experiments continued over the following half-century [e.g. Drake and Shreve, 1973].

The next step towards the development of regelation as an entrainment mechanism is the work of Philip [1980] with a theoretical treatise of ice flow past an array of cylinders by regelation. Experimental work supports the theory [Iverson, 1993; Iverson and Semmens, 1995] and demonstrates that regelation can occur around an array of englacial, cobble-sized, angular clasts and also into coarse-grained sediment. This unequivocally marks intrusion by regelation as a potential entrainment mechanism. Furthermore, isotopic analysis [Iverson and Souchez, 1996] demonstrates that the mechanism is consistent with existing basal isotopic data. Fine-grained sediment may not behave the same as coarse-grained sediment because silt to clay-sized particles have large surface-to-volume ratios and the correspondingly large surface energies may impede intrusion by regelation [Alley *et al.*, 1997].

### Theory

The steady intrusion speed  $v_r$  for ice at the pressure melting point moving into an array of clasts with a macroscopic pressure difference between the ice overburden and subglacial water pressure  $P_i - P_w$  across it is [Philip, 1980]

$$v_r = -\mathcal{K} \frac{P_i - P_w}{l_a}, \quad (4.3)$$

where  $\mathcal{K}$  ( $\text{m}^2 \text{Pa}^{-1} \text{s}^{-1}$ ) is the apparent conductivity of the array to the ice and  $l_a$  is the effective depth of grain-supported basal ice. Figure 4.2 illustrates the variables involved.

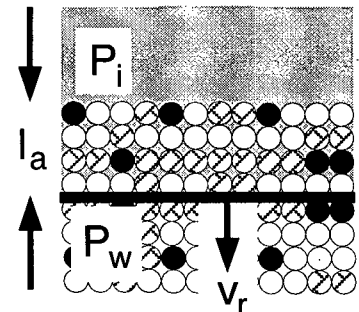


Figure 4.2. A sketch of intrusion showing ice overburden pressure  $P_i$ , subglacial water pressure  $P_w$ , effective depth of grain-supported basal ice  $l_a$  and intrusion speed  $v_r$ .

The conductivity  $\mathcal{K}$  is written in terms of the thermal conductivity of the clast and ice  $k_r$  and  $k_i$ , the porosity  $n^s$ , the pressure melting coefficient  $\mathcal{P}_c$ , ice density  $\rho_i$  and the latent heat of fusion for water  $L_{\text{fus}}$  as [Philip, 1980; Iverson and Semmens, 1995]

$$\mathcal{K} = \frac{2k_i + k_r}{k_i + k_r} \left[ \frac{\mathcal{P}_c \pi (k_i + k_r + k_1)}{L_{\text{fus}} \rho_i (1 - n^s) \left[ \pi + (1 - n^s) \left( \frac{\pi^2}{3} - 4\pi e^{-2\pi} \right) \right]} \right], \quad (4.4)$$

where the conductivity  $k_1$  is

$$k_1 = (k_r - k_i) \left\{ 1 - \sqrt{\pi(1 - n^s)} \left[ \coth \sqrt{\pi(1 - n^s)} - 2\sqrt{(1 - n^s)/\pi} \coth \left( \pi - \sqrt{\pi(1 - n^s)} \right) - (1 - 2\sqrt{(1 - n^s)/\pi}) \right] \right\}. \quad (4.5)$$

For pure ice (at 0° C),  $k_i = 2.10 \text{ W m}^{-1} \text{ K}^{-1}$ ,  $\mathcal{P}_C = 7.42 \times 10^{-8} \text{ K Pa}^{-1}$ ,  $L_{\text{fus}} = 3.34 \times 10^5 \text{ J kg}^{-1}$  and  $\rho_i = 910 \text{ kg m}^{-3}$ . The porosity  $n^s$  is taken as 0.40 (consistent with Section 5.2.1 on page 78) and a value of  $2.86 \text{ W m}^{-1} \text{ K}^{-1}$  is used for  $k_r$  as determined in Section 11 on page 30. These parameters result in  $\mathcal{K} = 2.01 \times 10^{-15} \text{ m}^2 \text{ Pa}^{-1} \text{ s}^{-1}$ .

Classical regelation theory requires ice to be at the pressure melting point. However, there is a theoretical basis for regelation at sub-freezing temperatures [Shreve, 1984] and observational evidence of cold sliding [Echelmeyer and Zhongxiang, 1987; Cuffey et al., 1999] and cold intrusion by regelation [Cuffey et al., 2000] although these processes are very sluggish in cold ice compared to their rates in ice at the pressure melting point.

#### 4.1.4 Englacial tectonics

##### Evidence for thrust faulting

The argument that sediment is scraped off the bed and incorporated englacially by thrust faults in the ice was put forward by Chamberlain [1895] to explain marginal debris bands in Greenland; it continued to be developed as the sole unchallenged entrainment mechanism over the following seven decades [e.g. Goldthwait, 1951; Bishop, 1957]. The theory was attacked as untenable by Weertman [1961] based on the observations of finely interbedded layers of clean and dirty ice and a lack of shear evidence across the debris bands; these features are a challenge to explain using the thrusting model of Chamberlain [1895]. In the same paper as the critique of the entrainment-by-shearing mechanism, Weertman [1961] proposed an alternate theory of bulk freeze-on to explain the observed debris bands, described in Section 4.1.2.

Souchez [1967] hypothesizes that multiple processes are active to produce two coincident yet distinct types of debris bands (with very different orientations and grain size assemblage); one is attributed to the net freeze-on mechanism of Weertman [1961], the other to thrust faulting. Further alternative mechanisms for the formation of the marginal debris bands of Greenland and Baffin Island are provided by Hooke [1973].

Nevertheless, outside the high arctic of Canada and Greenland, observational evidence of thrust

faults with associated debris continues to accumulate. Many Svalbard glaciers, both surge and non-surge type, regularly exhibit thrust faults with debris-laden ice [Hambrey *et al.*, 1996, 1999]. Tison *et al.* [1989] document a case from a tunnel in an Alpine glacier, Grubengletscher, that shows a thrust surface with frozen ground moraine being transported upward; similar evidence exists for large Alaskan glaciers [Hart, 1995]. Clarke and Blake [1991] document englacial debris emplacement by thrust faulting in Trapridge Glacier, Yukon Territory, a small surge-type glacier in a quiescent state and Sharp *et al.* [1988] directly observe thrust faulting at Variegated Glacier, Alaska during an active surge.

Thus the evidence that thrust faults act as conveyor belts transporting material away from the bed in alpine glaciers is irrefutable. A more subtle question remains: whether shearing at the bed can independently entrain material via basal décollement or whether the mechanism merely acts as a vehicle for previously entrained debris as suggested by Boulton [1970]. There are examples of debris bands with properties that are difficult to explain with a freeze-on paradigm. Hambrey *et al.* [1999] note in a review of twelve Svalbard glaciers that some bands have thick (0.5 m) zones of sediment with little interstitial ice while Clarke and Blake [1991] observe a thrust plane develop during a period of ice thickening and bed warming; neither observation is conducive to a freeze-on mechanism. However these examples could be consistent with intrusion (Section 4.1.3) and do not therefore constitute a convincing argument for entrainment by thrusting. The question of true entrainment by thrust faulting remains unanswered.

### Location of thrust faulting

Supraglacial debris ridges from shearing along thrust planes tend to be marginal features occurring within  $\approx 1$  km of the toe, but ice cliff observations in Svalbard show that many thrusts do not reach the surface [Hambrey *et al.*, 1999] as does a direct drilling program on Trapridge Glacier [Clarke and Blake, 1991]. Surficial expression of debris-laden faults is only possible where the ice is sufficiently thin. The corollary is that the evidence that thrusting only occurs at the margins is a biased one: unseen thrusting may take place under thick ice hidden from direct observation.

Thrust faults occur where there is strong longitudinal compression [Sharp *et al.*, 1988]. For quiescent glaciers this is most likely where warm-bedded sliding ice encounters relatively stationary cold-bedded ice as observed on Trapridge Glacier [Clarke and Blake, 1991] or in the vicinity of a bedrock obstruction [Boulton, 1970]. During an active surge there is a more complex stress regime and non-thermally initiated thrusts can be expected [Sharp *et al.*, 1988]. There are exceptions: Tison *et al.* [1993] document an example of a debris-laden fault over a part of the glacier well below the pressure melting point and Echelmeyer and Zhongxiang [1987] report movement along planes within an ice-laden drift at subfreezing temperatures from direct measurement.

Alley *et al.* [1997] suggest that the overall volumetric importance of thrust-fault debris is negligible

on a whole ice sheet debris budget; indeed, as indicated above, the contribution may be zero. Regardless, thrust faults play an important role for the vertical transport of englacial debris, which has implications for total englacial residence time and thus total distance of transport. Basal melt prevents concentrated debris proximal to the sole from logging substantial advected travel; this is especially true during times of vigorous sliding when frictional heat production is high. Thrust-fault transport away from the frictional surface can mitigate this problem.

### Folding

Evidence of folding is common in the basal ice of alpine glaciers [e.g. *Hudleston*, 1976; *Lorrain et al.*, 1981; *Hart and Waller*, 1999; *Waller et al.*, 2000] and is inferred in the central areas of ice sheets [*Paterson et al.*, 1977; *Taylor et al.*, 1993]. A change in either ice thickness or surface slope over a bedrock ridge can lead to recumbent and overturned folds [*Hudleston*, 1976]. This tectonic activity potentially entrains material as a recumbent fold can trap a section of the bed, thus incorporating it into an englacial position [*Tison et al.*, 1989; *Glasser et al.*, 1998]. The axis of a fold can also initiate the formation of a shear plane [*Sharp et al.*, 1994].

Basal ice can have isotopic sequences that cannot be explained using known entrainment mechanisms [*Lorrain et al.*, 1981; *Knight*, 1989]; englacial tectonic activity is invoked to reconcile these observations [*Lorrain et al.*, 1981; *Knight*, 1994]. Melting and refreezing around bedrock bumps can typically create  $\approx 10$  cm of basal ice (Section 33) while much thicker sequences of regelation ice is sometimes observed [*Sharp et al.*, 1994; *Hubbard and Sharp*, 1995]. Folding is again used to reconcile observation and theory by post-entrainment tectonic thickening of pre-existing basal layers.

#### 4.1.5 An entrainment model

The full spectrum of entrainment mechanisms is wide and I will narrow the scope. Net basal freezing, Weertman (or Lliboutry) regelation and intrusion are considered significant entrainment mechanisms while thrust faulting is accepted as a vertical transport mechanism and its implementation details are deferred until Section 4.2.3. A sketch of the modelled processes is shown in Figure 4.3.

Most existing entrainment models are based on the empirical observation of *Krumbein* [1937] that allochthonous debris concentration exponentially decays with distance from the source; this has proved expedient for the rich field of drift prospecting [e.g. *Clark*, 1987; *Parent et al.*, 1996] but a process-driven approach is required to make use of glaciological knowledge and models. *Boulton* [1984] describes a simple model where the basal ice thickness is held constant and entrainment and deposition are calculated using the continuity equation. *Tulley* [1995] offers a large-scale

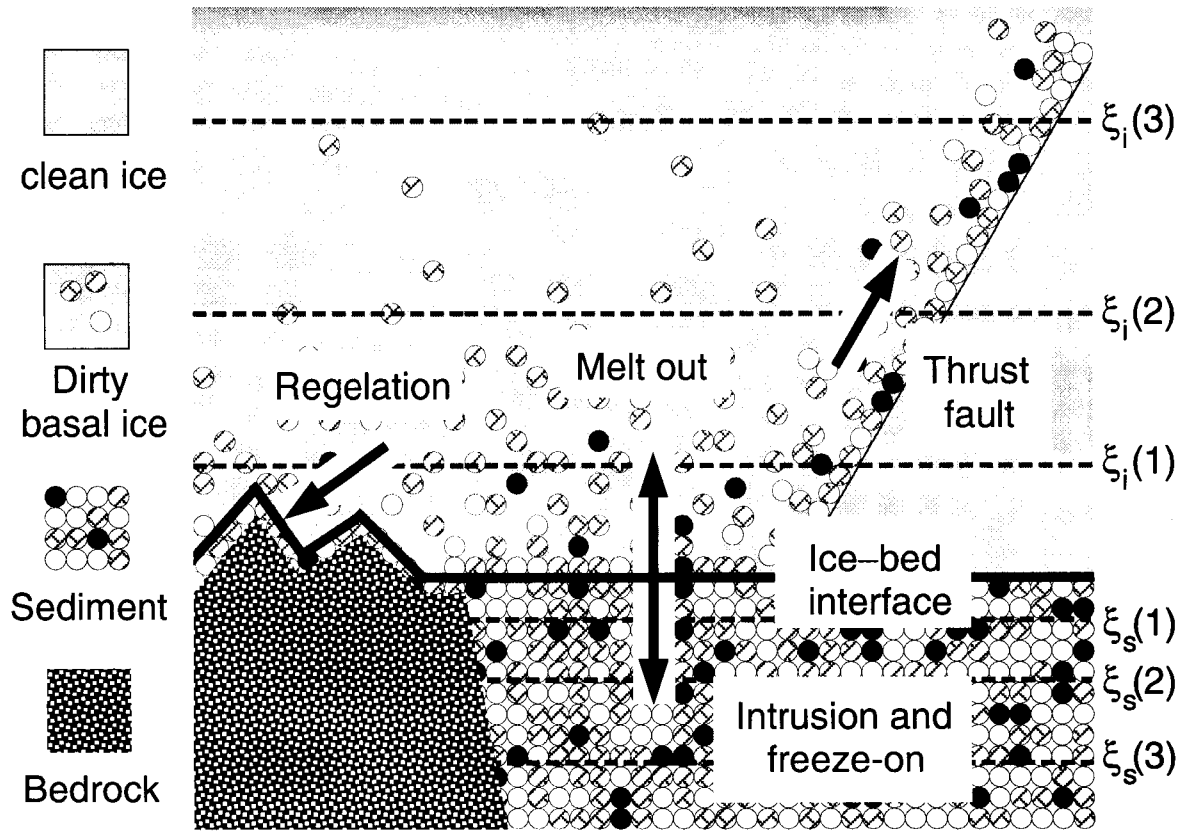


Figure 4.3. A sketch of entrainment processes. Both freeze-on and basal melt affect the basal ice layer; the latter competes against intrusion. Where the ice is sliding over bedrock, Weertman regelation around bedrock bumps entrains a small amount of debris. Thrust faults transport previously entrained material away from the bed (along with other mixing processes detailed in Section 4.2). The vertical grid, defined by (4.6) is logarithmic to concentrate grid cells towards the ice-bed interface.

Parameter	Ice			Sediment		
	$A_t^i$	$l_i$	$N_i$	$A_t^s$	$l_s$	$N_s$
Value	-3	30 m	10	-1	-10 m	5

Table 4.1. Parameters for the vertical grid, shown in Figure 4.4.

entrainment model of intrusion and *Iverson* [2000] also explores this mechanism in ice sheets with a channelized hydrology.

To concentrate computing resources towards the ice–bed interface, an exponential transform of the vertical coordinate  $z$  is used:

$$\xi_i = \exp(A_t^i z / l_i), \quad (4.6a)$$

$$\xi_s = \exp(A_t^s z / l_s), \quad (4.6b)$$

where  $A_t^{i,s}$  is a grid transformation parameter and  $l_{i,s}$  is the thickness of the modelled layer for the sediment ( $s$ ) and basal ice ( $i$ ). The grid is regularly spaced in  $\xi_{i,s}$  with

$$\Delta\xi_{i,s} = \frac{\exp(A_t^{i,s}) - 1}{N_{i,s}}, \quad (4.7)$$

where  $N_{i,s}$  is the number of vertical cells. These parameter are given in Table 4.1 and the grid is illustrated in Figure 4.4. The debris content  $C$  is defined at the cell centres from  $\xi_{1/2}$  to  $\xi_{N_i-1/2}$ ; the non-vertical velocities are similarly placed, therefore lateral advection (Section 4.3) also acts on the half grid. Conversely, vertical mixing (Section 4.2) is defined at the cell interface, on the integer  $\xi$  grid. The ice–bed interface at  $\xi_i = 0$  and  $\xi_s = N_s$  is not stationary and migrates with the interface.

Vertical stratification of the lithological assemblage is maintained in both the ice and the sediment during any motion of the ice–bed interface within the bounds of the vertical discretization<sup>4</sup>. Thus the grid repositioning from entrainment or deposition leads to vertical numerical diffusion. This is not a serious issue because non-numerical mixing mechanisms do operate within the ice and sediment. Englacial mixing is discussed in Section 4.2 and although mixing is not explicitly considered within the sediment, some physical mixing is expected.

The determination of net basal freezing is enigmatic. There must be an adequate source of water to ensure that the glacier’s basal temperature remains at the pressure melting point, otherwise the freezing front migrates into the sediment and the glacier becomes frozen to the bed. To rigorously solve for basal freezing is therefore a non-trivial problem and to date, no ice sheet model treats it adequately. The Marshall–Clarke (MC) ice model (described in Section 5.1.1 and references therein) provides the basal temperature necessary to balance the internal thermodynamics of the ice with a temporally constant geothermal heat flux. Latent heat of freezing is not included in this

<sup>4</sup>In contrast to the lateral distribution, no sub-grid scheme is used to describe intra-cell debris variations.

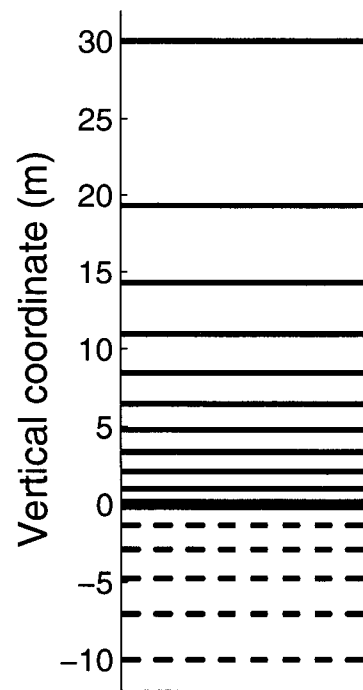


Figure 4.4. The vertical grid used for the basal ice and sediment. The spacing is regular in  $\xi_{s,i}$ -space which is defined by (4.6) with parameters  $A_{i,s}^t$ ,  $l_{i,s}$  and  $N_{i,s}$  from Table 4.1.

calculation and the bed cools to maintain the necessary heat flux through the basal ice rather than allowing freeze-on. I use the given fields from the MC ice model to estimate potential freeze-on.

Modelled adfreeze onto the bed is limited to a single time step when the basal temperature of the ice falls from the pressure melting point  $T_{pmp}$ . The characteristic time of water availability is taken as  $\mathcal{T} = \Delta t/2 = 200$  a; after this it is assumed that the sole of the ice becomes cold, as the MC model predicts. The temperature at the bed has an effect on a thermal boundary layer; the height of this layer is estimated by  $\sqrt{\kappa\mathcal{T}}$  where  $\kappa$  ( $\text{m}^2\text{s}^{-1}$ ) is the thermal diffusivity of the ice<sup>5</sup>; using values from Table 5.1,  $\kappa = 1.1 \times 10^{-6} \text{m}^2\text{s}^{-1}$ . This results in a thermal boundary layer of  $\approx 80$  m.

I integrate the energy leached from this layer (or from the entire ice thickness  $H^{ice}$ , whichever is less) over the grid cell through

$$\mathcal{F} = \int_0^{\min[\sqrt{\kappa_i\mathcal{T}}, H^{ice}]} \Delta T_i^{\text{bed}} c_i \rho_i dz. \quad (4.8)$$

The energy density  $\mathcal{F}$  ( $\text{J m}^{-2}$ ) is assumed to be available for freeze-on and translates into a freeze-on depth  $\mathcal{F}_d$  (m) by

$$\mathcal{F}_d = \frac{\mathcal{F}}{\rho_i L_{\text{fus}}} \quad (4.9)$$

where the specific heat of ice  $c_i$  is  $152.5 + 7.1222T_i \text{ J kg}^{-1} \text{ K}^{-1}$  and  $L_{\text{fus}}$  is  $3.34 \times 10^5 \text{ J kg}^{-1}$  [Paterson, 1994]. This estimate of freeze-on is not consistent with the MC ice model: I violate the conservation of energy as there is no feedback mechanism and the ice thermal regime is not altered as it rigorously should be. The method is illustrated in Figure 4.5.

Intrusion occurs when the ice is at the pressure melting point<sup>6</sup> at a rate given by (4.3). There is competition with basal melt  $\dot{b}_{\text{melt}}$  and an equilibrium depth of basal sediment  $l_a^{eq}$  is expected, corresponding to a balance when basal melt rate  $\dot{b}_{\text{melt}}$  is equal to the intrusion rate  $v_r$ . Therefore, by (4.3)

$$l_a^{eq} = \mathcal{K} \frac{P_i - P_w}{\dot{b}_{\text{melt}}}. \quad (4.10)$$

The response time to approach  $l_a^{eq}$  is generally short with respect to the time step and adjustment is instantaneous on the model time scale. If  $l_a > l_a^{eq}$ , the difference is melted off and till is deposited. If  $l_a < l_a^{eq}$ , sediment is entrained subject to availability. A maximum entrainment of

<sup>5</sup>The thermal diffusivity  $\kappa_i$  is defined in terms of the thermal conductivity  $k_i$ , specific heat capacity  $c_i$  and density  $\rho_i$  as  $\kappa_i = k_i/\rho_i c_i$

<sup>6</sup>depressed by  $\epsilon_T$  (0.1 K) to account for cold entrainment.

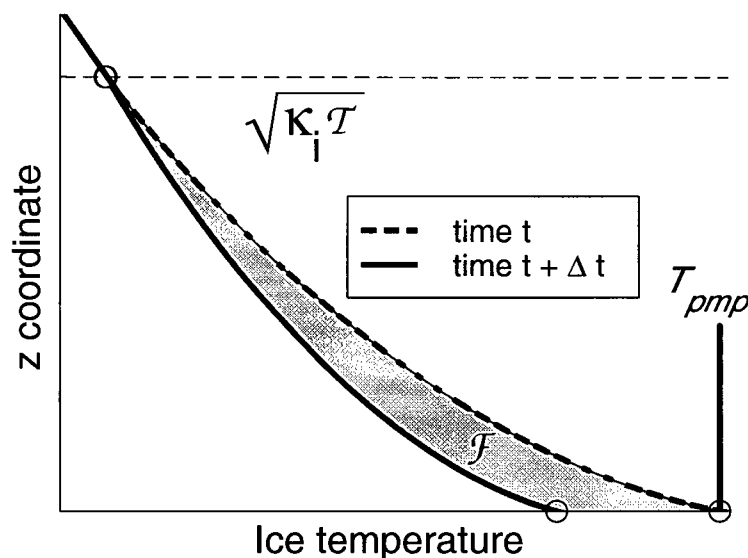


Figure 4.5. A sketch of the energy density  $\mathcal{F}$  available for freeze-on.

$l_a^{\max} \equiv l_a^{eq} - l_a$  of  $v_r^{1/2} \Delta t$  is imposed for any single time step where  $v_r^{1/2}$  is defined as

$$v_r^{1/2} = \frac{\mathcal{K}(P_i - P_w)}{(l_a + l_a^{eq})/2} \quad (4.11)$$

This ameliorates the situation when  $v_r^{1/2}$  is very small, resulting in a large  $l_a^{eq}$  that would violate the approximation of instantaneous response time. Similarly, a maximum melt of  $-\dot{b}_{\text{melt}} \Delta t$  is imposed for any single time step  $\Delta t$ .

Interpretation of  $l_a$  (or  $l_a^{eq}$ ) is not as straightforward as one may initially presume. Intrusion theory assumes that englacial debris forms a grain skeleton which takes up the pressure difference  $P_i - P_w$ ; a dispersed basal layer does not contribute to the grain skeleton and therefore does not impede intrusion. The right-hand side of Figure 4.6 illustrates the issue; in panel (A), where the debris concentration is equal to that of the sediment ( $1 - n^s$ ), the effective array depth is equivalent to the depth of englacial debris,  $l_a = z_1$ . However in panel (C) the englacial debris is dispersed and the effective array depth  $l_a = 0$ . Panel (B) represents an intermediate stage where  $0 < l_a < z_2$ . Quantification of this effect is needed.

An array depth modifier  $\check{l}_a$  is defined as

$$\check{l}_a = \frac{1}{2} [\tanh(20C - 8) + 1]. \quad (4.12)$$

The rationale for this function, shown in the left-hand panel of Figure 4.6, is that by assigning  $\check{l}_a$  a low weight when  $C \ll 0.3$ , dispersed debris is prohibited from acting as an effective agent of

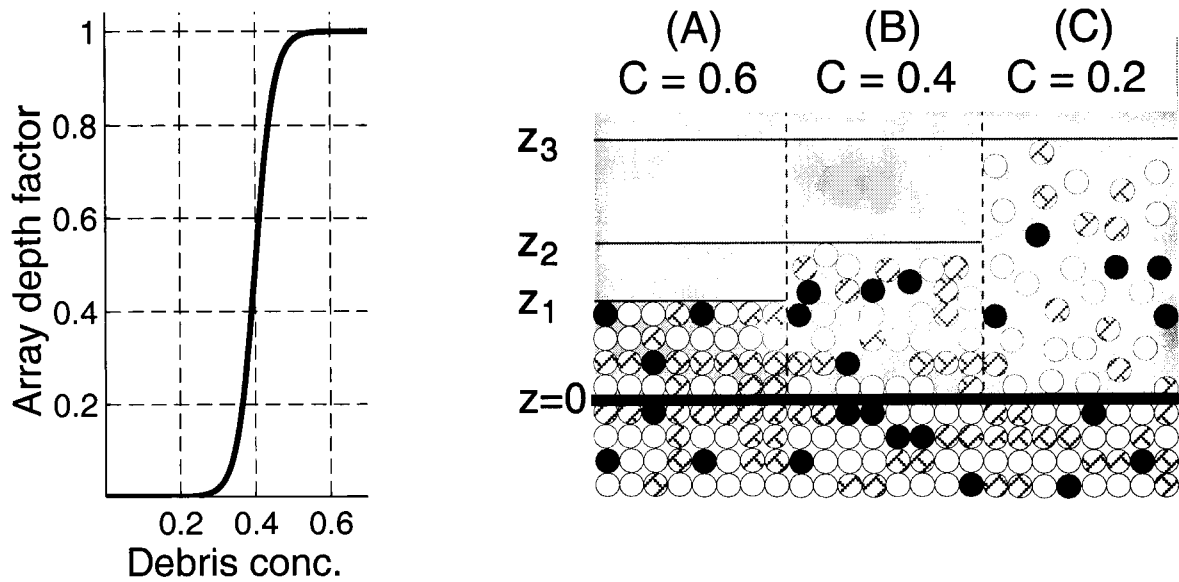


Figure 4.6. A plot of the array depth modifier  $\check{l}_a$ , which is a function of debris concentration  $C$ . The sketch on the right provides the physical motivation of the need for  $\check{l}_a$ . Details are in the text.

the grain skeleton. The effective array depth is defined as

$$l_a = \sum_{k=1, N_i} \check{l}_a \Delta z_k \quad (4.13)$$

where  $k$  indexes the vertical discretization of the basal ice.

In areas where the ice is sliding over bedrock (defined where  $d < d^{\text{reg}}$  and  $d^{\text{reg}} = 0.25$ ), Weertman regelation can entrain a dispersed facies in a thin layer next to the bed. Where these conditions exist, a 10 cm layer of basal ice with debris fraction  $C^{\text{reg}} = 0.1$  is entrained from the bed, subject to sediment availability and on condition that the debris fraction in the bottom layer  $C_{k=1}$  does not already exceed  $C^{\text{reg}}$ .

## 4.2 Englacial mixing

Mixing of basal debris within the ice has two facets of interest in this study. Firstly, mixing moves debris away from the ice–bed interface where friction and geothermal inputs concentrate the melt. This increases debris residence time, and as a corollary, transported distance. Secondly, mixing fragments the grain matrix to allow greater entrainment of debris by intrusion (see Figure 4.6 and Equations (4.13) and (4.12)). Various mixing mechanisms are summarized below followed by a

description of the mixing model and details of its implementation. The vertical velocity of the ice (determined from the MC ice model) also affects the vertical distribution of englacial sediment.

#### 4.2.1 Englacial tectonics — mixing

Englacial tectonics (shear planes and folding) have been examined with respect to their role in entrainment in Section 4.1.4; these processes also mix the ice. Small scale mixing has been attributed to englacial folding in the Greenland ice cores [Taylor *et al.*, 1993; Souchez *et al.*, 1995] and folding is suggested to be a crucial process in the formation of the dispersed facies of basal ice [Waller *et al.*, 2000]. Englacial tectonics can happen whenever steady ice flow is perturbed; basal bumps can provide this instability and produce recumbent folds [Hudleston, 1976].

The mixing from random encounters of debris-laden ice and basal topography has been conceptualized as an eddy-diffusion model with a debris diffusivity of  $D_{ed} \approx 1 \times 10^{-10} \text{ m}^2 \text{ s}^{-1}$  [Alley and MacAyeal, 1994; Alley *et al.*, 1997]<sup>7</sup> and a dependence on sliding speed  $v_s$  and basal topography  $\theta$  can be expected by heuristic arguments. Also, mixing is expected to be strongest proximal to the basal topography that causes it and a decaying effect dependent on distance from the bed is expected. I use

$$D_{ed} = \check{D}_{ed} \left( \frac{v_s}{\check{v}_s} \right) \left( \frac{|\theta|}{\check{\theta}} \right) e^{-z/\check{z}} \quad (4.14)$$

where the characteristic eddy-diffusion parameter  $\check{D}_{ed}$  is taken as  $1 \times 10^{-10} \text{ m}^2 \text{ s}^{-1}$  and typical sliding speeds  $\check{v}_s$  of  $100 \text{ m a}^{-1}$ , bed dips  $\check{\theta}$  of  $10^\circ$  and a decay depth scale  $\check{z}$  of  $5.0 \text{ m}$  are taken.

The mixing that can result from thrusting can be locally large; Clarke and Blake [1991] infer movement along a thrust plane of  $\approx 100 \text{ m}$  over a period of 7 a. If these values are taken as characteristic lengths and times, a diffusion coefficient for this process of  $4.5 \times 10^{-5} \text{ m}^2 \text{ s}^{-1}$  is expected. Hambrey *et al.* [1996] find thrust planes of width  $\approx 0.5 \text{ m}$  with spacings on the order of  $100 \text{ m}$  from a Svalbard glacier in active surge. With these values, a volumetrically corrected diffusion coefficient for thrusting  $D_{thrust}$  can be estimated as  $2 \times 10^{-7} \text{ m}^2 \text{ s}^{-1}$ . This must be accepted as an extreme upper limit and this frequency of thrusting would not be expected over an entire model grid cell. A more conservative estimate of  $1 \times 10^{-9} \text{ m}^2 \text{ s}^{-1}$  is taken here. This mechanism is only enabled when the cell is warm and the downstream cell is cold which creates the high compressive stress needed to initiate thrusting. Small thrusts from bedrock topography are assumed to be encompassed in  $D_{ed}$ .

<sup>7</sup>This mechanism was originally considered (and rejected) as a potential entrainment mechanism by Alley and MacAyeal [1994]. I assume that englacial tectonics are only mixing mechanisms and cannot entrain debris. The estimate  $D_{ed} \approx 1 \times 10^{-10} \text{ m}^2 \text{ s}^{-1}$  from Alley and MacAyeal [1994] is poorly constrained.

### 4.2.2 Particles in a shear flow

#### Rigid particle rotation

A single particle in a shear flow rotates and this causes mixing. Given a linear shear flow  $v_{iy} = \beta z$  where  $\beta$  is the vertical strain rate (see Figure B.1)<sup>8</sup>, analysis of a freely rotating cylinder with radius  $R$  gives an estimate of the rotational diffusion parameter  $D'_{\text{rot}}$  ( $\text{m}^2 \text{s}^{-1}$ ) as

$$D'_{\text{rot}} = \beta R^2 / 4. \quad (4.15)$$

This result is derived in Appendix B. The particle distribution from Section 3.1.4 is used to give a total rotational diffusion parameter as

$$D_{\text{rot}} = \sum_r \beta R^2 C_r / 4. \quad (4.16)$$

The assumption that the solution for a single cylinder can be used for many clasts has obvious shortcomings; for example clast interactions will affect the solution. Nevertheless, this approach provides an order of magnitude estimate of the rotational contribution to mixing. A value of  $\beta = 5 \times 10^{-8} \text{ s}^{-1}$  gives  $D_{\text{rot}} = 2 \times 10^{-13} \text{ m}^2 \text{ s}^{-1}$ .

#### Rigid particle collision

Clast interactions and collisions can disperse particles; the tendency for grains to move away from each other in a shear flow was first observed by *Reynolds* [1885] for a granular fluid and the effect was investigated in a suspension by *Bagnold* [1954, 1956] who coined the phrase “grain dispersion pressure”. *Weertman* [1968] develops a simple geometric relationship to describe the dispersion from two-particle collisions in a linear shear flow; a conceptual schematic of this process is shown in Figure 4.7. The collision-diffusion coefficient  $D_{\text{col}}$  is a function of the particle radius  $R$ , the particle volume fraction  $C_r$  and the vertical velocity gradient  $\beta$ . It is written as

$$D_{\text{col}} = \sum_r 8R^2 C_r \beta / (5\pi). \quad (4.17)$$

The mixing from particle collision is on the same order of magnitude as that from particle rotation. Three-body collisions are not considered in the derivation of (4.17).

### 4.2.3 A mixing model

Diffusion coefficients  $D_{\text{ed}}$ ,  $D_{\text{thrust}}$ ,  $D_{\text{rot}}$  and  $D_{\text{col}}$  have been outlined above and are summed to give a total diffusion coefficient  $D_{\text{tot}}(k)$  at the cell interface. The vertical velocity gradient  $\beta$  is

<sup>8</sup>Note that the coordinate system used in Appendix B differs from that used here.

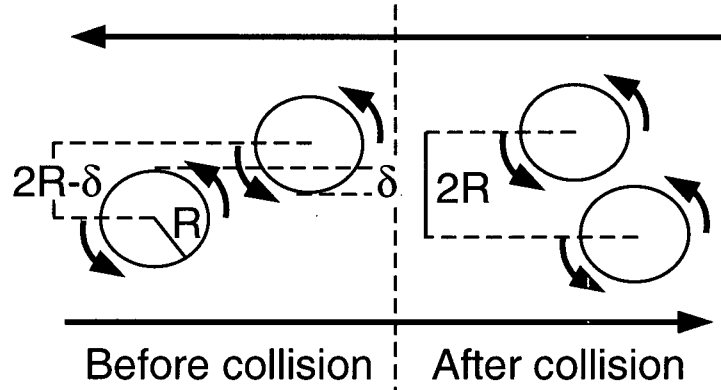


Figure 4.7. A conceptual picture of dispersion by collision.

calculated at the cell interface from the ice model discretization by a cubic Hermite interpolation scheme [Kahaner *et al.*, 1989], which guarantees a monotone interpolating function given monotone input data. A vertical mixed layer around the cell interface is defined with depth

$$\Delta z_{k+\frac{1}{2}}^{\text{mix}} = \sqrt{D_{\text{tot}}(k+1/2)\Delta t}. \quad (4.18)$$

This mixed layer has equal representation from  $C_k$  and  $C_{k+1}$ . This leads to a diffusion-like equation for the time evolution of  $C$  as

$$C_k(t + \Delta t) = C_k(t) + \frac{\Delta z_{k-\frac{1}{2}}^{\text{mix}} C_{k-1}(t) + \Delta z_{k+\frac{1}{2}}^{\text{mix}} C_{k+1}(t) - C_k(t) \left[ (\Delta z_{k-\frac{1}{2}}^{\text{mix}} + \Delta z_{k+\frac{1}{2}}^{\text{mix}}) \right]}{2\Delta z_k}. \quad (4.19)$$

Mixing is prohibited through both the top and bottom of the modelled basal layers.

Vertical velocity of the ice, also interpolated to the cell interfaces by the cubic Hermite scheme of Kahaner *et al.* [1989], advects material through the equation

$$\frac{\partial C}{\partial t} = -\frac{\partial(v_{i_z} C)}{\partial z}, \quad (4.20)$$

which is discretized using a simple upstream scheme. Therefore when the vertical velocities are negative (ice moving towards the bed),

$$C_k(t + \Delta t) = C_k(t) + \Delta t \frac{C_k(t)v_{i_{k-\frac{1}{2}}} - C_{k+1}(t)v_{i_{k+\frac{1}{2}}}}{\Delta z_k}, \quad (4.21)$$

and when the ice velocities are positive,

$$C_k(t + \Delta t) = C_k(t) + \Delta t \frac{C_{k-1}(t)v_{i_{k-\frac{1}{2}}} - C_k(t)v_{i_{k+\frac{1}{2}}}}{\Delta z_k}. \quad (4.22)$$

### 4.3 Advection

Englacial sediment is not known to be ambulatory; its lateral motion is wholly derived from that of the host ice. The governing equation for the evolution of the volume fraction  $C_l$  of a lithological component  $l$  stems from the continuity equation,

$$\frac{\partial C_l}{\partial t} = \underbrace{-\nabla \cdot ((\mathbf{v}_s + \mathbf{v}_i)C_l)}_{\text{advection}} + \underbrace{\phi_l^{\text{sed}}}_{\text{vert. ex.}}. \quad (4.23)$$

The vertical exchange term  $\phi_l^{\text{sed}}$  accounts for vertical flux through entrainment, deposition, mixing and a simple treatment of vertical advection, discussed in Sections 4.1 and 4.2.

There is no term in (4.23) to describe lateral diffusion. It is not a physical process and therefore any numerical scheme must strive to minimize the introduction of numerical diffusion. This is of particular importance in this problem as the advected lithologies are used as tracers which tend to have distributions with sharp lithological boundaries. For a numerical tracer to be useful, this sharp boundary must be preserved as accurately as possible. This is not a concern for the vertical advection as physical mixing processes are real and are modelled explicitly (Section 4.2); because vertical numerical diffusion is not a concern, it is implemented with a simpler treatment as described in Section 4.2.

This is a common situation in atmospheric transport models and a large body of work concerning numerical solutions to (4.23) has resulted. The advection scheme of *Prather* [1986] is recognized to be highly accurate, though not computationally cheap [*Müller*, 1992; *Lin and Rood*, 1996; *Xiaozhen and Xiaoen*, 1998]. In a recent review and comparison of nine Eulerian numerical advection schemes the *Prather* [1986] algorithm shows exemplary performance; it is best able to maintain a narrow peak and is the most accurate of the nine schemes tested [*Reames and Zapotocny*, 1999a]. It also rated well against semi-Lagrangian schemes in a companion review [*Reames and Zapotocny*, 1999b].

The *Prather* [1986] scheme is an Eulerian upstream finite-volume algorithm that conserves second-order moments. It incorporates sub-grid information by defining a second-order polynomial function for the lithology fraction  $C_l$  in each model cell. I use a two-dimensional version

$$C_l = a_0^C + a_x^C x + a_y^C y + a_{xx}^C x^2 + a_{yy}^C y^2 + a_{xy}^C xy \quad (4.24)$$

where the internal distribution of the tracer lithology is described through six  $a^C$  coefficients. If only the zero-order term  $a_0^C$  is used the scheme collapses to standard upstream differencing; the vertical exchange  $\phi_l^{\text{sed}}$  is done through the zero-order term  $a_0^C$ . The first order terms describe the slopes of the distribution while the second order terms describe the curvature. A pseudo positive definite condition (such that the mean concentration along any axis is positive) can be imposed with little cost in both computational time and diffusive properties.

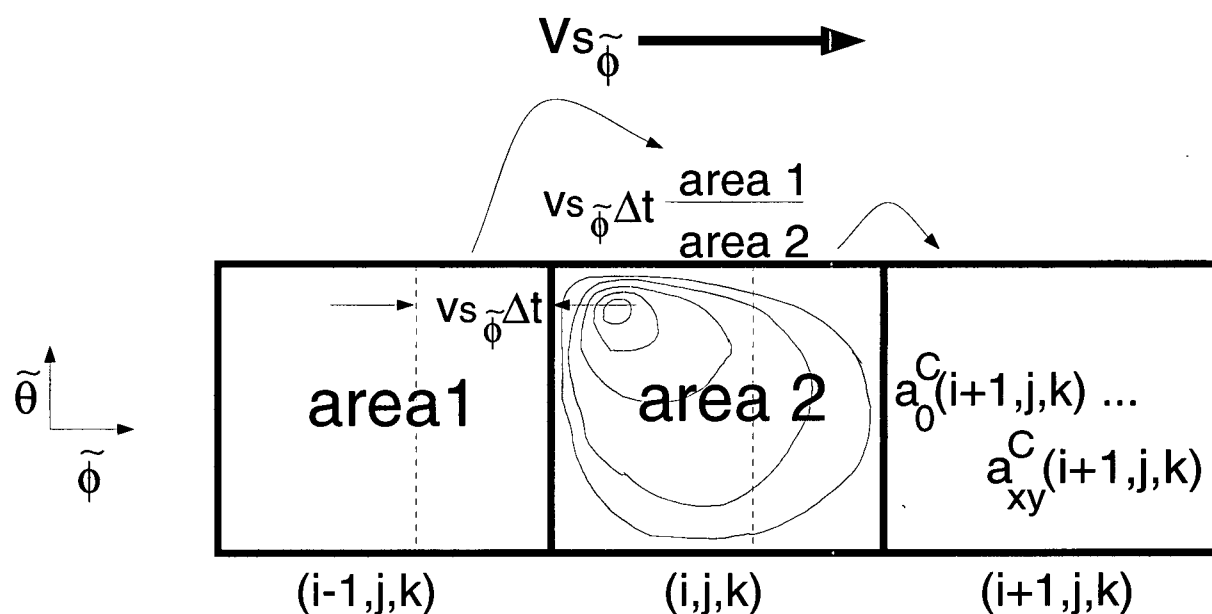


Figure 4.8. A sketch of the *Prather* [1986] advection scheme. Six coefficients are used for each  $(i, j, k)$  cell to define a second-order polynomial sub-grid function. When a portion is advected, the second order moments are conserved. An extension to spherical coordinates is made by considering the changing area of a grid cell on a spherical grid. Note that for purely meridional velocities as shown above,  $A1 = A2 = A3$  and there is no modification of the original scheme of *Prather* [1986].

The algorithm is explicit in time and must be initialized with values for each  $a^C$ . I set  $a_0^C$  to the initial concentration and the rest of the coefficients to zero. For each time-step the grid box is divided into two parts: the portion of the cell that is advected downstream and the portion of the cell that remains. Both inherit the same distribution of (4.24) but have new moments calculated with respect to their individual centres of mass. The advected portion of the cell is then combined with the downstream non-transported part of the receiving cell to create a new set of coefficients  $a^C$ . A correction for non-equal cell areas is introduced in this step to extend the method of *Prather* [1986] to a spherical grid. Figure 4.8 illustrates the scheme.

The advection is multidimensional and this is dealt with by time splitting (synonymously alternating direction integration). Thus a complete pass is made over the model domain with meridional velocities and advection, followed by a zonal treatment. Each vertical layer  $k$  is solved separately with its own set of coefficients  $a^C$ .

An example of the scheme in action is shown in Figure 4.9. The initial function is a box of unity height that is then transported by a series of purely zonal or meridional velocity fields and, finally, a more general velocity field. The velocities are such that approximately 40% of the grid cell is

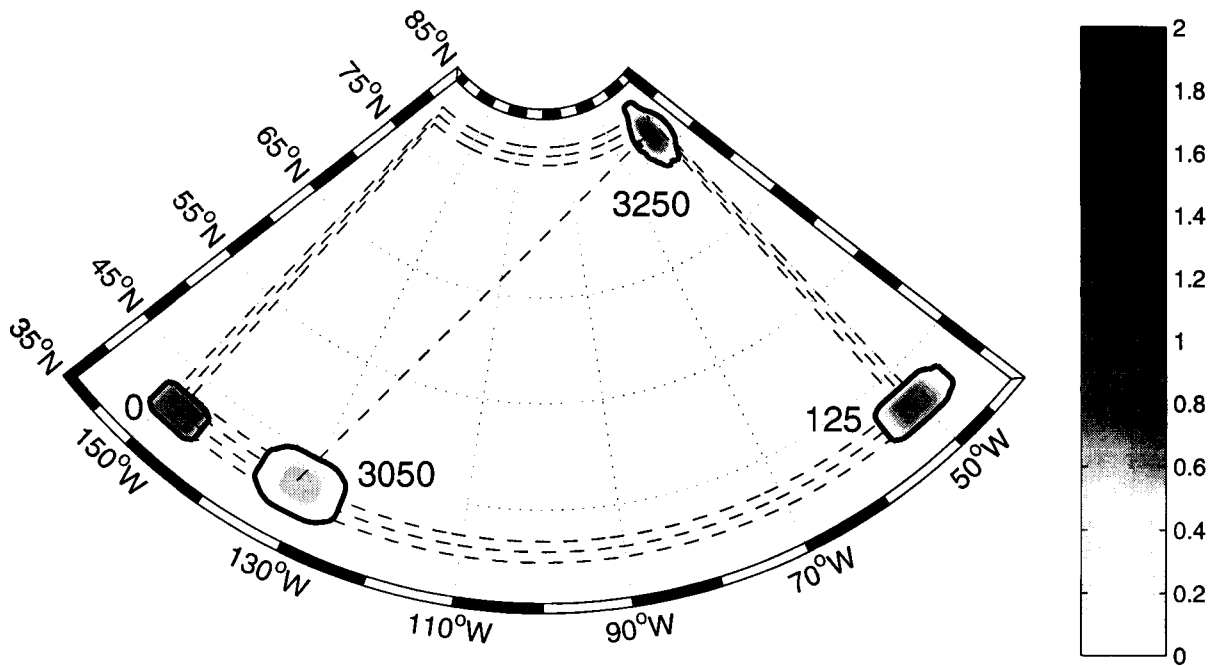


Figure 4.9. An example of an initial box function with  $C_l = 1.0$  transported with the *Prather* [1986] advection scheme. The dashed lines indicate the path of the tracer with outputs after 125, 3050 and 3250 time steps. The heavy line is a 0.01 contour to illustrate the numerical diffusion of the scheme.

advected in any single time step. Note that the 2-D velocity field is not divergence-free, which results in concentration at higher latitudes to honour mass conservation; this is not a physical realization for ice (where incompressibility requires  $\nabla \cdot (\mathbf{v}_i + \mathbf{v}_s) = 0$ ) but is useful as an illustration of the dispersive properties of the algorithm.

## Chapter 5

# Model Inputs

### 5.1 Ice model

The numerical reconstruction of the North American ice sheets is central to this work. An overarching goal is to provide a tool for ice sheet model validation that uses Quaternary geological data as a constraint. In addition, ice sheet output fields are crucial requirements for the model components described in Chapters 3 and 4 and the hydrology model described in Section 5.2.

#### 5.1.1 Theory

I use the Marshall–Clarke UBC ice sheet model (MC) [Marshall, 1996; Marshall and Clarke, 1997a,b; Marshall *et al.*, 2000], a three-dimensional thermo-mechanical ice model driven by climate forcings and ice physics. The dynamical evolution of the ice follows the scheme of Mahaffy [1976] with governing equations of mass and momentum balance. The continuity equation of the ice thickness  $H^{\text{ice}}$  with a constant density  $\rho_i$  leads to a mass balance relationship

$$\frac{\partial H^{\text{ice}}}{\partial t} + \nabla \cdot (\bar{\mathbf{v}}_i H^{\text{ice}}) = \dot{b} \quad (5.1)$$

where  $\bar{\mathbf{v}}^i$  is the vertically averaged velocity and  $\dot{b}$  is the mass balance rate.

Neglecting acceleration terms, the momentum balance is

$$\frac{\partial \sigma_{ab}}{\partial x_a} = \rho_i \mathbf{g}; \quad (5.2)$$

vertical integration reduces the system to a function of ice thickness and surface slope. To translate the stress tensor  $\sigma_{ab}$  into velocity, Glen's flow law [Glen, 1955] provides a constitutive relationship

between the strain rate  $\dot{\epsilon}_{i_{ab}}$  and the deviatoric stress  $\sigma'_{ab}$  tensors

$$\dot{\epsilon}_{i_{ab}} = B_0 \exp \left( -\frac{Q_i}{R^{\text{gas}} T_i} \left| \Sigma'_2 \right|^{(n_G-1)/2} \sigma'_{ab} \right) \quad (5.3)$$

where  $B_0$  is an empirical constant,  $Q_i$  is the creep activation energy,  $R^{\text{gas}}$  is the gas constant,  $T_i$  is the temperature of the ice,  $\Sigma'_2$  is the second invariant of the deviatoric stress and  $n_G$  is the Glen flow law exponent.

The three-dimensional temperature evolution follows *Jenssen* [1977] and the governing equation expresses conservation of internal energy. The local energy balance is

$$\frac{\partial T_i}{\partial t} = - \underbrace{\mathbf{v}_i \cdot \nabla T_i}_{\text{advection}} + \underbrace{\frac{k_i}{\rho_i c_i} \frac{\partial^2 T_i}{\partial z^2} + \frac{1}{\rho_i c_i} \frac{\partial k_i}{\partial T} \left( \frac{\partial T_i}{\partial z} \right)^2}_{\text{divergence of heat flux}} + \underbrace{\frac{\Phi_d}{\rho_i c_i}}_{\text{strain heating}} \quad (5.4)$$

Internal deformation of ice gives rise to strain heating  $\Phi_d$ . The specific heat capacity of ice  $c_i$  and the thermal conductivity of ice  $k_i$  are both functions of  $T_i$  (see Table 5.1).

Thermodynamic evolution is subject to boundary conditions on the surface and at the bed of the ice sheet. Basal ice receives heat from sliding friction and a geothermal heat flux determined from a North American heat flux map [*Blackwell and Steele*, 1992]. With these basal boundary conditions and the climatic surface boundary conditions (discussed below), the system can be solved to extract basal temperature  $T_i^{\text{bed}}$ . When the bed is at the pressure melting point, latent heat of fusion enters the analysis as a modifier to the basal boundary condition to yield the basal melt rate  $\dot{b}^{\text{melt}}$ .

The climate forcing delivers both the upper boundary condition for the thermodynamic evolution and the mass balance  $\dot{b}$  in (5.1). A base climate from CCCv2.0, the general circulation model of the Canadian Climate Centre for Modelling and Analysis [*McFarlane et al.*, 1992; *Vettoretti et al.*, 2000], is reconstructed for present day and Last Glacial Maximum (LGM) conditions. The difference between these results gives glacial maximum perturbation fields for temperature and precipitation which modulate present day observations [*Kalnay et al.*, 1996; *Legate and Willmott*, 1990] for a given time  $t$  based on a ‘‘glacial index’’ from the Greenland GRIP ice core  $\delta^{18}\text{O}$  record [*Dansgaard et al.*, 1993]. Full details of the methodology are found in *Marshall et al.* [2000].

A thermally regulated sliding mechanism dependent on basal shear stress is used following the linear model of *Payne* [1995]. The sliding velocity  $\mathbf{v}_s$  is calculated through

$$\mathbf{v}_s = \begin{cases} -B_s \rho_i g H^{\text{ice}} \nabla (H^{\text{ice}} + z^{\text{bed}}) & T_i^{\text{bed}} \geq T_{\text{pmp}} - \epsilon_T \\ 0 & T_i^{\text{bed}} < T_{\text{pmp}} - \epsilon_T \end{cases} \quad (5.5)$$

where  $T_{\text{pmp}}$  is the pressure-corrected melting point of ice and  $\epsilon_T$  is a modifier to initiate sliding when ice temperature is slightly below the melting point. This crudely accounts for the fact

that glaciers can slide at subfreezing temperatures, albeit slowly [Shreve, 1984; Echelmeyer and Zhongxiang, 1987].  $B_s$  is a free parameter used to restrain or enhance sliding.

Marshall *et al.* [2000] modify the thermally regulated sliding of Payne [1995] through a geological dependence on soft sediment. The deformation of sediment, a mode of glacier motion commonly associated with ice streaming, serves to reduce the Laurentide ice volume to match the inferred volume from geophysical measurements [Peltier, 1994, 1996] and has strong geological corroborating evidence [Marshall *et al.*, 1996]. Inclusion of deformable beds in reconstructions of the Laurentide Ice Sheet has enjoyed recent numerical modelling success [Clark *et al.*, 1996; Jenson *et al.*, 1996; Marshall and Clarke, 1997a,b] and the sliding law of Marshall *et al.* [2000] is designed to represent sediment deformation without an explicit treatment.

However, this approach is disastrous from an erosion modelling viewpoint. The scheme of Marshall *et al.* [2000] completely disables sliding on a hard bed; zero sliding translates to zero abrasion by Equation (3.12)<sup>1</sup> on page 28 and zero quarrying by Equation (3.19b)<sup>2</sup> on page 47. There is overwhelming geological evidence that glacial, hard-bed erosion takes place (e.g. striations), therefore the sliding model of Marshall *et al.* [2000] must be modified. I choose an intermediate path between Payne [1995] and Marshall *et al.* [2000]:  $B_s$  is enhanced over soft-bedded domains to account for sediment deformation and is non-zero over hard beds to allow for the reality of hard-bed glacial sliding.

### 5.1.2 Examples of the ice sheet model

The MC ice sheet model is run from 120 ka BP to present with  $H^{\text{ice}}$ ,  $\mathbf{v}_s$ ,  $b^{\text{melt}}$ ,  $T_i^{\text{bed}}$ ,  $\tau$  (the basal shear forcing),  $\epsilon_i^{\text{bed}}$  and  $T_i$  and  $\mathbf{v}_i$  output every 400 years. Parameters given in Table 5.1 are used.

Results at approximately LGM (21.2 ka BP) are shown in Figure 5.1. Note that the model domain is expansive enough that all the ice at LGM remains confined within model bounds thus disarming potential boundary condition issues. Basal melt and sliding tend to reach their maximum values later during deglaciation. The “spoking” or “fingering” pattern of the sliding speed is the direct result of the thermal regime. This type of patterning is endemic among thermally coupled ice sheet models [Payne *et al.*, 2000]; it is initiated by the interaction of ice thickness, temperature and velocity. The patterns are strongly correlated to the underlying grid and discretization, therefore caution must be exercised in detailed interpretation of the basal results [Payne and Baldwin, 2000].

<sup>1</sup>The particle velocity  $v_p$  in (3.12) requires  $v_s > 0$  in order to be non-zero as shown by (3.10) and the subsequent discussion.

<sup>2</sup>The existence of a cavity demands that  $v_s > 0$  by (3.19). If no cavity exists, the stress regime will not be such that  $v_I$  and  $v_{II} > 0$  in Equations (3.24) and (3.25).

Parameter	Variable	Value	Units
Flow law parameter <sup>a</sup> , $T_i < -10^\circ\text{C}$	$B_0$	$1.08 \times 10^{-12}$	$\text{s}^{-1} \text{Pa}^{-3}$
Flow law parameter <sup>a</sup> , $T_i \geq -10^\circ\text{C}$	$B_0$	$5.20 \times 10^3$	$\text{s}^{-1} \text{Pa}^{-3}$
Sliding law parameter, soft bed	$B_s$	$2.0 \times 10^{-10}$	$\text{m s}^{-1} \text{Pa}^{-1}$
Sliding law parameter, hard bed	$B_s$	$1.0 \times 10^{-10}$	$\text{m s}^{-1} \text{Pa}^{-1}$
Creep activation energy, $T_i < -10^\circ\text{C}$	$Q_i$	$6.00 \times 10^4$	$\text{J mol}^{-1}$
Creep activation energy, $T_i \geq -10^\circ\text{C}$	$Q_i$	$1.39 \times 10^5$	$\text{J mol}^{-1}$
Gas constant	$R_{\text{gas}}$	8.314	$\text{J mol}^{-1} \text{K}^{-1}$
Specific heat capacity of ice <sup>b</sup>	$c_i$	$152.5 + 7.122T_i$	$\text{J kg}^{-1} \text{K}^{-1}$
Thermal conductivity of ice <sup>b</sup>	$k_i$	$9.828 \exp(-5.7 \times 10^{-3}T_i)$	$\text{W m}^{-1} \text{K}^{-1}$
Flow law exponent	$n_G$	3	—
Density of ice	$\rho_i$	910	$\text{kg m}^{-3}$
Sliding temperature modifier	$\epsilon_T$	0.1	K

Table 5.1. Parameters used for ice sheet model.

<sup>a</sup>This value has an embedded enhancement factor of 3 to account for the effects of crystal anisotropy and ice impurities.

<sup>b</sup>from Paterson [1994].

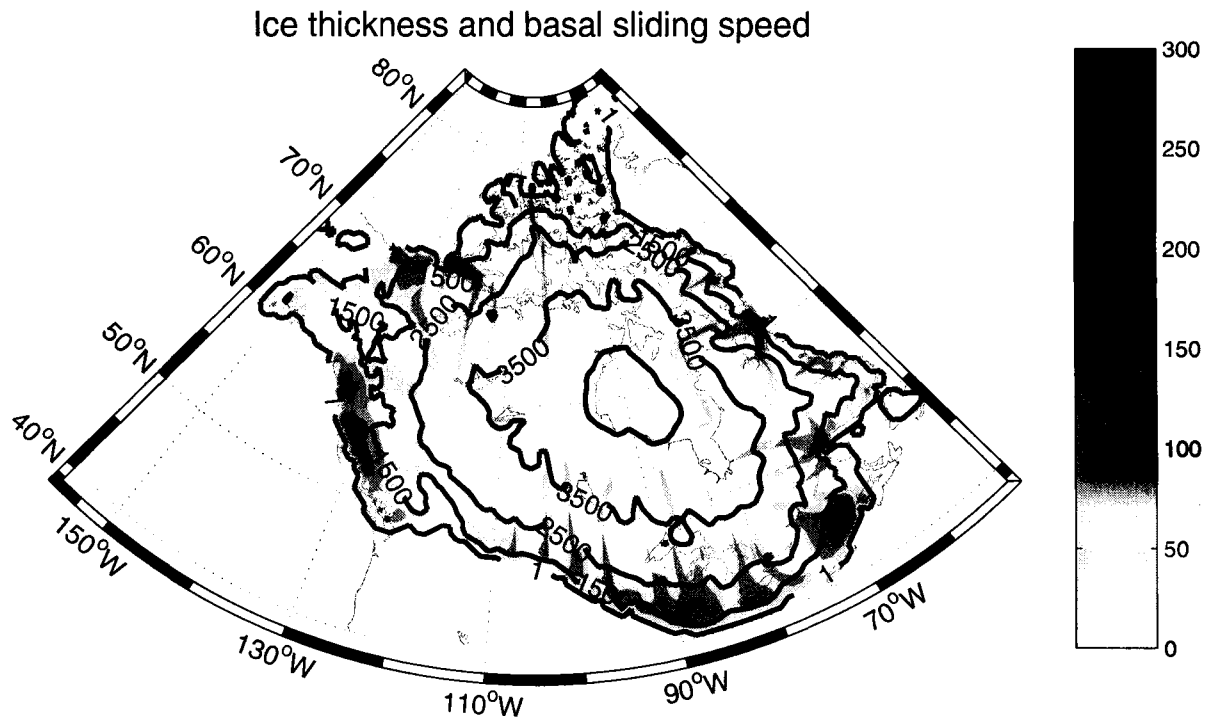


Figure 5.1. A reconstruction of the North American ice sheets at approximately LGM using parameters from Table 5.1. The grey scale contours of 50, 150 and 250 show sliding speed in  $\text{m a}^{-1}$  while the lines give ice thickness contours of 1, 1500, 2500, 3500 and 4500 m.

## 5.2 Hydrological model

The subglacial water pressure  $P_w$  has a lead role in quarrying (Section 3.2.5) and is instrumental in the calculation of intrusion (Section 4.1.3); the model of *Flowers* [2000] is used to calculate  $P_w$ . This model is designed for basin-scale subglacial drainage therefore a number of changes and simplifications are necessary and permissible to solve a continental-scale problem.

*Flowers* [2000] incorporates a multicomponent description of glacial hydrology. A surface component calculates ablation and surface runoff, which is coupled to the bed through moulins and crevasses. While this surface-bed communication is indisputably active in valley glaciers, any such link is unlikely on a continental ice sheet outside the marginal regions; surface-bed water exchange is prohibited to reflect this shift in scale. Similarly, the englacial water system which routes surface melt to the bed and has storage capabilities, is disabled for continental simulations.

### 5.2.1 Sheet flow

A subglacial water sheet system is assumed to exist wherever the bed is unfrozen (as determined by the MC ice model described in Section 5.1). The treatment is consistent with subglacial drainage through a transmissive macroporous horizon [*Clarke*, 1996]. Although this does not account for the myriad of possible drainage structures under an ice sheet such as ice-walled conduits [*Röthlisberger*, 1972], bedrock channels [*Nye*, 1976], linked cavities [*Walder*, 1986; *Kamb*, 1987] and water films and sheets [*Weertman*, 1972; *Walder*, 1982; *Weertman and Birchfield*, 1983], a macroporous horizon fits readily into the framework of continuum mathematics. This simplification is most suspect proximal to the ice margins where alternate flow morphologies become more probable.

The water balance equation for the sheet is

$$\frac{\partial H^w}{\partial t} + \nabla \cdot \mathbf{Q}^w = \dot{b}^{\text{melt}} - \phi^{s:a} \quad (5.6)$$

where  $H^w$  is the sheet water thickness,  $\mathbf{Q}^w$  is the vertically integrated sheet water flux,  $\dot{b}^{\text{melt}}$  is the basal melt rate (determined by the MC thermodynamic model) and  $\phi^{s:a}$  is the exchange term between the sheet and an underlying aquifer, discussed in Section 5.2.3.

Assuming Darcian flow allows an expression for the flux to be written as

$$\mathbf{Q}^w = -K^w H^w \nabla \psi^w \quad (5.7)$$

with the density of water  $\rho_w$  assumed constant for the sheet.  $K^w$  is the isotropic hydraulic conductivity and the hydraulic head  $\psi^w$  is given by

$$\psi^w = P_w / (\rho_w g) + z^{\text{bed}} \quad (5.8)$$

where  $z^{\text{bed}}$  is the mean bed elevation (sub-grid information is ignored).

Finally a relationship is needed between the sheet thickness  $H^w$  and the variable of interest, water pressure  $P_w$ . This is taken to be

$$P_w = P_i \left( \frac{H^w}{H_{\text{crit}}^w} \right)^{\frac{7}{2}} \quad (5.9)$$

for Trapridge Glacier, a small alpine glacier in the Yukon Territory.  $P_i$  is the ice overburden pressure and  $H_{\text{crit}}^w$  is the critical amount of sheet water needed for flotation, occurring when the saturation of sediment is complete; *Flowers* [2000] describes the theory behind (5.9) in detail. For lack of guidance on upscaling to a continental scale, I accept the form of (5.9) although the unknown scale effect on the exponent in (5.9) could affect model results.

Hydraulic conductivity has temporal dependence through its relationship to sheet thickness. Drainage networks can exhibit connected (high  $K^w$ ) or unconnected behaviour (low  $K^w$ ) which is parameterized through  $H^w$ . *Flowers* [2000] argues for the following relationship

$$\log_{10}(K^w) = \frac{1}{\pi} (\log_{10}(K_{\text{max}}^w) - \log_{10}(K_{\text{min}}^w)) \arctan \left[ k_a \left( \frac{H^w}{H_{\text{crit}}^w} - k_b \right) \right] + \frac{1}{2} (\log_{10}(K_{\text{max}}^w) + \log_{10}(K_{\text{min}}^w)) \quad (5.10)$$

with  $k_a = 15.0$  and  $k_b = 0.85$ . Again, I leave the form of (5.10) as well as the values for  $k_a$  and  $k_b$  unchanged.

However, several parameters are changed to reflect upscaling to continental scale. Observation yields a 0.375 m macroporous layer with 40% porosity at Trapridge Glacier [*Blake*, 1992; *Kavanaugh*, 2000] giving  $H_{\text{crit}}^w = 0.15$  m with minimum and maximum sheet hydraulic conductivities as  $K_{\text{min}}^w = 2.5 \times 10^{-2}$  and  $K_{\text{max}}^w = 5.0 \times 10^{-2} \text{ m s}^{-1}$ . The transmissivity of the layer can be interpreted as the product of  $H_{\text{crit}}^w$  and  $K_w$  based on (5.7). Numerical testing indicates that higher values of sheet transmissivity are necessary to evacuate water from the North American ice sheets; Trapridge Glacier parameters produce an ice sheet hydrology predominantly well above flotation pressures, an unreasonable realization of the model. Designations of  $H_{\text{crit}}^w = 4.0$  m,  $K_{\text{min}}^w = 2.5 \times 10^{-1}$  and  $K_{\text{max}}^w = 5.0 \times 10^{-1} \text{ m s}^{-1}$  are used. Numerical instabilities prevent further increase of the conductivity, which corresponds to increased water velocity; this has an adverse effect on the maximum stable time step. A thick sheet is therefore chosen as the vehicle to increase transmissivity. I do not suggest that the true thickness of an ice sheet macroporous horizon is  $\approx 10$  m, but the strategy is useful to reconcile high transmissivity with numerical stability of the continental-scale solution.

The necessary inflation of sheet transmissivity to produce physically reasonable results is suggestive of two scenarios: 1) The hydrology is never in equilibrium and the ice sheet evacuates water through subglacial outburst floods [e.g. *Shaw et al.*, 1996; *Shaw*, 1996] or; 2) Channels develop

that efficiently drain the bed. Neither of these possibilities can be explicitly accounted for with the current model; enhanced values of sheet transmissivity must suffice.

The conductivities are assumed to be isotropic and are universally applied to all subglacial warm-bedded ground. Ground that is frozen as determined by the MC ice thermodynamic model is assigned  $K_{\min}^w = K_{\max}^w = K_{\text{frozen}} = 1 \times 10^{-14} \text{ m s}^{-1}$ .

The model domain is large enough to always encompass the entire ice sheet therefore boundary conditions are not troublesome;  $P_w$  is set to zero at the margins. This is an advantage to running the full North American model; if warm ice exists at the edge of the hydrological domain, an arbitrary pressure must be prescribed to achieve mathematical closure. The appropriate choice for this boundary condition is a non-trivial task.

### 5.2.2 Groundwater flow

Groundwater flow under Pleistocene ice sheets has been explored using the Fennoscandian Ice Sheet as a testing ground [Boulton *et al.*, 1995; Piotrowski, 1997; van Weert *et al.*, 1997]. The model of Flowers [2000] distinguishes itself by explicitly considering sheet flow, nevertheless it is probable that groundwater also played an important role in the subglacial hydrology of the North American ice sheets.

Flowers [2000] follows the conventional treatment of groundwater based on Darcian flow [Freeze and Cherry, 1979]. A balance equation for both saturated and unsaturated groundwater flow is described as

$$\underbrace{\left(\frac{H^{gw}}{\rho_w}\right) \frac{\partial \rho_w}{\partial t}}_{\text{saturated}} + \underbrace{\frac{\partial H^{gw}}{\partial t}}_{\text{unsaturated}} + \nabla \cdot \mathbf{Q}^{gw} = \underbrace{\phi^{s:a}}_{\text{subglacial}} + \underbrace{\phi^{r:a}}_{\text{subaerial}} \quad (5.11)$$

where  $H^{gw}$  is the thickness of the groundwater layer and  $\mathbf{Q}^{gw}$  is the groundwater flux, similarly defined as for the water sheet in (5.7). The density of water  $\rho_w$  is a function of pressure with the equation of state

$$\rho_w = 1000 e^{\beta_w P_{gw}} \quad (5.12)$$

where  $\beta_w = 5.04 \times 10^{-10} \text{ Pa}^{-1}$ .

Equation (5.11) can operate either in unsaturated or saturated mode: only one of the pair  $\left[\frac{\partial \rho_w}{\partial t}, \frac{\partial H^{gw}}{\partial t}\right]$  can be significantly non-zero at any time. During unsaturated flow the water table is a free surface and  $\partial \rho_w / \partial t$  is small while  $\partial H^{gw} / \partial t$  is small in saturated flow. Also one of  $[\phi^{s:a}, \phi^{r:a}]$  must be zero;  $\phi^{r:a}$  controls subaerial/groundwater exchange while  $\phi^{s:a}$  covers subglacial/groundwater exchange. The exchange terms are developed below in Section 5.2.3.

As for the sheet flow a relationship between pressure and water thickness provides a link between (5.11) and the Darcian flux (the groundwater equivalent of (5.7)). This relationship is

$$P_{gw} = \begin{cases} \rho_w g H^{gw} & H^{gw} \leq n^{gw} d \text{ (unsaturated),} \\ \rho_w g H^{gw} + \frac{H^{gw} - n^{gw} d}{\alpha^{gw} d} & H^{gw} > n^{gw} d \text{ (saturated).} \end{cases} \quad (5.13)$$

where  $\alpha^{gw}$  is the sediment compressibility, the porosity  $n^{gw}$  is taken as 40% and  $d$  is the thickness of the aquifer.

The conductivity of the unfrozen aquifer is assumed constant throughout the study area and is taken as  $K^{gw} = 1 \times 10^{-7} \text{ m s}^{-1}$ . This value is consistent with some large-scale ice sheet hydrology models [Boulton *et al.*, 1995] while others use a higher value for their aquifer [Piotrowski, 1997; van Weert *et al.*, 1997]. Ground that is frozen (as determined by the MC ice model) is assigned  $K^{gw} = K_{\text{frozen}}$ .

The thickness of the aquifer varies with sediment depth as outlined in Section 5.3.2 (aquifer thickness  $\equiv$  sediment depth  $\equiv d$ ). To avoid numerical strife this is modified in areas where there is very thin or non-existent surficial cover so when  $d < d_{\text{min}}^w$ ,  $d = d_{\text{min}}^w$  where  $d_{\text{min}}^w$  is taken as 0.5 m. Water is discouraged from flowing in these virtual aquifers by assigning the hydraulic conductivities in these areas as  $K^{gw} = K_{\text{frozen}}$ .

As for the sheet flow, boundary conditions pose no difficulties because the ice margin is always several model cells away from the grid boundary.

### 5.2.3 The aquitard

The subglacial sheet and the groundwater system exchange water through a thin aquitard. Vertical coupling is parameterized to reduce the full three-dimensional problem to a set of adjacent two-dimensional systems. The exchange term between the sheet and the groundwater  $\phi^{s:a}$  is

$$\phi^{s:a} = \begin{cases} \frac{1}{\rho_w g} \frac{K^t}{d^t} [(P_w - P_{gw}) + \rho_w g d^t] & H^{gw} > n^{gw} d, \\ \frac{1}{\rho_w g} \frac{K^t}{d^t} [P_w + \rho_w g d^t] & H^{gw} \leq n^{gw} d, \end{cases} \quad (5.14)$$

where  $P_{gw}$  is calculated using only the second term from (5.13) as the pressure at the top of the aquifer is what drives the exchange. The aquitard thickness  $d^t$  divided by the hydraulic conductivity  $K^t$  gives the aquitard time constant.

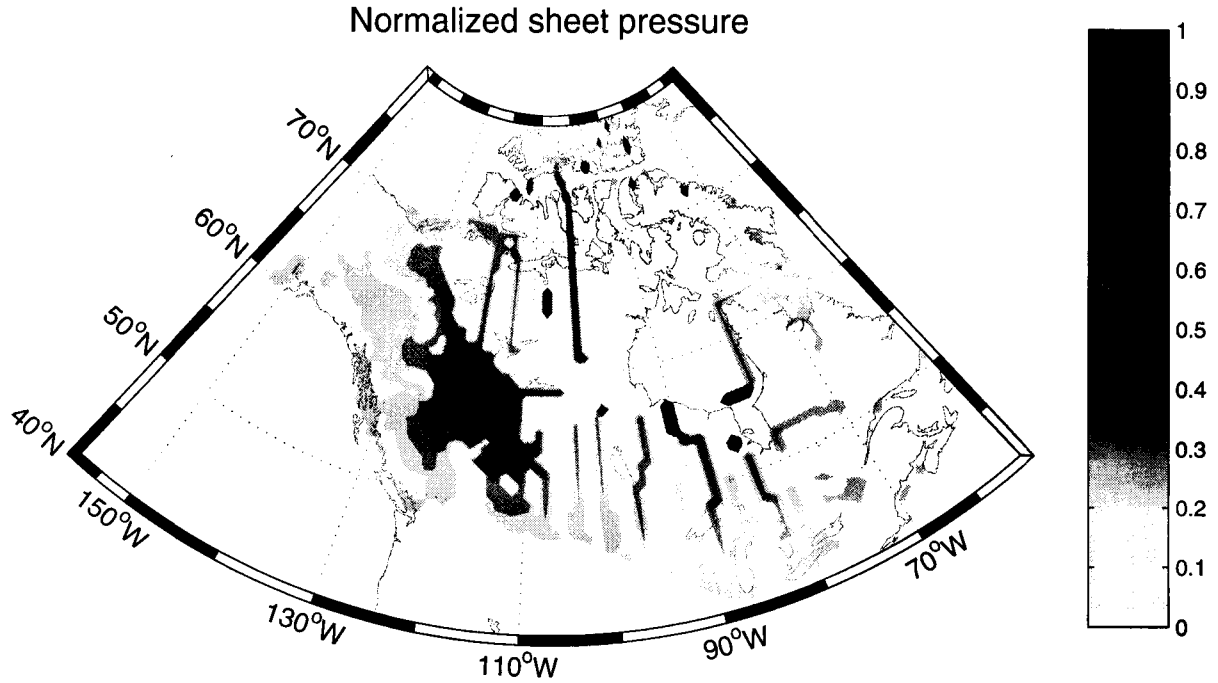


Figure 5.2. A reconstruction of the North American glacier complex hydrology at approximately LGM using parameters from Table 5.2. The ice sheet inputs are shown in Figure 5.1. The grey scale contours of 0.2 0.5 0.8 and 1.0 show sheet pressure normalized to ice overburden pressure (i.e. a value of 1.0 indicated that  $P_w = P_i$ ).

Similarly, the exchange between the groundwater and runoff  $\phi^{r:\alpha}$  is written as

$$\phi^{r:\alpha} = \begin{cases} \frac{1}{\rho_w g} \frac{K^t}{d^t} [-P_{gw} + \rho_w g d^t] & H^{gw} > n^{gw} d, \\ \frac{1}{\rho_w g} \frac{K^t}{d^t} [\rho_w g d^t] & H^{gw} \leq n^{gw} d. \end{cases} \quad (5.15)$$

An assumption in (5.15) is that the pressure of the runoff is atmospheric ( $\approx 0$ ). This is suspect especially during deglaciation when large pro-glacial lakes dominate the peri-glacial landscape [Marshall and Clarke, 1999] and serve to increase the marginal subglacial water pressure.

I leave the conductivity of the aquitard  $K^t$  identical to the value of Flowers [2000] at  $1 \times 10^{-9} \text{ m s}^{-1}$ . The thickness of the aquitard  $d_t$  is taken to be 0.2 m over significant sediments ( $d > d_{\min}^w$ ) and 1.0 m over negligible cover. The enhanced thickness over hard beds inhibits any attempt to exchange water from the sheet to a very thin or non-existent aquifer; this eases the numerics of the problem.

Parameter	Variable	Value	Units
Critical sheet thickness	$H_{\text{crit}}^w$	0.4	m
Min. sheet hydraulic conductivity	$K_{\text{min}}^w$	$2.5 \times 10^{-1}$	$\text{m s}^{-1}$
Max. sheet hydraulic conductivity	$K_{\text{max}}^w$	$5.0 \times 10^{-1}$	$\text{m s}^{-1}$
Aquitard hydraulic conductivity	$K^t$	$1.0 \times 10^{-9}$	$\text{m s}^{-1}$
Aquifer hydraulic conductivity	$K^{gw}$	$1.0 \times 10^{-7}$	$\text{m s}^{-1}$
Frozen ground sheet hydraulic conductivity	$K_{\text{frozen}}$	$1.0 \times 10^{-14}$	$\text{m s}^{-1}$
Aquitard thickness (soft bed)	$d^t$	0.2	m
Aquitard thickness (hard bed)	$d^t$	1.0	m
Sheet hydraulic conductivity parameter	$k_a$	15.0	—
Sheet hydraulic conductivity parameter	$k_b$	0.85	—
Aquifer porosity	$n^{gw}$	0.40	—
Aquifer compressibility	$\alpha^{gw}$	$1 \times 10^{-8}$	$\text{Pa}^{-1}$
Minimum aquifer thickness	$d_{\text{min}}^w$	0.5	m
Compressibility of water	$\beta_w$	$5.04 \times 10^{-10}$	$\text{Pa}^{-1}$

Table 5.2. Parameters used for hydrology model.

#### 5.2.4 Examples of hydrological results

Figure 5.2 shows results of the hydrological model at 21.2 ka BP (approximately LGM). The groundwater pressures (not shown in Figure 5.2) have similar patterns and magnitudes as the sheet pressures. The forcings for these plots are shown in Figure 5.1 and the hydrological parameters used are given in Table 5.2. The model is run for 50 a with the given static forcings; this integration time is sufficient for the hydrology to reach equilibrium if started with appropriate initial conditions (discussed below). The fingering pattern of Figure 5.2 is thermally induced and is discussed in Section 5.1.2

The hydrology model is not fully coupled to the ice: there is no feedback. The ice model is run without any regard for hydrology with a time slice of hydrologically important variables ( $H^{\text{ice}}$ ,  $\dot{b}_{\text{melt}}$  and  $T_i^{\text{bed}}$ ) written every 400 a. A single time slice is then used as a static forcing for the hydrology model with initial conditions being the results from the previous time slice (modified by setting  $P_w = 0$  and  $H^{gw} = n^{gw}d$ ) in cells where the ice had disappeared or the ground had frozen since the previous time step). Initial conditions for the start of the run at 120 ka BP is a saturated aquifer with  $P_w = 0$ . Between time slices, values of both sheet and aquifer pressures greater than  $5P_i$  are set equal to  $5P_i$  to prevent propagation of unphysical results.

### 5.3 Geological inputs

There are several aims in including an accurate lithological representation of the bed. The first is to use distinct lithologies as natural tracers of ice motion; the ice entrains loose debris from the bed, then transports it downstream depositing a debris train. These deposits are observable data on the modern landscape offering a constraint for the ice sheet model. To exploit these data, lithologically labelled englacial sediment must be tracked from bedrock to ice to till.

The second goal is to incorporate the differences in physical properties between various lithologies. This is of particular importance in the calculation of erosion where fundamental physical parameters of the bedrock (e.g. hardness) play a lead role in the erosion equations. For example, there appears to be some correlation between the shape of glacial valleys and lithological parameters based on examination of several sites in the Southern Alps, New Zealand [Augustinus, 1992, 1995] and this effect has been successfully modelled with a simple ( $v_s$ -dependent) erosion law [Harbor, 1995]. To date there has been no effort at incorporating lithological parameters on a large scale with a more complete erosion law (such as that outlined in Chapter 3).

The lithological assignments are done using the maps of Wheeler *et al.* [1997] for the bedrock lithology and Fulton [1996] for the surficial material. The bedrock map displays information at or near the surface of the land, as well as less detailed depiction of marine areas above the continental crust and offshore oceanic crust. The surficial map gives the nature of the cover encompassing broad depositional categories from which limited lithological and thickness information can be distilled.

#### 5.3.1 Bedrock geology

There are 49 distinct lithologies identified by Wheeler *et al.* [1997], listed in Table 5.3. The map domain is projected onto geographical coordinates then gridded into cells of  $0.02^\circ \times 0.02^\circ$  using standard ARC-INFO packages; the resultant map is shown in Figure 5.3. These sub-grid cells are binned into the model grid ( $1.0^\circ$  zonal  $\times$   $0.5^\circ$  meridional) by assigning each lithology a summed representative areal fraction of the model cell. This preserves an accurate account of the sub-grid areal fraction of each rock type while only losing sub-grid geometrical information. The fractions are stored as a linked list; calculations are therefore not performed on non-existent lithologies. Hard-bed parameters ( $h_s, h_p, n_L, K_L^*$ ) for a model cell are calculated as a weighted mean of the individual constituent's parameter value.

# Bedrock Geology

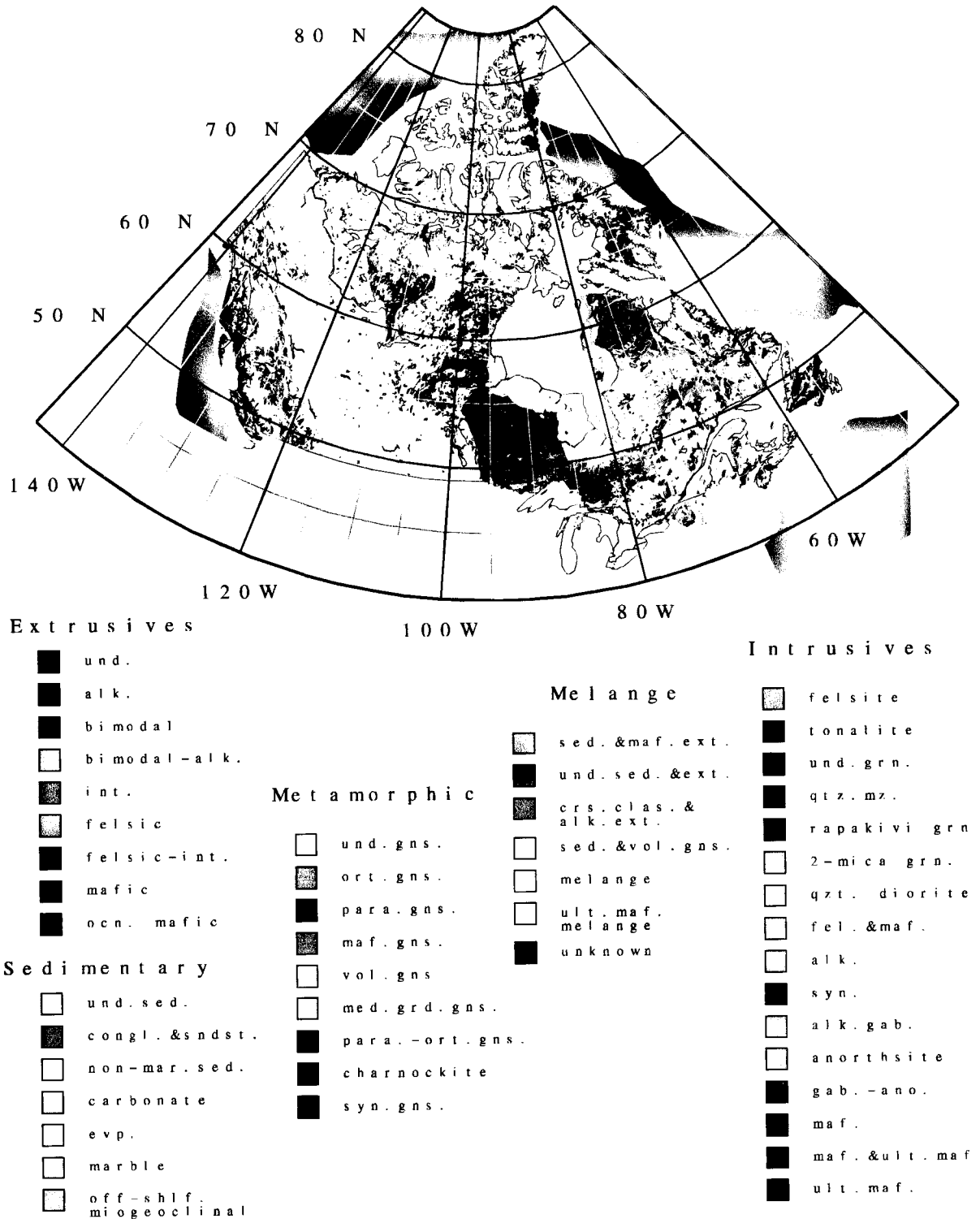


Figure 5.3. Bedrock geology by rock type from Wheeler et al. [1997].

Table 5.3: Bedrock types as designated by *Wheeler et al.* [1997] with hardness, Mode I and Mode II subcritical crack growth indices and critical stress intensities assigned.

Bedrock Type	$h_s, h_p$ Pa	$n_I, n_{II}$	$K_I^*$ Pa m <sup>1/2</sup>	$K_{II}^*$ Pa m <sup>1/2</sup>
<b>Extrusive</b>				
undivided alkaline bimodal bimodal alkaline intermediate felsic felsic-intermediate mafic oceanic mafic	$7.0 \times 10^9$	25	$2.2 \times 10^6$	$7.7 \times 10^6$
			$1.5 \times 10^6$	$5.3 \times 10^6$
			$1.85 \times 10^6$	$6.5 \times 10^6$
			$2.9 \times 10^6$	$1.0 \times 10^7$
<b>Intrusive</b>				
felsite tonalite undivided granitoid quartz monzonite, granite rapakivi granite two mica granite, diatexite granodiorite, quartz diorite felsic & mafic alkaline syenite, mozodiorite alkaline gabbro & syenite anorthosite gabbro-anorthosite mafic (diorite, gabbro) mafic & ultramafic ultramafic	$7.0 \times 10^9$	25	$1.5 \times 10^6$	$5.3 \times 10^6$
			$2.2 \times 10^6$	$7.7 \times 10^6$
			$2.9 \times 10^6$	$1.0 \times 10^7$
<b>Metamorphic</b>				
undivided gneiss orthogneiss paragneiss mafic gneiss volcanic gneiss medium-grade gneiss paragneiss-orthogneiss charnockite syenitic gneiss	$7.0 \times 10^9$	25	$2.2 \times 10^6$	$7.7 \times 10^6$

*continued on next page*

Table 5.3: *continued*

Bedrock Type	$h_s, h_p$ Pa	$n_I, n_{II}$	$K_I^*$ Pa m <sup>1/2</sup>	$K_{II}^*$ Pa m <sup>1/2</sup>
<b>Sedimentary</b>				
undivided sedimentary conglomerate & sandstone non-marine sedimentary carbonate evaporite marble offshelf miogeoclinal	$1.5 \times 10^9$	15	$6.2 \times 10^5$	$2.2 \times 10^6$
<b>Mélange and Unknown</b>				
sedimentary & mafic extrusive	$4.3 \times 10^9$	20	$1.7 \times 10^6$	$5.8 \times 10^6$
undivided sedimentary & extrusive				
coarse clastic sediments & alkaline extrusive				
sedimentary & volcanic gneiss				
mélange ultramafic mélange unknown				

Table 5.3: Bedrock types as designated by *Wheeler et al.* [1997]. Hardness, Mode I and Mode II subcritical crack growth indices and critical stress intensities are assigned based on Section 3.2.2.

The critical stress intensities and crack growth indices stem from data presented in Tables 3.5 and 3.6.  $K_I^*$  is divided into three categories based on Table 3.5: sedimentary (including all carbonates), felsic and mafic rocks with  $K_I^*$  of 0.62, 1.5 and  $2.9 \times 10^6$  Pa m<sup>1/2</sup> respectively. Intermediate igneous and metamorphic rocks are taken to lie between the felsic and mafic values while the mélanges and unknowns are averaged from all three categories. The minimum value rather than the mean from Table 3.5 is used with the following rationale: the natural range of  $K_I^*$  is quite large and as the law governing the rate of crack growth (3.16) is a power law with a large exponent ( $n_{I/II}$ ), the quarrying will be dominated by rocks that fall on the low end of the  $K_I^*$  spectrum.

The assignment of  $n_I$  is based on Table 3.6 with two categories identified: metamorphic/igneous with  $n_I = 25$  and sedimentary/carbonate with  $n_I = 15$ . The mélanges and unknowns are given  $n_I = 20$ . As with  $K_I^*$ , the minimum values of  $n_I$  will dominate and these parameter assignments reflect this. For mode II cracks,  $K_{II}^*$  is taken as  $3.5 \times K_I^*$  while  $n_{II}$  is taken as equal to  $n_I$  (see Section 3.1.3). Hardness is described in Section 3.1.3 and is assigned as either hard or soft with unknown lithologies and mélanges given intermediate values.

### 5.3.2 Surficial geology

Surficial materials are more enigmatic. While it is safe to assume that the bedrock composition of North America has not altered significantly in the past 120 000 years, the same cannot be said of the cover on top of the bedrock. Some deposits are a direct consequence of the last glacial period, thus formulation of initial conditions for a model to explore such consequences is necessarily suspect and circular. Nevertheless, the principle of uniformitarianism is applied and today's surficial geology is assumed to be a reasonable representation of what existed at the termination of the last inter-glacial period.

Twenty five surficial materials from *Fulton* [1996] are similarly projected and gridded as the bedrock information, however the binning into model cells is dealt with differently as depth information is not part of the data. Each surficial material is assigned a bedrock fraction  $b^f$  based on the descriptions of *Fulton* [1996]; this is summarized in Table 5.4. Sub-grid  $b^f$  values are transformed into a model grid sediment depth by summing the sub-grid bedrock fractions over the model grid cell then using the following second-order mapping

$$d_{ij} = d_{\max} \left[ 1 - \frac{\sum_{m,n} b_{mn}^f}{N_m N_n} \right]^2 \quad (5.16)$$

where  $d_{\max}$  is the maximum initial depth taken as 15.0 m,  $N_m$  and  $N_n$  are the number of longitudinal and latitudinal sub-grid cells. A minimum sediment thickness  $d_{\min}$  of 0.01 m is also imposed to avoid the improbable situation of completely clean bedrock, which can adversely affect the erosion modelling through (3.12) on page 28. A plot of initial sediment thickness using this methodology is shown in Figure 5.4.

The lithological makeup of the surficial cover is handled identically as the bedrock (except with multiple layers as described in Section 4.1.5): a linked list of particular rock types (from Table 5.3) is maintained for each layer in each model cell. Fresh glacial erosion produces sediment of identical lithological signature as the parent bed. However most of the initial surface cover has no guarantee of being autochthonous aside from a few categories specifically identified as locally derived (colluvial blocks, rubble, fines, sand and Quaternary volcanics). The allochthonous surficial categories are composed of transported materials and the lithology for these initial sediments is unknown.

Surficial Category	Bedrock Fraction $b^f$	Surficial Lithology 1.0 = Autochthonous 0.0 = Allochthonous)
undivided rock		
alpine complexes		
glaciers	1.0	—
water		
till veneer	0.9	0.0
glacio-fluvial complex		
lag marine	0.25	0.0
colluvial blocks		
colluvial rubble		
colluvial fines	0.0	1.0
colluvial sand		
Quaternary volcanics		
till blanket		
glacio-fluvial plain		
coarse-grained marine		
fine-grained marine		
coarse-grained lacustrian		
fine-grained lacustrian		
coarse-grained glacio-marine	0.0	0.0
fine-grained glacio-marine		
coarse-grained glacio-lacustrian		
fine-grained glacio-lacustrian		
organic deposits		
eolian deposits		
alluvial deposits		

Table 5.4. Surficial materials as designated by *Fulton* [1996]. Bedrock fraction is the amount of uncovered bedrock taken for that surficial assignment. Surficial lithology is 1 when the cover is locally derived, 0 when it is not.

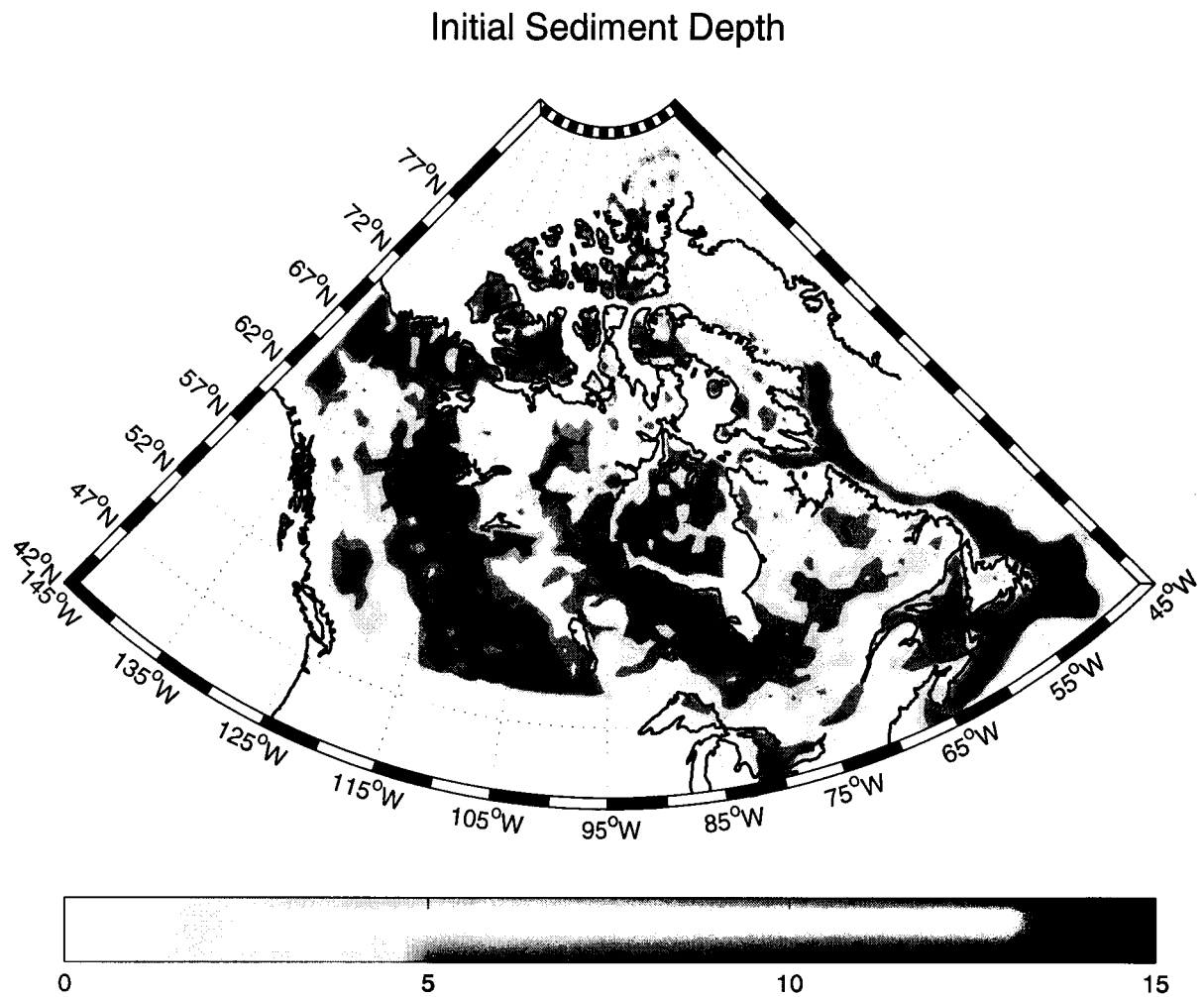


Figure 5.4. Initial sediment depths using (5.16) with  $d_{\max} = 15.0$  m, based on data from *Fulton* [1996]. The plot shows 2.5, 7.5 and 12.5 m contours.

## Chapter 6

# Modelled Simulations of North American Ice Sheets

### 6.1 Transport results

The use of erratics to infer past glaciological conditions dates back to the “glacial theory” of Venetz, de Charpentier and Agassiz in the early nineteenth century (Chapter 1). The characteristic length of a dispersal train varies over several orders of magnitude from local (a few km) to regional (tens of km) to continental (thousands of km) [Clark, 1987]. With the model grid ( $1^\circ \times 0.5^\circ$ ), only continental debris trains are resolvable. Two such debris trains are used to assess model results: the southward dispersal of Hudson Bay carbonates onto Precambrian shield and the eastward transport of Dubawnt Group erratics in Nunavut (formerly Keewatin District, Northwest Territories).

#### 6.1.1 Southward carbonate transport

A Paleozoic platform surrounds and underlies Hudson Bay (Figure 6.1). The sedimentary rocks comprise gently dipping carbonates and extend southwest from Hudson Bay for 100–200 km [Wheeler *et al.*, 1997]. Cradling the Paleozoic platform is a crystalline Precambrian shield on which carbonates are glacially disseminated. These allochthonous carbonates were noted in the early geologic mapping of the Precambrian shield in northern Ontario [e.g. Bell, 1872]. The northern limit<sup>1</sup> of exotic carbonates is sharply defined near the mouth of the Seal River, in the vicinity of Churchill, Manitoba [Shilts, 1980]. Aside from rare instances attributed to Late Wisconsinan ice rafting, the border between Ontario and Quebec ( $79^\circ 30'W$ ) marks roughly the

<sup>1</sup>This is a local limit; carbonate dispersal trains are found in the central Arctic [e.g. Dyke *et al.*, 1992].

eastern boundary of carbonate erratics [Shilts, 1980]; further detail of eastern Ontario, shown in Figure 6.1 is drawn from Karrow [1992]. Although groundmass carbonate can be derived locally from shield marbles or the weathering of feldspars, these sources can only provide 1–2% of the till matrix [Dredge, 1987], a relatively insignificant amount. Figure 6.1 shows a compilation of the carbonate dispersal data from the literature.

Time slices of model results (using parameters under  $\mathcal{M}_1$  in Table 6.1) from 60–10 ka BP in 10 ka intervals are shown in Figures 6.2 and 6.3. Percentage carbonate produced during the last glacial cycle of the sediment (dark grey) and of the englacial debris (light grey) are represented by scaled semi-circles at each grid point on the left-hand panel. Contours of presently observed percentage of carbonate in the till matrix from Dredge and Cowan [1989] are also plotted in the left-hand panel. On the right are snapshots of the ice model showing ice thickness and basal sliding. Figure 6.4 shows the final modelled debris train. Prior to 60 ka BP, the ice is largely cold based in this region.

Experiments using the initial surface lithology as described in Section 5.3.2 failed to produce an appreciable debris train and instead surface lithology of Model  $\mathcal{M}_1$  is assumed identical to bedrock lithology<sup>2</sup>. The model results show initial transport of the carbonate component during the ice flow reorganization from 60–40 ka BP. In the final years of the Wisconsin Glaciation, renewed southern flow firmly emplaces the carbonate erratics in greater concentration and to much greater distances than is observed in the geological record. Setting all mixing parameters  $D_{\text{thrust}}$ ,  $\check{D}_{\text{ed}}$ ,  $D_{\text{col}}$  and  $D_{\text{rot}}$  to zero resulted in a small decrease in southward dispersion but did not alleviate the overzealous southward carbonate transport. Modelled basal sliding appears too vigorous in this area.

In addition, the model produces carbonate dispersal into Quebec, east of Hudson Bay, which is absent in the geological record. This is indicative of either the modelled Labrador ice dome being insufficiently developed or the modelled Hudson Bay ice dome being excessively prominent.

---

<sup>2</sup>This is the equivalent to the right-hand column in Table 5.4 set to 1.0 for all surficial materials.

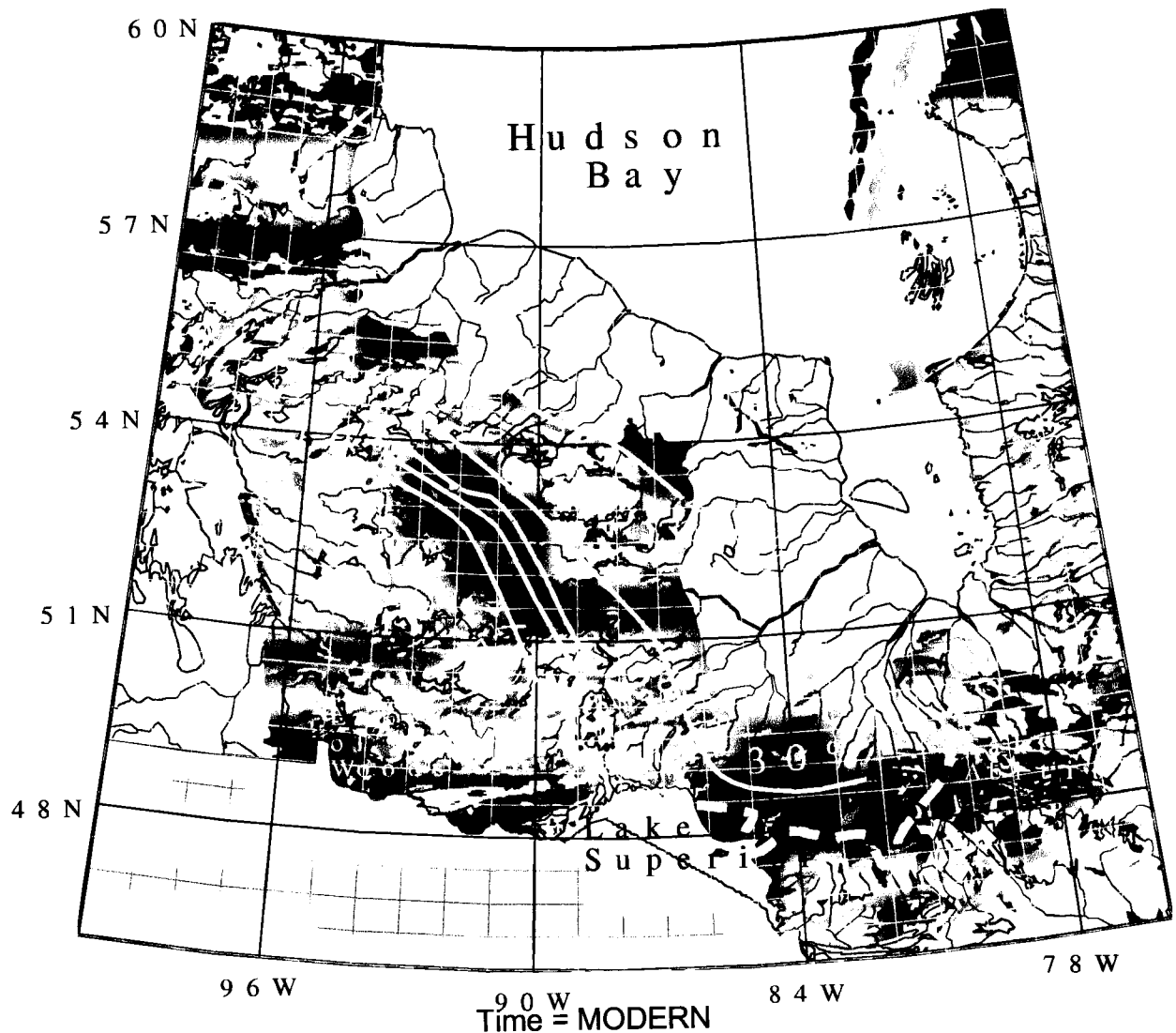
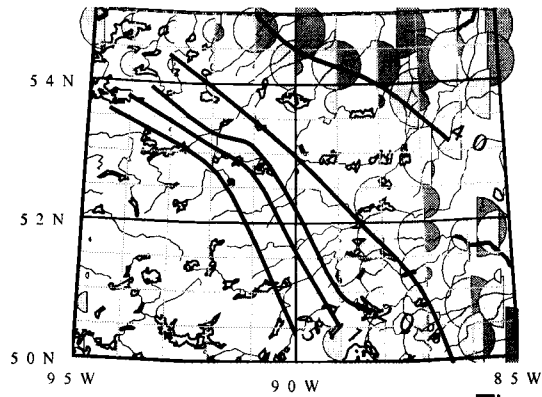


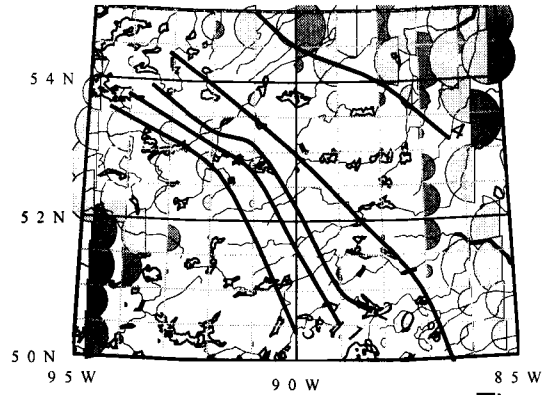
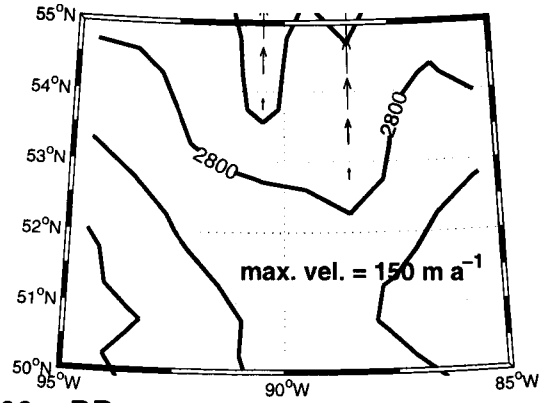
Figure 6.1. A map showing the bedrock lithology [Wheeler *et al.*, 1997] of the Hudson Bay area (colour key is identical to that of Figure 5.3 on page 85) and carbonate dispersal data. The yellow contours show the percentage carbonate in the till matrix (after Dredge and Cowan [1989]). The dashed yellow line represents an extension of the 10% contour through eastern Ontario after Karrow and Geddes [1987] and Karrow [1992]. Zoltai [1965] notes that no carbonates are found west of the Nipigon Moraine, marked by the dashed white line. The percentage of carbonate in the coarse fraction (pebbles) tends to be slightly higher than that of the fine fraction shown above, but the pattern and magnitude are similar.

Parameter	Units	$\mathcal{M}_1$	$\mathcal{M}_2$
$n^s$	—	0.4	0.4
$\rho_r$	$\text{kg m}^{-3}$	$2.7 \times 10^3$	$2.7 \times 10^3$
$\rho_i$	$\text{kg m}^{-3}$	$9.1 \times 10^2$	$9.1 \times 10^2$
$\mathcal{P}_c$	$\text{K Pa}^{-1}$	$7.42 \times 10^{-8}$	$7.42 \times 10^{-8}$
$\mu$	—	0.85	0.85
$J_{\text{bed}}^N$	—	2.4	2.4
$J_{\text{bed}}^T$	—	1.7	1.7
$\phi_{\text{grain}}^{\text{mean}}$	—	0.75	0.75
$\phi_{\text{grain}}^{\text{sd}}$	—	2.5	2.5
$k_i$	$\text{W m}^{-1} \text{K}^{-1}$	2.10	2.10
$k_r$	$\text{W m}^{-1} \text{K}^{-1}$	0.5	0.5
$L_{\text{fus}}$	$\text{J kg}^{-1}$	$3.34 \times 10^5$	$3.34 \times 10^5$
$C^{\text{reg}}$	—	0.1	—
$d^{\text{reg}}$	m	0.25	—
$z^{\text{reg}}$	m	0.1	—
$\check{d}_0$	m	2.0	—
$\check{d}_1$	m	10.0	—
$d_{\text{max}}$	m	15.0	—
$\mu_{\text{ice}}$	—	0.3	0.3
$S_c$	Pa	$6.5 \times 10^6$	$6.5 \times 10^6$
$S_s$	Pa	$1.2 \times 10^6$	$1.2 \times 10^6$
$\mathcal{F}_g$	—	3.0	3.0
$m_g$	—	0.7	0.7
$A_I$	$\text{m s}^{-1}$	$1.0 \times 10^{-8}$	$1.0 \times 10^{-8}$
$A_{II}$	$\text{m s}^{-1}$	$1.0 \times 10^{-8}$	$1.0 \times 10^{-8}$
$\mu_{\text{int}}$	—	0.6	0.6
$k_{\text{abr}}$	—	0.3	0.3
$\check{D}_{ed}$	$\text{m}^2 \text{s}^{-1}$	$1 \times 10^{-10}$	—
$\check{\theta}$	—	$10^\circ$	—
$\check{v}_s$	$\text{m a}^{-1}$	100	—
$\check{z}$	m	5.0	—
$D_{\text{thrust}}$	$\text{m}^2 \text{s}^{-1}$	$1 \times 10^{-9}$	—

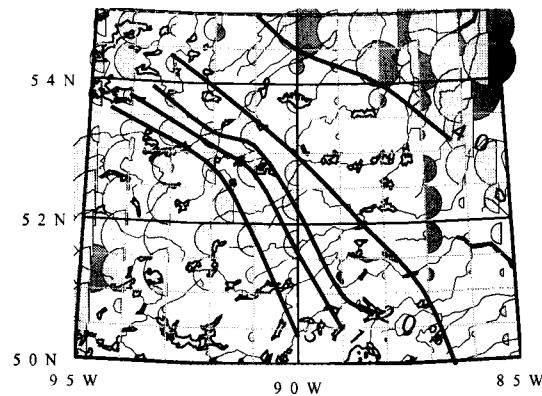
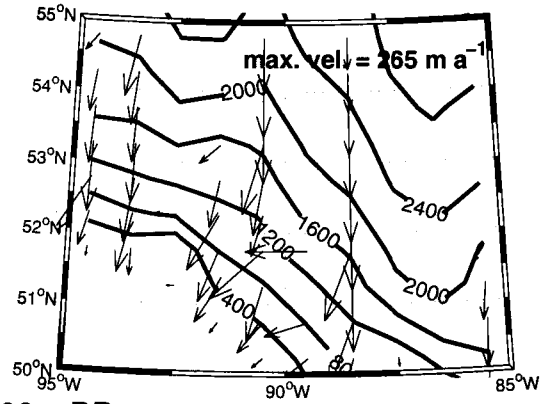
Table 6.1. Parameters for Models  $\mathcal{M}_1$  and  $\mathcal{M}_2$ .



Time = 60 000 a BP



Time = 50 000 a BP



Time = 40 000 a BP

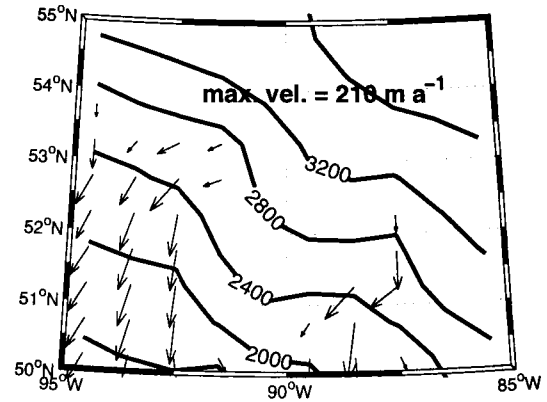
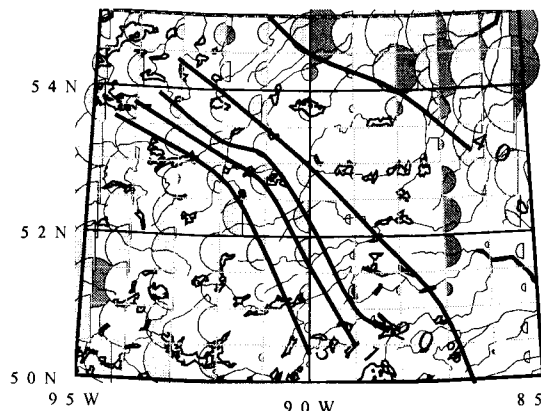
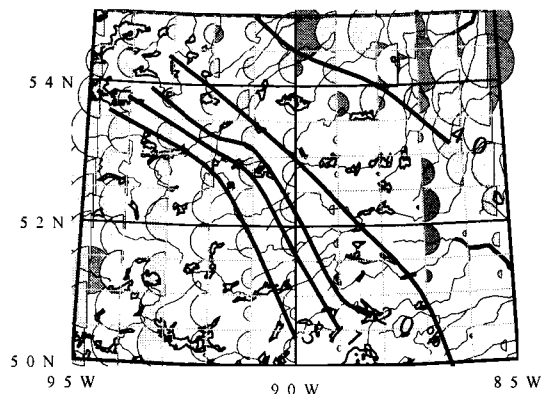
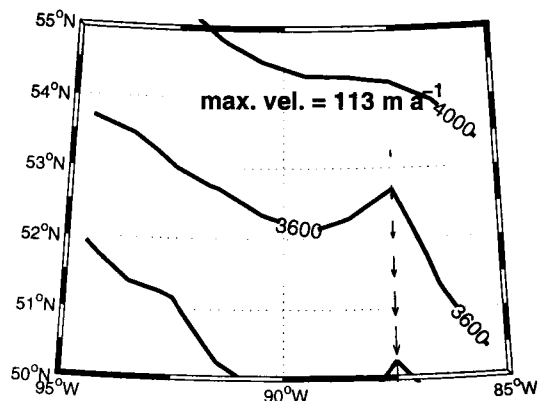


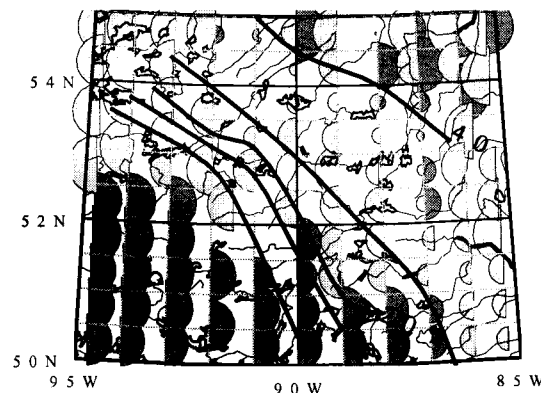
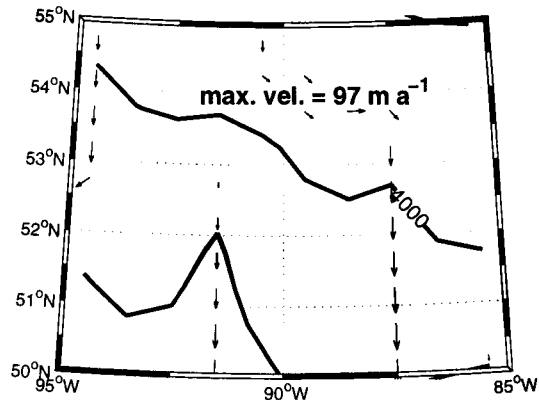
Figure 6.2. Simulation results of the Hudson Bay carbonate train, from 85°W to 95°W. The left-hand panels show model results (represented by filled half-circles) and observed carbonate contours from *Dredge and Cowan* [1989]. The right-hand panels show modelled ice thickness and sliding velocity. Figure 6.3 is a continuation of this figure.



Time = 30 000 a BP



Time = 20 000 a BP



Time = 10 000 a BP

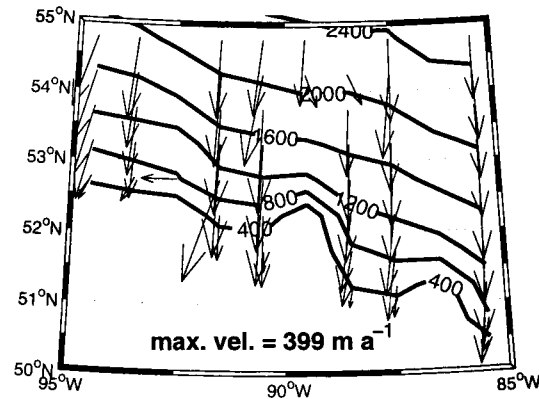


Figure 6.3. This figure continues Figure 6.2, showing simulation results of the Hudson Bay carbonate train, from 85°W to 95°W.

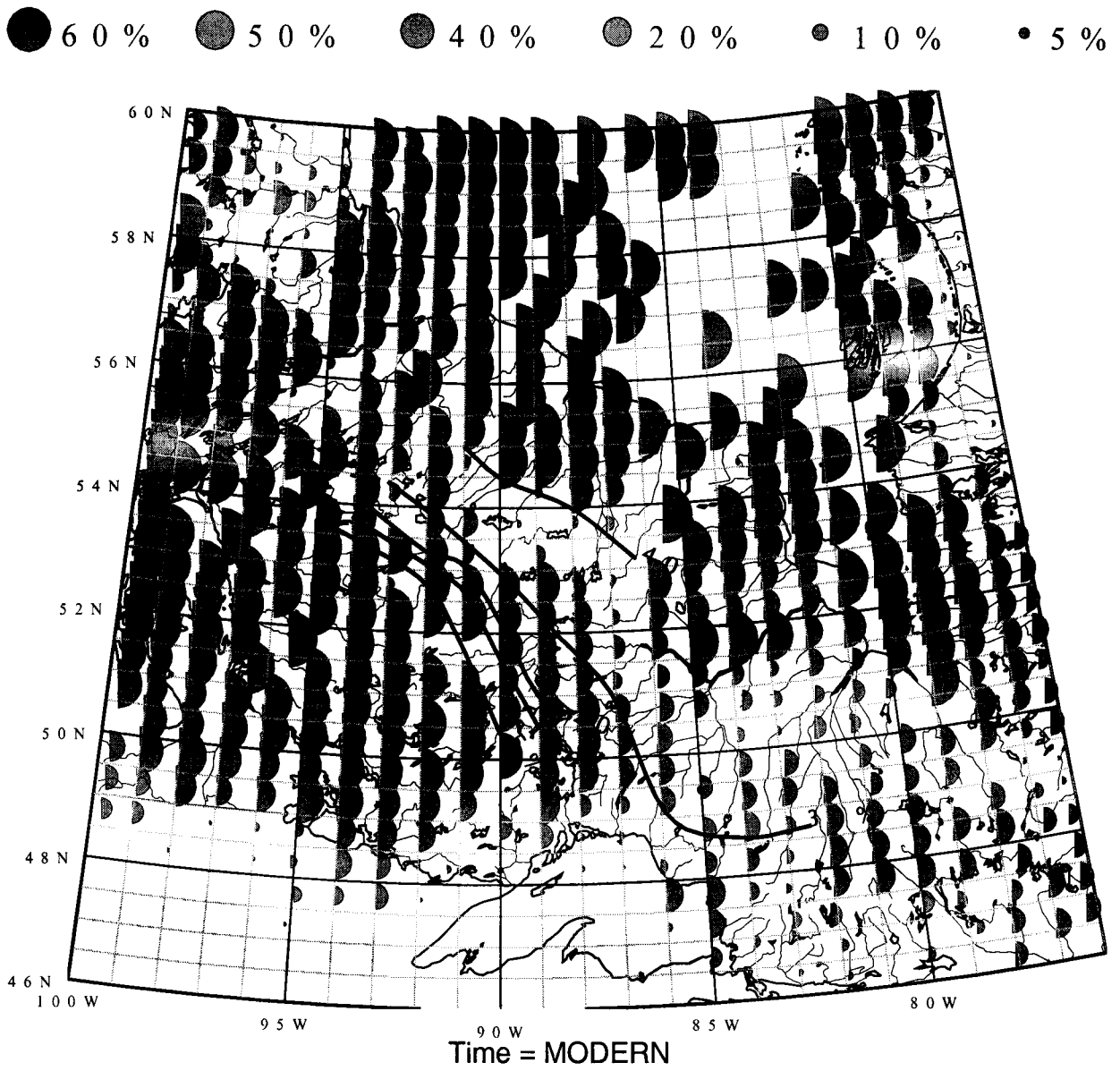


Figure 6.4. This figure continues Figure 6.3, showing simulation results of the Hudson Bay carbonate train, from 85°W to 95°W.

### 6.1.2 Eastward Dubawnt Group transport

The Dubawnt Group dispersal train in western Nunavut has particular importance as an argument against the sole dominance of a Hudson Bay dome throughout the Wisconsinan. The question of whether the Laurentide consisted of a single ice dome or whether it comprised a more complicated collection of centres has been debated over the past century. The extensive eastward dispersal of the distinctive red Dubawnt Group unequivocally demonstrates that a Keewatin centre must have been active for at least a portion of the Wisconsinan [Shilts *et al.*, 1979; Shilts, 1980]<sup>3</sup>.

The Dubawnt Group outcrops in the region northwest from a line connecting Dubawnt Lake (63°N, 102°W) and Baker Lake (64°N, 95°W) [Donaldson, 1965] and its debris train reaches southward to the Manitoba border (60°N) and eastward to Coats Island (62.5°N, 83°W) [Shilts *et al.*, 1979; Shilts, 1980]. A bedrock map of the area and contours of dispersed Dubawnt erratics is shown in Figure 6.5. The Dubawnt Group is not represented in the bedrock map; the purple and maroon volcanic Pitz Formation is mapped specifically as alkaline volcanic and the red sandstones as non-marine sedimentary rocks [Donaldson, 1965; Wheeler *et al.*, 1997]. Because the Dubawnt group cannot be traced directly, the alkaline volcanics are traced in their stead. The assumption that alkaline volcanic rock can be a proxy-tracer for the Dubawnt Group is buoyed by their similar, isolated occurrences. The proxy-tracer will however tend to underestimate the true Dubawnt dispersion as the red Dubawnt sandstones (more areally extensive than the Dubawnt volcanic rocks) are not included.

Time slices of model results (using parameters under  $\mathcal{M}_1$  in Table 6.1) from 60–10 ka BP in 10 ka intervals are shown in Figures 6.6 and 6.7. Percentage Dubawnt Group erratics produced during the last glacial cycle of the sediment (dark grey) and of the englacial debris (light grey) are represented by scaled semi-circles at each grid point on the left-hand panel. Contours of presently observed percentage of Dubawnt Group erratics from Shilts *et al.* [1979] are also plotted in the left-hand panel. On the right are snapshots of the ice model showing ice thickness and basal sliding. Figure 6.8 shows the final modelled debris train (note the scale in this figure is logarithmic in contrast to the linear scales in previous figures in this chapter). Prior to 60 ka BP, the ice is largely cold based in this region.

In contrast to the Hudson Bay area, the modelled response of Dubawnt Group erratics is far short of the observed debris train. Very little basal sliding occurs in the area and consequently any entrained debris is sluggish. Increasing the mixing parameters  $D_{\text{thrust}}$  to  $1 \times 10^{-8} \text{ m}^2 \text{ s}^{-1}$  and  $\check{D}_{\text{ed}}$  to  $1 \times 10^{-9} \text{ m}^2 \text{ s}^{-1}$  had a discernable, yet ultimately insignificant effect on the modelled debris train. A logarithmic scale is used in Figure 6.8 to examine the limits of Dubawnt Group dispersion. This shows that the debris train extends too far northeast, but almost reaches the eastward observed limit on Coats Island.

<sup>3</sup>There are other lines of evidence supporting a multi-domed Laurentide Ice Sheet. For example, the lack of eastward carbonate dispersal in Quebec suggests a well-developed Labrador dome.

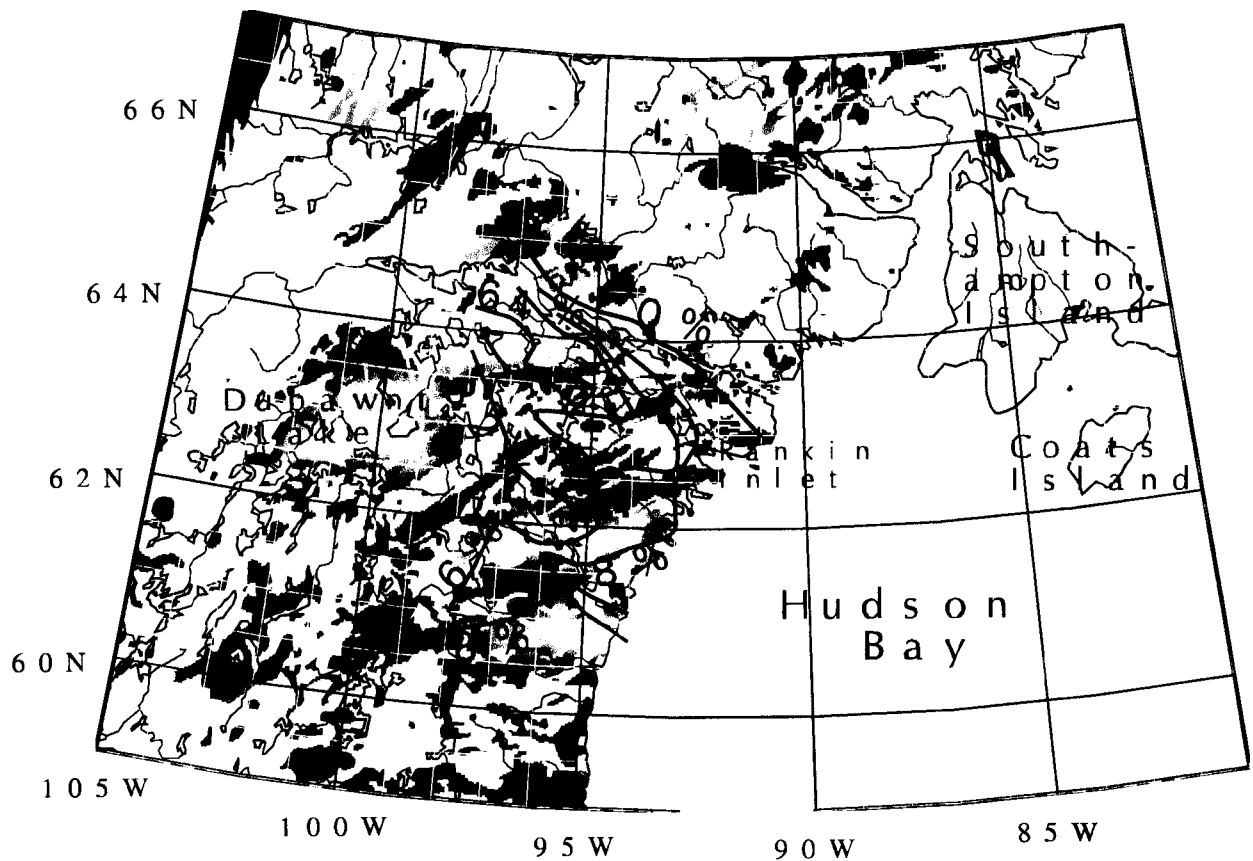


Figure 6.5. A map showing the bedrock lithology [Wheeler *et al.*, 1997] of the region west of Hudson Bay (colour key is identical to that of Figure 5.3 on page 85) and observed allochthonous Dubawnt Group dispersal. The Dubawnt Group consists mainly of pink and purple unmetamorphosed sandstones and volcanic rocks [Wright, 1957; Donaldson, 1965]; the distinctive red hue of many Dubawnt components enables visual identification of dispersed Dubawnt erratics. The black contours show the percentage of Dubawnt erratics in the coarse fraction (2–6 mm) [Shilts *et al.*, 1979; Kaszycki and Shilts, 1980]. Alternate size categories exhibit slightly different dispersal contours, but the pattern and magnitude remain similar to those shown. The source area of the Dubawnt Group does not appear in the bedrock map of Wheeler *et al.* [1997], however the mapped extent of the Pitz Formation (comprising deep purple and maroon volcanic rocks) of the Dubawnt Group [Donaldson, 1965] matches an isolated group of alkaline volcanic rocks in the compilation of Wheeler *et al.* [1997]. This is used as the tracer lithology.

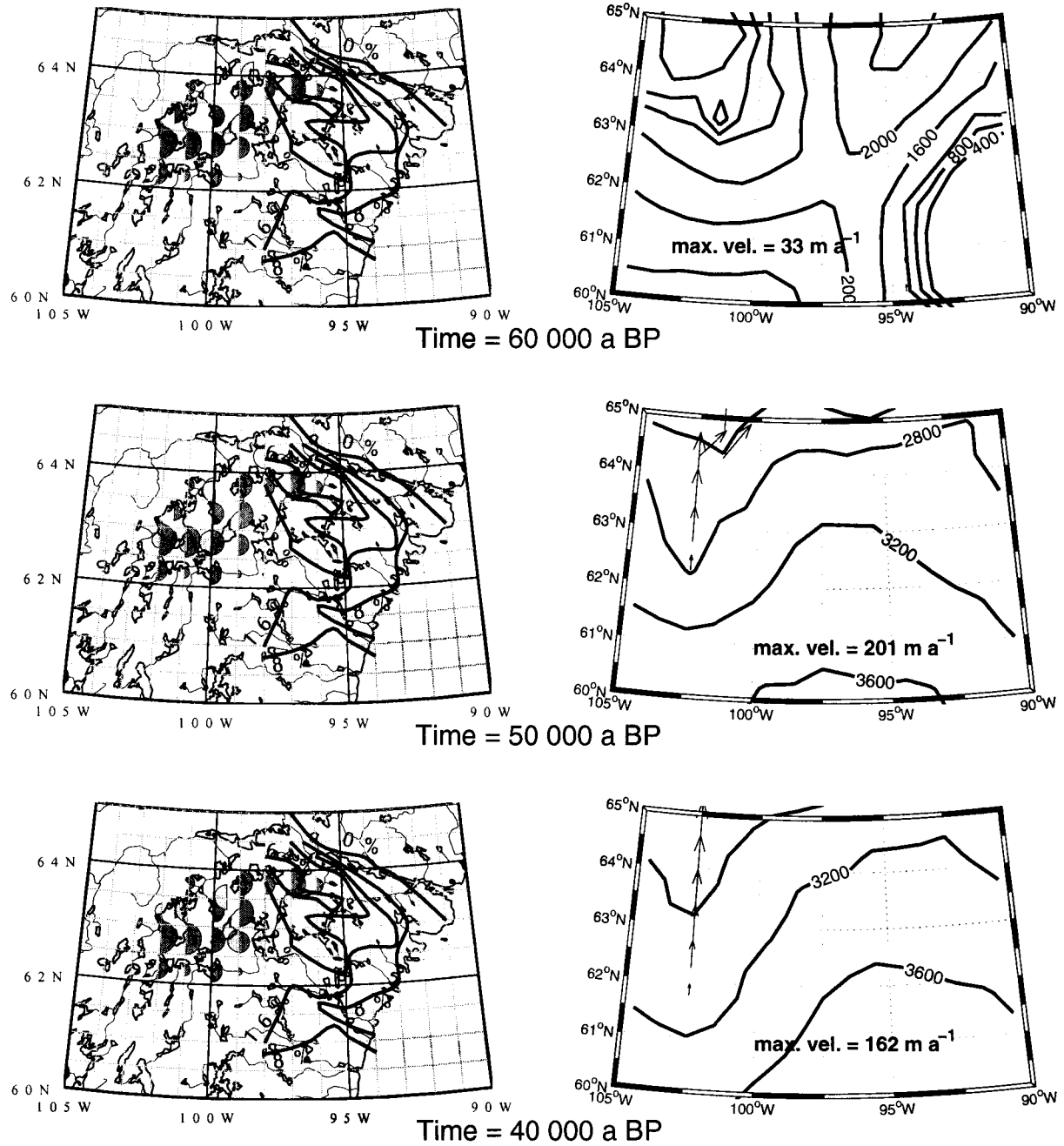
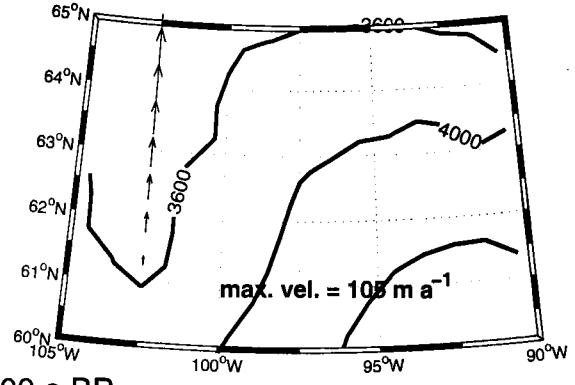
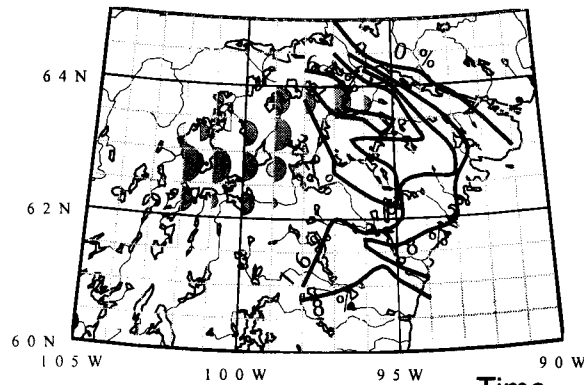
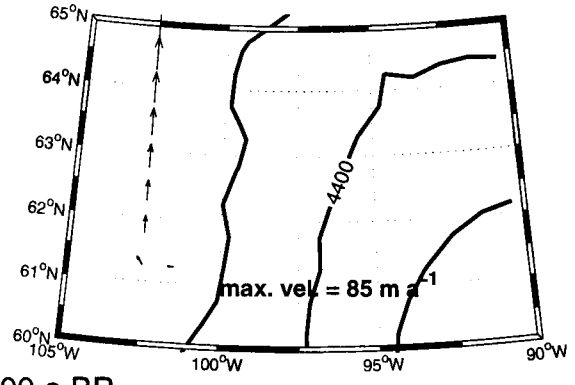
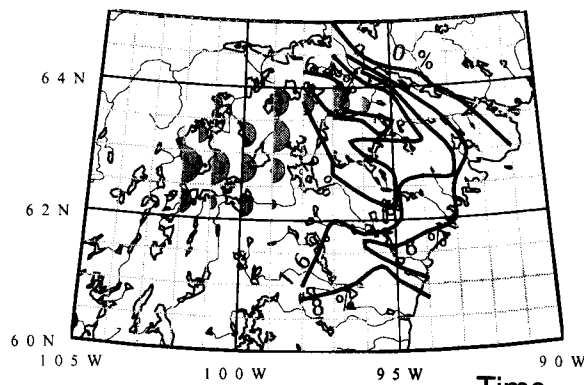


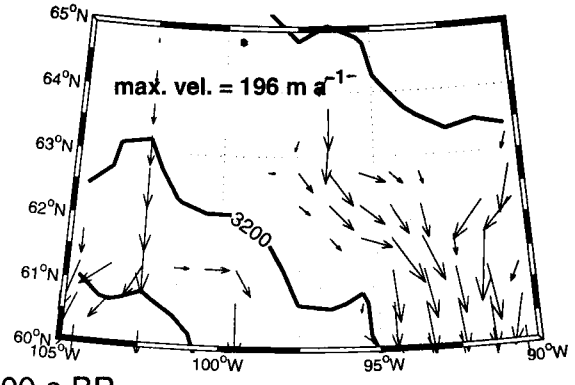
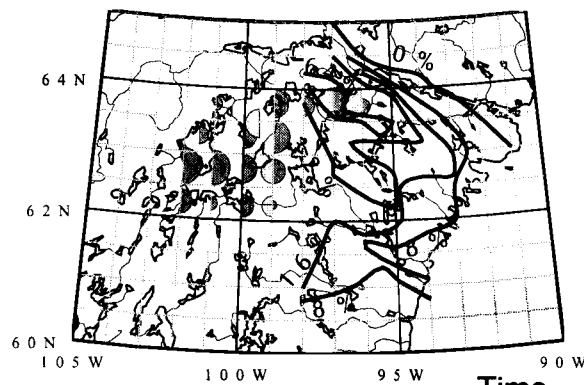
Figure 6.6. Simulation results of the Dubawnt Group dispersal train from 90°W to 100°W. The left-hand side shows model results (represented by filled half-circles) and observed Dubawnt Group erratic contours from *Shilts et al.* [1979]. The right-hand panels show modelled ice thickness and sliding velocity. Figure 6.7 is a continuation of this figure.



Time = 30 000 a BP



Time = 20 000 a BP



Time = 10 000 a BP

Figure 6.7. This figure continues Figure 6.6, showing simulation results of the Dubawnt Group dispersal train from 90°W to 100°W.

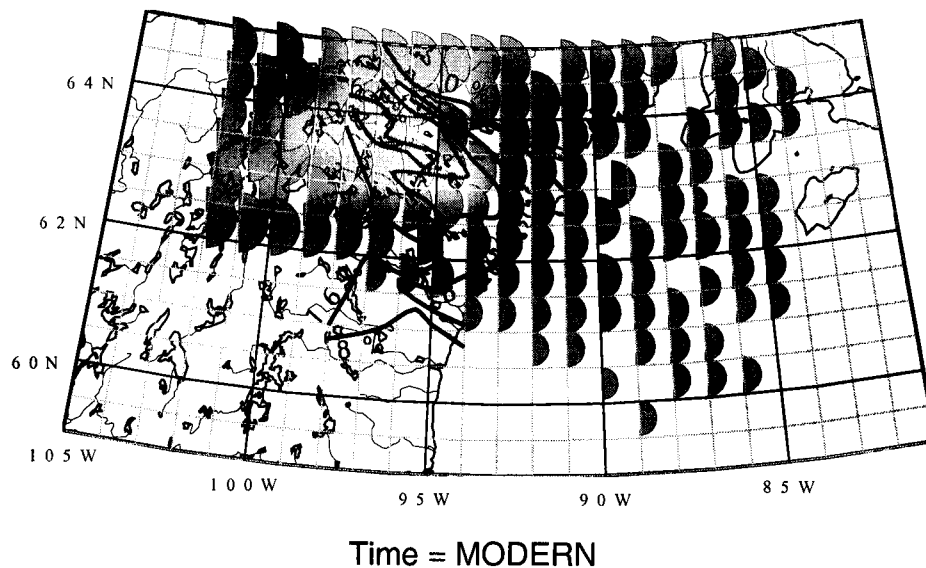
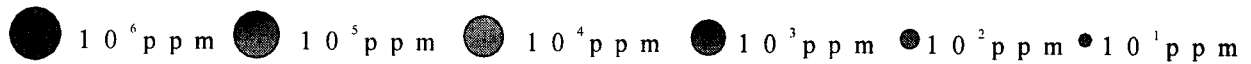


Figure 6.8. This figure continues Figure 6.7, showing simulation results of the Dubawnt Group debris train.

The different modes of failure between the two test cases is instructive. Clearly the transport is overly vigorous in the Hudson Bay carbonate area suggesting that the sliding coefficients used in the ice model ( $B_s = 1 \times 10^{-10} \text{ m s}^{-1} \text{ Pa}^{-1}$  for a hard bed and  $B_s = 2 \times 10^{-10} \text{ m s}^{-1} \text{ Pa}^{-1}$  for a soft bed) are too high. The modelled dispersion is also not selective enough to match the observations with eastward dispersal well beyond the Ontario–Quebec border and northern transport above the Manitoba–Nunavut border. The opposite situation prevails over western Nunavut where debris dispersal is sluggish. This can be attributed to an absence of a well-formed Keewatin Dome.

There is strong evidence that Hudson Strait acted as an ice stream conduit episodically during the Wisconsin Glaciation, drawing down the ice in the Hudson Bay basin and encouraging ice flow from the Keewatin District and western Quebec into the head of Hudson Strait. This would serve to ameliorate the lack of eastward dispersion of the Dubawnt Group, the excessive southward transport of carbonates and the existence of western Quebec carbonates in the model results.

The results presented in this section account only for dispersion from the Wisconsin Glaciation. Clearly this is inadequate as many glaciations have taken place over the study area (Figure 1.1). The exercise is nevertheless useful and explicit polycyclic modelling of glacial cycles is an obvious future step.

## 6.2 Erosion results

The measurement of paleo-erosion is problematic; proof of its existence is often ephemeral as transport agents work to disperse erosional products from their moment of creation. Nevertheless there are methods of obtaining denudation rates to compare and assess model results. If a dated paleosurface can be reconstructed, differencing the surface with modern topography results in time-integrated erosion. Sediment volume measured in a well-defined depositional basin yields the average erosion of the source area. Cosmogenically derived isotopes are used to give point measurements of erosion where good independent dating controls exist. With all methods, the problem of separating glacial and non-glacial erosion is always present.

A focus of this work is the reconstruction of the Laurentide Ice Sheet. It was the largest of the Wisconsinan North American ice sheets and the relatively coarse grid used for this study was chosen to enable a domain expansive enough for the entire Laurentide Ice Sheet. However, there are smaller ice complexes captured by the model domain (e.g. Newfoundland Ice Cap, Cordilleran Ice Sheet). The Cordillera is particularly instructive as several studies have examined paleo-erosion in Fennoscandia, an analogue of the Cordillera.

### 6.2.1 Cordilleran erosion

The Wisconsinan ice that encompassed the rugged accreted terrains of western North America is labelled the Cordilleran Ice Sheet; the St. Elias ice fields and the many Coast Range ice caps are its modern remnants. The Cordilleran winter climate is dominated by a succession of cyclonic storms from the North Pacific that, when combined with the orographic effect of several north-south trending mountain chains, lead to massive alpine precipitation. This wet climate maintains the abundant ice fields presently observed in the Coast Mountains and St. Elias Range.

The Cordilleran ice history is complex, but generally follows the conceptual model of *Kerr* [1934]: in a colder climate, small mountain glaciers, similar to their modern counterparts, can grow to cover an extensive area in mountainous regions. As the climate cooled, the alpine glaciers coalesced into an ice mass that blanketed the region, although ice dynamics were still largely topographically controlled. In some cycles of glaciation (likely excluding the ultimate one), the ice thickened, culminating in radially outward flowing domes, largely independent of subglacial topography. The evolution of the Cordilleran Ice Sheet over the past 120 ka has been punctuated by several glacial pulses. During the Wisconsin Glaciation there was at least one period (the Olympia non-glacial interval) where glacial limits were similar to present day configuration [*Clague*, 1981]. This pulsating character is partially captured by the ice model although major details, such as the Olympia non-glacial interval, are missed. A plot of model ice volume between 45–65°N, west of 120°W is shown in Figure 6.9.

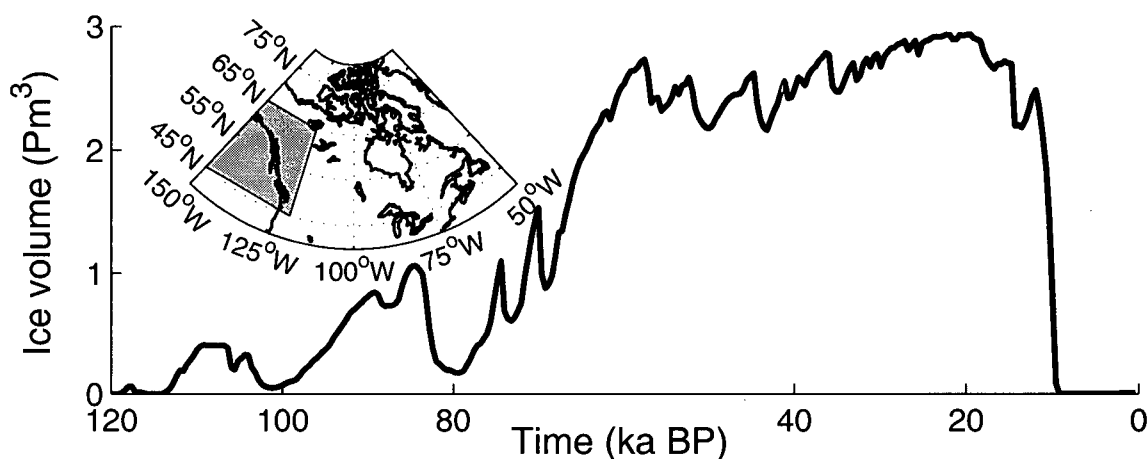


Figure 6.9. Modelled Wisconsin ice volume west of 120° W and between 45° and 65° N, which roughly coincides with the bounds of the Cordilleran Ice Sheet.

Paleo-erosion data from the Cordillera are scant, but such studies have been undertaken on the western seaboard of Fennoscandia. Both regions have maritime mountain chains with extremely wet winters and their Wisconsin ice history, both largely topographically controlled, includes episodic coastal glaciation [Clague, 2000; Elverhøi *et al.*, 1995a]. The analogue between the two is reasonable and studies of Fennoscandia can be used to constrain Cordilleran paleo-erosion despite notable differences in glacial landforms.

### Estimates of erosion

Isotope  $^{36}\text{Cl}$  is created by interaction of terrigenous elements with cosmogenic radiation, altering the background ratio of  $^{36}\text{Cl}/\text{Cl}$  to a depth of  $\approx 2$  m. Where the timing of glacial advance and retreat are well constrained, the expected  $^{36}\text{Cl}/\text{Cl}$  ratio can be calculated and deviations from the expected value is attributable to glacial erosion. Briner and Swanson [1998] present a  $^{36}\text{Cl}$  study where ice cover is well-constrained from 18–15 ka BP in Washington State. A maximum erosion of 0.26–1.06 m is calculated at abrasion sites (the upstream flank of local topography) while a minimum of  $\approx 2$  m is inferred in areas of inferred quarrying (lee faces); the study area is heavily fractured, which enables aggressive quarrying.

While the above represents an important result, it is nevertheless a single datum in space and wide-scope integrated erosion values are more directly comparable to model output. The differencing between ancient and modern topography gives an extensive spatial result and a study of Sognefjord, Norway [Nesje and Whillans, 1994; Andersen and Nesje, 1992; Nesje *et al.*, 1992] provides such an example. A smooth Tertiary surface is interpolated from remnants of the paleosurface in the basin highlands which have been nearly free of Quaternary erosion, with some

areas retaining a Tertiary regolith [Nesje and Whillans, 1994]. The difference between modern topography and the estimated paleosurface yields an average basinal erosion of 610 m, which is in agreement with the estimate from the marine sediment wedge [Riis and Fjeldskaar, 1992]. With the assumption that the entire difference is attributable to an estimated 600 ka of ice cover since the Tertiary, an average erosion rate of  $1.02 \text{ mm a}^{-1}$  is calculated [Nesje et al., 1992]. A more conservative estimate that allows for preglacial, fluvial channeling is an average of 320 m denudation over the basin [Andersen and Nesje, 1992], which yields  $0.53 \text{ mm a}^{-1}$ . As Nesje and Whillans [1994] note, neither of these estimates considers mass wastage of the headwall (where modern colluvial debris fans are observed) or a tectonic contribution to the fjord formation.

The assumption that the erosion rate has remained constant over the past 2.5 Ma is fraught with pitfalls. Aggressive early erosion of the less-competent Tertiary regolith is probable. From 1–0.6 Ma BP, there is a marked increase of ice-rafted debris (IRD) in the Norwegian Sea compared to earlier rates [Jansen and Sjøholm, 1991], indicating that glacial erosion in the later part of the integrated period may have outstripped the earlier years. Based on Figure 1.1 and ocean cores that capture predominantly Greenland IRD [Jansen et al., 2000], this increased trend is expected to continue throughout the most recent 0.6 Ma. This suggests that the estimates of erosion based on even distribution throughout the past 2.5 Ma underestimate the erosion rate of the past 120 ka.

Another method to obtain integrated denudation rates over a basin is to integrate the deposited sediments; this approach has been applied to marine sediment fans in Svalbard. The integration of the glacial sediments from Isfjorden Fan yields a total denudation over the past 120 ka of 24 m [Elverhøi et al., 1995b]. This estimate is based on seismic mapping of a “Glacial Unit” with tentative age assignment through identification of marine isotope stage 5e ( $\approx 120 \text{ ka BP}$ ) within the unit from ocean coring. This denudation rate is consistent with, though in the low end of the bracket, other estimates of long term erosion rates from other Barents Sea basin sediments (Storfjorden and Bear Island Trough) [Elverhøi et al., 1998].

Modern glaciated basins in Alaska provide a glimpse at a possible paleo-analogue of the Wisconsin Glaciation further south. Measurements show that modern day erosion from Alaskan glaciers is on the same order as the above paleo-estimates [Hallet et al., 1996]. The analogies between modern Alaskan glaciers, paleo-ice on Svalbard and Norway and the Cordilleran Ice Sheet are by no means exact, but can nevertheless serve to roughly constrain Cordilleran paleo-erosion.

### Modelled Cordilleran erosion

The modelled erosion results illustrated in Figure 6.10 show that this model produces erosion rates much lower than the above estimates. The erosion results shown in Figure 6.10 is a very favorable realization for erosion with parameters given by  $\mathcal{M}_2$  in Table 6.1. To maximize the erosion

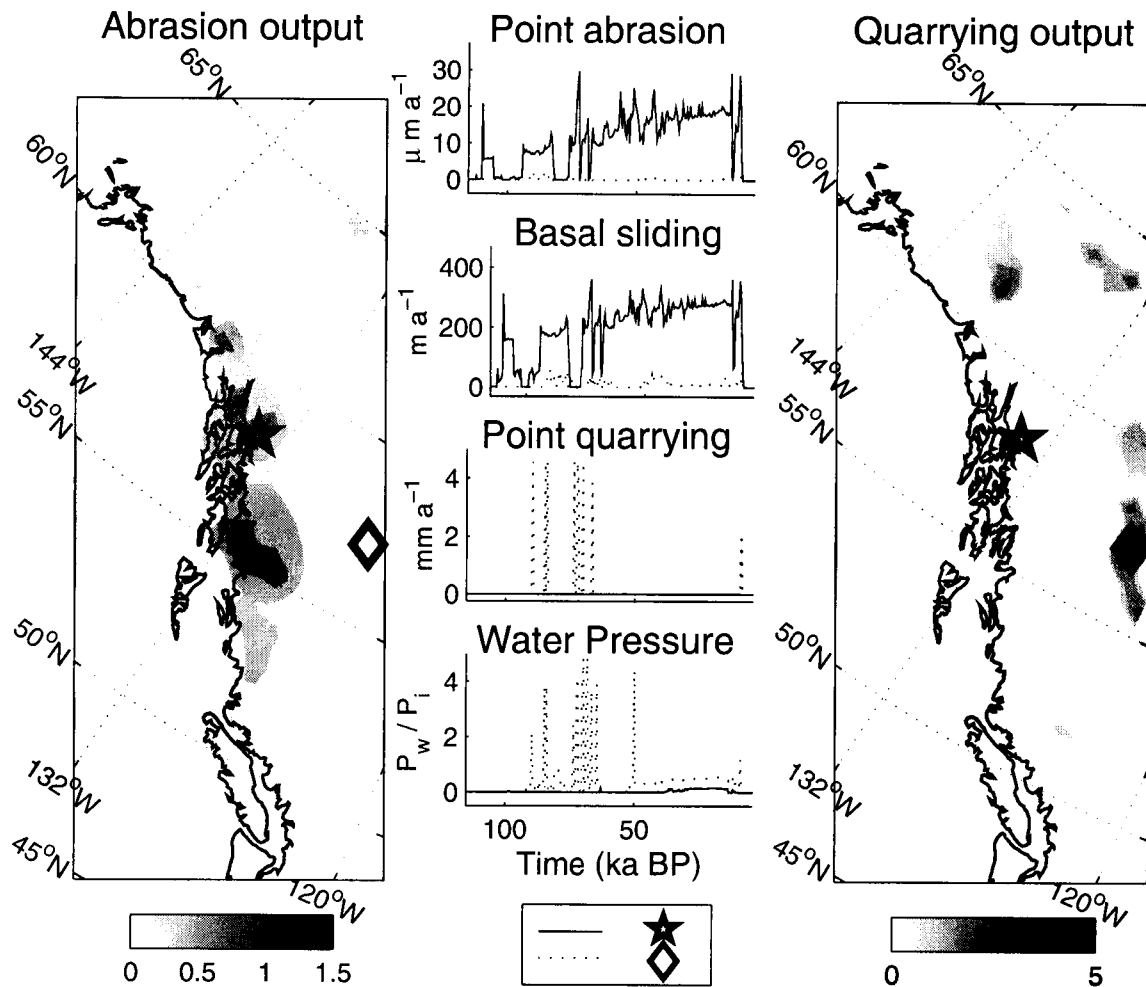


Figure 6.10. Simulation results for Cordilleran erosion, using favorable conditions for erosion. Time-integrated results are shown for the entire region and time series are plotted for the points  $133.5^{\circ}\text{W}$ ,  $58.25^{\circ}\text{N}$  (denoted by the star) and  $125.5^{\circ}\text{W}$ ,  $57.25^{\circ}\text{N}$  (denoted by the diamond). Time series are also shown for the basal sliding speed and normalized subglacial water pressure which are well correlated to abrasion (correlation coefficient = 0.79) and quarrying (correlation coefficient = 0.50) respectively.

potential (and to minimize the effects of other aspects of the complete model), the initial cover conditions are set to zero (bare basement) and no build up of sediment is allowed. Physically, this can be thought of as perfectly effective transport in action through either complete entrainment or through vigorous subglacial water flow.

The failure of the model to predict vigorous erosion stems from the lack of quarrying. In Section 5.2, the assumption was made that glacial routing of surface water is insignificant for the Wisconsin ice sheets. However for much of the past 120 ka, the ice volume in the Cordillera would not have been sufficient to engulf the mountains and coalesce into an extended ice mass.

Conditions more akin to present-day would have been prevalent and in these conditions, surface water can leak in down the sides of nunataks or valley walls. This input is unaccounted for and could raise the modelled subglacial water pressure to levels where quarrying could be expected.

Supraglacial debris production, very active in modern glaciers in the Cordillera and St. Elias, can be a significant source of erosion when ice volume is insufficient to drown nunataks. As this was the case during much of the Wisconsin Glaciation in the Cordillera, the exclusion of this process may lead to the underestimation of Cordilleran paleo-erosion.

### 6.2.2 Laurentide erosion

#### Estimates of erosion

Estimates of the Laurentide's erosional signature have historically fluctuated by several orders of magnitude from a few tens of metres [e.g. *Dyke et al.*, 1989] to very deep erosion (greater than 1000 m in Hudson Bay [*White*, 1972]<sup>4</sup>). The deep erosion hypothesis, while an attractive explanation of broad features of both the Laurentian and Fennoscandian landscape is inconsistent with many glacial geomorphic observations [e.g. *Gravenor*, 1975; *Sugden*, 1976; *Lidmar-Bergström*, 1997]. A tectonic origin for the Hudson Bay basin is generally accepted [e.g. *Sugden*, 1976; *Lidmar-Bergström*, 1997].

One method for estimating the integrated erosion is to examine the amount of deposited sediment. This approach is explored for North Atlantic deposits by *Laine* [1980, 1982] and for all the marine sediment repositories of the Laurentide<sup>5</sup> by *Bell and Laine* [1985] to yield an average denudation from the Laurentide source area of 120 m over 3 Ma, a value that begins to approach the deep erosion hypothesis of *White* [1972, 1988]. *Bell and Laine* [1985] consider this a minimum value although no allowance is made for non-glacial erosion and *Hay et al.* [1989] charge that the estimate of sediment with a Laurentide provenance in the Gulf of Mexico is greatly overestimated in the analysis of *Bell and Laine* [1985]. Reanalysis using the methodology of *Bell and Laine* [1985] with the more conservative estimate of *Hay et al.* [1989] for glacial sediments in the Gulf of Mexico gives an expected mean glacial erosion of 80 m through the Laurentide source area over 3 Ma<sup>6</sup>.

Integration of the Dubawnt dispersal train can be linked back to a specific source area because of its distinctive colour, which makes it as useful tracer lithology exploited in Section 6.1.2. As the entire debris train has been mapped, an estimate of the total amount of debris can be made,

<sup>4</sup>No value is actually given by *White* [1972] and this value is estimated from a conceptual sketch by *Sugden* [1976].

<sup>5</sup>The Cordilleran Ice Sheet is not included in the analysis

<sup>6</sup>*Hay* [1998] cites a corrected value of 16 m, although this appears to disregard all glacial sediments north of the Gulf of Mexico.

Model variable	Sliding distance	Water Pressure
$\mathcal{M}_1, \int_0^{120\text{ka}} \dot{A} \Delta t$	0.56	0.24
$\mathcal{M}_1, \int_0^{120\text{ka}} \dot{Q} \Delta t$	0.16	0.62
$\mathcal{M}_2, \int_0^{120\text{ka}} \dot{A} \Delta t$	0.79	0.25
$\mathcal{M}_2, \int_0^{120\text{ka}} \dot{Q} \Delta t$	0.12	0.50

Table 6.2. Correlation coefficients for total abrasion and quarrying with integrated sliding distance and normalized water pressure.

and because the source area is also well defined, a value for denudation can be calculated. This is the strategy of *Kaszycki and Shilts* [1980], who estimate 6–20 m of erosion during the last glacial cycle.

### Modelled Laurentide erosion

Figure 6.11 shows the total erosion for the Models  $\mathcal{M}_1$  and  $\mathcal{M}_2$  (see Table 6.1). The average erosion over the entire model domain for  $\mathcal{M}_1$  is 0.26 m and for  $\mathcal{M}_2$  is 0.73 m. These figures underestimate the true average erosion as they take the entire model domain for the whole integration time into consideration while the estimates outlined above generally restrict the integration to glaciated area. However this error at most could alter the results by a factor of 2, leaving the modelled erosion short of observed amount of sediment produced over the past 120 ka.

Table 6.2 shows that the abrasion is controlled mostly by the sliding while quarrying is correlated to water pressure. It is difficult to justify increased abrasion to better match the observations. This would require either a significant change in the physical parameters of the bed or increased sliding velocities. Given that the transport model results indicate that sliding velocity is already overestimated, an increase in quarrying is the more sensible solution to deal with the erosive deficit.

Quarrying results could be bolstered by two methods: either increasing the water pressures or by decreasing the resistance of the bedrock to subcritical fracture. Both solutions are feasible. The water pressure is kept at an arbitrary level through the sheet thickness  $H_{\text{crit}}^w$  as described in Section 5.2.1. There is no strong basis to this parameter and reducing  $H_{\text{crit}}^w$  by a nominal amount would lead to higher water pressures and thereby more aggressive quarrying. On the other hand, in the assignment of subcritical crack parameters in Section 5.3.1, no allowance is made for pre-fractured rock, which could increase quarrying significantly.

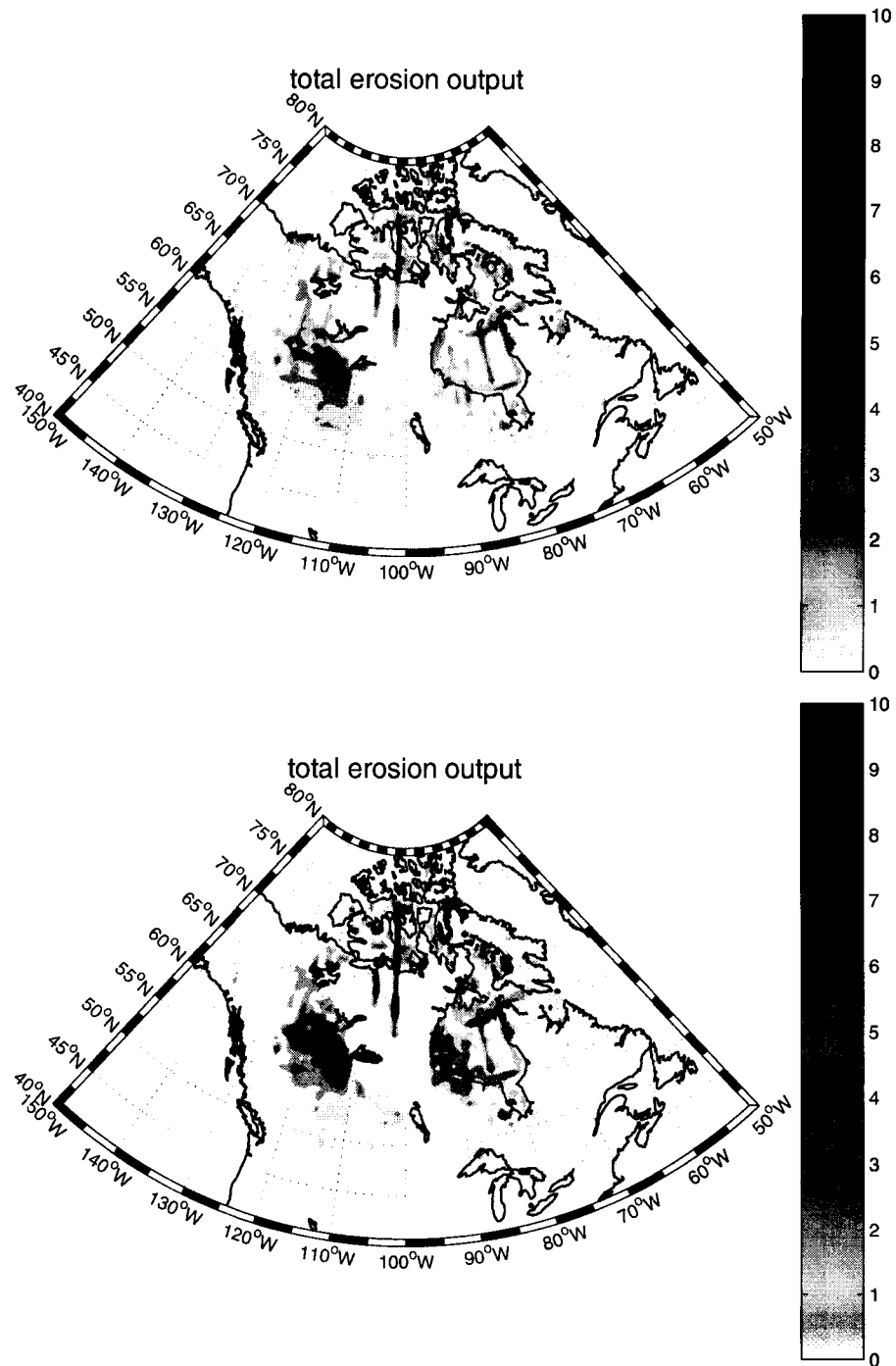


Figure 6.11. Integrated erosion (in metres) for  $M_1$  (top panel) and  $M_2$  (bottom panel), the parameters of which are listed in Table 6.1.

## Chapter 7

# Conclusions

### 7.1 Summary of work

This thesis presents a large-scale physically based model of subglacial processes driven by existing ice sheet and hydrological models. It comprises subglacial erosion, sediment entrainment and deposition, englacial mixing and advective transport components. A lithologically accurate description of the bed enables tracer capabilities and incorporation of geologically dependent parameters.

The modelled subglacial erosion proceeds by two mechanisms: abrasion and quarrying. Abrasion is calculated by the classic wear formula, proportional to the normal force presented by the abrading particle  $F^N$  and the particle velocity  $v_p$ , and inversely proportional to the hardness of the wear surface  $h_s$ . The normal force is calculated, following *Hallet* [1981], through the viscous force of the ice against the abrading particle. The wear is modified to account for the shielding effect that sediment has on further abrasion. Hardness is lithologically dependent and a sub-grid geological representation of the bed is used [*Wheeler et al.*, 1997]. A distribution of particle radii, upon which the viscous force is dependent, is taken from sedimentological studies in the literature. Bed topography is downscaled based on the scaling behavior of six test areas where both coarse and high resolution elevation data are available for calibration.

A quarrying model is constructed as a function of subcritical crack growth. This in turn depends on lithological parameters and the state of stress in the bedrock. As for abrasion, an accurate description of bed geology is used to assess the lithologically dependent parameters. The stress is calculated using a two dimensional convolution of the solution for a point load acting on the planar surface of an infinite half-space. Numerical experiments suggest that a topographic modifier to this planar solution is an acceptable approximation to the rigorous solution for the loading of a complex surface with topography. The stress induced by a continuous ice load is generally

sufficient to induce subcritical crack growth and the existence of water-filled cavities and joints are necessary for quarrying to proceed. Therefore, I formulate an expression for subglacial cavity areal extent and its effect on the stress solution. The quarrying rate is then calculated by modifying the crack growth rate by a tunable parameter  $\mathcal{A}_I$  and a sediment shielding term.

The total modelled abrasion over the Wisconsin Glaciation is highly correlated with the mean sliding speed of the ice; total quarrying is well correlated with water pressure normalized by the ice overburden. Thus for both processes, the input fields are crucial. The Marshall–Clarke ice sheet model [Marshall, 1996; Marshall and Clarke, 1997a,b; Marshall *et al.*, 2000], driven by estimates of paleoclimate, is used to predict ice dynamics and thermodynamics; this includes a thermally regulated sliding scheme with an enhancement for soft-bedded domains. The subglacial water pressure is solved using the model of Flowers [2000], modified for a continental-scale reconstruction.

Sensitivity tests show that the contribution of subcritical shear crack growth (Mode II/III) is limited in all but the most extreme cases and extensional crack growth (Mode I) is the primary method of subcritical crack propagation. Over a glacial cycle, quarrying is the more efficient excavator; even the most aggressive parameterization of abrasion cannot match the observed data and it is necessary to include quarrying to approach the estimates of paleo-erosion. It is therefore difficult to assess the appropriateness of the value used for the abrasive wear coefficient  $k_{abr}$ .

Quarrying, although deeper than abrasion, also does not achieve the quantity demanded by the geological record. This is suggestive of several possibilities

- (a) The quarrying factor of  $\mathcal{A}_I = 1 \times 10^{-8} \text{ m s}^{-1}$  used in this study is too low.
- (b) The modelled rock competency is too great.
- (c) The subglacial macroporous horizon, artificially thickened to increase its transmissivity, is too thick which results in low water pressures.
- (d) The assumption that englacial routing of surface melt to the bed can be ignored is false.

It is unlikely that  $\mathcal{A}_I$  should be increased by a significant amount. This does not serve to areally expand the quarrying domain, but rather to make the quarrying more aggressive. Already with  $\mathcal{A}_I$  set to  $1 \times 10^{-8} \text{ m s}^{-1}$ , point quarrying rates reach  $\approx 4 \text{ mm a}^{-1}$ , which is consistent with presently observed rates [Hallet *et al.*, 1996] and some areas are subject to deep quarrying ( $\approx 25 \text{ m}$ ). In some cases, the rock competency may be overestimated, as fractured or weathered rock is not considered. The macroporous horizon critical sheet thickness  $H_{crit}^w$  is a tunable parameter taken as 4 m for this study. A thinner value is plausible and would lead to higher water pressures and more aggressive quarrying. Another method to increase water pressure is to enable surface–bed melt coupling. The prohibition of this exchange is a good assumption at LGM for the majority

of the Laurentide, but there are areas and times where this component of the hydrological model of *Flowers* [2000] should be included. This is the most probable reason for the underestimation of modelled erosion in the Cordilleran Ice Sheet.

The englacial processes modelled in this thesis begin with sediment entrainment and end with deposition. Three methods of entrainment are considered: net basal adfreeze, intrusion by regelation and freeze-on by Weertman regelation. The thermodynamics of the ice sheet model do not allow for freeze-on making the calculation of net basal freezing problematic. Nevertheless, a physically based estimate is made when the bed makes a warm-to-cold transition. Calculation of intrusion follows *Iverson and Semmens* [1995] and is a strong function of water pressure. Limited entrainment can occur by Weertman regelation when the ice slides over a predominantly hard bed. Intrusion by regelation is the most significant of the three mechanisms examined. Deposition occurs when basal melt overtakes the combined entrainment.

Vertical redistribution of englacial sediment is modelled through a number of processes. Mixing by englacial tectonics is cast as an eddy-diffusion model following *Alley and MacAyeal* [1994] and a formulation is developed for mixing by thrust faults. An expression describing the mixing by rigid-particle rotation is developed, which is on the same order as the mixing by rigid-body collisions [Weertman, 1968]. Vertical advection of debris is accounted for with a simple upstream discretization. Lateral advection of sediment with the ice is calculated using the scheme of *Prather* [1986], which conserves second-order moments and has excellent numerical diffusion attributes.

Accurate tracking of the lithological signature of sediment through each of the above processes allows the transport of distinct lithological tracers to be predicted and compared to observed debris trains on the modern landscape. A detailed bedrock map of Canada [Wheeler *et al.*, 1997] is used for initialization. The comparison of observed Hudson Bay Paleozoic carbonate dispersal with model results shows an overzealous transport of carbonates in both amount and direction. This is suggestive of either an excessively vigorous sliding law used in the ice sheet model or incorrect central ice geometry which drives the sliding. Conversely, the modelled Dubawnt Group transport is minute compared to the observed debris train. The ice sheet model does not sufficiently capture the coarse structure of the Laurentide Ice Sheet to allow for this geological observation; more fully developed Keewatin and Labrador Domes are necessary.

## 7.2 Outlook

A primary objective of this thesis is to further the theoretical description of subglacial and englacial processes with the intent of creating a predictive forward model for glacial geology. The preceding chapters represent a step towards this goal. This effort is neither exhaustive nor complete. There is an abundance of geomorphic landforms not touched upon and there are many conceivable

improvements to the processes described.

Refined input models offer immediate potential for improvement. There is strong evidence of an ice stream in Hudson Strait from the provenance of Heinrich Layer ice-rafted debris; such an ice stream would drain and subsequently lower Hudson Bay ice. This would lessen the southward carbonate transport and enhance the eastward Dubawnt Group transport, ameliorating both problems evidenced in the comparisons of model results to observations. As discussed above, the prohibition of surface-bed water routing is too general a constraint that adversely affects the erosion results. Careful application, dependent on topography and ice thickness, of this model component of *Flowers* [2000] could alleviate this problem.

The melding of diverse models (climate, ice, hydrology and terrestrial) gives a wide scope to this study that is particularly relevant in the current atmosphere of interdisciplinary science. However, since there are no feedbacks between the models, the coupling is incomplete. This work provides an avenue of extension for existing ice sheet and hydrology models; basal conditions affect both ice and water dynamics and a large-scale description of bed evolution is a vehicle for feedback.

Much of the geomorphic data is of smaller scale than what is resolvable with the model grid used. A smaller model domain has potential economic interest; lithological tracing capabilities could be applied to drift prospecting. Two and half centuries after Daniel Tilas began drift prospecting using boulder erratics in Finland [*Kauranne*, 1992] a process-based forward model is at hand!

Glaciologists have increasingly recognized that basal processes are of great import to ice dynamics. The wealth of Quaternary geological data cannot be used as an effective constraint in an ad hoc manner. Predictive forward modelling of basal processes fully coupled to an ice sheet model (inclusive of subglacial hydrology) is crucial. I present a step in this direction.

*... this thread of ink which I have let run on for page after page, swarming with cancellations, corrections, doodles, blots and gaps, bursting at times into clear big berries, coagulating at others into piles of tiny starry seeds, then twisting away, forking off, surrounding buds of phrases with frameworks of leaves and clouds, then interweaving again, and so running on and on and on until it sputters and bursts into a last senseless cluster of words, ideas, dreams, and so ends. [Calvino, 1959, from *The Baron in the Trees*]*

## References

References annotated with † are included to acknowledge the original authors. The referenced works have not been examined due to inaccessibility of the original documents.

The number(s) within the double square brackets following each reference indicate the page(s) on which that reference is cited.

- Agassiz, L. *Études sur les glaciers*. Neuchâtel, Jent et Gassmann, 1840. [[1, 3, 117]]
- Agassiz, L. *Geological Sketches*. Second Series. James R. Osgood and Co., Boston, 1876. [[47]]
- Alley, R. B., D. D. Blankenship, C. R. Bentley, and S. T. Rooney. Deformation of till beneath Ice Stream B, West Antarctica. *Nature*, 322(6074):57–59, 1986. [[6]]
- Alley, R. B., D. D. Blankenship, C. R. Bentley, and S. T. Rooney. Till beneath Ice Stream B. 3. Till deformation: Evidence and implications. *Journal of Geophysical Research*, 92(B9):8921–8928, 1987. [[6]]
- Alley, R. B., K. M. Cuffey, E. B. Evenson, J. C. Strasser, D. E. Lawson, and G. J. Larson. How glaciers entrain and transport basal sediment: Physical constraints. *Quaternary Science Reviews*, 16(9):1017–1038, 1997. [[32, 55, 57, 58, 60, 68]]
- Alley, R. B., D. E. Lawson, E. B. Evenson, J. C. Strasser, and G. J. Larson. Glaciohydraulic supercooling: A freeze-on mechanism to create stratified, debris-rich basal ice: II. Theory. *Journal of Glaciology*, 44(148):562–568, 1998. [[57]]
- Alley, R. B. and D. R. MacAyeal. Ice-rafted debris associated with binge/purge oscillations of the Laurentide Ice Sheet. *Paleoceanography*, 9(4):503–511, 1994. [[68, 112]]
- Andersen, B. G. and A. Nesje. Quantification of Late Cenozoic glacial erosion in a fjord landscape. In Robertsson, A.-M., editor, *Quaternary Stratigraphy, Glacial Morphology and Environmental Changes*, volume Ca 81, pages 15–20. Geological Survey of Sweden, 1992. [[104, 105]]
- Anderson, R. S. A model of ablation-dominated medial moraines and the generation of debris-mantled glacier snouts. *Journal of Glaciology*, 46(154):459–469, 2000. [[6]]
- Archard, J. F. Contact and rubbing of flat surfaces. *Journal of Applied Physics*, 24:981–988, 1953. [[25]]

- Atkinson, B. K. Fracture toughness of Tennessee Sandstone and Carrara Marble using the double torsion testing method. *International Journal of Rock Mechanics and Mining Sciences & Geomechanics Abstracts*, 16:49-53, 1979. [[37]]
- Atkinson, B. K. Stress corrosion and the rate-dependent tensile failure of a fine-grained quartz rock. *Tectonophysics*, 65:281-290, 1980. [[37, 40]]
- Atkinson, B. K. Subcritical crack growth in geological materials. *Journal of Geophysical Research*, 89(B6):4077-4114, 1984. [[36, 37, 38, 40]]
- Atkinson, B. K., S. M. Dennis, P. G. Meredith, and J. Zheng. Stress corrosion and microseismic activity during tensile, shear and compressive failure of rocks<sup>†</sup>. Final technical report to the managers of the U.S. National Earthquake Hazard Reduction Program Contract No: 14-08-0001-21287, U.S. Geological Survey, Menlo Park, CA, 1984. [[38, 40]]
- Atkinson, B. K., S. M. Dennis, P. G. Meredith, and J. Zheng. Stress corrosion and microseismic activity during tensile, shear and compressive failure of rocks<sup>†</sup>. Final technical report to the managers of the U.S. National Earthquake Hazard Reduction Program Contract No: 14-08-0001-21287, U.S. Geological Survey, Menlo Park, CA, 1985. [[37, 38]]
- Atkinson, B. K. and P. G. Meredith. Experimental fracture mechanics data for rocks and minerals. In Atkinson, B. K., editor, *Fracture Mechanics of Rock*, chapter 11, pages 477-526. Academic Press Inc. (London) Ltd., 1987a. [[37, 38, 40]]
- Atkinson, B. K. and P. G. Meredith. The theory of subcritical crack growth with applications to minerals and rocks. In Atkinson, B. K., editor, *Fracture Mechanics of Rock*, chapter 4, pages 111-166. Academic Press Inc. (London) Ltd., 1987b. [[36]]
- Atkinson, B. K. and R. D. Rawlings. Acoustic emission during stress corrosion cracking in rocks. In Simpson, D. W. and P. G. Richards, editors, *Earthquake Prediction, an International Review*, volume 4 of *Maurice Ewing Ser.*, pages 605-616. American Geophysical Union, Washington, D.C., 1981. [[38, 40]]
- Augustinus, P. C. The influence of rock mass strength on glacial valley cross-profile morphometry: A case study from the Southern Alps, New Zealand. *Earth Surface Processes and Landforms*, 17:39-51, 1992. [[84]]
- Augustinus, P. C. Glacial valley cross-profile development: The influence of in situ rock stress and rock mass strength, with examples from the Southern Alps, New Zealand. *Geomorphology*, 14:87-97, 1995. [[84]]
- Bagnold, R. A. Experiments on a gravity-free dispersion of large solid spheres in a Newtonian fluid under shear. *Proceedings of the Royal Society of London. Series A*, 225:49-63, 1954. [[69]]

---

<sup>†</sup>See preamble on page 114

<sup>†</sup>See preamble on page 114

- Bagnold, R. A. The flow of cohesionless grains in fluids. *Philosophical Transactions of the Royal Society of London. Series A*, 249(964):235-297, 1956. [[69]]
- Ball, R. *The Cause of an Ice Age*. Kegan Paul, Trench, Trübner & Co. Ltd., London, 3<sup>rd</sup> edition, 1906. [[5]]
- Bell, M. and E. P. Laine. Erosion of the Laurentide region of North America by glacial and glaciofluvial processes. *Quaternary Research*, 23:154-175, 1985. [[5, 107]]
- Bell, R. Report on the country north of Lake Superior between the Nipigon and Michipicaten Rivers. In *Report of Progress, 1870-1871*, chapter 8, pages 322-351. Geological Survey of Canada, 1872. [[91]]
- Bishop, B. C. Shear moraines in the Thule area, northwest Greenland. Research report 17, SIPRE, 1957. [[59]]
- Blackwell, D. B. and J. L. Steele. Geothermal map of North America. Decade of North American geology. Map 006, Geological Society of America, Boulder, Colorado, 1992. [[75]]
- Blake, E. W. *The Deforming Bed Beneath a Surge-Type Glacier: Measurements of Mechanical and Electrical Properties*. Ph.D. thesis, University of British Columbia, 1992. [[79]]
- Blankenship, D. D., C. R. Bentley, S. T. Rooney, and R. B. Alley. Seismic measurements reveal a saturated porous layer beneath an active Antarctic ice stream. *Nature*, 322(6074):54-57, 1986. [[6]]
- Bottomley, J. T. Melting and regelation of ice. *Nature*, 5:185, 1871/72. [[57]]
- Boulton, G. S. On the origin and transport of englacial debris in Svalbard glaciers. *Journal of Glaciology*, 9(56):213-229, 1970. [[53, 60]]
- Boulton, G. S. Processes of glacial erosion on different substrata. *Journal of Glaciology*, 23(89):15-38, 1979. [[25, 29]]
- Boulton, G. S. Development of a theoretical model of sediment disposal by ice sheets. In *Prospecting in Areas of Glaciated Terrain 1984*, pages 213-223. The Institute of Mining and Metallurgy, 1984. [[61]]
- Boulton, G. S. Theory of glacial erosion, transport and deposition as a consequence of subglacial sediment deformation. *Journal of Glaciology*, 42(140):43-62, 1996. [[7]]
- Boulton, G. S., P. E. Caban, and K. van Gijssel. Groundwater flow beneath ice sheets: Part I - large scale patterns. *Quaternary Science Reviews*, 14(6):545-562, 1995. [[80, 81]]
- Boulton, G. S. and C. D. Clark. A highly mobile Laurentide ice sheet revealed by satellite images of glacial lineations. *Nature*, 346(6287):813-817, 1990. [[3]]
- Boulton, G. S. and A. S. Jones. Stability of temperate ice caps and ice sheets resting on beds of deformable sediment. *Journal of Glaciology*, 24(90):29-43, 1979. [[6]]

- Boussinesq, J. *Application des potentiels à l'étude de l'équilibre et du mouvement des solides élastiques, principalement au calcul des déformations et des pressions que produisent, dans ces solides, des efforts quelconques exercés sur une petite partie de leur surface ou de leur intérieur: mémoire suivi de notes étendues sur divers points de physique mathématique et d'analyse*. Paris: Gauthier-Villars, 1885. [[133]]
- Briner, J. P. and T. W. Swanson. Using inherited cosmogenic  $^{36}\text{Cl}$  to constrain glacial erosion rates of the Cordilleran Ice Sheet. *Geology*, 26(1):3–6, 1998. [[104]]
- Butkovich, T. R. The ultimate strength of ice. Research paper 11, SIPRE, 1954. [[49, 51]]
- Butkovich, T. R. Crushing strength of lake ice. Research paper 15, SIPRE, 1955. [[49, 51]]
- Byerlee, J. D. Friction of rocks. In Byerlee, J. D. and M. Wyss, editors, *Rock Friction and Earthquake Prediction*, Contributions to current research in geophysics; 6, pages 615–626. Basel: Birkhauser Verlag, 1978. Reprinted from *Pure and Applied Geophysics v.116*. [[30]]
- Calvino, I. *The Baron in the Trees*. Random House, 1959. Translated by A. Colquhoun. [[113]]
- Carozzi, A. V., editor. *Studies on Glaciers Preceded by the Discourse of Neuchâtel*. Hafner Publishing Company, 1967. Translation of Agassiz [1840] with additional historical notes and introduction. [[1]]
- Cerruti, V. Ricerche intorno all' equilibrio de' corpi elastici istropi. *Reale Accademia dei Lincei, Memorie della Classe di Scienze Fisiche, Matematiche e Naturali, Serie 3*, 13:81–123, 1881/82. [[138]]
- Chamberlain, T. C. Recent glacial studies in Greenland. *Geological Society of America Bulletin*, 6:199–220, 1895. [[53, 54, 59]]
- Chandler, H., editor. *Hardness Testing*. ASM International, 2<sup>nd</sup> edition, 1999. [[29]]
- Charles, R. Static fatigue of glass. *Journal of Applied Physics*, 29:1549–1560, 1958. [[36]]
- Chase, C. G. Fluvial landsculpting and the fractal dimension of topography. *Geomorphology*, 5(1–2):39–57, 1992. [[16]]
- Clague, J. J. Late Quaternary geology and geochronology of British Columbia. Part 2: Summary and discussion of radiocarbon-dated Quaternary history. Paper 80-35, Geological Survey of Canada, 1981. [[103]]
- Clague, J. J. Recognizing order in chaotic sequences of Quaternary sediments in the Canadian Cordillera. *Quaternary International*, 68–71:29–38, 2000. [[104]]
- Clark, P. U. Subglacial sediment dispersal and till composition. *Journal of Geology*, 95(4):527–541, 1987. [[61, 91]]
- Clark, P. U., J. M. Licciardi, D. R. MacAyeal, and J. W. Jenson. Numerical reconstruction of a soft-bedded Laurentide Ice Sheet during the last glacial maximum. *Geology*, 24(8):679–682, 1996. [[7, 76]]

- Clarke, G. K. C. Subglacial till: A physical framework for its properties and processes. *Journal of Geophysical Research*, 92(B9):9023-9036, 1987. [[6]]
- Clarke, G. K. C. Lumped-element analysis of subglacial hydraulic circuits. *Journal of Geophysical Research*, 101(B8):17547-17599, 1996. [[78]]
- Clarke, G. K. C. and E. W. Blake. Geometric and thermal evolution of a surge-type glacier in its quiescent state: Trapridge Glacier, Yukon Territory, Canada, 1969-89. *Journal of Glaciology*, 37(125):158-169, 1991. [[55, 60, 68]]
- Costin, L. S. and J. J. Mecholsky. Title unknown<sup>†</sup>. In *Proceedings of the 24<sup>th</sup> U.S. Symposium of Rock Mechanics*, pages 285-394. 1983. [[37, 38, 40]]
- Cox, S. J. D. and C. H. Scholz. A direct measurement of shear fracture energy in rocks. *Geophysical Research Letters*, 12(12):813-816, 1985. [[38]]
- Cuffey, K. and R. B. Alley. Is erosion by deforming subglacial sediments significant? (Towards till continuity). *Annals of Glaciology*, 22:17-24, 1996. [[28]]
- Cuffey, K. M., H. Conway, A. M. Gades, B. Hallet, R. Lorrain, J. P. Severinghaus, E. J. Steig, B. Vaughn, and J. W. C. White. Entrainment at cold glacier beds. *Geology*, 28(4):351-354, 2000. [[59]]
- Cuffey, K. M., H. Conway, B. Hallet, A. M. Gades, and C. F. Raymond. Interfacial water in polar glaciers, and glacier sliding at  $-17^{\circ}\text{C}$ . *Geophysical Research Letters*, 26(6):751-754, 1999. [[59]]
- Dansgaard, W., S. J. Hojnsen, H. B. Clausen, D. Dahljensen, N. S. Gundestrup, C. U. Hammer, C. S. Fvidberg, N. P. Steffensen, A. E. Sveinbjornsdottir, J. Jouzel, and G. Bond. Evidence for general instability of past climate from a 250-kyr ice-core record. *Nature*, 364(6434):218-220, 1993. [[75]]
- Deeley, R. M. and P. H. Parr. The Hintereis Glacier. *Philosophical Magazine. Series 6*, 27(157):153-176, 1914. [[57]]
- Der, V., D. C. Holloway, and T. Kobayashi. Techniques for dynamic fracture toughness measurements<sup>†</sup>. Report to U.S. National Science Foundation, Photomech. Lab., Mechanical Engineering Department, University of Maryland, 1978. [[38]]
- Donaldson, J. A. The Dubawnt Group, Districts of Keewatin and Mackenzie. Paper 64-20, Geological Survey of Canada, 1965. [[98, 99]]
- Drake, L. D. and R. L. Shreve. Pressure melting and regelation of ice by round wires. *Proceedings of the Royal Society of London. Series A*, 332:51-83, 1973. [[58]]

---

<sup>†</sup>See preamble on page 114

<sup>†</sup>See preamble on page 114

- Dredge, L. A. Drift carbonate on the Canadian Shield. II: Carbonate dispersal and ice-flow patterns in northern Manitoba. *Canadian Journal of Earth Science*, 25(5):783–787, 1987. [[92]]
- Dredge, L. A. and W. R. Cowan. Quaternary geology of the southwestern Canadian Shield. In Fulton, R. J., editor, *Quaternary Geology of Canada and Greenland*, volume 1 of *Geology of North America*, chapter 3, pages 214–235. Geological Survey of Canada, 1989. [[92, 93, 95]]
- Dubayah, R., E. F. Wood, and D. Lavallée. Multiscaling analysis in distributed modeling and remote sensing: An application using soil moisture. In Quattrochi, D. A. and M. F. Goodchild, editors, *Scale in Remote Sensing and GIS*, chapter 5, pages 93–112. CRC Press, 1997. [[15]]
- Dyke, A. S. Landscapes of cold-centred Late Wisconsinan ice caps, Arctic Canada. *Progress in Physical Geography*, 17(2):223–247, 1993. [[5]]
- Dyke, A. S., L. A. Dredge, and J.-S. Vincent. Configuration and dynamics of the Laurentide Ice Sheet during the Late Wisconsin maximum. *Géographie physique et Quaternaire*, 36(1–2):5–14, 1982. [[3]]
- Dyke, A. S., T. F. Morris, D. E. C. Green, and J. England. Quaternary geology of Prince of Wales Island, Arctic Canada. Memoir 433, Geological Survey of Canada, 1992. [[91]]
- Dyke, A. S. and V. K. Prest. Late Wisconsinan and Holocene history of the Laurentide Ice Sheet. *Géographie physique et Quaternaire*, 41:237–263, 1987. [[3]]
- Dyke, A. S., J.-S. Vincent, J. T. Andrews, L. A. Dredge, and W. R. Cowan. The Laurentide Ice Sheet and an introduction to the Quaternary geology of the Canadian Shield. In Fulton, R. J., editor, *Quaternary Geology of Canada and Greenland*, volume 1 of *Geology of North America*, chapter 3, pages 178–189. Geological Survey of Canada, 1989. [[107]]
- Echelmeyer, K. and W. Zhongxiang. Direct observation of basal sliding and deformation of basal drift at sub-freezing temperatures. *Journal of Glaciology*, 33(113):83–98, 1987. [[59, 60, 76]]
- Elverhøi, A., E. S. Andersen, T. Dokken, D. Hebbeln, R. Spielhagen, J. I. Svendsen, M. Sørflaten, A. Rørnes, M. Hald, and C. F. Forsberg. The growth and decay of the Late Weichselian ice sheet in western Svalbard and adjacent areas based on provenance studies of marine sediments. *Quaternary Research*, 55:303–316, 1995a. [[104]]
- Elverhøi, A., R. L. Hooke, and A. Solheim. Late Cenozoic erosion and sediment yield from the Svalbard-Barents Sea region: Implications for understanding erosion of glacierized basins. *Quaternary Science Reviews*, 17(1–3):209–241, 1998. [[5, 105]]
- Elverhøi, A., J. I. Svendsen, A. Solheim, E. S. Andersen, J. Milliman, J. Mangerud, and R. L. Hooke. Late Quaternary sediment yield from the high arctic Svalbard area. *Journal of Geology*, 103(1):1–17, 1995b. [[105]]
- EROS Data Center. US GeoData. USGS web-site, 2000. <http://edc.usgs.gov/>. [[11, 12]]

- Fischer, U. H. *Mechanical Conditions Beneath a Surge-Type Glacier*. Ph.D. thesis, University of British Columbia, 1995. [[32]]
- Flowers, G. E. *A Multicomponent Coupled Model of Glacier Hydrology*. Ph.D. thesis, University of British Columbia, 2000. [[ii, 9, 78, 79, 80, 82, 111, 112, 113]]
- Forbes, J. D. *Travels Through the Alps of Savoy and Other Parts of the Penine Chain, with Observations on the Phenomena of Glaciers*. A. and C. Black, Edinburgh, 2<sup>nd</sup> edition, 1845. [[5]]
- Freeze, R. A. and J. A. Cherry. *Groundwater*. Prentice Hall, Englewood Cliffs, N.J., 1979. [[80]]
- Fulton, R. J., compiler. *Surficial materials of Canada*. Map D1880A, Geological Survey of Canada, 1996. [[9, 84, 88, 89, 90]]
- Gemmell, A. M. D., M. J. Sharp, and D. E. Sugden. Debris from the basal ice of the Agassiz Ice Cap, Ellesmere Island, Arctic Canada. *Earth Surface Processes and Landforms*, 11(2):123-130, 1986. [[53]]
- Geophysical Data Center. GDCTOPO1. Geological Survey of Canada, 1998. [[11, 12, 22, 23]]
- Gilbert, G. K. *Glaciers and Glaciation*, volume 3 of *Harriman Alaska Series*. Smithsonian Institute, Washington, DC, 1910. [[24]]
- Glasser, N. F., M. J. Hambrey, K. R. Crawford, M. R. Bennett, and D. Huddart. The structural glaciology of Kongsvegan, Svalbard, and its role in landform genesis. *Journal of Glaciology*, 44(146):136-148, 1998. [[61]]
- Glen, J. W. The creep of polycrystalline ice. *Proceedings of the Royal Society of London. Series A*, 228:519-538, 1955. [[74]]
- Goldthwait, R. P. Development of end moraines in east-central Baffin Island. *Journal of Geology*, 59(6):567-577, 1951. [[59]]
- Goodwin, I. D. Basal ice accretion and debris entrainment within the coastal ice margin, Law Dome, Antarctica. *Journal of Glaciology*, 39(131):157-166, 1993. [[55]]
- Goran, S. L. The normal force exerted by creeping flow on a small sphere touching a plane. *Journal of Fluid Mechanics*, 41(3):619-625, 1970. [[26]]
- Gow, A. J., S. Epstein, and W. Sheeny. On the origin of stratified debris in ice cores from the bottom of the Antarctic Ice Sheet. *Journal of Glaciology*, 23(89):185-192, 1979. [[55, 56]]
- Gow, A. J. and D. A. Meese. Nature of basal debris in the GISP2 and Byrd ice cores and its relevance to bed processes. *Annals of Glaciology*, 22:134-140, 1996. [[53, 55]]
- Gradshteyn, I. S. and I. M. Ryzhik. *Table of Integrals, Series, and Products*. Academic Press, 4<sup>th</sup> edition, 1965. [[136]]

- Gravenor, C. P. Erosion by continental ice sheets. *American Journal of Science*, 275(5):595-604, 1975. [[107]]
- Hallet, B. A theoretical model of glacial abrasion. *Journal of Glaciology*, 23(3):22-25, 1979. [[ii, 25, 26, 28, 30]]
- Hallet, B. Glacial abrasion and sliding: Their dependence on the debris concentration in basal ice. *Annals of Glaciology*, 2:23-28, 1981. [[ii, 25, 26, 28, 30, 110]]
- Hallet, B. Glacial quarrying: A simple theoretical model. *Annals of Glaciology*, 22:1-8, 1996. [[35, 43, 48, 49, 52]]
- Hallet, B., L. Hunter, and J. Bogen. Rates of erosion and sediment evacuation by glaciers: A review of field data and their implications. *Global and Planetary Change*, 12:213-235, 1996. [[5, 105, 111]]
- Hambrey, M. J., M. R. Bennett, J. A. Dowdeswell, N. F. Glasser, and D. Huddart. Debris entrainment and transfer in polythermal valley glaciers. *Journal of Glaciology*, 45(149):69-86, 1999. [[53, 60]]
- Hambrey, M. J., J. A. Dowdeswell, T. Murray, and P. R. Porter. Thrusting and debris entrainment in a surging glacier: Bakaninbreen, Svalbard. *Annals of Glaciology*, 22:241-248, 1996. [[60, 68]]
- Harbor, J. M. Numerical modeling of the development of U-shaped valleys by glacial erosion. *Geological Society of America Bulletin*, 104:1364-1375, 1992. [[24]]
- Harbor, J. M. Development of glacial-valley cross sections under conditions of spatially variable resistance to erosion. *Geomorphology*, 14:99-107, 1995. [[84]]
- Hart, J. K. An investigation of the deforming layer/debris-rich basal-ice continuum, illustrated from three Alaskan glaciers. *Journal of Glaciology*, 41(139):619-633, 1995. [[60]]
- Hart, J. K. and R. I. Waller. An investigation of the debris-rich basal ice from Worthington Glacier, Alaska, U.S.A. *Journal of Glaciology*, 45(149):54-62, 1999. [[61]]
- Hay, W. W. Detrital sediment fluxes from continents to oceans. *Chemical Geology*, 145(3-4):287-323, 1998. [[107]]
- Hay, W. W., C. A. Shaw, and C. N. Wold. Mass-balanced paleogeographic reconstructions. *Geologische Rundschau*, 78(1):207-242, 1989. [[107]]
- Henry, J.-P. and J. Paquet. Mécanique de la rupture de roches calcitiques. *Bulletin de la Société géologique de France, Série 7*, 18(6):1573-1582, 1976. [[40]]
- Herron, S. and C. C. Langway, Jr. The debris-laden ice at the bottom of the Greenland Ice Sheet. *Journal of Glaciology*, 23(89):193-207, 1979. [[56]]

- Hetényi, M. A method of solution for the elastic quarter-plane. *Journal of Applied Mechanics*, 27:289–296, 1960. [[52]]
- Ho, B. P. and L. G. Leal. Inertial migration of rigid spheres in two-dimensional unidirectional flows. *Journal of Fluid Mechanics*, 65:365–400, 1974. [[148]]
- Holm, R. *Electric Contacts*. Almqvist and Wiksells, Stockholm, 1946. [[25]]
- Hooke, R. L. Flow near the margin of the Barnes Ice Cap, and the development of ice-cored moraines. *Geological Society of America Bulletin*, 84:3929–3948, 1973. [[59]]
- Hooke, R. L. and N. R. Iverson. Grain-size distribution in deforming subglacial tills: Role of grain fracture. *Geology*, 23(1):57–60, 1995. [[32]]
- Hubbard, B. and M. Sharp. Basal ice formation and deformation: A review. *Progress in Physical Geography*, 13(4):529–558, 1989. [[55]]
- Hubbard, B. and M. Sharp. Weertman regelation, multiple refreezing events and the isotopic evolution of the basal ice layer. *Journal of Glaciology*, 39(132):275–291, 1993. [[56, 57]]
- Hubbard, B. and M. Sharp. Basal ice facies and their formation in the western Alps. *Arctic and Alpine Research*, 27(4):301–310, 1995. [[57, 61]]
- Hubbard, B., M. Sharp, and W. J. Lawson. On the sedimentological character of Alpine basal ice facies. *Annals of Glaciology*, 22:187–193, 1996. [[32, 33]]
- Hudleston, P. J. Recumbent folding in the base of the Barnes Ice Cap, Baffin Island, Northwest Territories, Canada. *Geological Society of America Bulletin*, 87(12):1684–1692, 1976. [[61, 68]]
- Ingraffea, A. R. Title unknown<sup>†</sup>. In *Proceedings of the 22<sup>th</sup> U.S. Symposium of Rock Mechanics*, pages 186–191. MIT, Cambridge, MA, 1981. [[38]]
- Ingraffea, A. R. and P. A. Wawrzynek. FRANC2D: A case study in transfer of software technology. In Colville, A. and A. Amde, editors, *Research Transformed into Practice: Implementations of NSF Research*, pages 233–344. ASCE Press, New York, 1995. [[41]]
- Ingraffea, A. R., P. A. Wawrzynek, and B. J. Carter. FRANC2D. Cornell Fracture Group web-site, 1997. <http://www.cfg.cornell.edu/software/FRANC2D.html>. [[41]]
- Iverson, N. R. Laboratory simulations of glacial abrasion: Comparisons with theory. *Journal of Glaciology*, 36(124):304–313, 1990. [[25, 28, 30]]
- Iverson, N. R. Potential effects of subglacial water-pressure fluctuations on quarrying. *Journal of Glaciology*, 37(125):27–36, 1991. [[35, 43, 48]]
- Iverson, N. R. Regelation of ice through debris at glacier beds: Implications for sediment transport. *Geology*, 21(6):559–562, 1993. [[58]]

---

<sup>†</sup>See preamble on page 114

- Iverson, N. R. Sediment entrainment by a soft-bedded glacier: A model based on regelation into the bed. *Earth Surface Processes and Landforms*, 25(8):881–893, 2000. [[63]]
- Iverson, N. R. and D. J. Semmens. Intrusion of ice porous media by regelation: A mechanism of sediment entrainment by glaciers. *Journal of Geophysical Research*, 100(B7):10219–10230, 1995. [[ii, 58, 112]]
- Iverson, N. R. and R. Souchez. Isotopic signature of debris-rich ice formed by regelation into a subglacial sediment bed. *Geophysical Research Letters*, 23(10):1151–1154, 1996. [[58]]
- Jaeger, J. C. and N. G. W. Cook. *Fundamentals of Rock Mechanics*, chapter 3. Chapman and Hall Ltd, 3<sup>rd</sup> edition, 1979. [[30, 38]]
- Jansen, E., T. Fronval, F. Rack, and J. E. T. Channell. Pliocene-Pleistocene ice rafting history and cyclicity in the Nordic seas during the last 3.5 Myr. *Paleoceanography*, 15(6):709–721, 2000. [[105]]
- Jansen, E. and J. Sjøholm. Reconstruction of glaciation over the past 6 Myr from ice-borne deposits in the Norwegian Sea. *Nature*, 349(6310):600–603, 1991. [[105]]
- Jenson, J. W., P. U. Clark, D. R. MacAyeal, C. Ho, and J. C. Vela. Numerical modeling of advective transport of saturated deforming sediment beneath the Lake Michigan Lobe, Laurentide Ice Sheet. *Geomorphology*, 14:157–166, 1995. [[6, 7]]
- Jenson, J. W., D. R. MacAyeal, P. U. Clark, C. L. Ho, and J. C. Vela. Numerical modeling of subglacial sediment deformation: Implications for the behavior of the Lake Michigan Lobe, Laurentide Ice Sheet. *Journal of Geophysical Research*, 101(B4):8717–8728, 1996. [[7, 76]]
- Jenssen, D. A three-dimensional polar ice sheet model. *Journal of Glaciology*, 18:373–389, 1977. [[75]]
- Jouzel, J. and R. A. Souchez. Melting–refreezing at the glacier sole and the isotopic composition of the ice. *Journal of Glaciology*, 28(98):35–42, 1982. [[55]]
- Kachanov, M. and J. P. Laures. Three-dimensional problems of strongly interacting arbitrarily located penny-shaped cracks. *International Journal of Fracture*, 41:289–331, 1989. [[36]]
- Kahaner, D., C. Moler, and S. Nash. *Numerical Methods and Software*. Prentice Hall, 1989. [[70]]
- Kalnay, E., M. Kanamitsu, R. Kistler, W. Collins, D. Deaven, L. Gandin, M. Iredell, S. Saha, G. White, J. Woollen, Y. Zhu, M. Chelliah, W. Ebisuzaki, W. Higgins, J. Janowiak, K. C. Mo, C. Ropelewski, J. Wang, A. Leetmaa, R. Reynolds, R. Jenne, and D. Joseph. The NCEP/NCAR 40-year reanalysis project. *Bulletin of the American Meteorological Society*, 77(3):437–471, 1996. [[75]]
- Kamb, B. Glacier surge mechanism based on linked cavity configuration of the basal water conduit system. *Journal of Geophysical Research*, 92(B10):16585–16595, 1987. [[78]]

- Karrow, P. F. Carbonates, granulometry, and color of tills on the south-central Canadian Shield and their implications for stratigraphy and radiocarbon dating. *Boreas*, 21:379–391, 1992. [[92, 93]]
- Karrow, P. F. and R. S. Geddes. Drift carbonate on the Canadian Shield. *Canadian Journal of Earth Science*, 24(2):365–369, 1987. [[93]]
- Kaszycki, C. A. and W. W. Shilts. Glacial erosion of the Canadian Shield — calculation of average depths. Technical record TR-106, Atomic Energy of Canada Limited, 1980. [[99, 108]]
- Kauranne, L. K. History of soil geochemical prospecting. In Govett, G. J. S., editor, *Regolith Exploration Geochemistry in Arctic and Temperate Terrains*, volume 5 of *Handbook of Exploration Geochemistry*, chapter 1, pages 3–6. Elsevier, 1992. [[113]]
- Kavanaugh, J. L. *Hydromechanical Behavior of a Surge-Type Glacier: Trapridge Glacier, Yukon Territory, Canada*. Ph.D. thesis, University of British Columbia, 2000. [[7, 79]]
- Kerr, F. A. Glaciation in northern British Columbia. *Transactions of the Royal Society of Canada, Series 3*, 28:17–31, 1934. [[103]]
- Kleman, J. Preservation of landforms under ice sheets and ice caps. *Geomorphology*, 9(1):19–32, 1994. [[5]]
- Knight, P. G. Stacking of basal debris layers without bulk freezing-on: Isotopic evidence from west Greenland. *Journal of Glaciology*, 35(120):214–216, 1989. [[61]]
- Knight, P. G. Two-facies interpretation of the basal layer of the Greenland ice sheet contributes to a unified model of basal ice formation. *Geology*, 22(11):971–974, 1994. [[33, 56, 57, 61]]
- Knight, P. G. The basal ice layer of glaciers and ice sheets. *Quaternary Science Reviews*, 16(9):975–993, 1997. [[53, 55]]
- Knight, P. G. and D. A. Knight. Glacier sliding, regelation water flow and development of basal ice. *Journal of Glaciology*, 40(136):600–601, 1994. [[57]]
- Knight, P. G. and D. A. Knight. Experimental observations of subglacial debris entrainment into the vein network of polycrystalline ice. *Glacial Geology and Geomorphology*, 1999. <http://boris.qub.ac.uk/ggg/papers/full/1999/rp051999/rp05.html>. [[57]]
- Kobranova, V. N. *Petrophysics*. Mir Publishers, 1989. Translated from the Russian by V.V. Kuznetsov. [[30]]
- Krumbein, W. C. Sediments and exponential curves. *Journal of Geology*, 45(6):577–601, 1937. [[61]]
- Laine, E. P. New evidence from beneath western North Atlantic for the depth of glacial erosion in Greenland and North America. *Quaternary Research*, 14:188–198, 1980. [[5, 107]]
- Laine, E. P. Reply to Andrew's comment. *Quaternary Research*, 17:125–127, 1982. [[107]]

- Lavallée, D., S. Lovejoy, D. Schertzer, and P. Ladoy. Nonlinear variability of landscape topography: Multifractal analysis and simulation. In Lam, N. S.-N. and L. de Cola, editors, *Fractals in Geography*, chapter 8, pages 158–192. PRT Prentice-Hall, 1993. [[16]]
- Lawn, B. R. and T. R. Wilshaw. *Fracture of Brittle Solids*. Cambridge University Press, 1975. [[35]]
- Lawson, D. E. Sedimentological analysis of the Western terminus region of the Matanuska Glacier. Technical report 79-9, CRREL, 1979. [[33]]
- Lawson, D. E. and J. B. Kulla. An oxygen isotope investigation of the origin of the basal zone of the Matanuska Glacier, Alaska. *Journal of Geology*, 86:673–685, 1978. [[53]]
- Lawson, D. E., J. C. Strasser, E. B. Evenson, R. B. Alley, G. J. Larson, and S. A. Arcone. Glaciohydraulic supercooling: A freeze-on mechanism to create stratified, debris-rich basal ice: I. Field evidence. *Journal of Glaciology*, 44(148):547–561, 1998. [[57]]
- Legate, D. R. and C. J. Willmott. Mean seasonal and spatial variability in gauge-corrected global precipitation. *International Journal of Climatology*, 10(2):111–127, 1990. [[75]]
- Lidmar-Bergström, K. A long-term perspective on glacial erosion. *Earth Surface Processes and Landforms*, 22(3):297–306, 1997. [[107]]
- Lin, S.-J. and R. B. Rood. Multidimensional flux-form semi-Lagrangian transport schemes. *Monthly Weather Review*, 124(9):2046–2070, 1996. [[71]]
- Lindström, E. Are roches moutonnées mainly periglacial forms? *Geografiska Annaler*, 70A(4):323–331, 1988. [[35]]
- Lliboutry, L. Contribution à la théorie du frottement du glacier sur son lit. *Comptes Rendus Hebdomadaires des Séances de l'Académie des Science*, 247(3):318–320, 1958. [[47]]
- Lliboutry, L. General theory of subglacial cavitation and sliding of temperate glaciers. *Journal of Glaciology*, 7(49):21–58, 1968. [[47]]
- Lliboutry, L. Internal melting and ice accretion at the bottom of temperate glaciers. *Journal of Glaciology*, 39(131):50–64, 1993. [[56, 57]]
- Lorrain, R. D., R. A. Souchez, and J.-L. Tison. Characteristics of basal ice from two outlet glaciers in the Canadian Arctic — implications for glacier erosion. In *Current Research, Part B*, Paper 81-1B, pages 137–144. Geological Survey of Canada, 1981. [[61]]
- MacGregor, K. R., R. S. Anderson, S. P. Anderson, and E. D. Waddington. Numerical simulations of glacial-valley longitudinal profile evolution. *Geology*, 28(11):1031–1034, 2000. [[11, 24]]
- Mahaffy, M. W. A three-dimensional numerical model of ice sheets: Tests on the Barnes Ice Cap, Northwest Territories. *Journal of Geophysical Research*, 81:1059–1066, 1976. [[74]]

- Mark, D. M. and P. B. Aronson. Scale-dependent fractal dimensions of topographic surfaces: An empirical investigation, with applications in geomorphology and computer mapping. *Mathematical Geology*, 16, 1984. [[16]]
- Marshall, S. J. *Modelling Laurentide Ice Stream Thermodynamics*. Ph.D. thesis, University of British Columbia, 1996. [[ii, 9, 74, 111]]
- Marshall, S. J. and G. K. C. Clarke. A continuum mixture model of ice stream thermomechanics in the Laurentide Ice Sheet. 1. Theory. *Journal of Geophysical Research*, 102(B9):20599–20613, 1997a. [[ii, 7, 74, 76, 111]]
- Marshall, S. J. and G. K. C. Clarke. A continuum mixture model of ice stream thermomechanics in the Laurentide Ice Sheet. 2. Application to the Hudson Strait Ice Stream. *Journal of Geophysical Research*, 102(B9):20615–20637, 1997b. [[ii, 7, 74, 76, 111]]
- Marshall, S. J. and G. K. C. Clarke. Modeling North American freshwater runoff through the last glacial cycle. *Quaternary Research*, 52(3):300–315, 1999. [[82]]
- Marshall, S. J., G. K. C. Clarke, A. S. Dyke, and D. A. Fisher. Topographic and geologic controls on fast flow in the Laurentide and Cordilleran Ice Sheets. *Journal of Geophysical Research*, 101(B8):17827–17840, 1996. [[76]]
- Marshall, S. J., L. Tarasov, G. K. C. Clarke, and W. R. Peltier. Glaciological reconstruction of the Laurentide Ice Sheet: Physical processes and modelling challenges. *Canadian Journal of Earth Science*, 37(5):769–793, 2000. [[ii, 7, 74, 75, 76, 111]]
- McFarlane, N. A., G. J. Boer, J.-P. Blanchet, and M. Lazare. The Canadian Climate Centre second generation general circulation model and its equilibrium climate. *Journal of Climate*, 5(10):1013–1044, 1992. [[75]]
- Meredith, P. G. and B. K. Atkinson. Stress corrosion and acoustic emission during tensile crack propagation in Whin Sill Dolerite and other basic rocks. *Geophysical Journal of the Royal Astronomical Society*, 75(1):1–21, 1983. [[38, 40]]
- Meredith, P. G. and B. K. Atkinson. Fracture toughness and subcritical crack growth during high-temperature tensile deformation of Westerly Granite and black gabbro. *Physics of the Earth and Planetary Interiors*, 39(1):33–51, 1985. [[38]]
- Meredith, P. G., B. K. Atkinson, and N. B. Hillman. *Progress in Experimental Petrology*<sup>†</sup>, pages 228–232. Number 25 in NERC Pubs. Ser. D. Natural Environmental Research Council, Swindon, England, 1984. [[37, 38]]
- Metcalf, R. C. Energy dissipation during subglacial abrasion at Nisqually Glacier, Washington U.S.A. *Journal of Glaciology*, 23(89):233–246, 1979. [[30]]

---

<sup>†</sup>See preamble on page 114

- Morland, L. W. and G. S. Boulton. Stress in an elastic hump: The effects of glacier flow over elastic bedrock. *Proceedings of the Royal Society of London. Series A*, 344(1637):157-173, 1975. [[35, 41, 45]]
- Morland, L. W. and E. M. Morris. Stress in an elastic bedrock hump due to glacier flow. *Journal of Glaciology*, 18(78):67-75, 1977. [[35, 41, 45]]
- Mott, B. W. *Micro-indentation Hardness Testing*. Butterworths Scientific Pub., London, 1956. [[29]]
- Müller, R. The performance of classical versus modern finite-volume advection schemes for atmospheric modeling in a one-dimensional test-bed. *Monthly Weather Review*, 120(7):1407-1415, 1992. [[71]]
- Nesje, A., S. O. Dahl, V. Valen, and J. Øvstedal. Quaternary erosion in the Sognefjord drainage basin, western Norway. *Geomorphology*, 5:511-520, 1992. [[104, 105]]
- Nesje, A. and I. M. Whillans. Erosion of Sognefjord, Norway. *Geomorphology*, 9:33-45, 1994. [[5, 104, 105]]
- NOAA. Data Announcement 88-MGG-02, Digital relief of the surface of the Earth. National Geophysical Data Center, Boulder, Colorado, 1988. [[22, 23]]
- Nye, J. F. The flow law of ice from measurements in glacier tunnels, laboratory experiments and the jungfraufirn borehole experiment. *Proceedings of the Royal Society of London. Series A*, 219(1139):477-489, 1953. [[47]]
- Nye, J. F. Water flow in glaciers: Jökulhlaups, tunnels and veins. *Journal of Glaciology*, 17(76):181-207, 1976. [[78]]
- Oerlemans, J. Numerical experiments on large-scale glacial erosion. *Zeitschrift für gletscherkunde und glazialgeologie*, 20:107-126, 1985. [[11, 24]]
- Ohnaka, M. Frictional characteristics of typical rocks. *Journal of the Physics of the Earth*, 23:87-112, 1975. [[30]]
- O'Neill, M. E. A sphere in contact with a plane wall in a slow linear shear flow. *Chemical Engineering Science*, 23(11):1293-1298, 1968. [[27]]
- Ornstein, L. S. On the motion of a metal wire through a lump of ice. *Proceedings of the Koninklijke Nederlandse Akademie van Wetenschappen te Amsterdam. Part 2*, 8:653-659, 1906. [[57]]
- Parent, M., S. J. Paradis, and A. Doiron. Palimpsest glacial dispersal trains and their significance for drift prospecting. *Journal of Geochemical Exploration*, 56:123-140, 1996. [[61]]
- Paterson, W. S. B. *The Physics of Glaciers*. Elsevier Science Ltd, 3<sup>rd</sup> edition, 1994. [[26, 51, 65, 77]]

- Paterson, W. S. B., R. M. Koerner, D. Fisher, S. J. Johnsen, H. B. Clausen, W. Dansgaard, P. Bucher, and H. Oeschger. An oxygen-isotope climate record from the Devon Island Ice Cap, arctic Canada. *Nature*, 266(5602):508–511, 1977. [[61]]
- Payne, A. J. Limit cycles in the basal thermal regime of ice sheets. *Journal of Geophysical Research*, 100(B3):4249–4263, 1995. [[75, 76]]
- Payne, A. J. and D. J. Baldwin. Analysis of ice-flow instabilities identified in the EISMINT intercomparison exercise. *Annals of Glaciology*, 30:204–210, 2000. [[76]]
- Payne, A. J., P. Huybrechts, A. Abe-Ouchi, R. Calov, J. L. Fastook, R. Greve, S. J. Marshall, I. Marsiat, C. Ritz, L. Tarasov, and M. P. A. Thomassen. Results from the EISMINT model intercomparison: The effects of thermomechanical coupling. *Journal of Glaciology*, 46(153):227–238, 2000. [[76]]
- Peltier, W. R. Ice-age paleotopography. *Science*, 265(5197):195–201, 1994. [[4, 76]]
- Peltier, W. R. Mantle viscosity and ice-age ice sheet topography. *Science*, 273(5280):1359–1364, 1996. [[4, 76]]
- Philip, J. R. Thermal fields during regelation. *Cold Regions Science and Technology*, 3:193–203, 1980. [[58]]
- Piotrowski, J. A. Subglacial hydrology in north-western Germany during the last glaciation: Groundwater flow, tunnel valleys and hydrological cycles. *Quaternary Science Reviews*, 16(2):169–185, 1997. [[80, 81]]
- Prather, M. J. Numerical advection by conservation of second-order moments. *Journal of Geophysical Research*, 91(D6):6671–6681, 1986. [[viii, 71, 72, 73, 112]]
- Prest, V. K. and E. Nielsen. The Laurentide Ice Sheet and long-distance transport. In Kujan-suu, R. and M. Saarnisto, editors, *INQUA Till Symposium*, Special Paper 3, pages 91–101. Geological Survey of Finland, 1987. [[6]]
- Puranen, R. Modelling of glacial transport of basal tills in Finland. Report of Investigation 81, Geological Survey of Finland, 1988. [[24]]
- Rabinowicz, E. *Friction and Wear of Materials*. John Wiley & Sons, 2<sup>nd</sup> edition, 1995. [[24, 25, 30]]
- Reames, F. M. and T. H. Zapotocny. Inert trace constituent in sigma and hybrid isentropic-sigma models. Part I: Nine advection algorithms. *Monthly Weather Review*, 127(2):173–187, 1999a. [[71]]
- Reames, F. M. and T. H. Zapotocny. Inert trace constituent in sigma and hybrid isentropic-sigma models. Part II: Twelve semi-Lagrangian algorithms. *Monthly Weather Review*, 127(2):188–200, 1999b. [[71]]

- Reynolds, O. Dilatancy of media composed of rigid particles in contact. *Philosophical Magazine. Series 5*, 20:469–481, 1885. [[69]]
- Rice, J. R. Thermodynamics of the quasi-static growth of Griffith cracks. *Journal of the mechanics and physics of solids*, 26:61–78, 1978. [[36]]
- Riis, F. and W. Fjeldskaar. On the magnitude of the Late Tertiary and Quaternary erosion and its significance for the uplift of Scandinavia and the Barents Sea. In Larsen, R. M., H. Brekke, B. T. Larsen, and E. Talleraas, editors, *Structural and Tectonic Modelling and its Application to Petroleum Geology*, 1, pages 163–185. Elsevier, 1992. [[105]]
- Röthlisberger, H. Water pressure in intra- and subglacial channels. *Journal of Glaciology*, 11(62):177–203, 1972. [[78]]
- Scholz, C. H. Wear and gouge formation in brittle faulting. *Geology*, 15:493–495, 1987. [[30]]
- Segall, P. Rate-dependent extensional deformation resulting from crack growth in rock. *Journal of Geophysical Research*, 89(B6):4185–4195, 1984. [[36]]
- Shackleton, N. J., A. Berger, and W. R. Peltier. An alternative astronomical calibration of the lower Pleistocene timescale based on ODP site 677. *Transactions of the Royal Society of Edinburgh - Earth Sciences*, 81:251–261, 1990. [[2]]
- Sharp, M., J. Jouzel, B. Hubbard, and W. Lawson. The character, structure and origin of the basal ice layer of a surge-type glacier. *Journal of Glaciology*, 40(135):327–340, 1994. [[57, 61]]
- Sharp, M., W. Lawson, and R. S. Anderson. Tectonic processes in a surge-type glacier. *Journal of Structural Geology*, 10(5):499–515, 1988. [[60]]
- Shaw, J. A meltwater model for Laurentide subglacial landscapes. In McCann, S. B. and D. C. Ford, editors, *Geomorphology sans frontières*, pages 181–239. Wiley, 1996. [[79]]
- Shaw, J., R. B. Rains, R. Eyton, and L. Weissling. Laurentide subglacial outburst floods: Landform evidence from digital elevation models. *Canadian Journal of Earth Science*, 8(33):1154–1168, 1996. [[79]]
- Shilts, W. W. Flow patterns in the central North American ice sheet. *Nature*, 286:213–218, 1980. [[91, 92, 98]]
- Shilts, W. W., C. M. Cunningham, and C. A. Kaszycki. Keewatin Ice Sheet—re-evaluation of the traditional concept of the Laurentide Ice Sheet. *Geology*, 7:537–541, 1979. [[98, 99, 100]]
- Shreve, R. L. Glacier sliding at subfreezing temperatures. *Journal of Glaciology*, 30(106):341–347, 1984. [[59, 76]]
- Souchez, R., M. Lemmens, and J. Chappellaz. Flow-induced mixing in the GRIP basal ice deduced from the CO<sub>2</sub> and CH<sub>4</sub> records. *Geophysical Research Letters*, 22(1):41–44, 1995. [[68]]

- Souchez, R., R. Lorrain, J. L. Tison, and J. Jouzel. Co-isotopic signature of two mechanisms of basal-ice formation in Arctic outlet glaciers. *Annals of Glaciology*, 10:163–166, 1988. [[57]]
- Souchez, R. A. The formation of shear moraines: An example from south Victoria Land, Antarctica. *Journal of Glaciology*, 6(48):837–843, 1967. [[59]]
- Souchez, R. A. and J. Jouzel. On the isotopic composition in  $\delta D$  and  $\delta^{18}O$  of water and ice during freezing. *Journal of Glaciology*, 30(106):369–372, 1984. [[55]]
- Souchez, R. A., J.-L. Tison, R. Lorrain, M. Lemmens, L. Janssens, M. Stievenard, J. Jouzel, A. Sveinbjörnsdóttir, and S. J. Johnsen. Stable isotopes in the basal silty ice preserved in the Greenland Ice Sheet at Summit: Environmental implications. *Geophysical Research Letters*, 21(8):693–696, 1994. [[55]]
- Strasser, J. C., D. E. Lawson, G. J. Larson, E. B. Evenson, and R. B. Alley. Preliminary results of tritium analyses in basal ice, Matanuska Glacier, Alaska, U.S.A.: Evidence for subglacial ice accretion. *Annals of Glaciology*, 22:126–133, 1996. [[53]]
- Sugden, D. E. A case against deep erosion of shield by ice sheets. *Geology*, 4(10):580–582, 1976. [[107]]
- Sugden, D. E. Glacial erosion by the Laurentide Ice Sheet. *Journal of Glaciology*, 20(83):367–391, 1978. [[5]]
- Sugden, D. E., P. G. Knight, N. Livesey, R. D. Lorrain, R. A. Souchez, J.-L. Tison, and J. Jouzel. Evidence for two zones of debris entrainment beneath the Greenland Ice Sheet. *Nature*, 328(6127):238–241, 1987. [[56, 57]]
- Swanson, P. L. *Stress Corrosion Cracking in Westerly Granite: An Examination by the Double Torsion Method*<sup>†</sup>. Master's thesis, University of Colorado, Boulder, 1980. [[38, 40]]
- Swanson, P. L. Subcritical crack growth and other time- and environment- dependent behavior in crustal rocks. *Journal of Geophysical Research*, 89(B6):4137–4152, 1984. [[39]]
- Taylor, K., C. U. Hammer, R. B. Alley, H. B. Clausen, D. Dahl-Jensen, A. J. Gow, N. S. Gundestrup, J. Kipfstul, J. C. Moore, and E. D. Waddington. Electrical conductivity measurements from the GISP2 and GRIP Greenland ice cores. *Nature*, 366(6455):549–552, 1993. [[61, 68]]
- Thomson, J. On recent theories and experiments regarding ice at or near its melting-point. *Proceedings of the Royal Society of London*, 10:152–160, 1859/60. [[57]]
- Tison, J.-L., J.-R. Petit, J.-M. Barnola, and W. C. Mahaney. Debris entrainment at the ice-bedrock interface in sub-freezing temperature conditions (Terre Adélie, Antarctica). *Journal of Glaciology*, 39(132):303–315, 1993. [[60]]

---

<sup>†</sup> See preamble on page 114

- Tison, J.-L., R. Souchez, and R. Lorrain. On the incorporation of unconsolidated sediments in basal ice: Present-day examples. *Zeitschrift für Geomorphologie. Supplement*, 72:173-183, 1989. [[56, 60, 61]]
- Tulley, M. J. C. *Numerical Modelling of Erosion and Deposition Beneath Quaternary Ice Sheets*. Ph.D. thesis, University of Cambridge, 1995. [[11, 24, 32, 61]]
- van der Meer, J. J. M. Particle and aggregate mobility in till: Microscopic evidence of subglacial processes. *Quaternary Science Reviews*, 16:827-831, 1997. [[143]]
- van Weert, F. H. A., K. van Gijssel, A. Leijnse, and G. S. Boulton. The effects of Pleistocene glaciations on the geohydrological system of Northwest Europe. *Journal of Hydrology*, 195(1-4):137-159, 1997. [[80, 81]]
- Vettoretti, G., W. R. Peltier, and N. A. McFarland. Global water balance and atmospheric water vapour transport at Last Glacial maximum. *Canadian Journal of Earth Science*, 37(5):695-723, 2000. [[75]]
- Walder, J. S. Stability of sheet flow of water beneath temperate glaciers and implications for glacier surging. *Journal of Glaciology*, 28(99):273-293, 1982. [[78]]
- Walder, J. S. Hydraulics of subglacial cavities. *Journal of Glaciology*, 32(112):439-445, 1986. [[47, 78]]
- Waller, R. I., J. K. Hart, and P. G. Knight. The influence of tectonic deformation on facies variability in stratified debris-rich basal ice. *Quaternary Science Reviews*, 19(8):775-786, 2000. [[61, 68]]
- Watts, P. A. *Inclusions in Ice*. Ph.D. thesis, University of Bristol, 1974. [[26]]
- Waza, T., K. Kurita, and H. Mizutani. The effect of water on the subcritical crack growth in silicate rocks. *Tectonophysics*, 67:25-34, 1980. [[40]]
- Weertman, J. On the sliding of glaciers. *Journal of Glaciology*, 3(21):33-38, 1957. [[56, 57]]
- Weertman, J. Mechanism for the formation of inner moraines found near the edge of cold ice caps and ice sheets. *Journal of Glaciology*, 3(30):965-978, 1961. [[56, 59]]
- Weertman, J. The theory of glacier sliding. *Journal of Glaciology*, 5(39):287-303, 1964. [[26]]
- Weertman, J. Diffusion law for the dispersion of hard particles in an ice matrix that undergoes simple shear deformation. *Journal of Glaciology*, 7(50):161-165, 1968. [[69, 112]]
- Weertman, J. General theory of water flow at the base of a glacier or ice sheet. *Reviews of Geophysics and Space Science*, 10(1):287-333, 1972. [[78]]
- Weertman, J. and G. E. Birchfield. Basal water film, basal water pressure, and velocity of travelling waves on glaciers. *Journal of Glaciology*, 29(101):20-27, 1983. [[78]]

- Wheeler, J. O., P. F. Hoffman, K. D. Card, A. Davidson, B. V. Sanford, A. V. Okulitch, and W. R. Roest, compilers. Geological map of Canada. Map D1860A, Geological Survey of Canada, 1997. [[9, 84, 85, 86, 87, 91, 93, 98, 99, 110, 112]]
- White, W. A. Deep erosion by continental ice sheets. *Geological Society of America Bulletin*, 83:1037-1056, 1972. [[107]]
- White, W. A. More on deep glacial erosion by continental ice sheets and their tongues of distributary ice. *Quaternary Research*, 30:137-150, 1988. [[107]]
- Wright, G. M. Geological notes on eastern District of Mackenzie Northwest Territories. Paper 56-10, Geological Survey of Canada, 1957. [[99]]
- Xiaozhen, G. and L. Xiaoen. Application and numerical experiments with a highly-accurate advection scheme in a regional transfer model. *Meteorology and Atmospheric Physics*, 66(3-4):131-142, 1998. [[71]]
- Yoshioka, N. Fracture energy and the variation of gouge and surface roughness during frictional sliding of rocks. *Journal of the Physics of the Earth*, 34:335-355, 1986. [[30]]
- Zdanowicz, C. M., F. A. Michel, and W. W. Shilts. Basal debris entrainment and transport in glaciers of southwestern Bylot Island, Canadian Arctic. *Annals of Glaciology*, 22:107-113, 1996. [[56]]
- Zoltai, S. C. Glacial features of the Quetico-Nipigon area, Ontario. *Canadian Journal of Earth Science*, 2(4):247-269, 1965. [[93]]

# Appendix A

## 2D Stress

### A.1 Evaluation of state of stress

#### A.1.1 Normal loading

Consider an infinite line of force  $\bar{F}^N$  with no variation in the  $\hat{y}$  direction acting normally to the surface of a solid at  $z = 0$ , with the solid extending  $\rightarrow \infty \hat{z}$  (see Figure A.1). The stress due to this force is given by the following response functions, which are the two dimensional version of the Boussinesq solution for a normal load on a half-space [*Boussinesq*, 1885]<sup>1</sup>. These define  $G_{ab}^\perp$  the Green's functions for a line source,

$$\sigma_{xx} = -\frac{2\bar{F}^N}{\pi} \frac{x^2 z}{r^4} \quad \implies \quad G_{xx}^\perp = -\frac{2}{\pi} \frac{x^2 z}{r^4}, \quad (\text{A.1a})$$

$$\sigma_{zz} = -\frac{2\bar{F}^N}{\pi} \frac{z^3}{r^4} \quad \implies \quad G_{zz}^\perp = -\frac{2}{\pi} \frac{z^3}{r^4}, \quad (\text{A.1b})$$

$$\sigma_{xz} = -\frac{2\bar{F}^N}{\pi} \frac{z^2 x}{r^4} \quad \implies \quad G_{xz}^\perp = -\frac{2}{\pi} \frac{x z^2}{r^4}, \quad (\text{A.1c})$$

$$\text{where } r^2 = x^2 + z^2. \quad (\text{A.1d})$$

Extending the above concept, consider a surface with no variation in the  $\hat{y}$  direction representing an ice sheet sitting on top of the  $z = 0$  plane defined by ice heights  $H_1^{\text{ice}}, H_2^{\text{ice}}, \dots, H_{i+1}^{\text{ice}}$  for  $i$

<sup>1</sup>Although it appears that the solution of normal traction postdates that of the more complicated tangential traction (see references in Section A.1.2), this is not the case. Boussinesq published a number of notes concerning the solution of a point normal force on an infinite half space in *Comptes Rendus de l'Academie des Sciences* in 1878 and 1879. These notes, among others, are gathered in the more complete work cited above.

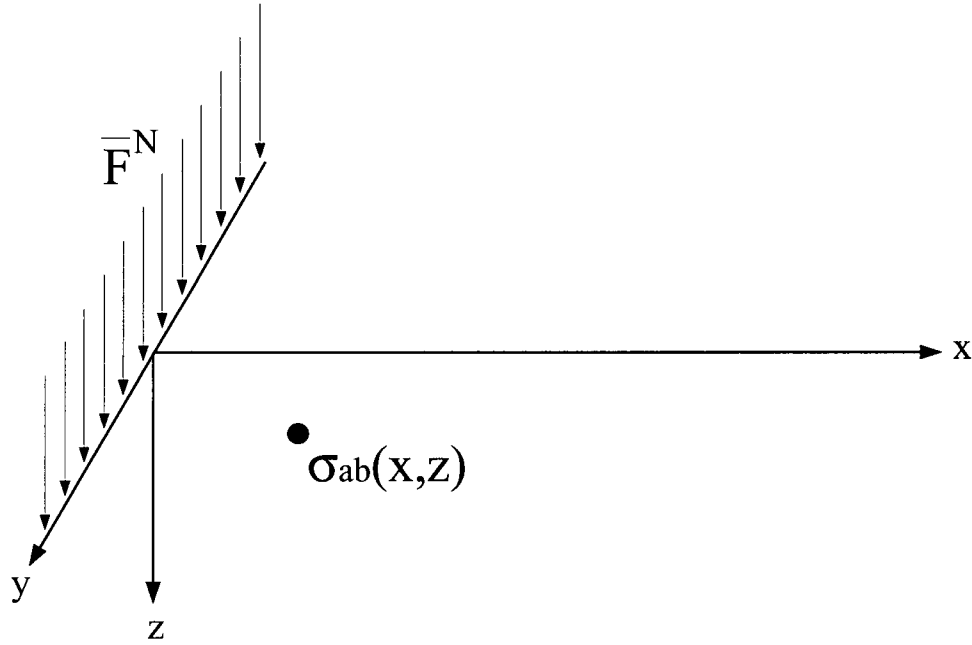


Figure A.1. An infinite line of force normal to the  $z = 0$  plane. The coordinate system is positive  $\hat{z}$  down into the substrate, positive  $\hat{x}$  to the right along the surface. The response at any point on the  $xz$  plane is given by (A.1).

intervals of ice, each of  $\Delta x_i$  in width; the forcing on the boundary is calculated from these. Let the ice heights be defined on the integer grid and the forcing on the half integer grid (see Figure A.2). The normal forcing is given by

$$\bar{F}_{i+\frac{1}{2}}^N = \rho_i g \frac{H_i^{\text{ice}} + H_{i+1}^{\text{ice}}}{2} \quad \text{and} \quad \bar{F}_i^N = \rho_i g H_i^{\text{ice}} \quad (\text{A.2})$$

and the normal forcing slope  $m^N$  is

$$m_{i+\frac{1}{2}}^N = \frac{\bar{F}_{i+1}^N - \bar{F}_i^N}{\Delta x_i}. \quad (\text{A.3})$$

To consider the effect of a continuous ice surface from  $x_{i-\frac{1}{2}}$  to  $x_{i+\frac{1}{2}}$ , a convolution integral must be solved of the form

$$\sigma_{ab} = \int_{x_{i-\frac{1}{2}}}^{x_i} \left[ \bar{F}_{i-\frac{1}{2}}^N + m_{i-\frac{1}{2}}^N (x' - x_{i-\frac{1}{2}}) \right] \mathcal{G}_{ab}^\perp((x - x'), z) dx' + \int_{x_i}^{x_{i+\frac{1}{2}}} \left[ \bar{F}_i^N + m_{i+\frac{1}{2}}^N (x' - x_i) \right] \mathcal{G}_{ab}^\perp((x - x'), z) dx'. \quad (\text{A.4})$$

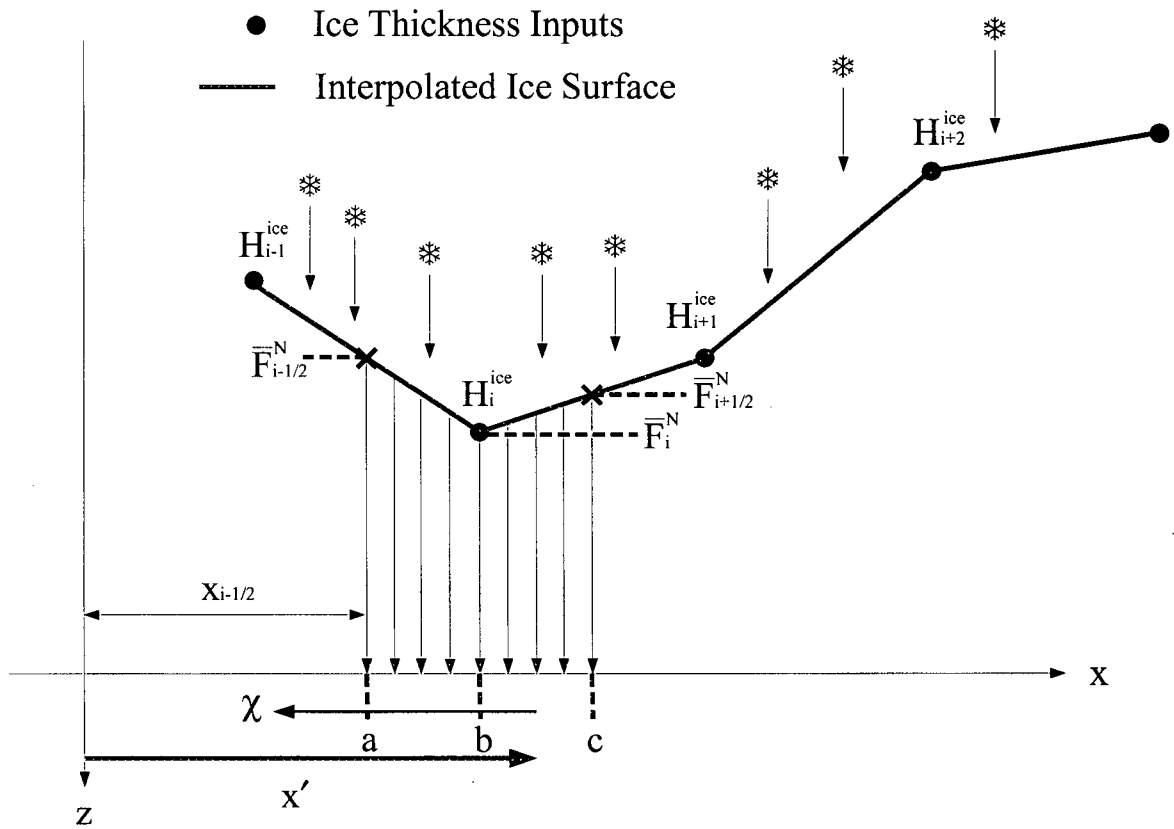


Figure A.2. Discretization of the boundary normal forcing on the  $z = 0$  plane, due to the ice surface defined by  $H_i^{ice}$ ,  $H_{i+1}^{ice}$ , ...

Using (A.1) and substituting  $\chi = x - x'$  in (A.4) (therefore  $dx' = -d\chi$ ),

$$\begin{aligned} \sigma_{xx} = \frac{2z}{\pi} & \left[ - \left( \bar{F}_{i-\frac{1}{2}}^N + m_{i-\frac{1}{2}}^N (x - x_{i-\frac{1}{2}}) \right) \left( \int_{x-x_{i-\frac{1}{2}}}^{x-x_i} -\frac{\chi^2}{(z^2 + \chi^2)^2} d\chi \right) + \right. \\ & m_{i-\frac{1}{2}}^N \left( \int_{x-x_{i-\frac{1}{2}}}^{x-x_i} -\frac{\chi^3}{(z^2 + \chi^2)^2} d\chi \right) - \left( \bar{F}_i^N + m_{i+\frac{1}{2}}^N (x - x_i) \right) \left( \int_{x-x_i}^{x-x_{i+\frac{1}{2}}} -\frac{\chi^2}{(z^2 + \chi^2)^2} d\chi \right) \\ & \left. + m_{i+\frac{1}{2}}^N \left( \int_{x-x_i}^{x-x_{i+\frac{1}{2}}} -\frac{\chi^3}{(z^2 + \chi^2)^2} d\chi \right) \right], \quad (\text{A.5a}) \end{aligned}$$

$$\begin{aligned} \sigma_{zz} = \frac{2z^3}{\pi} & \left[ - \left( \bar{F}_{i-\frac{1}{2}}^N + m_{i-\frac{1}{2}}^N (x - x_{i-\frac{1}{2}}) \right) \left( \int_{x-x_{i-\frac{1}{2}}}^{x-x_i} -\frac{1}{(z^2 + \chi^2)^2} d\chi \right) + \right. \\ & m_{i-\frac{1}{2}}^N \left( \int_{x-x_{i-\frac{1}{2}}}^{x-x_i} -\frac{\chi}{(z^2 + \chi^2)^2} d\chi \right) - \left( \bar{F}_i^N + m_{i+\frac{1}{2}}^N (x - x_i) \right) \left( \int_{x-x_i}^{x-x_{i+\frac{1}{2}}} -\frac{1}{(z^2 + \chi^2)^2} d\chi \right) \\ & \left. + m_{i+\frac{1}{2}}^N \left( \int_{x-x_i}^{x-x_{i+\frac{1}{2}}} -\frac{\chi}{(z^2 + \chi^2)^2} d\chi \right) \right], \quad (\text{A.5b}) \end{aligned}$$

$$\begin{aligned} \sigma_{xz} = \frac{2z^2}{\pi} & \left[ - \left( \bar{F}_{i-\frac{1}{2}}^N + m_{i-\frac{1}{2}}^N (x - x_{i-\frac{1}{2}}) \right) \left( \int_{x-x_{i-\frac{1}{2}}}^{x-x_i} -\frac{\chi}{(z^2 + \chi^2)^2} d\chi \right) + \right. \\ & m_{i-\frac{1}{2}}^N \left( \int_{x-x_{i-\frac{1}{2}}}^{x-x_i} -\frac{\chi^2}{(z^2 + \chi^2)^2} d\chi \right) - \left( \bar{F}_i^N + m_{i+\frac{1}{2}}^N (x - x_i) \right) \left( \int_{x-x_i}^{x-x_{i+\frac{1}{2}}} -\frac{\chi}{(z^2 + \chi^2)^2} d\chi \right) \\ & \left. + m_{i+\frac{1}{2}}^N \left( \int_{x-x_i}^{x-x_{i+\frac{1}{2}}} -\frac{\chi^2}{(z^2 + \chi^2)^2} d\chi \right) \right]. \quad (\text{A.5c}) \end{aligned}$$

All of the convolution integrals are of the form

$$\int_{\chi_1}^{\chi_2} -\frac{\chi^m}{(z^2 + \chi^2)^2} d\chi. \quad (\text{A.6})$$

The necessary integrals follow [Gradshteyn and Ryzhik, 1965, page 69] which are not valid for  $z = 0$ ;

$$\begin{aligned} \int_{\chi_1}^{\chi_2} -\frac{1}{(z^2 + \chi^2)^2} d\chi = -\frac{1}{2z^2} & \left[ \frac{\chi_2}{(z^2 + \chi_2^2)} - \frac{\chi_1}{(z^2 + \chi_1^2)} \right] \\ & - \frac{1}{2z^3} \left[ \tan^{-1} \left( \frac{\chi_2}{z} \right) - \tan^{-1} \left( \frac{\chi_1}{z} \right) \right], \quad (\text{A.7a}) \end{aligned}$$

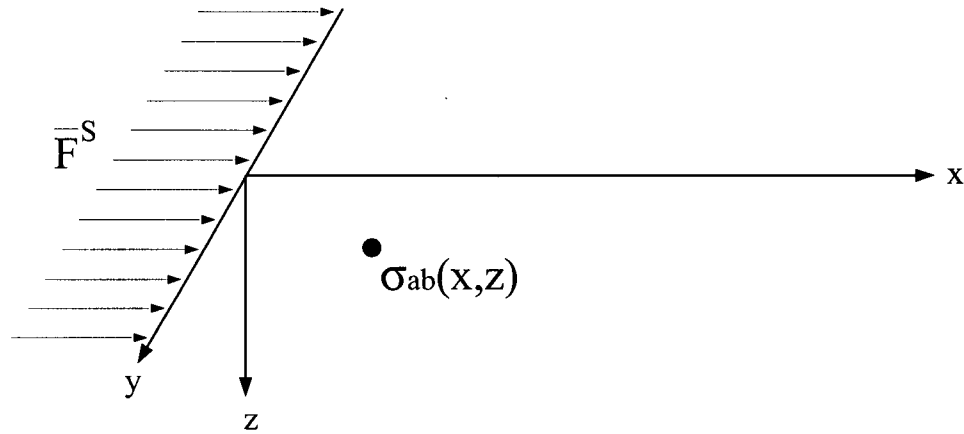


Figure A.3. An infinite line force tangential to the  $z = 0$  plane. The response at any point in the  $xz$  plane is given by (A.8).

$$\int_{\chi_1}^{\chi_2} -\frac{\chi}{(z^2 + \chi^2)^2} d\chi = \frac{1}{2} \left[ \frac{1}{(z^2 + \chi_2^2)} - \frac{1}{(z^2 + \chi_1^2)} \right], \quad (\text{A.7b})$$

$$\int_{\chi_1}^{\chi_2} -\frac{\chi^2}{(z^2 + \chi^2)^2} d\chi = \frac{1}{2} \left[ \frac{\chi_2}{(z^2 + \chi_2^2)} - \frac{\chi_1}{(z^2 + \chi_1^2)} \right] - \frac{1}{2z} \left[ \tan^{-1} \left( \frac{\chi_2}{z} \right) - \tan^{-1} \left( \frac{\chi_1}{z} \right) \right], \quad (\text{A.7c})$$

$$\int_{\chi_1}^{\chi_2} -\frac{\chi^3}{(z^2 + \chi^2)^2} d\chi = -\frac{1}{2} \left[ \ln \left( \frac{(z^2 + \chi_2^2)}{(z^2 + \chi_1^2)} \right) \right] - \frac{z^2}{2} \left[ \frac{1}{(z^2 + \chi_2^2)} - \frac{1}{(z^2 + \chi_1^2)} \right], \quad (\text{A.7d})$$

$$\int_{\chi_1}^{\chi_2} -\frac{\chi^4}{(z^2 + \chi^2)^2} d\chi = -\left[ \frac{\chi_2^3}{(z^2 + \chi_2^2)} - \frac{\chi_1^3}{(z^2 + \chi_1^2)} \right] + 3z^2 \left[ -\frac{1}{2} \left( \frac{\chi_2}{(z^2 + \chi_2^2)} - \frac{\chi_1}{(z^2 + \chi_1^2)} \right) + \frac{1}{2z} \left[ \tan^{-1} \left( \frac{\chi_2}{z} \right) - \tan^{-1} \left( \frac{\chi_1}{z} \right) \right] \right]. \quad (\text{A.7e})$$

### A.1.2 Shear loading

Now consider an analogous case to Figure A.1, but with the line of force acting tangential to the  $z = 0$  plane in the  $\hat{x}$  direction (see Figure A.3). The state of stress due to such an infinite line

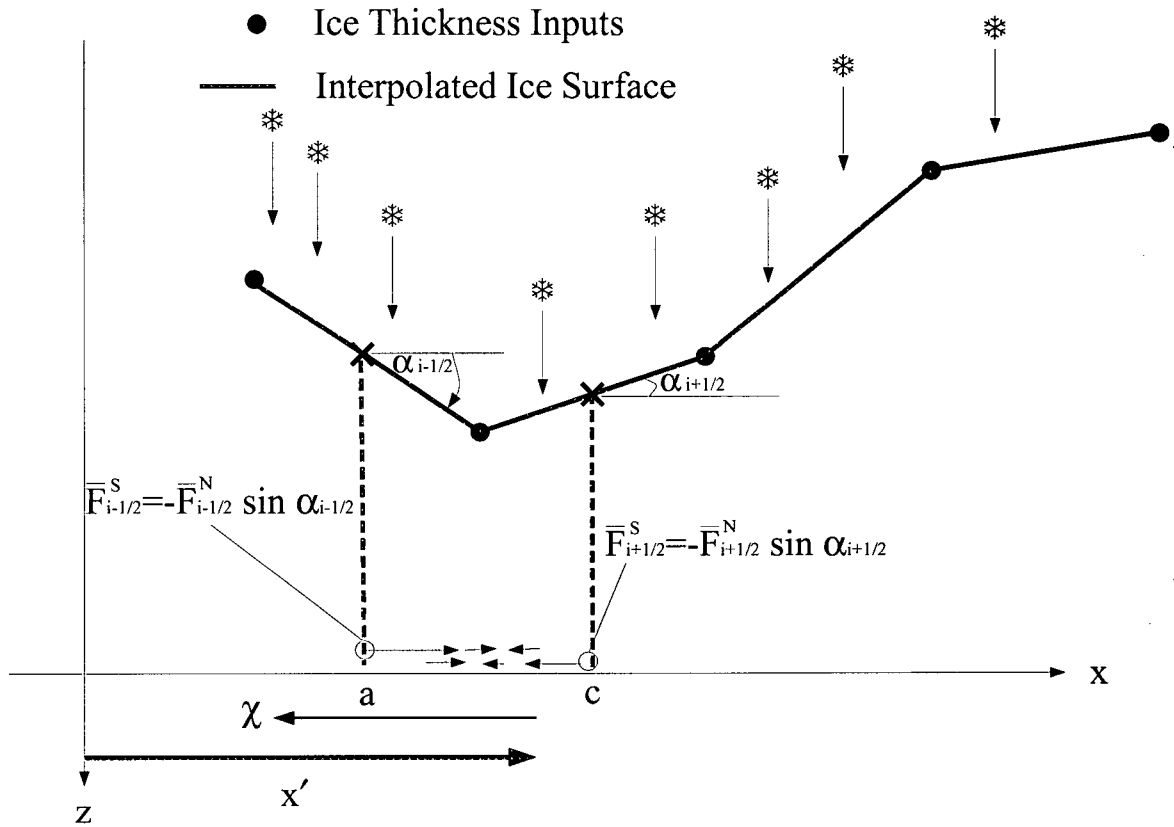


Figure A.4. Discretization of the boundary tangential forcing on the  $z = 0$  plane due to a given ice surface.

of tangential force has the following response functions, which are the two dimensional version of the Cerruti solution for a tangential load on a half-space [Cerruti, 1881/82]. These define  $G_{ab}^{\parallel}$  the Green's functions for a line source

$$\sigma_{xx} = -\frac{2\bar{F}^S x^3}{\pi r^4} \implies G_{xx}^{\parallel} = -\frac{2x^3}{\pi r^4}, \quad (\text{A.8a})$$

$$\sigma_{zz} = -\frac{2\bar{F}^S xz^2}{\pi r^4} \implies G_{zz}^{\parallel} = -\frac{2xz^2}{\pi r^4}, \quad (\text{A.8b})$$

$$\sigma_{xz} = -\frac{2\bar{F}^S x^2z}{\pi r^4} \implies G_{xz}^{\parallel} = -\frac{2x^2z}{\pi r^4}. \quad (\text{A.8c})$$

The tangential forcing is calculated by

$$\bar{F}_{i+\frac{1}{2}}^S = -\bar{F}_{i+\frac{1}{2}}^N \sin \alpha_{i+\frac{1}{2}}^{\text{ice}} \quad (\text{A.9})$$

where  $\alpha^{\text{ice}}$  is the ice-surface dip (see Figure A.4). The tangential forcing slope is given by

$$m_i^S = \frac{\bar{F}_{i+\frac{1}{2}}^S - \bar{F}_{i-\frac{1}{2}}^S}{\Delta x_i}. \quad (\text{A.10})$$

Consider the effect of continuous tangential loading from  $x_n$  to  $x_{n+1}$ ; a convolution integral of the form

$$\sigma_{ab} = \int_{x_{i-\frac{1}{2}}}^{x_{i+\frac{1}{2}}} \left[ \bar{F}_i^S + m_i^S(x' - x_{i-\frac{1}{2}}) \right] \mathcal{G}_{ab}^{\parallel}((x - x'), z) dx' \quad (\text{A.11})$$

must be evaluated. Substituting  $\chi = x - x'$  as above and using the expression for  $\mathcal{G}_{ab}^{\parallel}$  from (A.8)

$$\sigma_{xx} = \frac{2}{\pi} \left[ - \left( \bar{F}_i^S + m_i^S(x - x_{i-\frac{1}{2}}) \right) \left( \int_{x-x_{i-\frac{1}{2}}}^{x+x_{i+\frac{1}{2}}} - \frac{\chi^3}{(z^2 + \chi^2)^2} d\chi \right) + m_i^S \left( \int_{x-x_{i-\frac{1}{2}}}^{x+x_{i+\frac{1}{2}}} \frac{\chi^4}{(z^2 + \chi^2)^2} d\chi \right) \right], \quad (\text{A.12a})$$

$$\sigma_{zz} = \frac{2z^2}{\pi} \left[ - \left( \bar{F}_i^S + m_i^S(x - x_{i-\frac{1}{2}}) \right) \left( \int_{x-x_{i-\frac{1}{2}}}^{x+x_{i+\frac{1}{2}}} - \frac{\chi}{(z^2 + \chi^2)^2} d\chi \right) + m_i^S \left( \int_{x-x_{i-\frac{1}{2}}}^{x+x_{i+\frac{1}{2}}} \frac{\chi^2}{(z^2 + \chi^2)^2} d\chi \right) \right], \quad (\text{A.12b})$$

$$\sigma_{xz} = \frac{2z}{\pi} \left[ - \left( \bar{F}_i^S + m_i^S(x - x_{i-\frac{1}{2}}) \right) \left( \int_{x-x_{i-\frac{1}{2}}}^{x+x_{i+\frac{1}{2}}} - \frac{\chi^2}{(z^2 + \chi^2)^2} d\chi \right) + m_i^S \left( \int_{x-x_{i-\frac{1}{2}}}^{x+x_{i+\frac{1}{2}}} \frac{\chi^3}{(z^2 + \chi^2)^2} d\chi \right) \right]. \quad (\text{A.12c})$$

The integrals are solved using (A.7).

For each grid interval, the effect of the tangential and normal loading is calculated for every point  $x_i - \epsilon_x < x_i < x_i + \epsilon_x$  where  $\epsilon_x$  is chosen such that the effect of the loading beyond  $x_i - \epsilon_x$  and  $x_i + \epsilon_x$  is small. The effect of each ice interval's normal and tangential loading is calculated and summed together to get a final state of stress  $\sigma_{ab}(m, n, z)$  at any arbitrarily fine sub-grid.

## A.2 Evaluation of failure criterion

In soil science, a different sign convention is used than in elasticity; compressive forces are positive and the major principal stress is the most compressive. In order to be consistent with the soil

science literature, from which the failure criterion is taken, a new stress tensor  $\tilde{\sigma}_{ab}$  is used defined by  $\tilde{\sigma}_{ab} = -\sigma_{ab}$ .

For any state of stress, a coordinate system can be found on which there is zero shear stress on the planes associated with the coordinate directions; these are the principal axes. For a principal axis direction  $\hat{\nu}_a$ , the traction vector acting on a plane normal to  $\hat{\nu}_a$  is  $\tilde{\sigma}_{ab}\hat{\nu}_a$ . As the stress is acting on a principal plane, it can be described by  $\lambda^{(a)}\hat{\nu}_a$  where the scalar  $\lambda^{(a)}$  is the principal stress associated with the principal axis  $\hat{\nu}_a$ . Therefore we can write

$$\tilde{\sigma}_{ab}\hat{\nu}_b = \lambda^{(a)}\hat{\nu}_a \quad (\text{A.13})$$

$$\text{or } \tilde{\sigma}_{ab}\hat{\nu}_b - \lambda^{(a)}\delta_{ab}\hat{\nu}_a = 0 \quad (\text{A.14})$$

where  $\delta_{ab}$  is the Kronecker delta. Equation (A.14) has a non-trivial solution when

$$\|\tilde{\sigma}_{ab} - \lambda^{(a)}\delta_{ab}\| = 0. \quad (\text{A.15})$$

This is solved to give the two principal stresses  $\lambda^{\alpha=1,2}$  where they are ordered such that  $\lambda^1 > \lambda^2$ . The components of the principal direction vector  $\hat{\nu}_a$  are given by solving (A.14) for each  $\lambda^{(a)}$ .

Consider the stress acting on a plane rotated by  $\gamma$  with respect to the major principal plane (the plane for which  $\hat{\nu}_1$  is the normal). In terms of the principal coordinate system, the normal vector  $n_a$  of this plane will be given by

$$n_a = \cos \gamma \hat{\nu}_1 + \sin \gamma \hat{\nu}_2. \quad (\text{A.16})$$

The normal stress  $\tilde{\sigma}_N$  and the shear stress  $\tilde{\sigma}_S$  on a surface with a normal vector  $n_a$  are given by

$$\tilde{\sigma}_N = \lambda^{(1)}n_1^2 + \lambda^{(2)}n_2^2 \quad \text{and} \quad \tilde{\sigma}_S = n_1n_2(\lambda^{(1)} - \lambda^{(2)}) \quad (\text{A.17})$$

and using the trigonometric identities that

$$\cos^2 \gamma = \frac{\cos 2\gamma + 1}{2} \quad \text{and} \quad \sin \gamma \cos \gamma = \frac{\sin 2\gamma}{2}, \quad (\text{A.18})$$

$\tilde{\sigma}_N$  and  $\tilde{\sigma}_S$  can be expressed in terms of functions of  $2\gamma$  as

$$\tilde{\sigma}_N = \frac{\lambda^{(1)} + \lambda^{(2)}}{2} + \frac{(\lambda^{(1)} - \lambda^{(2)}) \cos 2\gamma}{2}, \quad (\text{A.19})$$

$$\tilde{\sigma}_S = \frac{(\lambda^{(1)} - \lambda^{(2)}) \sin 2\gamma}{2}. \quad (\text{A.20})$$

The interplay between the shear stress and the normal stress acting on a plane as in (A.19) and (A.20) describe a half circle in  $\tilde{\sigma}_S$  versus  $\tilde{\sigma}_N$  space when  $\gamma$  varies from 0 to  $\pi/2$ . This is a Mohr circle and every point on the circle corresponds to a plane at an angle  $\gamma$  to the plane of the major

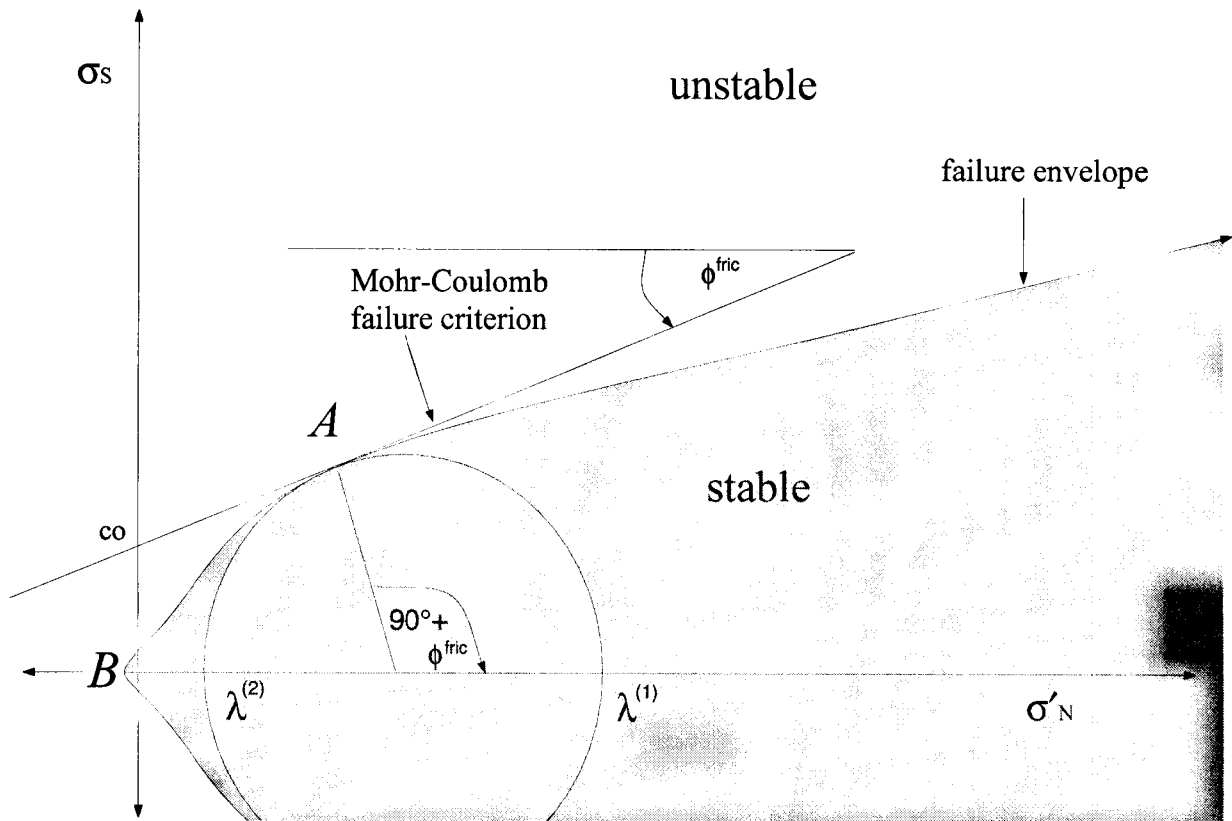


Figure A.5. A sketch of  $\tilde{\sigma}'_N$  versus  $\tilde{\sigma}_S$  showing a Mohr circle, a failure envelope and the Mohr-Coulomb failure criterion, which is a linearization of the failure envelope.

principal direction (see Figure A.5 and note that the abscissa  $\bar{\sigma}'_N$  is related to  $\bar{\sigma}_N$  by a translation described below).

Also shown in Figure A.5 is the failure envelope<sup>2</sup> — at a shear stress above the envelope, shear failure will occur (a tensile mode I failure can occur at point *B* which has zero shear). This can be approximated by the Mohr-Coulomb failure criterion that predicts failure when

$$\bar{\sigma}_S > c_0 + \mu^{\text{int}} \bar{\sigma}'_N \quad (\text{A.21})$$

where  $c_0$ , the cohesion, and  $\mu^{\text{int}} = \tan \phi^{\text{fric}}$  ( $\phi^{\text{fric}}$  is the internal angle of friction) are properties of the soil.  $\bar{\sigma}'_N$  is a modified normal stress that takes into account the normal stress due to the forcing at the  $z = 0$  boundary (given by (A.19)) as well as a hydrostatic compressive stress due to the overlying soil and a hydrostatic tensile stress due to pore water pressure. The soil overburden increases the confining pressure which shifts the Mohr circle away from failure (recall that a compressive stress is positive using the current sign convention) while the pore pressure has the opposite effect and forces the Mohr circle left in Figure A.5. This can be written as

$$\bar{\sigma}'_N = \rho_s g z + \bar{\sigma}_N - P_w \quad (\text{A.22})$$

where  $\rho_s$  is the density of the soil and  $P_w$  is the cavity water pressure.

The failure will occur first at the point labelled *A* in Figure A.5 corresponding to a plane at an angle of  $45^\circ + \phi^{\text{fric}}/2$  to the plane of the major principal axis. This corresponds to an angle of  $45^\circ - \phi^{\text{fric}}/2$  between the plane of failure and the major principal axis.

---

<sup>2</sup>This is the catastrophic failure envelope. Subcritical failure can occur within the stable region as discussed in Section 3.2.1.

## Appendix B

# Single Clast Rotational Mixing

A particle in a shear flow will rotate to produce a perturbation velocity field, which leads to perpendicular motion not present in the initial field. In the context of a shear flow at the base of a glacier, this represents vertical mixing. Rotational structures of this kind are observed in deformed sediment [*van der Meer*, 1997] and analogies are expected in basal ice.

I begin by seeking a perturbation flow caused by a freely rotating cylinder immersed in a background regular shear flow. The steady state solution is then explored and the resultant mixing examined.

### B.1 Perturbation due to a cylinder

Consider a viscous fluid flowing in a uniform linear shear flow. In Cartesian coordinates, such a flow is described as (see Figure B.1)

$$\mathbf{v}_i = \beta y \hat{\mathbf{x}}. \quad (\text{B.1})$$

Polar coordinates  $(r, \theta, z)$  are better suited to the problem and (B.1) is re-written as

$$\mathbf{v}_i = [\beta r \sin \theta \cos \theta] \hat{\mathbf{r}} + [-\beta r \sin^2 \theta] \hat{\boldsymbol{\theta}}. \quad (\text{B.2})$$

It will be convenient below to write the angular dependence of  $\mathbf{v}_i$  in terms of  $\sin s\theta$  and  $\cos s\theta$  and the trigonometric identities  $\sin^2 \theta \equiv \frac{1}{2} - \frac{\cos 2\theta}{2}$  and  $\sin \theta \cos \theta \equiv \frac{\sin 2\theta}{2}$  are used to write (B.2) as

$$\mathbf{v}_i = \left[ \frac{\beta r}{2} \sin 2\theta \right] \hat{\mathbf{r}} + \left[ \frac{\beta r}{2} \cos 2\theta - \frac{\beta r}{2} \right] \hat{\boldsymbol{\theta}}. \quad (\text{B.3})$$

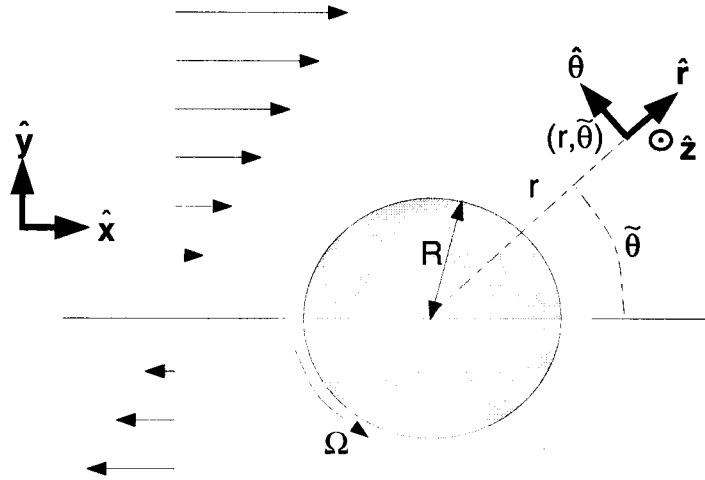


Figure B.1. The geometry of the rotating cylinder problem. The cylinder is infinite in the  $\hat{z}$  direction, has a radius of  $R$  and can rotate with angular velocity  $\Omega\hat{z}$ . The background shear flow described in (B.1) and (B.2) is also shown.

An infinitely long cylinder of radius  $R$  is introduced into this background flow aligned along the  $\hat{z}$  direction, rotating about this axis with an angular velocity  $\Omega$  (see Figure B.1). The total fluid velocity  $\mathbf{u}$  is

$$\mathbf{u} = \mathbf{v}_i + \mathbf{p} \quad (\text{B.4})$$

where  $\mathbf{p}$  is the perturbation flow from the cylinder.

The governing equations for  $\mathbf{u}$  are conservation of mass for an incompressible fluid and the Navier-Stokes equation,

$$\nabla \cdot \mathbf{u} = 0, \quad (\text{B.5})$$

$$\rho \left( \frac{\partial \mathbf{u}}{\partial t} + \mathbf{u} \cdot \nabla \mathbf{u} \right) = -\nabla P + \eta \nabla^2 \mathbf{u}, \quad (\text{B.6})$$

where  $\eta$  is the viscosity,  $P$  is the pressure and fluid body forces are assumed negligible. The effective viscosity of ice  $\eta$  is large (for example,  $\eta = 1 \times 10^6$  Pa a in Table 3.3) and the inertial terms of (B.6) can be discarded, as is typical for creeping flows, to obtain

$$\nabla P = \eta \nabla^2 \mathbf{u}. \quad (\text{B.7})$$

The divergence and the Laplacian in cylindrical coordinates are given by

$$\nabla \cdot \mathbf{A} = \frac{1}{r} \left[ \frac{\partial(rA_r)}{\partial r} + \frac{\partial A_\theta}{\partial \theta} + \frac{\partial(rA_z)}{\partial z} \right], \quad (\text{B.8})$$

$$\nabla^2 A_n = \frac{\partial^2 A_n}{\partial r^2} + \frac{1}{r} \frac{\partial A_n}{\partial r} + \frac{1}{r^2} \frac{\partial^2 A_n}{\partial \theta^2} + \frac{\partial^2 A_n}{\partial z^2}. \quad (\text{B.9})$$

Substitution of (B.2) or (B.3) into the above expressions shows that  $\nabla \cdot \mathbf{v}_i = 0$ ,  $\nabla^2 v_{i_r} = 0$  and  $\nabla^2 v_{i_\theta} = 0$ . Linear superposition of the background flow and the perturbation flow allows the governing equations (B.5) and (B.7) to be rewritten in terms of the perturbation velocity  $\mathbf{p}$  so that

$$\nabla \cdot \mathbf{p} = 0, \quad (\text{B.10})$$

$$\nabla P = \eta \nabla^2 \mathbf{p}. \quad (\text{B.11})$$

Symmetry disallows any perturbation flow in the  $\hat{\mathbf{z}}$  direction and the problem is two dimensional. Therefore it is advantageous to introduce a stream function  $\psi$  such that

$$\mathbf{p} \equiv \nabla \times \psi \hat{\mathbf{z}}. \quad (\text{B.12})$$

From this definition it follows that

$$\mathbf{p} = \frac{1}{r} \frac{\partial \psi}{\partial \theta} \hat{\mathbf{r}} - \frac{\partial \psi}{\partial r} \hat{\boldsymbol{\theta}} \quad (\text{B.13})$$

and because of the vector identity  $\nabla \cdot (\nabla \times \mathbf{A}) = 0$ , the form of  $\mathbf{p}$  in (B.12) automatically satisfies the requirement from (B.10) that  $\nabla \cdot \mathbf{p} = 0$ .

Another expedient manipulation is to take the curl of (B.7) which then reduces to Laplace's equation

$$\nabla^2 \mathbf{w} = 0, \quad (\text{B.14})$$

where  $\mathbf{w}$  is the vorticity of the perturbation field, defined as  $\mathbf{w} \equiv \nabla \times \mathbf{p}$ . As for the stream function, the two-dimensional flow reduces the vorticity to a single component

$$\mathbf{w} = \frac{1}{r} \left[ \frac{\partial(r p_\theta)}{\partial r} - \frac{\partial p_r}{\partial \theta} \right] \hat{\mathbf{z}} \quad (\text{B.15})$$

and using (B.13) this becomes

$$\mathbf{w} = \left[ -\frac{\partial^2 \psi}{\partial r^2} - \frac{1}{r} \frac{\partial \psi}{\partial r} - \frac{1}{r^2} \frac{\partial^2 \psi}{\partial \theta^2} \right] \hat{\mathbf{z}} = -\nabla^2 \psi. \quad (\text{B.16})$$

Because the vorticity satisfies Laplace's equation in (B.14), the stream function satisfies the biharmonic equation

$$\nabla^4 \psi = 0. \quad (\text{B.17})$$

By assuming that  $\psi$  has a solution that is separable in variables and is of the form  $\mathcal{R}(r)\mathcal{I}(\theta)$ , (B.17) can be expanded by repeated application of (B.9) to

$$\mathcal{R} \frac{\partial^4 \mathcal{I}}{\partial \theta^4} - 2 \frac{\partial^2 \mathcal{I}}{\partial \theta^2} \left[ -r^2 \frac{\partial^2 \mathcal{R}}{\partial r^2} + r \frac{\partial \mathcal{R}}{\partial r} - 2\mathcal{R} \right] + \mathcal{I} \left[ r^4 \frac{\partial^4 \mathcal{R}}{\partial r^4} + 2r^3 \frac{\partial^3 \mathcal{R}}{\partial r^3} - r^2 \frac{\partial^2 \mathcal{R}}{\partial r^2} + r \frac{\partial \mathcal{R}}{\partial r} \right] = 0. \quad (\text{B.18})$$

The  $\mathcal{T}(\theta)$  portion of the solution must be periodic in  $2\pi$ , which prompts the search for angular solutions of the form  $\mathcal{T} = e^{is\theta}$  where  $s$  is restricted to integers. The fact that each term has the form  $r^p \partial^p \mathcal{R} / \partial r^p$  suggests Euler radial solutions of the form  $\mathcal{R} = r^p$ . By substitution of  $\Omega = e^{is\theta}$  and  $\mathcal{R} = r^p$  into (B.18) the following expression is obtained relating  $p$  and  $s$  for the basis functions  $r^p e^{is\theta}$

$$s^4 + 2s^2 [-p(p-1) + p - 2] + [p(p-1)(p-2)(p-3) + 2p(p-1)(p-2) - p(p-1) + p] = 0,$$

or

$$p^4 - 4p^3 + (4 - 2s^2)p^2 + 4s^2p - 4s^2 + s^4 = 0. \quad (\text{B.19})$$

The particular solution for  $\psi$  will be of the form

$$\psi = \sum_s \sum_p A_s^p r^p e^{is\theta}. \quad (\text{B.20})$$

The appropriate choices for  $s$  become apparent when the boundary conditions at the cylinder surface are considered. There is an impermeable boundary at  $r = R$  which requires the flow normal to the cylinder to be zero. Also at this boundary a no-slip condition is imposed. These can be expressed as

$$\text{at } r = R \begin{cases} \mathbf{u} \cdot \hat{\mathbf{r}} = u_r = 0, & \text{impermeable boundary,} \\ \mathbf{u} \times \hat{\mathbf{r}} = u_\theta = \Omega R, & \text{no slip.} \end{cases} \quad (\text{B.21})$$

This is transformed into conditions for  $\mathbf{p}$  using (B.3) and (B.4)

$$\text{at } r = R \begin{cases} p_r = -\frac{\beta R}{2} \sin 2\theta, & \text{impermeable boundary,} \\ p_\theta = -\frac{\beta R}{2} \cos 2\theta + \frac{\beta R}{2} + \Omega R, & \text{no slip.} \end{cases} \quad (\text{B.22})$$

By inspection of the assumed form of the angular function  $\mathcal{T}$  and the boundary condition on  $p_\theta$  at  $r = R$  it is clear that  $s$  must take values of 0 and 2. The 4 roots of (B.19) when  $s = 0$  are double roots of  $p = 0$  and 2; when  $s = 2$ , the roots of (B.19) are  $p = 0, 2, -2$  and 4. Therefore (B.20) can be expanded to

$$\begin{aligned} \psi = & A_0^0 + {}^*A_0^0 \ln r + A_0^2 r^2 + {}^*A_0^2 r^2 \ln r \\ & + A_2^{-2} r^{-2} \cos 2\theta + A_2^0 \cos 2\theta + A_2^2 r^2 \cos 2\theta + A_2^4 r^4 \cos 2\theta, \end{aligned} \quad (\text{B.23})$$

where the starred coefficients account for the double roots. The boundary condition far from the cylinder is that all components of the perturbation field must vanish, implying that positive

powers of  $r$  must be disallowed<sup>1</sup> and  $A_2^2 = A_2^4 = A_0^2 = {}^*A_0^2 = 0$ . Using (B.13) the perturbation flow is given by

$$p_r = \frac{1}{r} \frac{\partial \psi}{\partial \theta} = -2A_2^{-2} r^{-3} \sin 2\theta - 2A_2^0 r^{-1} \sin 2\theta, \quad (\text{B.24a})$$

$$p_\theta = -\frac{\partial \psi}{\partial r} = -{}^*A_0^0 r^{-1} + 2A_2^{-2} r^{-3} \cos 2\theta. \quad (\text{B.24b})$$

By applying the boundary conditions at  $r = R$  set forth in (B.22) the remaining non-zero coefficients  $A_s^p$  can be written in terms of  $\beta$ ,  $\Omega$  and  $R$  as

$$\frac{2A_2^{-2}}{R^3} + \frac{2A_2^0}{R} = \frac{\beta R}{2} \quad \text{from } \sin 2\theta \text{ terms in } p_r, \quad (\text{B.25a})$$

$$\frac{2A_2^{-2}}{R^3} = -\frac{\beta R}{2} \quad \text{from } \cos 2\theta \text{ terms in } p_\theta, \quad (\text{B.25b})$$

$$-\frac{{}^*A_0^0}{R} = \frac{\beta R}{2} + \Omega R \quad \text{from constant terms in } p_\theta. \quad (\text{B.25c})$$

By simplifying and substituting (B.25b) into (B.25a),

$$A_2^{-2} = -\frac{\beta R^4}{4}, \quad (\text{B.26a})$$

$$A_2^0 = \frac{\beta R^2}{2}, \quad (\text{B.26b})$$

$${}^*A_0^0 = -\frac{\beta R^2}{2} - \Omega R^2. \quad (\text{B.26c})$$

Therefore the solution for the perturbation flow from the cylinder is

$$\mathbf{p} = \left[ \frac{\beta R^4}{2} \frac{1}{r^3} \sin 2\theta - \beta R^2 \frac{1}{r} \sin 2\theta \right] \hat{\mathbf{r}} + \left[ \left( \frac{\beta R^2}{2} + \Omega R^2 \right) \frac{1}{r} - \frac{\beta R^4}{2} \frac{1}{r^3} \cos 2\theta \right] \hat{\boldsymbol{\theta}}, \quad (\text{B.27})$$

and the complete solution is

$$\mathbf{u} = \left[ \beta \sin 2\theta \left( \frac{R^4}{2r^3} - \frac{R^2}{r} + \frac{r}{2} \right) \right] \hat{\mathbf{r}} + \left[ \left( \frac{\beta R^2}{2} + \Omega R^2 \right) \frac{1}{r} - \frac{\beta r}{2} + \beta \cos 2\theta \left( \frac{r}{2} - \frac{R^4}{2r^3} \right) \right] \hat{\boldsymbol{\theta}}. \quad (\text{B.28})$$

## B.2 Steady state rotation

The previous section described the velocity field in terms of  $\beta$ ,  $R$  and  $\Omega$ . The flow parameter  $\beta$  and the radius  $R$  are both free parameters, but steady-state angular  $\Omega$  is determined by the

<sup>1</sup>The boundary condition is imposed on the perturbation field, not the stream function. Therefore a  $\ln r$  solution for  $\psi$  is permissible.

viscous forces on the cylinder given by the non-zero components of the viscous stress tensor  $\sigma_{ab}$ . Symmetry dictates that the total force on the cylinder be zero but the moment of the forces will, in general, be non-zero because of off-diagonal components given by

$$\sigma_{r\theta} = \sigma_{\theta r} \equiv \eta \left[ \frac{1}{r} \left( \frac{\partial(ru_\theta)}{\partial r} + \frac{\partial u_r}{\partial \theta} \right) \right]. \quad (\text{B.29})$$

Using (B.28) into (B.29) gives

$$\sigma_{r\theta} = \eta \left[ r \left( -\frac{2}{r^3} \left( \frac{\beta R^2}{2} + \Omega R^2 \right) + \frac{4}{r^5} \left( \frac{\beta R^4}{2} \cos 2\theta \right) \right) + \frac{1}{r} \left( 2 \cos 2\theta \left( \frac{\beta R^4}{2r^3} - \frac{\beta R^2}{r} + \frac{\beta r}{2} \right) \right) \right], \quad (\text{B.30})$$

and at  $r = R$ ,

$$\sigma_{r\theta} = \eta \left[ -2 \left( \frac{\beta}{2} + \Omega \right) + 2\beta \cos 2\theta \right]. \quad (\text{B.31})$$

Cross the viscous force (purely in the  $\hat{\theta}$  direction) with  $R\hat{r}$  to get the moment  $\mathcal{M}$  as

$$\mathcal{M} = \eta R \left[ -2 \left( \frac{\beta}{2} + \Omega \right) + 2\beta \cos 2\theta \right] \hat{z}. \quad (\text{B.32})$$

Integrate (B.32) around the surface of the cylinder to get the total moment  $\mathcal{M}^T$ ,

$$\begin{aligned} \mathcal{M}^T &= \int_0^1 \int_0^{2\pi} \eta R \left[ -2 \left( \frac{\beta}{2} + \Omega \right) + 2\beta \cos 2\theta \right] (R d\theta) dz, \\ &= \eta \left[ -2 \left( \frac{\beta}{2} + \Omega \right) \right] 2\pi R^2, \end{aligned} \quad (\text{B.33})$$

for a unit length strip of cylinder. A steady state solution is sought, requiring  $\mathcal{M}^T = 0$ . Thus the steady state rotation is

$$\Omega = -\frac{\beta}{2} \quad (\text{B.34})$$

which is equivalent to the vorticity of the background flow. This is consistent with the results of *Ho and Leal* [1974] where a similar result is derived for an isolated sphere.

### B.3 Resultant mixing

Figure B.2 shows the total field  $\mathbf{u}$  as described by (B.28). The contours are of the vertical component (entirely from the perturbation field) with dashed contours for negative vertical velocities and solid contours for positive vertical velocities.

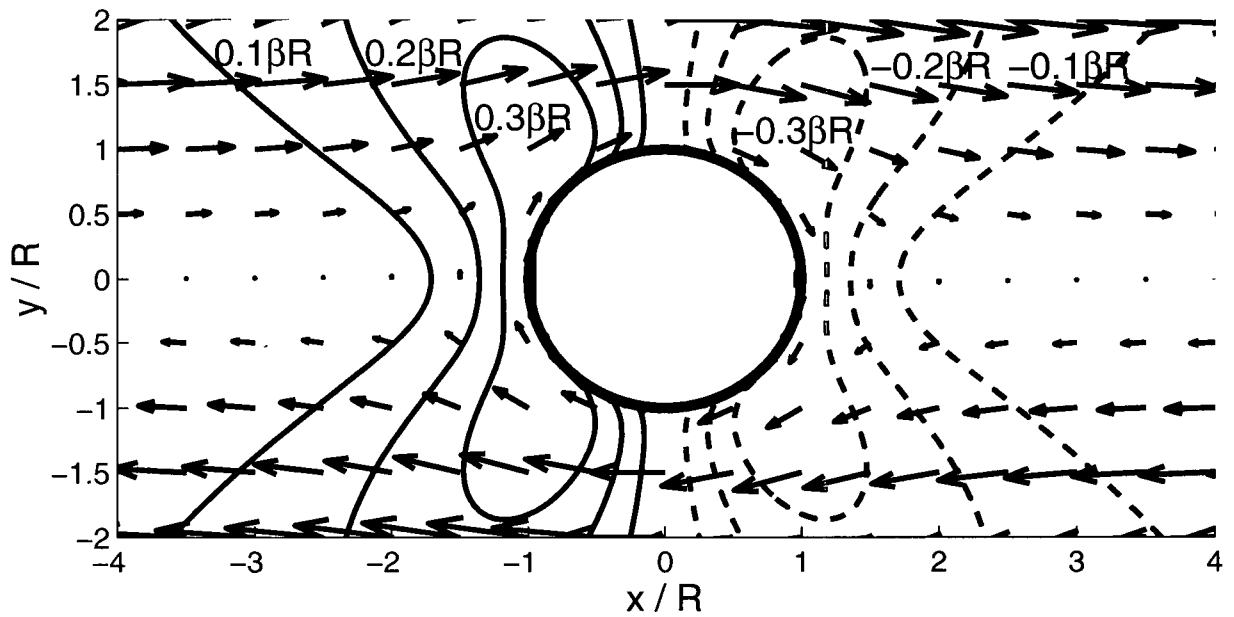


Figure B.2. The total field  $\mathbf{u}$  with  $\Omega = -\beta/2$ . The contours are of vertical velocity with dashed contours showing downward fluxes and the solid contours showing upward fluxes.

To examine vertical mixing, integrate the vertical component of the velocity from (B.28) along the  $\theta = 0^\circ$  line for the steady state. This gives  $D_{\text{rot}}$ , an estimate of the diffusion coefficient associated with the process, as

$$D_{\text{rot}} = \int_{\infty}^R \left[ -\frac{\beta r}{2} + \beta \left( \frac{r}{2} - \frac{R^4}{2r^3} \right) \right] dr = \left| \frac{\beta R^4}{4} \frac{1}{r^2} \right|_{\infty}^R = \frac{\beta R^2}{4} \quad (\text{B.35})$$